

NASA TECHNICAL NOTE



NASA TN D-8408 *c.l*

NASA TN D-8408



LOAN COPY: RE
AFWL TECHNICAL LIBRARY
KIRTLAND AFB, N. M.

**LASER VELOCIMETER SYSTEMS ANALYSIS
APPLIED TO A FLOW SURVEY ABOVE
A STALLED WING**

*Warren H. Young, Jr., James F. Meyers,
and Timothy E. Hepner*

*Langley Research Center
and*

*Langley Directorate,
U.S. Army Air Mobility R&D Laboratory
Hampton, Va. 23665*





0134117

1. Report No. NASA TN D-8408		2. Government Accession No.		3. Recipient's Catalog No.	
4. Title and Subtitle LASER VELOCIMETER SYSTEMS ANALYSIS APPLIED TO A FLOW SURVEY ABOVE A STALLED WING				5. Report Date August 1977	
				6. Performing Organization Code	
7. Author(s) Warren H. Young, Jr., James F. Meyers, and Timothy E. Hepner				8. Performing Organization Report No. L-11105	
				10. Work Unit No. 505-10-21-01	
9. Performing Organization Name and Address NASA Langley Research Center and Langley Directorate, USAAMRDL Hampton, VA 23665				11. Contract or Grant No.	
				13. Type of Report and Period Covered Technical Note	
12. Sponsoring Agency Name and Address National Aeronautics and Space Administration Washington, DC 20546 and U.S. Army Air Mobility R&D Laboratory Moffet Field, CA 94035				14. Army Project No. 1F161102A35A	
15. Supplementary Notes Warren H. Young, Jr., and Timothy E. Hepner: Langley Directorate, U.S. Army Air Mobility R&D Laboratory. James F. Meyers: Langley Research Center. Appendix A by William V. Feller. Appendix B by Janet W. Campbell.					
16. Abstract <p>A laser velocimeter operating in the backscatter mode was used to survey the flow above a stalled wing installed in the Langley high-speed 7- by 10-foot tunnel. Polarization was used to separate the two orthogonal velocity components of the fringe-type laser velocimeter, and digital counters were used for data processing. The velocities of the kerosene seed particles were measured with less than 2-percent uncertainty. The particle velocity measurements were collected into histograms.</p> <p>The flow-field survey was carried out above an aspect-ratio-8 stalled wing with an NACA 0012 section. The angle of attack was 19.5°, the Mach number was 0.49, and the Reynolds number was 1.4×10^6. The flow field was characterized by the periodic shedding of discrete vortices from near the crest of the airfoil.</p>					
17. Key Words (Suggested by Author(s)) Laser Doppler velocimeter Velocity measurement Aerodynamic stalling Unsteady flow Vortex streets Wakes Vortices Kármán vortex street Histograms				18. Distribution Statement Unclassified - Unlimited Subject Category 01	
19. Security Classif. (of this report) Unclassified		20. Security Classif. (of this page) Unclassified		21. No. of Pages 157	22. Price* \$6.75

LASER VELOCIMETER SYSTEMS ANALYSIS APPLIED TO A FLOW SURVEY ABOVE A STALLED WING

Warren H. Young, Jr.,* James F. Meyers,
and Timothy E. Hepner*
Langley Research Center

SUMMARY

A laser velocimeter operating in the backscatter mode was used to survey the flow above a stalled wing installed in the Langley high-speed 7- by 10-foot tunnel. Polarization was used to separate the two orthogonal velocity components of the fringe-type laser velocimeter, and digital counters were used for data processing. The velocities of the kerosene seed particles were measured with less than 2-percent uncertainty. The particle velocity measurements were collected into histograms.

The flow-field survey was carried out above an aspect-ratio-8 stalled wing with an NACA 0012 section. The angle of attack was 19.5° , the Mach number was 0.49, and the Reynolds number was 1.4×10^6 . The flow field was characterized by the periodic shedding of discrete vortices from near the crest of the airfoil.

INTRODUCTION

An extensive investigation into the process of the dynamic stall of an airfoil at large angles of attack, summarized in reference 1, has delineated the features of the stalling process. The physical processes involved in recovery from stall and the effects of compressibility are considerably less understood. The present experiment was designed to determine the applicability of a laser velocimeter to velocity measurements in a separated region and to provide a preliminary definition of the flow field about a fully stalled airfoil at a Mach number typical of the retreating blade of a helicopter rotor.

References 2 and 3 describe the use of both hot wires and pitot probes to measure the flow in the separated regions on an airfoil at angles larger than the stall angle. The limitations on the use of a probe in a separated flow include directional ambiguity, uncertainty in probe alignment with flow direction, and probe interference effects. However, a laser velocimeter offers no flow interference or flow alignment difficulties and is capable of being modified to eliminate directional ambiguity. The laser velocimeter can

*Langley Directorate, U.S. Army Air Mobility R&D Laboratory.

also make virtually instantaneous measurements and features a small common volume. However, the assessment of the applicability of the laser velocimeter to the measurements above the stalled wing requires the consideration of the entire laser velocimeter, seed generation, and data-acquisition system.

A fringe-type laser velocimeter was installed in the Langley high-speed 7- by 10-foot tunnel. The laser velocimeter used polarization separation to measure two components of velocity. Operation in the backscatter mode allowed the measurement location (the common volume) to be readily scanned. The scan and velocity measurements were carried out in a vertical plane through the tunnel center line near a wing with an NACA 0012 cross section that was set to an angle of attack of 19.5° . The Mach number was 0.49, and the nominal value of Reynolds number was 1.4×10^6 . Because the wing was straight, unyawed, and had an aspect ratio of 8, and because all the measurements were made in the plane of the center span, the flow was treated as two-dimensional. Frequencies and time histories were obtained from absolute pressure transducers on the wing surface. In addition, interpretation of the laser velocimeter results was assisted by observation of tufts in the separated region to determine the local flow direction. The wing was completely stalled, and the flow was separated over the portion of the upper surface that was aft of the crest.

The use of kerosene smoke for seeding the flow is described in appendix A by William V. Feller. An explanation of the significance and interpretation of the statistical nature of histograms is given in appendix B by Janet W. Campbell.

SYMBOLS

C	chordwise position at which normal meets surface, percent chord
C_i	number of velocity measurements in i th histogram interval as percent of D
D	total number of velocity measurements in one histogram
D_{cv}	diameter of common volume, m
E	excess (or kurtosis) (see eq. (B4))
f	signal frequency received from laser velocimeter, Hz
H	spanwise distance measured from the center span, percent chord

I	number of histogram intervals
i	histogram interval number
L_{cv}	length of common volume, m
L_{fr}	fringe spacing, m
M_{∞}	free-stream Mach number
N	distance from airfoil measured along normal to surface, percent chord
P	probability density function
Q	number of cycles in signal burst
R_c	airfoil Reynolds number based on chord
S_R	skewness of histogram (see eq. (B3))
s	distance along airfoil surface measured from leading edge, m
T	period, sec
T.E.	trailing edge
T_r	transducer number
t	time, sec
U, V	velocities in free-stream and vertical direction, m/sec
U_L	velocities in coordinate direction 45° below free-stream direction, m/sec
u, v	velocities U/V_{∞} and V/V_{∞}
V_L	velocities in coordinate direction 45° above free-stream direction, m/sec

V_p	speed of pressure pulses, m/sec
V_∞	free-stream velocity, m/sec
X, Y	coordinate axes (fig. 16)
x	distance upstream from airfoil trailing edge, m
y	vertical height above airfoil trailing edge, m
α_s	angle between N and vertical, deg
α_w	wing angle of attack, deg
ΔU	width of histogram interval, m/sec
ΔZ	distance between beam focus and common volume, m
ϵ	error, percent
θ	angle between crossing laser beams, deg
λ	laser radiation wavelength, m
σ	standard deviation, m/sec (see eq. (B2))
Ω	pressure pulse passage frequency, Hz
ω	frequency, rad/sec

Subscripts:

a	average or mean as defined by equation (B1)
m	median
u	direction 45° below horizontal

- v direction 45° above horizontal
- 1 mode or velocity of highest peak in histogram
- 2 velocity of second highest peak in histogram

APPARATUS AND CALIBRATION

Laser Velocimeter Optics System

A fringe-type laser velocimeter optics system operating in the backscatter mode was used for the tests discussed in this report. The system is described in detail in reference 4. The primary advantage of the backscatter mode of operation is the ease of maintaining optical alignment between the primary transmitting and collecting optics since common optical components serve both functions. Aside from the practical necessity of operating in this mode in large facilities, the backscatter mode also permits the use of simplified optical and mechanical scanning mechanisms necessary for obtaining a three-dimensional spatial survey of the velocity flow field of interest. A two-component configuration, using polarization separation, was used to measure the velocity components $\pm 45^\circ$ about a flow streamline parallel to the test-section longitudinal center line. The two velocity measurement directions are called U_L and V_L . The laser velocimeter optics are illustrated in figure 1.

The laser velocimeter depends on the monochromatic and coherence properties of the laser. A laser beam is optically split into two parallel beams which are then focused with a lens to the point where the two beams cross. In the common volume, at the cross-over point, the light waves from each beam interfere constructively and destructively forming a fringe pattern. If the two beams are aligned in the horizontal plane, the fringes appear as vertical planes extending along the optical axis. The separation between two adjacent fringe planes is found from

$$L_{fr} = \frac{\lambda}{2 \sin \frac{\theta}{2}}$$

where λ is the wavelength of the laser radiation and θ is the angle between the two crossing laser beams. As a μm -sized particle passes through the fringe pattern, light is scattered with an intensity proportional to the incident intensity in the fringe pattern. If a portion of this scattered light is collected by a photomultiplier tube, an electrical signal is obtained whose oscillation rate is the same as that of the scattered light

oscillations generated as the particle passes through the fringe pattern. The frequency of this oscillation is related to the particle velocity by

$$f = \frac{V}{L_{fr}}$$

Since the laser beam is linearly polarized, appropriate polarization techniques were used to separate the scattered light from a second set of fringes located at the crossover point and orthogonal to the original fringes. This second fringe pattern is obtained by focusing three parallel laser beams instead of two beams, with each beam located at an apex of an isosceles right triangle. The resulting fringe patterns of the two components are shown in figure 2. With the two beams on the hypotenuse of opposite polarization and the polarization of the third beam rotated 45° , the scattered light from each set of fringes formed in the minor legs of the triangle can be separated by depolarizing optics. This technique allows the measurement of two orthogonal velocity components.

The argon-ion continuous-wave laser and the laser velocimeter optical system were located in the tunnel plenum chamber to obtain the maximum optical acceptance solid angle of the scattered laser radiation. The laser operated at about 2 W and 514.5 nm. The laser velocimeter had a focal length of 1.9 m (sufficient to reach the tunnel center line) and a collecting solid angle of 0.0458 sr. The common volume, 0.6 cm long with a diameter of 0.20 mm, yielded 20 fringes with a fringe spacing of $10.1 \mu\text{m}$. The optical system was placed on a mechanical two-component traversing mechanism to allow movement of the common volume in the x- and y-directions. The x-direction was parallel to the flow, and the y-direction was perpendicular to the flow in the vertical direction. The movement was controlled, and the position was calculated by a programmable calculator. This entire system was then placed on a pneumatic isolation platform to protect it against vibration. The laser was placed in a sealed case vented to atmospheric pressure to protect it from the plenum chamber environment during run conditions. The overall assembly, including the isolation platform, traversing system, laser, and laser velocimeter optical system, is shown in figure 3.

Laser Velocimeter Electronics System

The interface between the optics system and electronics system consisted of two S-20 response photomultiplier tubes, one for each component, and signal conditioning electronics. The signal conditioning electronics were composed of line driving amplifiers attached to the photomultipliers and low-pass filter banks to remove high-frequency noise.

The laser velocimeter electronics system, shown schematically in figure 4, measures the frequency of the output signal from the optics system, converts it to velocity,

and develops velocity histograms from which the mean velocity and standard deviation of velocity fluctuations are determined. The histogram data are then stored on magnetic tape for offline data reduction.

High-speed burst counter. - The high-speed burst counter is a device designed to measure the period of a high-frequency burst (1 kHz to 100 MHz) of the type received from a laser velocimeter. The instrument outputs data in either period measurements (time mode) or inverse period measurements (velocity mode). An idealized burst received from the laser velocimeter is illustrated in figure 5(a). The pedestal is removed by high-pass filters so that the burst is symmetric at about 0 V (fig. 5(b)). A Schmitt trigger is then used to convert the burst into a digital pulse train (fig. 5(c)). The first pulse in the train is used to clear the counter circuits; the second is used to arm the counters; and the third triggers the counters to begin counting pulses from the 500-MHz reference clock. When the tenth signal pulse occurs, the counters are halted. The counter now contains the measurement of the period average of the eight previous signal cycles based on a reference clock of 500 MHz yielding a period average measurement with a resolution of 2 nsec. However, since the counter has a finite size (9 bits for 8 cycles), frequencies below 3.9 MHz have periods too long to be counted. When this occurs, the counter register is shifted to the right by 1 bit, and this shift effectively halves the reference clock frequency. The number of shifts is output as a 4-bit exponent, $n + 6$. (The exponent bits are biased by 6, e.g., exponent 7 is 1 shift.) For example, if the number 1011010110 exponent 0101 (726_{10} exponent 5) were output, the measured period would be $726 \times 2 \times 10^{-9} \times 2^{(5-6)}$ or $0.726 \mu\text{sec}$ for 1 cycle which yields a frequency of 1.38 MHz. Thus, the digital word from the high-speed burst counter consists of 10 data bits and 4 exponent bits. The conversion equation to signal frequency is

$$\text{Frequency} = \frac{3.2 \times 10^{10}}{2^n \times \text{Reading}}$$

Since the high-speed burst counter was placed in the velocity mode for the present test, the most significant 8 bits of the time reading are used to address a read-only memory which contains the appropriate 8-bit conversion to inverse time. The conversion equation to signal frequency in the velocity mode is

$$\text{Frequency} = 7.5 \times 2^n \times \text{Reading}$$

These readout schemes permit resolutions of 0.4 percent of full scale in the time mode on all exponent scales and 1.6 percent of full scale in the velocity mode on all exponent scales.

The digital output section in the high-speed burst counter was designed to interface with a minicomputer; thus, the digital word was designed to shift exponent scales when appropriate to seek the maximum resolution of the measurement. However, the pulse height analyzer was designed to accept only 10 bits; this design required the burst counter exponent to be set and held for a given histogram.

Pulse height analyzer. - A pulse height analyzer (PHA) was an instrument used to record the number of occurrences of pulses of given amplitudes. In the PHA used in this study, the normal analog front end was replaced with a two-channel digital multiplexer designed to accept two 10-bit words from the two high-speed burst counters. The capacity of the memory of the PHA was 2048 channels, a number sufficient for full digital resolution (i.e., a 10-bit word had 2^{10} or 1024 possible values). (In the velocity mode, the counter outputs 8 bits which address only the lowest 256 channels.) When the PHA received a digital word from the high-speed burst counter, the word was placed on the memory address bus. The addressed memory location was then incremented. After a large number of words had been received, a histogram was formed in which each channel location contained the number of occurrences in that particular digital address (i.e., output word from the high-speed burst counter, during the measurement sample). The histogram was related to the velocity probability density when the memory addresses or PHA bin numbers were converted to velocity by using

$$V = L_{fr} (7.5 \times 2^n \times \text{Bin number})$$

where L_{fr} is the laser velocimeter fringe spacing, and the high-speed burst counter is in the velocity mode. The histogram was then stored on digital magnetic tape.

Seeding

The particles used to scatter laser radiation were generated by a vaporization-condensation smoke generator. Kerosene was used as the smoke material. The details of the system installation and operation of the smoke generator are found in appendix A.

Since the laser velocimeter measures particle velocity instead of gas velocity, the response of the particle to variations in a flow field must be known. The size distribution of the particles used to obtain the velocity measurement must be known to calculate this response. The distribution was measured in still air with an electro-optical particle size analyzer. The instrument measures the size of particles from 0.5 to 8.0 μm . Its principle of operation is based on the light scattering criteria from small particles developed by Mie (ref. 5). As the smoke is pulled through the optical system with a small air pump, the particles are illuminated with white light, and the scattered radiation is collected over

a large collecting solid angle at 90° with respect to the illuminating radiation. The combination of white light and the large collecting solid angle smooths the Mie intensity function (ref. 5) to a straight line on a log-log scale. The collected scattered radiation impinges on a photomultiplier tube which yields an electrical pulse of a height proportional to the particle size. The pulse is then shaped into a rectangular pulse, whose height is equal to the peak of the photomultiplier output pulse, and is transmitted to a PHA in which the particle size distribution is obtained. A diagram of the system is shown in figure 6. The particle size distribution for the generator used in the present test is discussed in appendix A.

Sufficient smoke of a size large enough to be detected by the laser velocimeter (above about $3 \mu\text{m}$) was generated to yield from 2 to 50 laser velocimeter measurements per second. The data-acquisition rate depended not only on the smoke-generator operation, but also on the part of the flow field under investigation. The penetration of the smoke into the separated region of the flow field was noticeably poor.

Model and Pressure Transducers

The model wing was installed horizontally near the center line of the Langley high-speed 7- by 10-foot tunnel. The test section was slotted and was about 2 m high by 3 m wide. The stagnation pressure was atmospheric, but the stagnation temperature rose as much as 30°C above atmospheric because of the fan power dissipation in the closed circuit tunnel.

The model wing is shown in figure 7. The model was an untwisted, unswept, untapered wing with an aspect ratio of 8 and 0.1524-m chord. The wingtips were bowed down a few mm so that the top center span surface of the wing was accessible to laser beams from the windows in the side of the tunnel. The wing section was an NACA 0012 airfoil, and the surface was smooth aluminum. The wing was mounted so that aerodynamic response or buffet was negligible. The wing mount had a natural frequency in excess of 40 Hz, and the sting was reinforced. Both the wing and sting were prestressed so that no vibration was detectable by means of closeup examination by a motion-picture camera. Consequently, it was assumed that all the unsteadiness in the flow was due to aerodynamic sources.

The wing position was slightly upstream of the window which was about 18 cm square. The laser beams were therefore angled 15° upstream to reach the wing. The field of view of the laser beams was thus cut off from the airfoil surface forward of the airfoil crest. Also, when the common volume was behind but near the trailing edge, one of the beams intersected the trailing edge after passing through the common volume. This condition allowed the location of the common volume to be precisely determined when it intersected the trailing edge.

The center insert of the wing is shown in figure 8. The upper surface was tapped for pressure in nine locations with a 0.7-mm drill. Absolute pressure transducers with a silicon diaphragm 3.2 mm in diameter were mounted inside the wing. The transducers nearest the trailing edge were mounted with the diaphragm flush with the surface. The nominal natural frequency of the transducers was 125 kHz. The drilled holes that transmitted pressure to the transducers had resonant frequencies above 14 kHz. Within the frequency range of this test, the response of the transducers mounted inside the wing was found to be as large in magnitude as the flush-mounted transducers. The transducers at the 0.978-, 3.955-, 8.927-, 14.925-, 23.952-, 34.988-, 59.985-, 74.905-, and 95.8-percent chord locations were operational throughout the test. The locations of all the pressure transducers are shown in figure 9.

The pressure transducers were calibrated by installing the entire wing in a vacuum chamber. Recordings of transducer output were made for five pressures from 1 to about 1/2 and for temperatures of about 6°, 17°, 26°, 38°, and 43° C. The transducer outputs and a reference voltage were filtered and amplified by dc amplifiers and were recorded on FM analog tape.

The letters in figure 9 denote the location of seven tufts that were mounted on four small rods protruding from the airfoil surface. The tufts were mounted at staggered spanwise locations from 8-percent to 18-percent semispan from the center line. The tufts were not run simultaneously with the laser velocimeter.

DATA ACQUISITION AND REDUCTION

Pressure Measurement

The outputs from the pressure transducers in the model were recorded on 10 channels of an FM tape recorder. The signals were amplified and low-pass filtered with 1-kHz filters to eliminate higher frequencies. Recordings were made at 19 cm/sec ($7\frac{1}{2}$ in/sec) on an intermediate band carrier. The tapes were again low-pass filtered at 2.5 kHz and digitized at 5000 samples per second. Because of drift in the zero point in the recording system, no valid measurement of the average pressure was possible. The digitized records were used to find the standard deviation and the amplitude spectra.

In addition, the pressure signals were analyzed online by a 100-bin crosscorrelator. These data were taken as photographs of an oscilloscope screen. The delay time between bins was 20 μ sec, except for the autocorrelation of transducer 20 which was taken with a 5- μ sec delay time. The horizontal scope scale was 0.2- μ sec delay time per division. The vertical scale was linear.

Laser Velocimeter Data Processing

The number of reference clock pulses for 8 cycles of the laser velocimeter signal from two (U_L and V_L) high-speed burst counters was input to the digital multiplexer in the PHA. This allowed two histograms, one each for U_L and V_L , to be simultaneously determined, placed, and displayed side by side on the 2048-channel (bin) analyzer – that is, one histogram was contained in bins 1 to 1024 and the second was contained in bins 1025 to 2048. Depending on the seeding rate, the time to position the laser and to acquire a histogram was about 3 to 10 min. The online determination of the velocity interval with the greatest number of measurement occurrences (mode) required about another minute.

The dual histogram data were then stored on a digital magnetic tape. Online, the component velocities were estimated by conversion to velocity of the mode. Offline, the histogram data were retrieved from the magnetic tape and transferred to the programmable calculator for data reduction and permanent storage on magnetic disk.

Two pairs of histograms are displayed in figure 10. The horizontal axis is the velocity value associated with the velocity intervals. The height of each line is the percent of measurements that fell into that velocity interval. As explained in appendix B, the histogram is an approximation to a probability density function. Appendix B also defines the relationship between the quantities determined from the histogram and time-averaged values. A synopsis of the physical significance of some characteristic histogram shapes is also given.

For each pair of histograms, the average velocity magnitudes, $U_{L,a}$ and $V_{L,a}$, were calculated for each component. The average or mean velocity in the histogram (eq. (B1)) was physically significant because it was also the time-averaged velocity. Three other velocities that were calculated are displayed in figure 10. The median velocity, $U_{L,m}$ or $V_{L,m}$, has its customary definition; that is, one-half of the particles have velocities higher than the median, and one-half have velocities lower than or equal to the median. The mode 1 velocity, $U_{L,1}$ or $V_{L,1}$, is the velocity interval with the largest percentage of measurements. The mode 2 velocity, $U_{L,2}$ or $V_{L,2}$, was determined visually and is the speed at the second highest peak in the histogram when that peak is higher than its neighbors. For most histograms, there is only one peak. The differences between the mean, median, and mode 1 velocities are usually much smaller than the illustrative histograms in figure 10. Figures 11, 12, and 13 were constructed by assuming that both U_L and V_L were in the positive direction. This assumption defines a velocity vector in the prime direction. Careful examination of the three velocity maps reveals small differences near the airfoil surface or in regions of highly skewed histograms, but for purposes of examining the overall steady flow pattern, the



three are essentially the same. Thus, the overall flow picture is not distorted either by the fine details of the histogram shape or by variations in the data-reduction process.

The higher moments of the histogram were also taken. The standard deviation (eq. (B2)) is the root mean square of the variation from the mean or average and is a measure of the unsteadiness of the flow. The skew (eq. (B3)) was calculated to indicate the degree of symmetry about the average. The excess (or kurtosis) was calculated (eq. (B4)) to complete the moments. Excess is a measure of the degree of peakedness of the histogram. A few measurements of skew and excess are available for boundary layers in references 6, 7, and 8.

The fidelity with which the shape of the true probability density function is represented by a histogram depends on the total number of measurements D in the histogram. Figure 14(a) shows a histogram with fewer than 2 points per bin. Even histograms with a sufficient number of points contain by chance empty bins and have a ragged profile (fig. 14(b)).

System Measurement Precision

The overall measurement precision is obtained by determining the accuracies of all variables in the system which affect the accuracy of each velocity measurement. The differentiation of $f = V/L_{fr}$ indicates which variables cause inaccuracies in the velocity measurement

$$V = \frac{\lambda f}{2 \sin \frac{\theta}{2}}$$

$$dV = \frac{\lambda}{2} \left(\frac{df}{\sin \frac{\theta}{2}} - \frac{f d\theta}{2 \sin \frac{\theta}{2} \tan \frac{\theta}{2}} \right)$$

Because of the stability of the laser wavelength, the wavelength is not considered a source of error

$$\frac{dV}{V} = \frac{df}{f} - \frac{d\theta}{2 \tan \frac{\theta}{2}}$$

For the angle θ used in the present test

$$\frac{\theta}{2} \approx \tan \frac{\theta}{2}$$

$$\frac{dV}{V} \approx \frac{df}{f} - \frac{d\theta}{\theta}$$

The frequency error df/f is affected by errors in the optics system: parallelism of the fringe pattern, measurement of the crossbeam angle, and position of the common volume. The frequency error is also affected by errors in the electronics systems: limiter threshold error, reference clock synchronization error, and quantizing error. The crossbeam angle error $d\theta/\theta$ is affected by the accuracy of the physical measurement of θ .

Optics system. - The three sources of inaccuracies due to the optics system are measurement of the crossbeam angle, parallelism of the fringe pattern, and the measurement dead zone. The inaccuracy in the measurement of the crossbeam angles yields a fixed bias error in the velocity measurement. These angles were measured by obtaining a displacement pattern of the three laser beams approximately 6 m from the common volume, locating the center of each beam, and calculating the angle based on the beam separation and distance from the common volume. The center of each beam was located within an estimated uncertainty of ± 1.5 mm, which yielded an uncertainty in angle measurement of ± 0.6 percent.

If the fringe pattern is not parallel, the fringe spacing is not constant over the length of the common volume, and a measurement inaccuracy occurs. (See ref. 9.) This problem occurs when the focus of each beam does not coincide with the beam crossover point. The lack of coincidence is caused by the small divergence in the laser beam due to the concave reflectors inside the laser. The problem also adds a bias error since the fringe spacing, based on the measured crossbeam angle, applies only when the beam focal point coincides with the crossover point.

The measured beam focal point was located 0.055 m from the crossover point at a focal length of 1.9 m. The common-volume diameter 0.20 mm was found by magnifying the common volume and determining the number of fringes within the $1/e^2$ intensity points and multiplying by the fringe spacing $10.1 \mu\text{m}$. The broadening caused by nonparallel fringes is determined to be 0.46 percent by the equation

$$\frac{df}{f} = \frac{L_{cv}}{\Delta Z \left[1 + \left(\frac{\pi D_{cv}^2}{\lambda \Delta Z} \right)^2 \right]}$$

where L_{cv} is the length of the laser velocimeter common volume, ΔZ is the distance between the beam focus and the common volume, and D_{cv} is the diameter of the common volume.

The bias error caused by the change in fringe spacing is found by a ratio of the diameters since the number of fringes within the common volume is a constant

$$\epsilon_{\text{bias}} = \frac{D_{\text{cv}} - D_{\text{BW}}}{D_{\text{cv}}} = -2.1 \text{ percent}$$

where the beam waist diameter D_{BW} is given by

$$D_{\text{BW}} = \sqrt{D_{\text{cv}}^2 \left[1 + \left(\frac{\lambda \Delta Z}{\pi D_{\text{cv}}^2} \right)^2 \right]}$$

Since the common-volume diameter is always larger than the beam waist diameter, the bias error always results in a bias toward the lower velocities.

The measurement dead zone is caused by trajectories through the fringe pattern at large angles from the normal. When a particle does not cross the required number of fringes (10) for the data processing instrumentation to determine the signal frequency, that data point is lost. This loss occurs if the particle passes too far above or below the center of the common volume, or when the angle between the particle trajectory and the fringe plane is too small, or when a combination of both conditions occurs. Since 20 fringes are contained in the 0.20-mm-diameter common volume of the present system, the particle must pass within ± 0.086 mm of the center of the common volume with an angle no less than 30° to the plane of the fringes. With the fringes oriented $\pm 45^\circ$ to the tunnel center line, flow angles of less than $\pm 15^\circ$ are required to obtain simultaneous measurements in both components.

Electronic instrumentation. - The sources of measurement error caused by the electronics are: limiter threshold, reference clock synchronization, and quantizing. The limiter threshold error (ref. 10) is caused by the time jitter in measuring the threshold crossing points due to the Gaussian envelope of the signal burst. This error is given by

$$\epsilon = \frac{1}{12 Q} + \frac{1}{96 Q^2} = 1.06 \text{ percent}$$

where Q is the number of cycles (8) in the signal burst used for processing. This error is a positive error which biases the measurement toward the higher frequencies.

The clock-synchronization error is caused by the integer operation of the reference clock counting circuits. At the maximum signal frequency of 20 MHz, the error is less than 0.5 percent for a reference clock frequency of 500 MHz. This error is a bias error

toward the higher frequencies. The quantizing error is similar. This error is caused by the 8-bit accuracy of the high-speed burst counter which yields a bias error of $0.78 \leq \epsilon \leq 1.55$ percent toward the higher frequencies. The 8-bit output also sets the resolution of the instrument:

Resolution, m/sec	Range, m/sec
2.56	160 to 200
1.28	80 to 160
.64	40 to 80
.32	20 to 40
.16	10 to 20

However, for the purpose of plotting the histograms, the ranges were combined so that the histogram resolutions, or velocity interval widths, were

Resolution, m/sec	Range, m/sec
2.56	20 to 200
1.28	10 to 100
.64	5 to 50

Velocity error summary. - The summary of system errors is as follows:

Velocity error source	Bias error, percent	Random error, percent
Crossbeam angle measurement	± 0.6	----
Diverging fringes	-2.1	± 0.46
Time jitter	+1.06	----
Clock synchronization	+0.25	± 0.25
Quantizing	+1.17	± 0.38
Total error	+0.98, - 0.22	± 0.65

The total effective error is obtained by taking the square root of the sum of the squares of the total error. Thus, the total effective error is between 0.69 and 1.18 percent.

Velocity Measurement Accuracy

In addition to these system errors, errors caused by common-volume position error and particle lag error must be considered for overall measurement accuracy.

Particle lag.- Since the laser velocimeter measures particle velocities and not the gas velocity, the final measurement accuracy is dependent on the ability of the particle to follow the flow faithfully. The particle dynamic work performed by several researchers, notably Walsh (ref. 11), indicates that the smaller the particle, down to the size of the gas molecule, the more faithfully it follows a given flow. However, the particle light scattering work performed by Mie (ref. 5) indicates that the smaller the particle, the less light it scatters. A compromise was reached by using the laser velocimeter simulation program developed by Meyers (ref. 12). This program showed that the optimum particle size for the research conducted during this study was between $1\mu\text{m}$ and $4\mu\text{m}$. Kerosene particles were the seeding material for this study. (See appendix A.) Fewer than 2 percent of the particles were larger than $3\mu\text{m}$ in diameter.

A test was performed to determine experimentally the response of the particles to a flow gradient comparable with the expected gradient in the wing study. The test measured the velocity along the stagnating streamline of a hemispherical model at Mach 0.55. The experimental results and theoretical prediction are compared with the theoretical gas velocity (ref. 13) in figure 15. Based on these results, the small uncertainty due to particle lag can be neglected in the flow regions accessible to this investigation. However, in the unsteady flow field described in the results section, particle lag errors as large as 5 percent for $3\text{-}\mu\text{m}$ particles and 10 percent for $5\text{-}\mu\text{m}$ particles were found by applying the methods of reference 10.

Common-volume location.- The common-volume position was determined using two rack-and-pinion driven linear potentiometers for the two mechanical scan components. The position accuracy of $\pm 1\text{ mm}$ in the x-component (along the tunnel center line) was caused by gear backlash in the rack and pinion. The vertical component also suffered from gear backlash but had an additional problem of vertical uncertainty which was caused by the action of the pneumatic vibration isolation system. The system's height was dependent upon tunnel pressure and weight shift, which occurred as the optical system was traversed in the x-direction. This problem was removed by touching the model with the beam crossover point and obtaining a new zero before making a scan. This resulted in inaccuracies of $\pm 1\text{ mm}$ in the vertical component far from the wing. Inaccuracies decreased to $\pm 0.3\text{ mm}$ near the model surface. The scans were taken along the line normal to the surface of the airfoil as shown by the coordinate system in figure 16.

Histogram Interpretation

Velocity measurements. - The velocity measurements cannot be interpreted without consideration of the direction ambiguity. The laser velocimeter measured two components, U_L and V_L . The positive direction of each of the components is shown in figure 16. These two components may be combined to give the velocity. However, since only the speed, or velocity magnitude, was measured for each separate component, it is not known whether U_L is actually in the positive or the negative direction. A similar ambiguity is present for V_L . When both components are set to positive directions, the resultant velocity vector is said to be in the prime direction. The prime direction is probably the correct direction for most of the points measured. There are three alternatives to the prime direction: the V_L component alone may be taken in the negative direction, the U_L component alone may be taken in the negative direction, or both may be taken in the negative direction. Thus, the resultant velocity vector has a fourfold directional ambiguity.

Any particle that crossed fewer than 10 of the fringes for a component was rejected by the data-acquisition system for that component only. Figure 17 illustrates the fringe pattern for the U_L component. The situation for the V_L component is similar but, of course, the fringe pattern is rotated 90° . For the U_L component, a particle trajectory that made an angle with the fringe plane of less than 30° was not measured. Also, trajectories that were too far from the center of the common volume to cross 10 fringes were not measured. This accounts for the large disparity in the number of particles between the U_L and V_L component that often occurs. The actual experimental situation is complicated by the noncircularity of the common-volume cross section, the uncertainty in the number of fringes (18 to 20), and the oblate spheroidal shape of the common volume. The trajectories are assumed to be straight lines, but since the maximum diameter of the common volume is 0.2 mm, this is not a serious source of error. This total dropout zone of velocities for the U_L component is shown in figure 18. The radii represent velocity vectors. For the 1.28-m/sec velocity interval resolution, no measurements are made in the shaded region. Similar diagrams can be drawn for the V_L component and for the other velocity interval resolutions.

Velocity bias. - The histograms can be biased toward the higher velocities by the velocity bias effect described in references 14, 15, and 16. This effect is caused by the tendency of higher velocity air to pass a greater number of seed particles through the common volume than lower velocity air. This effect is based on the assumption that the seed particles were homogeneously distributed in the streamline tubes passing through the common volume.

Because the smoke arrived in the test section in streamline tubes, the assumption is again made that the seed particles were homogeneously distributed when the smoke

entered the fringe pattern. The histograms were corrected for velocity bias by dividing the number of occurrences of each velocity interval by the value of the velocity.

Statistical uncertainties. - Each histogram is a discrete approximation of a probability density function. The probability that a value of velocity u lies within an interval $u - \frac{\Delta U}{2}$ to $u + \frac{\Delta U}{2}$ was approximated. (See appendix B.) Further, the laser velocimeter measurement was made over a finite period of time, obtained a finite number of discrete velocity measurements, and is thus an approximation of a stationary condition. Therefore, there is a degree of uncertainty that the calculated mean velocity and standard deviation of velocity are the true stationary mean and standard deviation of the flow. The measurement uncertainty in the mean value (from ref. 17) is expressed for a 95-percent confidence limit as

$$\text{Uncertainty in } U_a = \pm \frac{2\sigma}{\sqrt{D}}$$

where σ is the standard deviation of the histogram, and D is the number of discrete velocity measurements in the histogram. That is, with 95-percent confidence, the true stationary mean velocity of the flow lies within a radius of the uncertainty about the measured mean calculated from the histogram. Similarly, the measurement uncertainty in the standard deviation for a 95-percent confidence limit is

$$\text{Uncertainty in } \sigma = \sigma \sqrt{\frac{2}{D} \left(1 + \frac{E}{2} \right)^{1/2}}$$

where E is the excess (or kurtosis) of the histogram.

In this study, the average uncertainty in all the mean velocity magnitudes measured is ± 3.0 m/sec or approximately ± 3 percent of the local velocity. The average uncertainty in the flow angle measurement is $\pm 1.5^\circ$. The average uncertainty in the standard deviation measurement is ± 2.1 m/sec or approximately ± 6 percent of the local standard deviation.

RESULTS

Histogram Data

The histograms for all the measured points are presented in figures 19 to 28. The figures are arranged in the order of the chordwise location C at which a line from the measurement point, normal to the surface, strikes the surface. The histograms within each figure are arranged in order of decreasing distance from the surface N to the

measurement point. The airfoil contour and arrows proportional in length to the mean velocities for the scan are displayed above each set of histograms. Figure 16 illustrates the coordinate systems. Many of the histograms for measurement scans above transducer positions 3, 5, and 7 show double peaks. Examination of the histograms for scans above transducer position 17 or 19 shows the change of histogram range that was needed as the measurement location was moved nearer to the surface. Since the histograms are considered raw data, no correction for velocity bias has been applied.

The aerodynamic conditions corresponding to each measurement point are recorded in table I. Although the Mach number was close to 0.49 throughout the test, the free-stream velocity and Reynolds number varied from day to day. The nominal value of Reynolds number was 1.4×10^6 and the nominal value of free-stream velocity was 170 m/sec. The day to day variation in free-stream velocity was less than 10 m/sec. Occasionally, because of the fixed upper limit on the velocity of the laser velocimeter measurements, a change in tunnel velocity caused some data to be lost. (See fig. 19, points l and m.)

The wing angle of attack changed from 19.44° to 19.50° as the cables from the sting to the floor stretched (fig. 7). Table I identifies the location in the x,y and in the C,N coordinate systems. In addition, the transducer identification number T_r that corresponds to the chordwise position C is tabulated. The angle α_s between a normal to the surface and the vertical is also presented. The histogram data corrected for velocity bias include the U_L and V_L components of average velocity, median velocity, mode 1 velocity, standard deviation, skew, excess, and number of particles.

The histogram characteristics are summarized in figures 29 to 38. The consistency of the measurements is poor for transducer positions 3 and 5 but improves considerably for the subsequent transducer positions. The consistency of the measurements is affected by changes in the velocity range of the laser velocimeter and by changes in the free-stream velocity for cases when there were significant numbers of particles near the upper limit of the range. The measurements at low average velocities (below about 40 m/sec) are affected by the low velocity dropout zone. The scatter is expected to increase for the higher moments of the histograms. However, definite trends can often be detected in skew and, occasionally, can be detected in excess. The plots of standard deviation indicate that there is considerable unsteadiness in the flow. Values of 25 to 50 m/sec of standard deviation are seen in most of the plots. The free-stream velocity component in both the U_L and V_L directions is $V_T \cos 45^\circ$ or about 120 m/sec. The magnitude of the velocity fluctuations is a large fraction of the free-stream velocity.

Pressure Correlations

The outputs of the pressure transducers show evidence of large, nonrandom fluctuations in the flow. The crosscorrelations and autocorrelations of the pressures are shown in figures 39 to 45. The pattern of correlation among the transducers indicates a moving pressure pattern. The correlations for transducer 9 in figure 42 afford a good example. The picture for 9D1 (9D1 indicates the crosscorrelation between transducers 9 and 1 with the delay on 1) shows a relatively weak correlation that peaks at bin 36. Bin 36 corresponds to a delay time Δt of 720 μsec . This correlation means that the pressure variations at transducer 1 resemble the pressure variations that occur 720 μsec later at transducer 9. If the cause of the pressure variations was moving downstream from transducer 1 to transducer 9, the speed V_p could be estimated by dividing the distance between the two transducers by the delay time.

The pictures for 9D3, 9D5, and 9D7 exhibit a much closer correlation than 9D1. The delay times decrease in a systematic manner from transducers 3 to 5 to 7. The delay time between transducers 3 and 5, for example, can be obtained by subtracting the delay 9D5 from 9D3. A more reliable value is the crosscorrelation 5D3 shown in figure 39 or the one shown in figure 40. The delay times are summarized in figure 46.

The autocorrelation of transducer 9 (labeled 9D9) is shown in figure 42(e). The shape is characteristic of a sinusoidally varying pressure with some variation in period. The first peak indicates a delay of 240 μsec or a frequency of 2083 Hz. If the frequency is associated with the passage of the pressure pulse at speed V_p , the spacing of the pulses can be determined. The results for all transducers are displayed in figure 46.

Figure 42 shows that for transducers downstream of transducer 9 there is a decrease in the degree of correlation. The correlation 19D9 does not allow the calculation of a reliable delay time.

Figure 46 summarizes the correlations of the pressure transducers. The delay times in figure 46(a) are the times required for the pressure pulses to move from the upstream transducer to the downstream transducer. Since the distance between the two transducers is known, the average speed of the pressure pulse over the distance between the transducers can be calculated. These speeds are displayed in figure 46(b) for adjacent pairs of transducers. The points are plotted at a surface distance s halfway between the two transducers.

Additional information is available from the autocorrelations. Figure 46(c) shows the frequency of the response of each transducer to the pressure pulse passage. The ratio of the speed of the pulse V_p to the frequency of the pulse passage Ω gives a spacing for the pulses. The spacing, shown in figure 46(d), is calculated from the effect of the pressure pulses on the surface. Since the pulse speed is calculated halfway between the

transducers and since the frequency of passage is known at each transducer, the frequency of passage was interpolated to find the pulse spacing.

INTERPRETATION OF RESULTS

Vortex Modeling

The double peaks in the histograms of transducers 5 and 7 are shown in figures 20 and 21. The discussion of histogram shapes in appendix B indicates that a periodic variation of velocity in time is characterized by a two-peaked histogram.

The correlations of pressure data taken together with the double peaks seen in the histograms suggest that a series of vortices is shed periodically from near the crest of the airfoil and that these vortices move downstream at an increasing speed. The phenomenon of vortex shedding from bluff bodies has been well documented at lower Reynolds numbers (ref. 18) and has been named as a cause of noise generation on airfoils at higher Reynolds numbers (ref. 19). The present case was examined for the presence of a region through which vortices move downstream. A model of a vortex region was constructed and was programmed on the calculator. Simulated histograms were then constructed by using a Monte Carlo approach with the calculator by simulating the laser velocimeter method of histogram generation as closely as possible.

The vortex model is illustrated in figure 47. The vortex region extended 10.5 cm upstream and downstream of the point at which the histogram was to be calculated even though the velocities were dominated by only one or two vortices near the center. The vortices moved parallel to the line chosen as the center line. The distance above or below the center line was random with a standard deviation of 1 cm. The vortex spacing was set at 3 cm in the direction parallel to the vortex path center line which corresponds to the spacing determined from the crosscorrelation measurements. Each vortex generated a tangential velocity given by $\left(\frac{3 \text{ m}^2}{\text{sec}}\right) \left[\frac{1 - \exp\left(-\frac{r}{5 \text{ mm}}\right)}{2\pi r}\right]$ where r is the radial distance from the vortex to the calculation point. The vortex circulation of $3 \text{ m}^2/\text{sec}$ was chosen by trial and error. Although only a qualitative reproduction of the double peak histograms was possible, the value of circulation was probably better defined than the other empirical values in the vortex model. When compared with an equivalent airfoil lift coefficient (about 0.23), the vortex circulation did not seem excessive. However, the circulation was sufficient to reproduce the large velocity difference in the two peaks of the histograms above transducer positions 5 and 7.

In the application of the vortex model to the simulation of the histograms in the scan above transducer position 7 (fig. 48), the center line of the vortex path was taken to be horizontal and was fixed in height at the location $y = 0.0673 \text{ m}$ which is the height of the

measurement point labeled "f" in figure 48 or run 39 in table I. Above the vortex path center line, the simulated histograms showed velocities far above the free-stream value. The free-stream velocity was 170 m/sec, so the two components of the free stream in the U_L and V_L directions were about 120 m/sec. The measured histograms at point "a" also showed the high velocities. At point "a," both the measured and simulated histograms showed a relatively small standard deviation. This small deviation indicates a flow that has only small fluctuations. At points "b," "c," and "d," the measured histograms showed a dominance of velocities below the free-stream value. For the simulated histograms, the below-free-stream velocities did not appear until point "d" was reached. This indicated some defect in the geometry of the vortex model. At points "e" and "f," both measured and simulated histograms showed double peaks and an extremely large standard deviation. The velocities at which the peaks occur do not match exactly, but the trend of increasing dominance of the lower peak is clear in both the simulated and measured histograms. Points "g" to "j" showed very good correspondence in shape between the measured and simulated histograms. At these points below the vortex path center line, the double peaks changed to a single low-speed peak below free-stream velocity. The measured histograms nearest the surface were not simulated because the model did not include viscous forces.

A closer correspondence between the measured and simulated histograms could probably be achieved by empirical adjustment of the geometry and strength of the vortex model. This was not attempted primarily because a quantitative simulation would require the inclusion of a prohibitive number of factors. The present model does not account for the expansion of the flow about the model, viscous effects, free-stream fluctuations, differences in the U_L and V_L components, curvature of the vortex path center line, the starting point of the vortices, random variations in vortex strength (although random variations in location were simulated), nor any variation in core size. The simulated vortex spacing of 3 cm along the center line was based on the results of the pressure crosscorrelation measurements. Vortex spacing was the only parameter in the vortex model that was not set by trial and error comparison of the measured and simulated histograms.

The histograms for the scan above transducer position 5 exhibited double peaks near the surface. As shown in figure 30 and figure 49, the points away from the surface showed a much higher velocity for the U_L component than for the V_L component. This characteristic was simulated by using exactly the same vortex model except for a 15° tilt of the center line to the free-stream direction. The pattern of the measured histograms for transducer position 5 was not as clear as for transducer position 7. The simulation shows enough correspondence, however, to support the supposition that the nonsymmetric appearance of the measured histogram was caused by a tilt of the vortex path center line.

Vortex Locations

The model vortex path center line is very close to the surface at transducer 5, but it is much higher from the surface at transducer 7. This large vertical movement of the vortices is not consistent with the time-averaged velocity flow field. However, it is possible that at the time of the vortex passage, the instantaneous flow field could have a large vertical component. This hypothesis can be illustrated by the oscillating-airfoil dynamic stall work in reference 1. Another illustration of the possibility of large vertical velocities is found by combining the mode 1 and mode 2 peaks of this investigation. Since the histograms lack time information, the mode 2 peak of one component might occur at the same time as either the mode 1 or mode 2 peak of the other component. If both histograms have two peaks, there are four such possible combinations, as shown in figure 50. Thus, the instantaneous vortex convection velocity may not resemble the mean velocity.

Similar simulations of the histograms downstream of transducer position 7 were not attempted. Many of the histograms for transducer 9 (fig. 22) were not sufficiently well defined. Also, the vortex model assumptions of inviscid vortices with fixed spacing became less valid for the downstream flow. However, double peaks were also observed in the trailing-edge region. The points labeled "r," "s," and "t" in figure 28 were for flow from the lower or pressure side of the airfoil. This indicates that vortices were shed from both the suction and pressure sides of the airfoil. The transducer near the pressure side trailing edge, transducer 20, was crosscorrelated to transducer 7 and to transducer 3 as shown in figure 45. The delay time for a positive correlation was very long (between 130 and 160 μsec). Although the cause or effect cannot be discerned, the lower and upper surface unsteady pressures are definitely correlated.

Frequency Analysis

The photographs of figures 39 to 47 were digitized, and the waveforms were processed by a conventional computer fast Fourier transform. The real part of the Fourier transform is presented in figures 51 to 57. The frequency resolution of the transforms is 500 Hz only. The thickness of the spectrum peaks would probably be much less if a higher frequency resolution were possible. The correlations show very little high-frequency content, and there is generally one dominant frequency in the spectrum.

The Fourier transform of a pressure autocorrelation is the power spectrum of the pressure. The narrowness of the frequency peak for the pressure transducers near the airfoil crest indicated that the vortex initiation occurs at very regular time intervals. The narrow peaks of the spectra for the pressure transducers near midchord imply that the convection speed of the vortices varies little from vortex to vortex. The extreme regularity in time of the vortex shedding is reminiscent of the shedding of a Kármán vortex street at much lower Reynolds numbers on a circular cylinder.

The power spectrum of the pressures was also found directly from the analog tape recording. The results in figure 58 have been analyzed from 0 to 2500 Hz with a bandwidth of 9.77 Hz. Above 1 kHz, a large roll-off (an effect of the low-pass filter) can be seen by comparison with figures 51 to 57. Consequently, only transducers 20 and 2 show the peaks found in the unfiltered autocorrelation data since the peak for each transducer is about 1160 Hz. The frequency on the lower surface is about one-half of the frequency on the upper surface.

The peaks of the Fourier transforms of the crosscorrelations could be broadened by changes in the timing of the vortex passage just as the Fourier transforms of the autocorrelations are broadened. In addition, the peaks could be broadened by changes in the magnitude of the pressure pulses. Since the strength of vortices is conserved in potential flow, the most likely explanation of the broadening of the peaks of the crosscorrelation is a variation in the height of the paths of the vortices. From figures 51 to 56 the path irregularity along the length of the chord can be seen. The vertical position of the horizontal axis of some of the scope pictures could have been affected by the instrument memory overflow. In addition, the unusually large dc component in several crosscorrelations could be caused by this phenomenon.

Vortex Paths

The vortices that pass over the upper surface of the airfoil cause large variations from the average velocity. Figures 59 and 60 can be used to compare the average velocity vector and the two components of standard deviation. Regions of high velocity and large standard deviation can be discerned in the flow field. To aid in the visualization of these regions, the resultant average velocity vector was converted to Mach number by assuming that the sonic speed was frozen at its free-stream value. Figure 61 shows the contours of constant Mach number that result from this representation of average velocity. The figure was constructed by means of a spline fit on a 1-mm grid. A tolerance in Mach number of ± 0.002 was applied to each contour line.

Two significant regions of high speed can be seen. The highest Mach numbers occur above the midchord of the airfoil. This could occur because of an expansion about the separated region combined with the action of the vortex sheet. The high velocity region just behind the crest of the airfoil was also seen in the vortex simulation for the scan above transducer position 7 (fig. 48).

A similar procedure was followed for drawing Mach contours of the standard deviation. Figure 62 shows the regions of unsteadiness in the flow. Three significant regions of high standard deviation are apparent. One is near the midchord, and one is above the crest. Relatively large values of standard deviations should occur near the center line of the paths of the vortices shed from near the crest.

The center line of the vortex path can be expected to be characterized by relatively high values of standard deviation of velocity and zero histogram skew. To track the vortex paths from the two locations found by vortex modeling for transducer positions 5 and 7, figure 63 was constructed. In addition to positions of relative maxima of the resultant standard deviation, the locations of low values of skew are shown. Also plotted are the points where the average velocity component along the chord equals the pressure pulse velocity found from the crosscorrelations of pressure. The criteria chosen for the path center line did not coincide to define a single track. The center line of the path of the vortex system might also influence the average velocity values. The location of relative minimums of average velocity with respect to y is also shown in figure 63. Except for the simulations at transducer positions 5 and 7, the attempts to fix the center line of the vortex paths have not been successful. This failure may be due to the existence of a multiplicity of vortex tracks, misapplication of the criteria chosen to define the center line, or obfuscation of the data by influences such as viscosity or flow expansion.

Before proceeding to consideration of viscous-dominated histograms, the inferences drawn from the vortex modeling are summarized. The following statements were based on the correlations of the pressure measurements, the well-known phenomenon of vortex shedding from bluff bodies, and the simulation of the histograms by the vortex model:

- (1) A series of discrete vortices are shed from near the crest of the airfoil at regular time intervals.
- (2) The vortices initially move upward, but the movement is nearly in the free-stream direction by the chordwise position of 15-percent chord.
- (3) The vortex speed accelerates from about one-half of the free-stream velocity near the crest to nearly free-stream velocity near the trailing edge.
- (4) The vortex paths become somewhat less regular toward the trailing edge, but the repeatability of the time of the vortex passage remains high from leading edge to trailing edge.
- (5) A second region of vortex shedding originates on the lower surface of the airfoil.

Histograms for Small Average Velocities

A consideration of the overall flow picture as shown by figures 59 and 60 suggested that the flow near the surface behind the midchord of the airfoil should be reversed. This reversal was confirmed by the behavior of the tufts. The location of the tufts is shown in figure 9. The tufts were observed by a television camera closeup and were recorded on video tape. For several tufts, a predominant direction could be discerned. The flow at locations A, B, and F of figure 9 was definitely in the downstream direction. Tufts C, D, E, and G oscillated between the upstream and downstream directions, and

tufts C and D were particularly unsteady. The dominant direction of tufts D, E, and G was in the reversed flow or upstream direction. Thus, the average velocity, as plotted in figure 36, for example, should have been negative in the region from $y = 0.03$ to 0.05 m.

The laser velocimeter measurement of absolute velocity components, combined with a range that did not extend to zero, precluded the direct detection of negative velocities. However, an attempt was made to infer the flow-reversal region and to assess the effects of the measurement dropout zone near zero velocity.

An interpretation of the minimum velocity calculated from the measured histograms can be given from figure 64 which illustrates a Gaussian velocity probability density function with an average velocity of 30 m/sec. The full probability density function is drawn in figure 64(a). The present laser velocimeter measured only the magnitudes of velocity so that the part of the curve to the left of the zero velocity is folded over to the right and added to the positive velocity probabilities. Figure 64(b) illustrates this effect combined with a dropout zone of ± 5 m/sec. The 5 m/sec dropout zone in the laser velocimeter is caused by a high-pass filter used to remove the laser velocimeter signal pedestal so that figure 64(c) is the probability density function that the laser velocimeter would have constructed. The theoretical probability density function had a mean value of 30 m/sec and a standard deviation of 40 m/sec. The mean in figure 64(c) is 44 m/sec, and the standard deviation is 24 m/sec. This increase in average velocity and decrease in standard deviation were seen in figure 36.

Figure 65 reproduces the average velocity and standard deviation for transducer position 17 histograms. The symbols in figure 65(a) are measured values. A hypothetical velocity profile, labeled profile 1, has been superimposed on the measured velocities. The average measured velocities above 40 m/sec have been assumed to be unaffected by the histogram dropout zone, and the hypothetical profile closely coincides with the measured values. The corresponding standard deviation profile is also labeled profile 1. Assuming the velocities followed a Gaussian probability density function permitted use of the computer to generate simulated histograms. The values of average velocity and standard deviation (the hypothetical profile 1 values) were input to the computer simulation. The computer was programmed for the dropout zone and velocity interval resolution of the measured histogram. Thus, the computer simulated the distortion that the laser velocimeter dropout zone and resolution introduced into the measured histograms. The average velocity was assumed to be in the free-stream direction. Once the simulated histograms were generated, they were used to calculate a simulated average velocity and standard deviation. The computer results are shown as symbols in figure 65(b). The average velocity reaches a minimum value of about 20 m/sec and levels off. The three values of U_L at $y = 0.0298$, 0.0352 , and 0.0396 m are smaller than the V_L component because they were taken with a smaller velocity range. The standard deviation

exhibits a similar behavior. This similarity shows that the simulated average velocity and standard deviation (the symbols in fig. 65(b)) are a reasonable match for the measured values (the symbols in fig. 65(a)). Thus, the dropout zone affects the hypothetical velocities given by profile 1 by causing the simulation to give the measured results. The simulated histograms could be considered a satisfactory approximation (fig. 66) to the measured histograms when the uncertainty in the real probability density function, the approximation to the exact size and shape of the dropout zone, and the possible bias toward higher velocities (ref. 12) have been taken into account.

The low velocity dropout zone and the measurement of velocity magnitude apparently destroy the possibility of deducing average velocities below 40 m/sec. To confirm this, a second profile for transducer position 17 data was drawn. Figure 67(a) illustrates the assumed profile, and figure 67(b) shows the resulting average velocities and standard deviations. The changes from profile 1 to profile 2 are nearly insignificant. Figure 66 illustrates the measured, profile 1, and profile 2 histograms. No satisfactory basis could be found for preferring one set of simulated histograms over the other. Therefore, it was concluded that any further analysis of the histograms with an average velocity below 40 m/sec was futile, and that histograms with larger average velocities were little affected by the low velocity dropout zone.

EVALUATION OF SYSTEM PERFORMANCE

The experimental system comprised the laser velocimeter and data-acquisition system, the model and model instrumentation, the wind tunnel, and the seeding. The advantages of the system are readily apparent and need little analysis. The major defects are peculiar to the present investigation and are correctable.

The laser velocimeter optics system yielded velocity measurements over a small volume with no flow interference. These features were vital for the successful measurement of the separated flow above the model. The principal disadvantages of the laser velocimeter were the dropout zone that affected the mean velocity below 40 m/sec and the minimum seed size (about 3 μm) visible to the system. A Bragg cell and increased optical efficiency will correct both defects. The scan system was satisfactory but was limited by the size of the window and the fixed viewing angle of the model.

The data-acquisition process was never limited by the accuracy of the measurement of the seed particle velocities. Even the principal inaccuracies, which were introduced by interpretation of the individual velocity measurements, had an inconsequential influence on the conclusions of this investigation. The histogram velocity bias, the lag between gas and particle velocity, and the statistical uncertainty in the histogram moments are the areas presenting the greatest opportunity for improvements in accuracy. The statistical

uncertainty can be better controlled, and the velocity bias can be eliminated by an automated data-acquisition system that records the value and time of each measurement. The time information will also allow frequency spectrum analysis of the velocities. The particle lag is calculable for flows for which the time history is known by the methods in reference 11.

The data-acquisition rate was controlled by the seeding of the flow. Improvements in both data-acquisition rate and particle lag minimization could be achieved by control of the smoke injection position and smoke particle size. Injection of the smoke directly into the separated region would be desirable.

The instrumented model had two major deficiencies. Definition of the magnitude of the pressure measurements would be valuable. A larger model chord would have the advantages of more realistic Reynolds number simulation and reduced error (relative to model size) because of the control volume position uncertainty and control volume size. The point of closest approach to model was limited by the diffuse reflection from the wing surface. The effects of diffuse reflection can be minimized by smooth model surfaces and improved error rejection in the signal processing electronics.

CONCLUSIONS

A survey of the flow field above a stalled wing was conducted using a laser velocimeter that used an argon-ion laser, a backscatter mode of operation, and polarization separation of the two components of velocity. The data acquisition, including the interpretation of the histograms of velocity, was analyzed for accuracy. The model was an aspect-ratio-8 wing installed in the Langley high-speed 7- by 10-foot tunnel at an angle of attack of 19.5° , a nominal Reynolds number of 1.4×10^6 , and a Mach number of 0.49. Unsteady pressure measurements were made on the wing surface. An analysis of the results has led to the following conclusions:

1. The laser velocimeter has measured the components of high velocity smoke particles with less than 2-percent uncertainty. The accuracy of the mean velocity data was limited by the data-acquisition and data-reduction process rather than by the measurement process.
2. Velocity measurements below 40 m/sec cannot be made by the present technique. The removal of the dropout zone, and incidentally the fourfold ambiguity in direction, by a Bragg cell is the preferred solution to this problem.
3. A flow pattern has been deduced which is consistent with the pressure measurements and the histograms. It does not explain all the features of the data and must be regarded as tentative. The primary feature of this flow pattern is a series of discrete vortices that are shed from near the crest of the airfoil at regular time intervals. The

vortices initially move upward away from the airfoil surface. The movement is very nearly in the free-stream direction by the chordwise position of 15-percent chord. The vortex motion accelerates from about one-half the free-stream speed near the crest to near free-stream speed near the trailing edge. The vortex passage time occurs at very regular intervals although the trajectory heights are somewhat irregular from vortex to vortex. A second set of shed vortices originates from the airfoil lower surface.

Langley Research Center
National Aeronautics and Space Administration
Hampton, VA 23665
February 10, 1977

APPENDIX A

SEEDING

William V. Feller
Langley Research Center

Kerosene was chosen as the flow seeding material as a compromise between the requirements of low vapor pressure at tunnel conditions to reduce particle size loss by evaporation, and high enough vapor pressure to avoid accumulation of liquid on the tunnel walls. Because kerosene is flammable, the potential fire hazard had to be evaluated.

The concentration of kerosene vapor in air at its lower explosive limit is 0.7 percent by weight (ref. 20). One-fifth of this value was chosen as the maximum concentration allowed to accumulate in the tunnel. When the air exchange during the tunnel cycle is neglected (a conservative approach) and when evaporation of all kerosene added for seeding is assumed, calculation from the tunnel volume (8000 m³) and mass of air (9750 kg) indicates that the maximum total amount of kerosene that can be introduced is 13.6 kg. At an estimated input rate of 3.78 liters (3.17 kg) per hour, seeding for a period of 4.3 hours would be permitted before reaching the limiting concentration selected. After this time, the kerosene would be shut off, and the tunnel would be run for 5 minutes with maximum air exchange to reduce the concentration and to evaporate any local accumulation of liquid kerosene. The calculation outlined is conservative and neglects the continuous air exchange during flow. Consequently, the fire hazard is believed to be acceptably low.

The particle production and distribution system was mounted on the tunnel turning vanes 25 m upstream of the test section. (See fig. A1.) Earlier smoke visualization tests had demonstrated the need for distributing the smoke over an area because the streamline tubes whip around in the test section with an amplitude greater than the width of the smoke plume from a single ('point') source, giving an intermittent laser velocimeter signal.

The smoke distribution apparatus shown in figure A1 consists simply of a half-cylinder 3.8 cm in diameter upstream of each outlet tube. The half-cylinder extends laterally about 1 m. The cylinders are fastened to the turning vanes and are, therefore, swept 45° to the flow direction. The smoke produced at the vapor outlet tube is trapped in the wake flow of the swept cylinder and is spread laterally as the smoke escapes through the wake-stream mixing region. A flow rate of about 0.3 kg per hour was found to be sufficient to generate 2 to 50 laser velocimeter measurements per second.

The smoke (particle) generator (fig. A2) was a Howerton evaporating-condensing system that was mounted on the tunnel turning vanes. The kerosene is driven from a

APPENDIX A

pressurized reservoir through three parallel tubes 3 m long (1.8-mm o.d., 1.3-mm i.d.) wrapped helically around a 600-W electrical cartridge heater. The kerosene is vaporized in the tubes. On mixing with the tunnel airflow, the kerosene vapor condenses to droplets. Size distributions taken before tunnel installation and measured by an electro-optical particle size analyzer are shown in figure A3. (The distribution is normalized to the peak value and is cut off below 0.5 μm because of limitations of the particle size analyzer.) The median particle size is below 1 μm and fewer than 2 percent are larger than 3 μm .

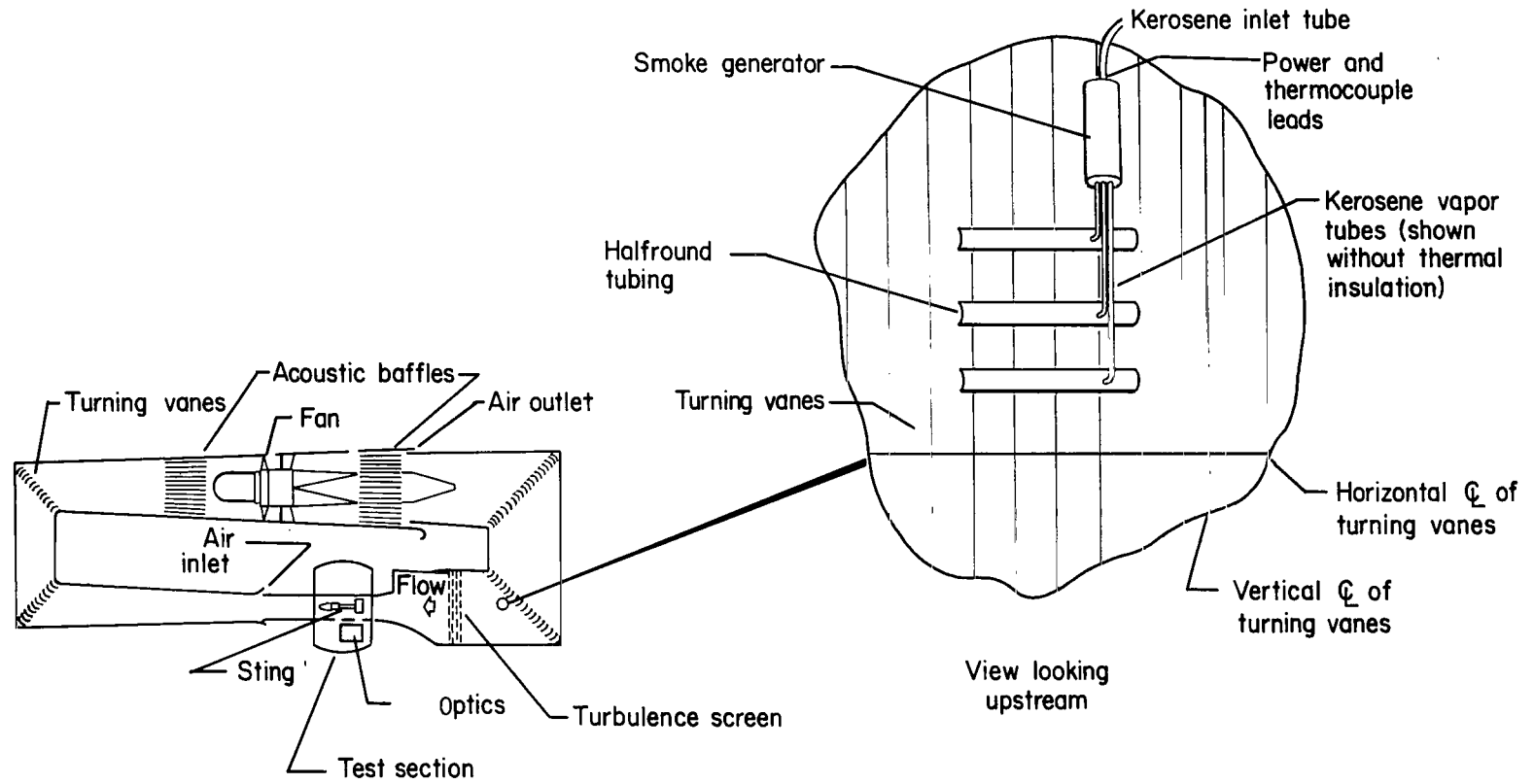
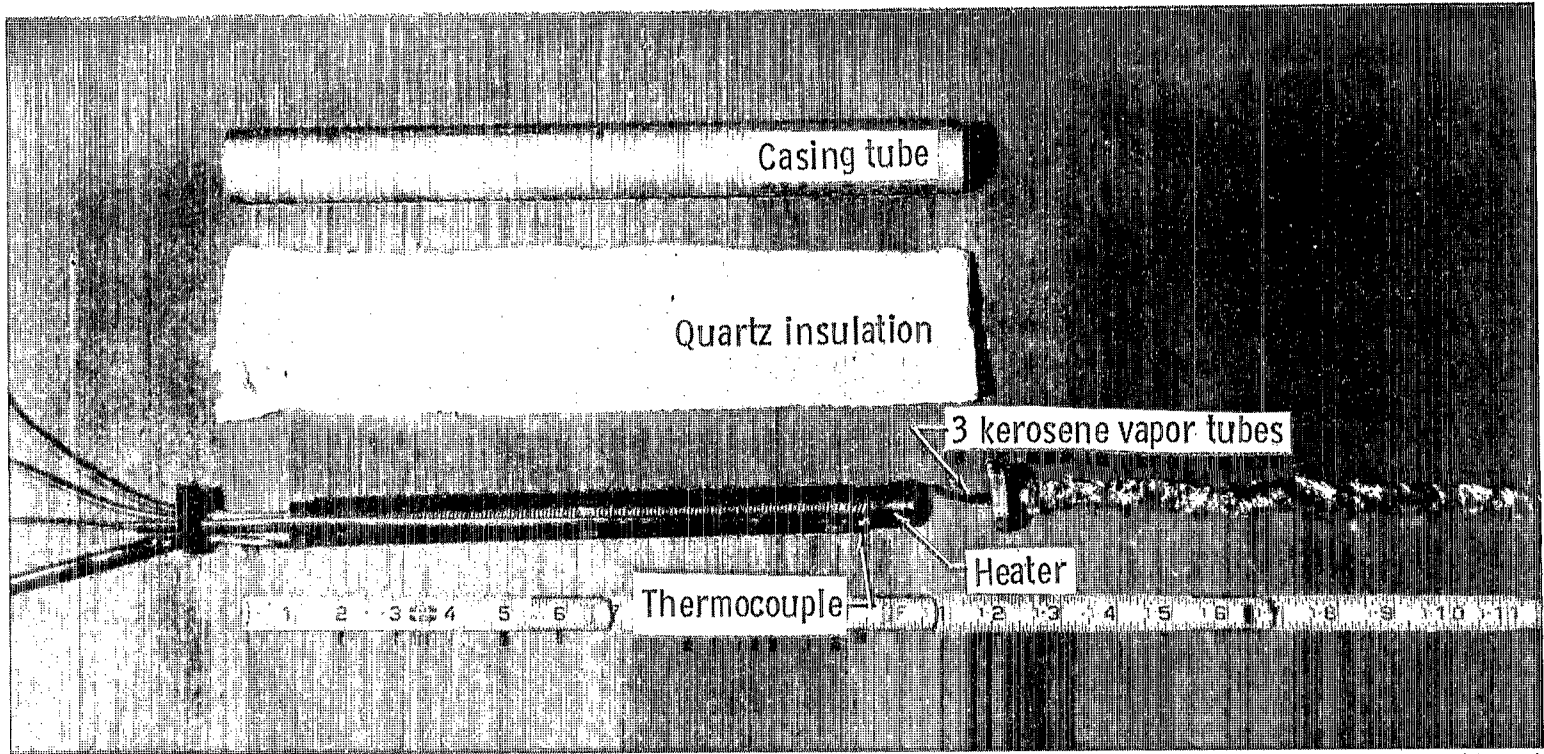


Figure A1.- Installation of smoke generator in Langley high-speed 7- by 10-foot tunnel.



L-76-1350.1

Figure A2.- Disassembled smoke generator.

APPENDIX A

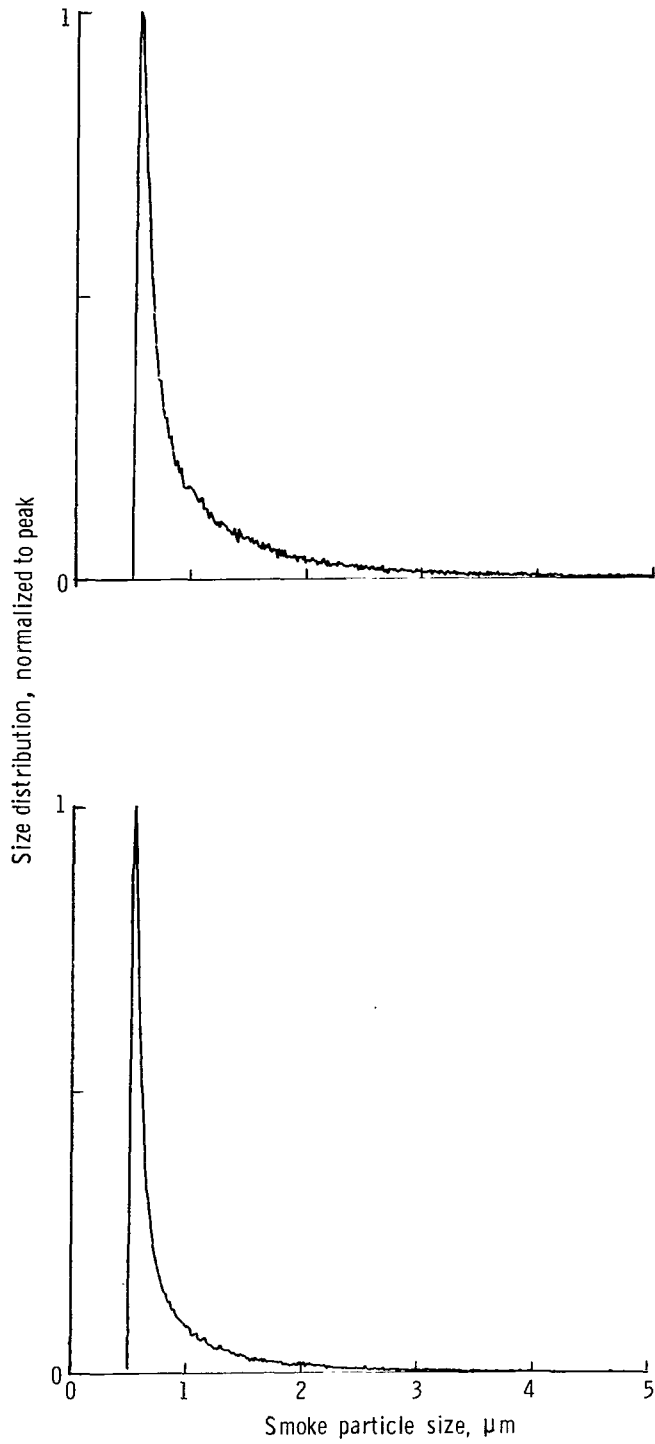


Figure A3.- Measured size distribution of smoke particles.

APPENDIX B

INTERPRETATION OF HISTOGRAMS

Janet W. Campbell
Langley Research Center

At any fixed point in the airflow, an instantaneous velocity measurement at time t is considered a sample of the time-varying velocity $U(t)$. However, neither the exact measured value of $U(t)$ nor the value of time at which the measurement was made is recorded. Instead, the fact that the measured velocity lies in the velocity interval $U_i \pm \frac{\Delta U}{2}$ is recorded by incrementing the count in a bin labeled "i." No record is kept of the exact value $U(t)$, and the time t is thereafter unknown. The number of measurements D is large so that the length of time required to make these measurements is much longer than any of the periodic variations of the velocity. An assumption is made that the velocity $U(t)$ is repetitive in time in the sense that the percentage of measurements in each bin is stationary in time. The number of counts in bin i as a percentage of total number of measurements is denoted as C_i . The distribution of C_i is thus assumed to be stationary or constant in time. This assumption allows the measurements to be analyzed by the statistics of a random variable and allows the values of C_i to be assembled into an approximation of a probability density function that is called a histogram.

A probability density function $P(U)$ is the mathematical tool used to define the probability that a value of U lies in an interval $U - \frac{dU}{2}$ to $U + \frac{dU}{2}$. It is by definition a function that satisfies the following criteria:

$$P(U) \geq 0$$

$$\int_{-\infty}^{\infty} P(U) dU = 1$$

and

$$\int_{U_1}^{U_k} P(U) dU = \text{Probability that } U \text{ is between } U_1 \text{ and } U_k$$

The histograms constructed from the experimental measurements are approximations to a probability density function. To construct each histogram, the range of observed

APPENDIX B

velocities was divided into I intervals (or bins) of equal width ΔU with midpoints $U_i = \left(i - \frac{1}{2}\right)\Delta U$. The fraction of the velocities falling into the i th interval, $U_i - \frac{\Delta U}{2}$ to $U_i + \frac{\Delta U}{2}$, was counted and denoted C_i . Then the probability of the velocity lying between $U_i - \frac{\Delta U}{2}$ and $U_i + \frac{\Delta U}{2}$ is estimated by C_i , where

$$\sum_{i=1}^I C_i = 1$$

The value of C_i is an approximation of $P(U_i)\Delta U$ where $P(U_i)$ is the probability density evaluated at the center of the i th velocity interval, and ΔU is the width of the velocity intervals used to construct the histogram.

In addition to the histogram, other quantities used to describe the probability density of the velocity are its mean (or average) U_a , standard deviation σ , variance σ^2 , skewness S_R , and excess (or kurtosis) E . The mean of a velocity probability density is simply the average velocity defined by

$$U_a = \int_{-\infty}^{\infty} UP(U) dU$$

The mean is estimated from a histogram by

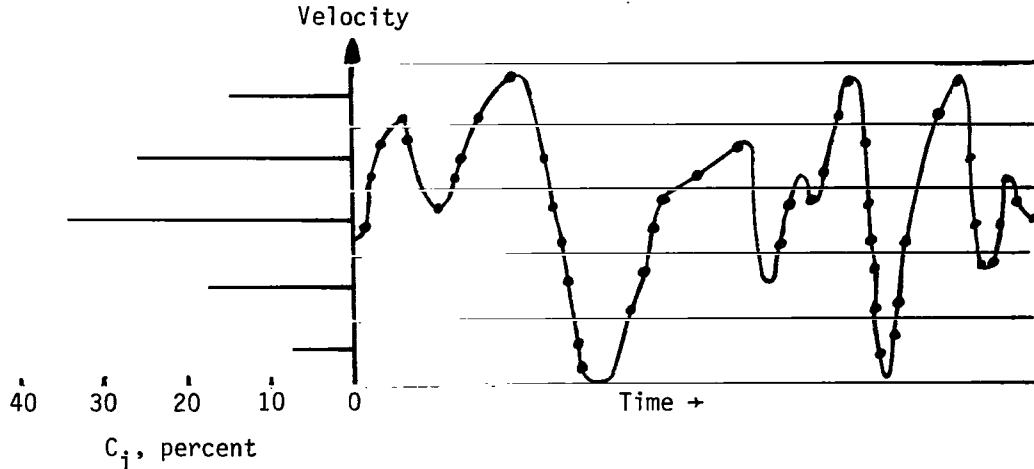
$$U_a = \sum_{i=1}^I C_i U_i \tag{B1}$$

The mean of the histogram can be shown to be equal to the time averaged velocity \bar{U} which is given by

$$\bar{U} = \lim_{T \rightarrow \infty} \frac{1}{T} \int_0^T U(t) dt$$

The equivalence of the histogram mean and the time average can be visualized by considering the construction of a histogram from a time-varying signal. In sketch (a), the spaces between horizontal lines represent the velocity intervals or bins. The distance between the horizontal lines is the velocity interval or resolution ΔU . The line representing $U(t)$ has been dotted to show points at which measurements were made.

APPENDIX B



Sketch (a)

In this example, a total of 47 measurements was made. The bin at the bottom, which corresponds to the smallest velocity, contains a count of four measurements. The C_i for that velocity interval is therefore 0.085 or 8.5 percent. The central or third bin has the largest count. The velocity associated with this bin ($2.5 \Delta U$) is called the mode velocity. To find the mean velocity, the velocities U_i , weighted by the values of C_i , are averaged

$$U_a = 0.085U_1 + 0.170U_2 + 0.340U_3 + 0.255U_4 + 0.148U_5 = 2.706\Delta U$$

The mean velocity of the histogram does not necessarily occur at the highest peak or mode. The mean reflects the amount of time spent by $U(t)$ in each of the bins or velocity intervals. This is what makes the histogram mean or average equal to the velocity average in the time domain.

Further information on the time dependence of $U(t)$ can be extracted from the histogram. The variance of a probability density function is the average squared distance from the mean. It is defined by

$$\sigma^2 = \int_{-\infty}^{\infty} (U - U_a)^2 P(U) dU$$

The variance is approximated from a histogram by

$$\sigma^2 = \sum_{i=1}^I C_i (U_i - U_a)^2 \tag{B2}$$

APPENDIX B

Since the variance has units of velocity squared, a more physically meaningful measure of the dispersion of the velocity distribution is σ , the square root of the variance σ^2 . The quantity σ is called the standard deviation which can be interpreted in terms of the time-dependent velocity $U(t)$ as the root-mean-square value of $(U(t) - \bar{U})$. The standard deviation is thus a measure of the magnitude of velocity fluctuations. The standard deviation, of course, gives no information on the temporal frequency spectra of the velocity fluctuations.

The skewness of a histogram can be estimated by

$$S_R = \sum_{i=1}^I \frac{(U_i - U_a)^3 C_i}{\sigma^3} \quad (B3)$$

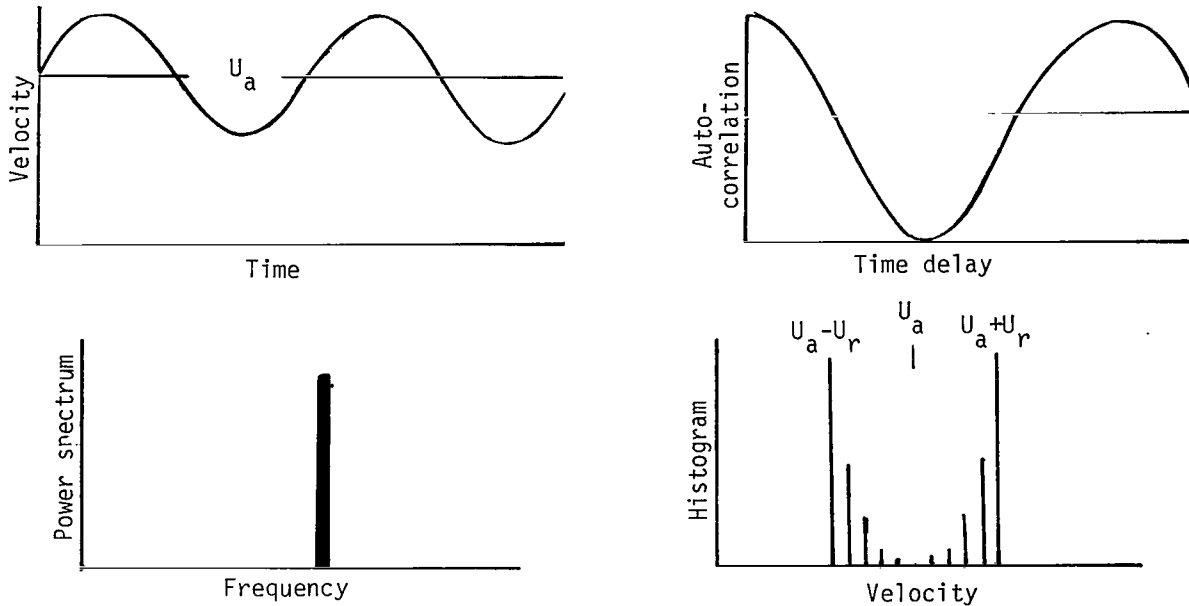
A histogram that is symmetric about the mean velocity has zero skew. A positive value of skew indicates that the histogram is weighted toward velocities higher than the mean or that it has a long tail above the mean. There is no familiar analogy to the histogram skew in the analysis of time-dependent functions. This is also true of the excess (or kurtosis) E . The excess is calculated by

$$E = \sum_{i=1}^I \frac{(U_i - U_a)^4 C_i}{\sigma^4} - 3 \quad (B4)$$

In the absence of velocity shear, the velocity in turbulent flow has often been characterized by the classical Gaussian, or normal, velocity probability density function. The normal probability density is symmetric so that the skew is zero. The excess is defined in such a way that a normal density has zero excess. Negative values of excess indicate a velocity probability density function that is more peaked or pointed than a normal density function. That is, negative excess means that the velocities for the measured probability density, when compared to a normal distribution with the same standard deviation, are more closely bunched about the mean. Positive values of excess characterize a probability density that is flatter than a normal density function.

The usual methods of analyzing time-varying signals (ref. 21), such as a power spectrum or autocorrelation, allow the identification of many common functions of time by characteristic shapes. For example, Gaussian white noise yields a power spectrum that is a constant (a straight line). The corresponding autocorrelation is a spike at a delay time of zero. A histogram of white noise also has a characteristic shape, that is, that of a Gaussian or normal probability density function. The interpretation of histograms is greatly aided by the ability to recognize some characteristic shapes and relate them to shapes of power spectra and autocorrelations.

APPENDIX B



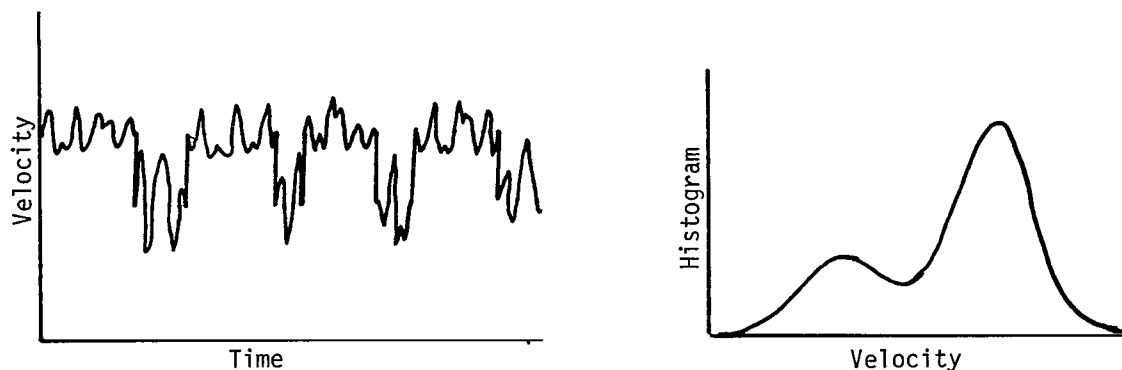
Sketch (b)

A velocity that varies sinusoidally with time, $U(t) = U_a + U_r \sin \omega t$, is illustrated in sketch (b). The power spectrum is a spike at the frequency ω . The width of the spike is the frequency resolution $\Delta\omega$, and the height of the spike is proportional to the value of U_r . The shape of the autocorrelation is a cosine function of delay time. The delay time between the peaks of the autocorrelation is the period of $U(t)$. The constant magnitude of the cosine wave indicates that neither the frequency ω nor the magnitude of U_r varies with time. The shape of the corresponding histogram is symmetric about mean velocity U_a . The width of the histogram is twice the velocity variation U_r . The two-peaked (bimodal) shape indicates that the velocity is fluctuating between two values.

The exact time variation that causes a measured histogram is difficult to determine for several reasons. Turbulence is present in many flow situations. For example, the square wave in sketch (c) has a low turbulence level superimposed on the high velocity, and a larger turbulence fluctuation exists at the lower velocity state. The resultant histogram resembles the sum of two normal probability density distributions. However, no reliable method of defining the two separate flow states by direct examination of the histogram has been found.

The most useful method for the analysis of histograms of time-dependent velocities has been found to be an indirect method of three steps. The first step is to form an analytical hypothesis of the type of time variation that yields the histogram. The hypothesis accounts for as much of the time variation as possible by estimation of the physics

APPENDIX B



Sketch (c)

of the flow situation. The remainder of the time variation may be accounted for by a Monte Carlo method. That is, one of the flow parameters is a random variable. The hypothetical model is then used to generate a time history of the velocity.

The second step is to form an analytical model of the data-acquisition process so that a simulated histogram can be generated. The pertinent features of the data-acquisition and data-reduction process are modeled so that the simulated histogram will be identical to the measured histogram if there is no defect in the hypothetical flow model.

The third step is to compare the simulated and measured histograms. If the comparison is not satisfactory, the hypothetical flow model must be corrected. If the measured and simulated histograms agree perfectly, the hypothetical flow model may not be accepted with complete assurance as representing the true time variation because other models could yield the same result. The fact that the time and frequency information is lost in the process of histogram construction precludes the possibility of eliminating all other time variations that may yield the same histogram. Therefore, care must be taken to assure that simulations satisfy the physical constraints of the flow.

REFERENCES

1. McCroskey, W. J.; Carr, L. W.; and McAlister, K. W.: Dynamic Stall Experiments on Oscillating Airfoils. *AIAA J.*, vol. 14, no. 1, Jan. 1976, pp. 57-63.
2. Gault, Donald E.: An Experimental Investigation of Regions of Separated Laminar Flow. NACA TN 3505, 1955.
3. Seetharam, H. C.; and Wentz, W. H., Jr.: Experimental Studies of Flow Separation and Stalling on a Two-Dimensional Airfoil at Low Speeds. NASA CR-2560, 1975.
4. Meyers, James F.; Couch, Lana M.; Feller, William V.; and Walsh, Michael J.: Laser Velocimeter Measurements in a Large Transonic Wind Tunnel. Minnesota Symposium on Laser Anemometry – Proceedings, E. R. G. Eckert, ed., Univ. of Minnesota, Oct. 1975, pp. 84-111.
5. Mie, G.: Optics of Turbid Media. *Ann. Phys.*, vol. 25, no. 3, 1908, pp. 377-445.
6. Yanta, William J.: Turbulence Measurements With a Laser Doppler Velocimeter. NOL-TR-73-94, Naval Air Systems Command, May 1973. (Available from DDC as AD-766 781.)
7. Yanta, William J.: Laser Doppler Velocimeter Measurements of Turbulence Properties of a Mach 3 Turbulent Boundary Layer. Proceedings of Second International Workshop on Laser Velocimetry, Volume I, H. D. Thompson and W. H. Stevenson, eds., Purdue Univ., Mar. 1974, pp. 115-141.
8. Johnson, Dennis A.; Bachalo, William D.; and Modarress, Daryoush: Laser Velocimeter Supersonic and Transonic Wind Tunnel Studies, Minnesota Symposium on Laser Anemometry – Proceedings, E. R. G. Eckert, ed., Univ. of Minnesota, Oct. 1975, pp. 69-82.
9. Hanson, Steen: Broadening of the Measured Frequency Spectrum in a Differential Laser Anemometer Due to Interference Plane Gradients. *J. Phys. D: Appl. Phys.*, vol. 6, no. 2, Jan. 1973, pp. 164-171.
10. Wang, James C. F.: Laser Velocimeter Turbulence Spectra Measurements. Minnesota Symposium on Laser Anemometry – Proceedings, E. R. G. Eckert, ed., Univ. of Minnesota, Oct. 1975, pp. 538-567.
11. Walsh, Michael J.: Influence of Drag Coefficient Equations on Particle Motion Calculations. Paper presented at Symposium on Laser Anemometry (Bloomington, Minnesota), Oct. 1975, pp. 293-326.

12. Meyers, James F.; and Walsh, Michael J.: Computer Simulation of a Fringe Type Laser Velocimeter. Proceedings of Second International Workshop on Laser Velocimetry, Volume I, H. D. Thompson and W. H. Stevenson, eds., Purdue Univ., Mar. 1974, pp. 471-510.
13. South, Jerry C., Jr.; and Jameson, Antony: Relaxation Solutions for Inviscid Axisymmetric Transonic Flow Over Blunt or Pointed Bodies. AIAA Computational Fluid Dynamics Conference, July 1973, pp. 8-17.
14. Tiederman, W. G.; McLaughlin, D. K.; and Reischman, M. M.: Individual Realization Laser Doppler Technique Applied to Turbulent Channel Flow. Proceedings of Symposium on Turbulence in Liquids (Rolla, Missouri), 1973.
15. Simpson, Roger L.: Interpreting Laser and Hot-Film Anemometer Signals in a Separating Boundary Layer. AIAA J., vol. 14, no. 1, Jan. 1976, pp. 124-126.
16. Flack, Ronald D.; and Thompson, H. Doyle: The LDV's Potential in Understanding Turbulent Structure. Minnesota Symposium on Laser Anemometry - Proceedings, E. R. G. Eckert, ed., Univ. of Minnesota, Oct. 1975, pp. 1-67.
17. Yule, G. Udny; and Kendall, M. G.: An Introduction to the Theory of Statistics. Charles Griffin & Co., Ltd., 1940.
18. Roshko, Anatol: On the Development of Turbulent Wakes From Vortex Streets. NACA Rep. 1191, 1954. (Supersedes NACA TN 2913.)
19. Sadler, S. Gene; and Loewy, Robert G.: A Theory for Predicting the Rotational and Vortex Noise of Lifting Rotors in Hover and Forward Flight. NASA CR-1333, 1969.
20. Sax, N. Irving: Dangerous Properties of Industrial Materials. Fourth ed., Van Nostrand Reinhold Co., c.1975.
21. Bendat, Julius S.; and Piersol, Allan G.: Random Data: Analysis and Measurement Procedures. John Wiley & Sons, Inc., c.1971.

TABLE I - LASER VELOCIMETER DATA AND FREE-STREAM FLOW CONDITIONS

Run	x, m	y, m	T _r	C, percent chord	N, percent chord	α _s , deg	α _w , deg	U _{L,a} , m/sec	V _{L,a} , m/sec	U _{L,m} , m/sec	V _{L,m} , m/sec	U _{L,1} , m/sec	V _{L,1} , m/sec	α _u , m/sec	α _v , m/sec	S _{R,u}	S _{R,v}	E _u	E _v	D _u	D _v	V _∞ , m/sec	M _∞	R _c	Date
1	0.1362	0.0981	3	4.01	29.28	0.00	19.44	114	109	125	113	102	113	24	25	-0.30	0.26	-0.36	-0.40	148	141	178.6	0.493	1.331	Feb. 18
2	.1362	.0874	3	4.02	22.26	.01	19.44	112	103	122	113	133	93	27	34	-.71	-.41	1.25	.04	169	200	178.6	.493	1.331	Feb. 18
3	.1362	.0824	3	4.02	18.98	.02	19.44	104	104	107	103	138	93	30	25	.18	.82	-.38	.47	289	226	178.6	.493	1.331	Feb. 18
4	.1362	.0773	3	4.02	15.63	.03	19.44	116	104	128	111	105	87	30	31	.33	.22	-.25	-.34	202	187	178.5	.493	1.327	Feb. 18
5	.1364	.0742	3	3.95	13.60	-.13	19.50	112	131	115	165	174	175	36	40	.56	-.10	-1.05	-1.73	419	463	170.6	.490	1.469	Feb. 25
6	.1362	.0723	3	4.02	12.35	.04	19.44	107	117	120	124	130	165	29	34	-.35	.07	-.32	-.98	288	154	178.5	.493	1.327	Feb. 18
7	.1364	.0694	3	3.94	10.45	-.15	19.50	145	147	174	175	184	180	41	40	-.56	-.72	-1.34	-1.23	359	827	170.6	.490	1.469	Feb. 25
8	.1363	.0673	3	3.98	9.07	-.08	19.44	104	108	102	105	130	93	28	33	.70	.47	.48	-.28	200	132	178.5	.493	1.327	Feb. 18
9	.1364	.0643	3	3.94	7.10	-.16	19.50	55	73	74	90	81	196	35	48	1.20	1.02	1.92	.53	1747	1438	171.3	.489	1.449	Feb. 25
10	.1364	.0643	3	3.94	7.10	-.16	19.50	79	83	97	93	87	87	43	38	.15	.11	-.86	-.17	1668	1778	171.3	.489	1.449	Feb. 25
11	.1364	.0643	3	3.94	7.10	-.16	19.50	109	132	112	170	194	196	42	48	.72	.11	-.48	-1.69	470	566	171.3	.489	1.449	Feb. 25
12	.1363	.0623	3	4.02	5.88	.01	19.44	84	90	97	98	97	124	34	36	-.16	-.75	-.31	-.04	133	137	178.5	.493	1.327	Feb. 18
13	.1364	.0623	3	3.97	5.88	-.08	19.50	70	103	76	186	71	198	31	68	1.25	.27	3.89	-1.46	1333	682	171.2	.490	1.453	Feb. 25
14	.1364	.0603	3	3.96	4.57	-.08	19.50	64	78	76	103	71	196	40	57	1.44	1.02	2.54	-.19	842	815	171.0	.490	1.461	Feb. 25
15	.1364	.0583	3	3.96	3.26	-.09	19.50	67	77	79	95	71	188	42	53	1.43	1.00	1.88	-.04	1141	1002	171.0	.490	1.461	Feb. 25
16	.1363	.0571	3	4.02	2.47	.01	19.44	82	77	99	95	92	103	46	38	.30	.15	-.83	-.61	697	524	177.9	.490	1.316	Feb. 18
17	.1364	.0563	3	3.96	1.95	-.10	19.50	57	67	71	82	79	196	36	45	1.52	1.34	3.30	1.47	1398	1285	171.0	.490	1.461	Feb. 25
18	.1364	.0544	3	3.96	.70	-.11	19.50	51	52	74	74	79	87	32	34	.86	1.08	.64	1.09	1283	1159	170.6	.490	1.469	Feb. 25
19	.1364	.0534	3	3.95	.04	-.12	19.50	137	156	186	191	197	196	49	45	-.04	-.71	-1.62	-1.02	318	288	171.3	.489	1.449	Feb. 25
20	.1363	.0533	3	4.02	-.02	.01	19.44	93	67	140	95	145	98	58	40	.07	.24	-1.33	-1.04	365	570	177.9	.490	1.316	Feb. 18
21	.1363	.0533	3	4.02	-.02	.01	19.44	108	84	133	98	130	93	48	38	-.40	-.18	-.72	-.67	427	489	177.9	.490	1.314	Feb. 18
22	.1225	.0923	5	8.93	26.32	8.81	19.50	143	110	163	108	166	108	33	13	-.96	1.16	-.26	6.60	264	366	175.4	.490	1.420	Feb. 24
23	.1235	.0872	5	8.83	22.92	8.71	19.50	151	110	169	111	174	108	29	13	-1.02	2.10	-.08	8.64	231	262	175.4	.490	1.420	Feb. 24
24	.1240	.0823	5	8.95	19.69	8.83	19.50	144	106	169	105	174	108	34	18	-.62	1.54	-.99	4.31	395	325	175.4	.490	1.420	Feb. 24
25	.1247	.0774	5	8.97	16.44	8.86	19.50	124	102	133	98	174	98	33	20	.35	1.93	-1.17	4.21	364	489	175.4	.490	1.420	Feb. 24
26	.1255	.0723	5	8.97	13.05	8.86	19.50	125	104	138	98	176	93	36	26	.33	1.47	-1.31	1.37	768	493	170.1	.491	1.476	Feb. 24
27	.1263	.0675	5	8.94	9.86	8.82	19.50	125	106	145	98	184	95	43	29	.27	1.38	-1.39	.93	594	289	170.1	.491	1.476	Feb. 24
28	.1262	.0673	5	9.01	9.74	8.90	19.50	146	95	174	93	176	98	40	22	-.78	2.24	-.99	6.42	491	384	168.8	.490	1.507	Feb. 25
29	.1270	.0626	5	8.97	6.61	8.86	19.50	176	107	184	98	184	93	24	35	-2.79	1.51	7.17	.91	1738	704	168.8	.490	1.507	Feb. 25
30	.1277	.0602	5	8.78	4.99	8.64	19.50	184	127	189	142	189	191	21	45	-3.73	.55	14.55	-1.44	1870	533	168.8	.490	1.507	Feb. 25
31	.1277	.0592	5	8.87	4.34	8.74	19.50	170	131	194	157	194	196	44	47	-1.34	.33	.19	-1.48	1227	679	169.7	.490	1.487	Feb. 25
32	.1282	.0567	5	8.79	2.67	8.66	19.50	116	100	169	118	194	103	61	50	-.02	.17	-1.32	-.61	1188	1368	169.7	.490	1.487	Feb. 25
33	.1283	.0540	5	8.99	.91	8.88	19.50	31	36	38	43	24	41	17	20	1.19	.94	1.54	.65	683	1413	170.1	.489	1.474	Feb. 25
34	.1091	.0947	7	14.85	29.60	13.60	19.50	140	122	163	124	166	124	32	12	-.85	-.24	-.47	7.34	436	590	173.7	.491	1.431	Feb. 24
35	.1102	.0894	7	14.94	26.05	13.60	19.45	117	109	117	105	102	103	28	21	.45	.79	-.04	1.27	1004	351	179.3	.491	1.383	Feb. 20
36	.1105	.0848	7	15.36	23.07	13.85	19.45	101	106	102	105	102	105	27	24	.96	.97	.98	1.83	663	176	179.3	.491	1.383	Feb. 20
37	.1124	.0770	7	15.37	17.80	13.86	19.45	105	112	110	111	102	103	35	30	.49	.82	-.20	.01	807	458	179.0	.490	1.379	Feb. 20
38	.1133	.0751	7	15.14	16.45	13.72	19.45	114	114	117	121	97	95	34	37	.54	.51	-.65	-.70	1336	521	179.5	.491	1.378	Feb. 20
39	.1148	.0673	7	15.37	11.24	13.85	19.45	134	144	156	175	189	196	42	43	.00	-.14	-1.37	-1.50	514	819	179.0	.490	1.379	Feb. 20
40	.1157	.0634	7	15.40	8.62	13.87	19.45	105	107	115	118	97	108	39	38	.20	.12	.09	-.05	913	1157	179.0	.490	1.379	Feb. 20

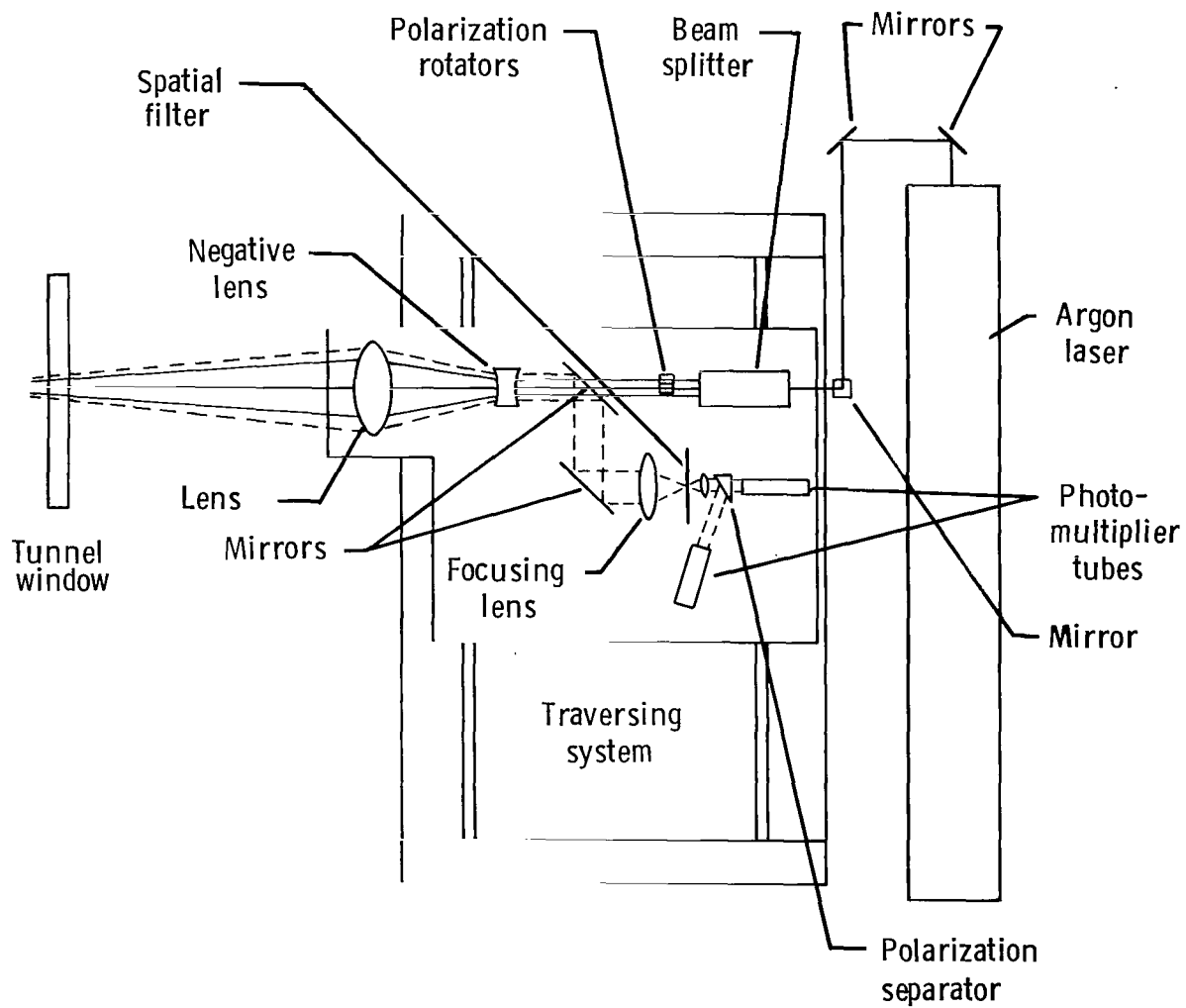


Figure 1. - Diagram of laser velocimeter optics.

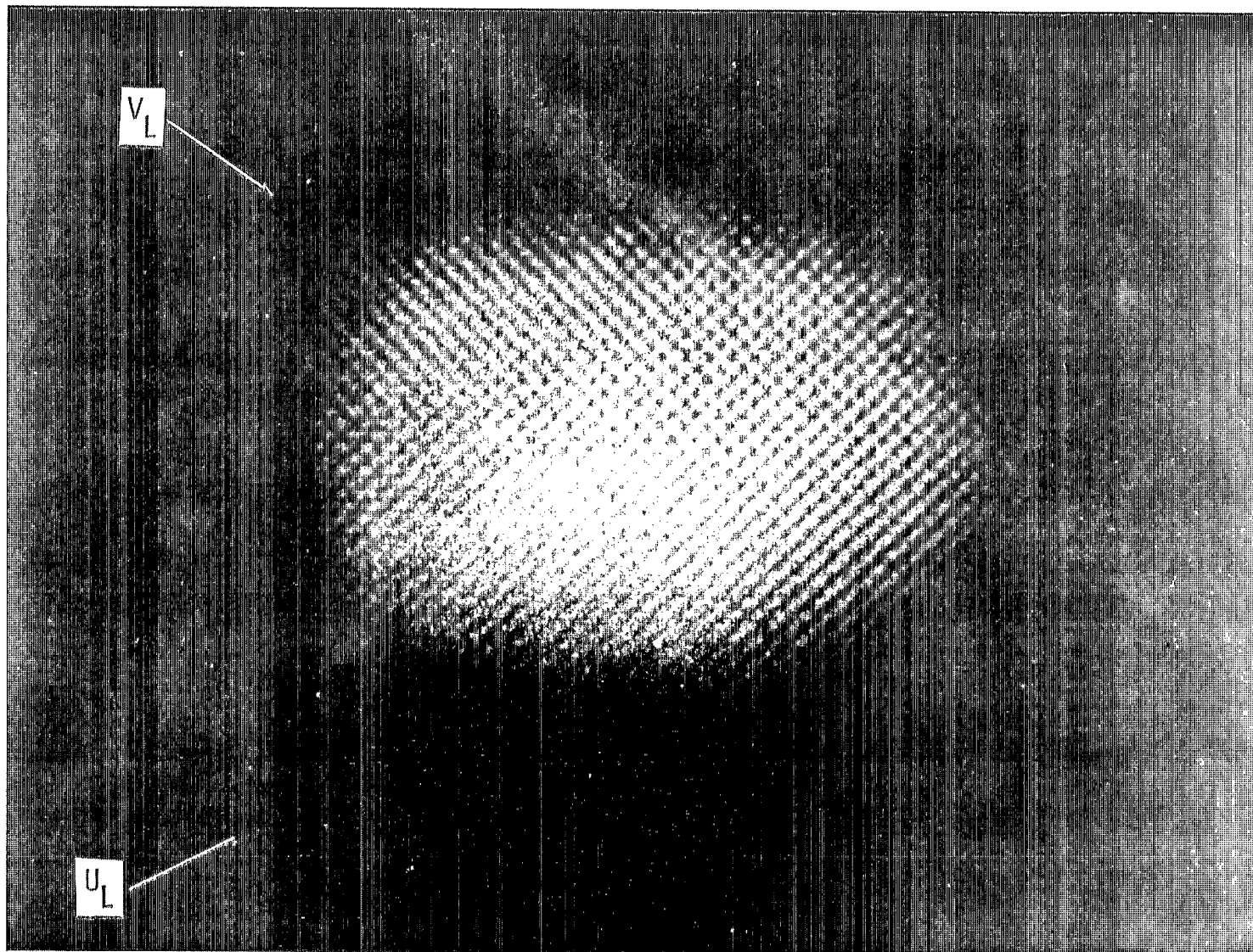
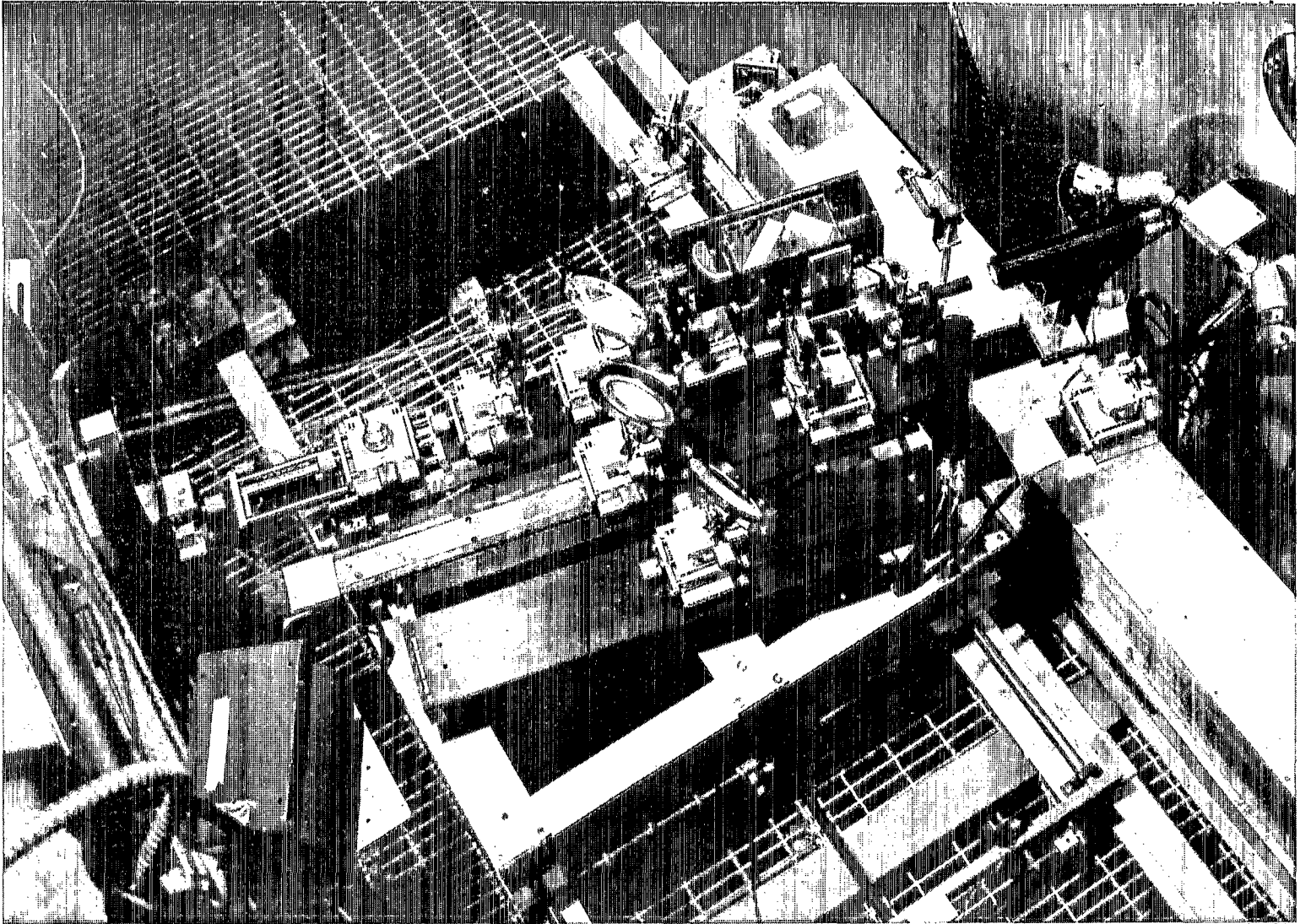


Figure 2.- Two-component fringes in sample volume.

L-77-150



L-76-1349

Figure 3.- Laser and optics table installation in plenum chamber of Langley high-speed 7- by 10-foot tunnel.

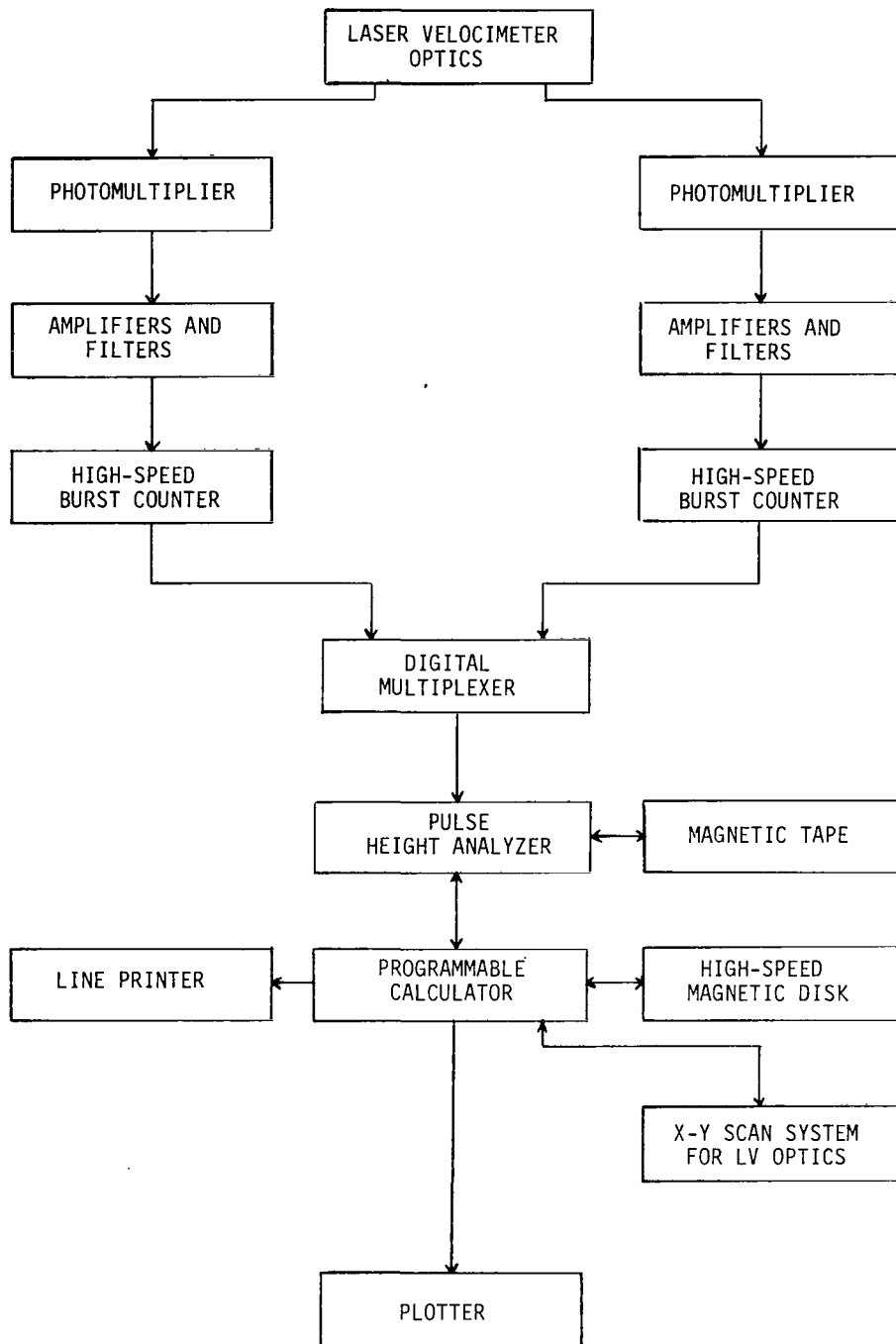
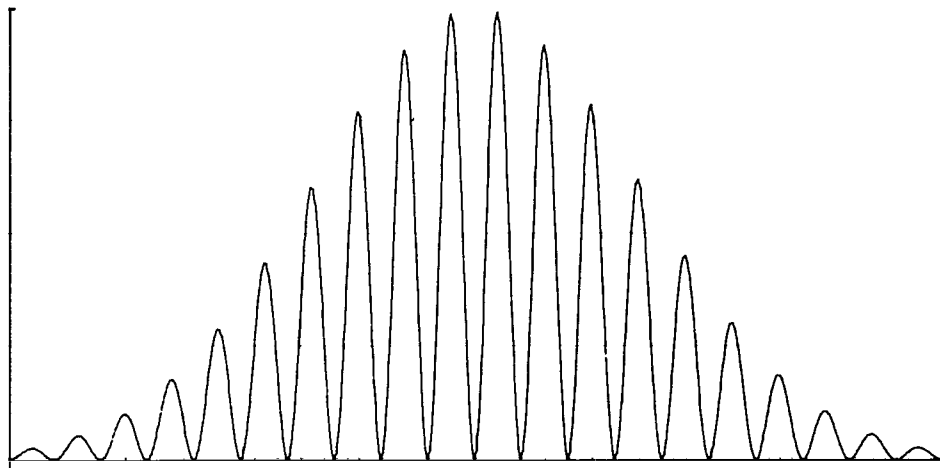
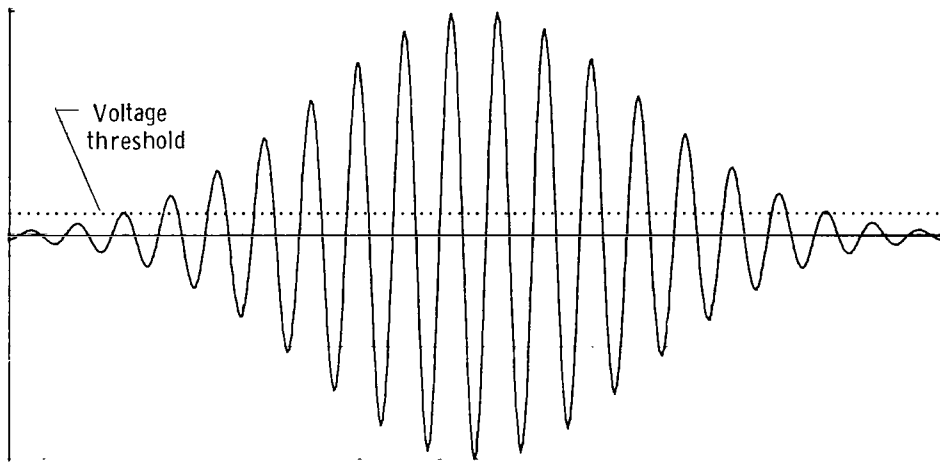


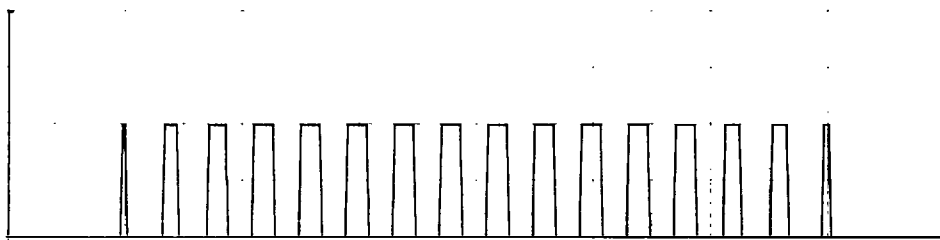
Figure 4.- Laser velocimeter (LV) electronics system diagram.



(a) Idealized burst from photomultiplier tube.



(b) Burst with pedestal removed.



(c) Digital pulse train from Schmitt trigger.

Figure 5.- Processing of burst received from laser velocimeter.

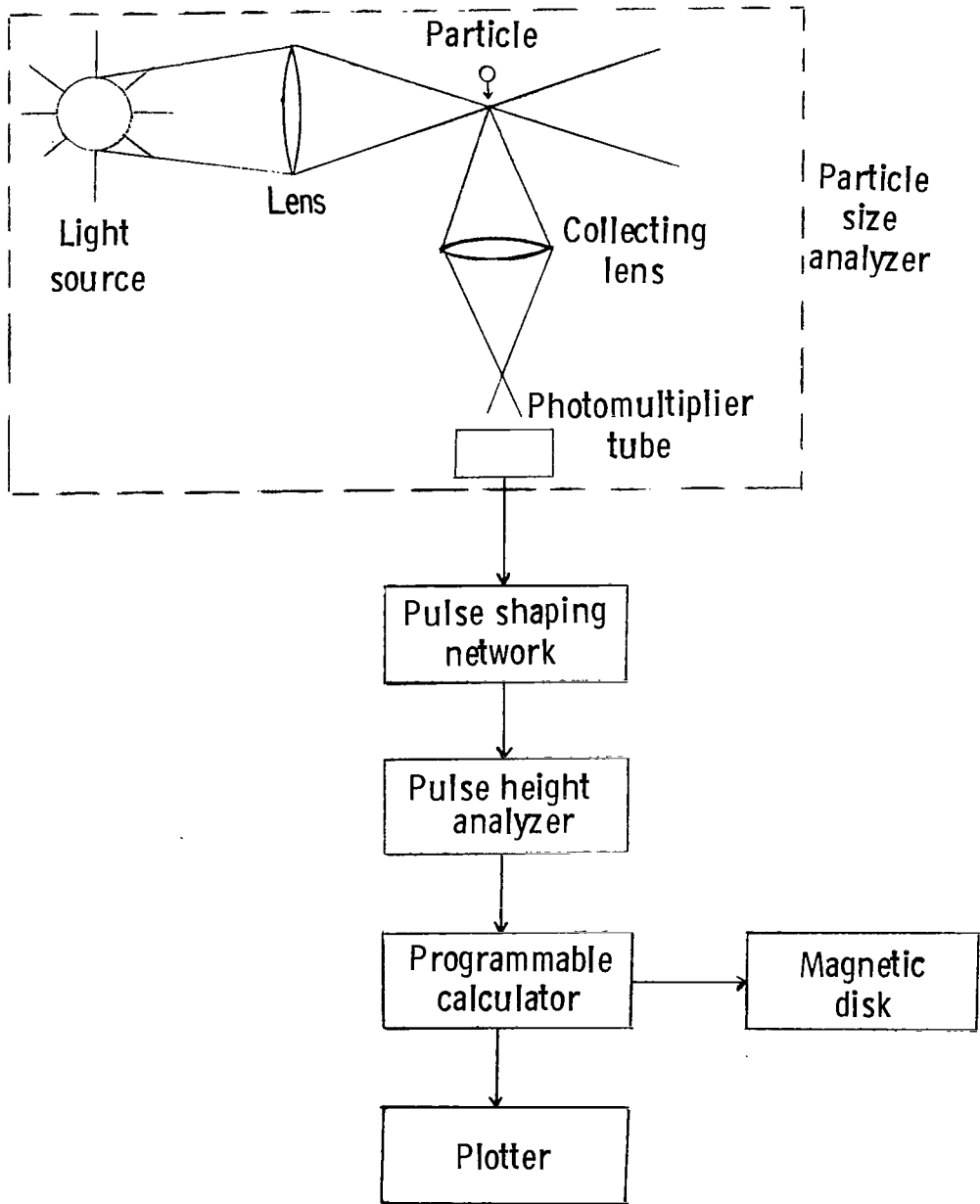
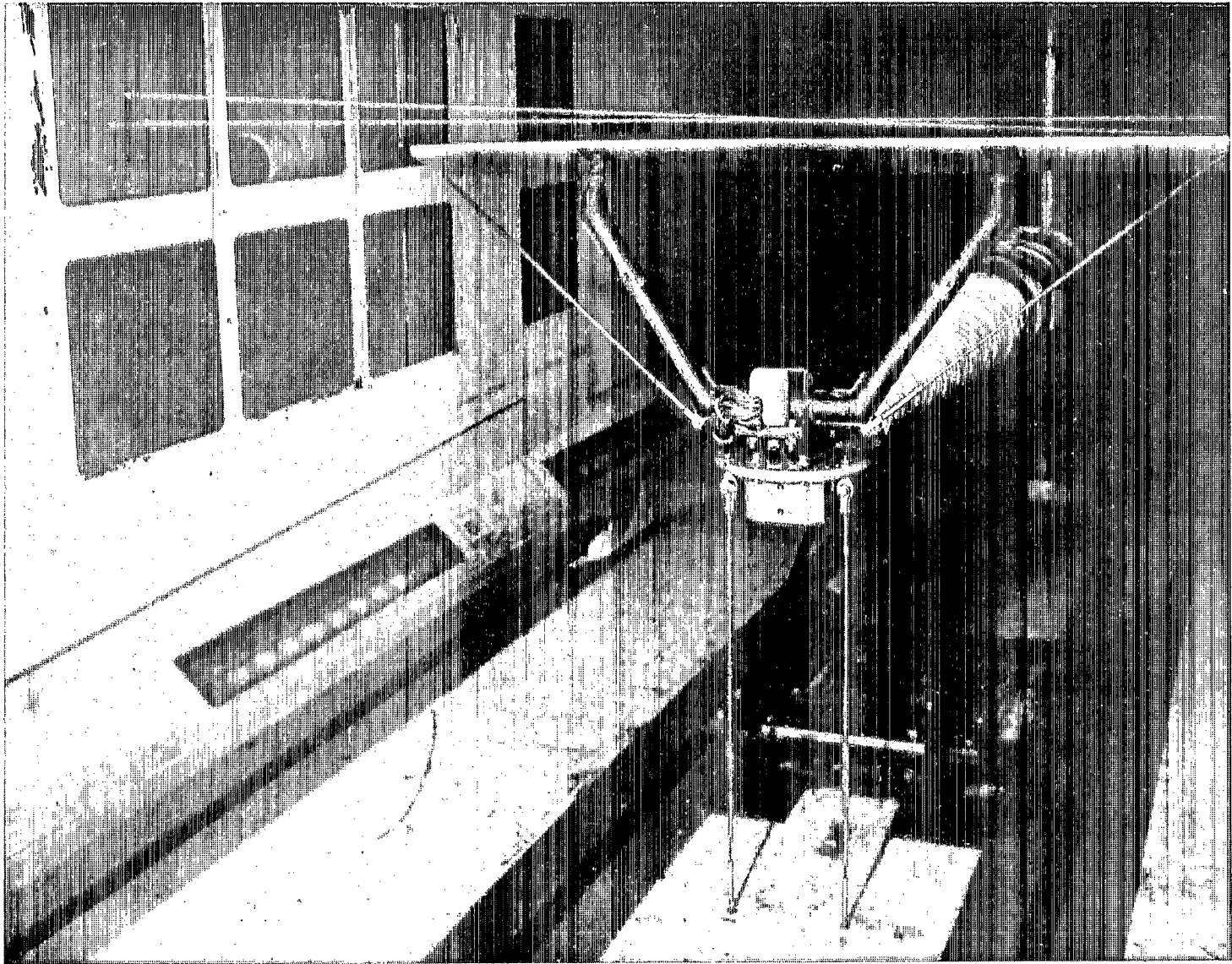
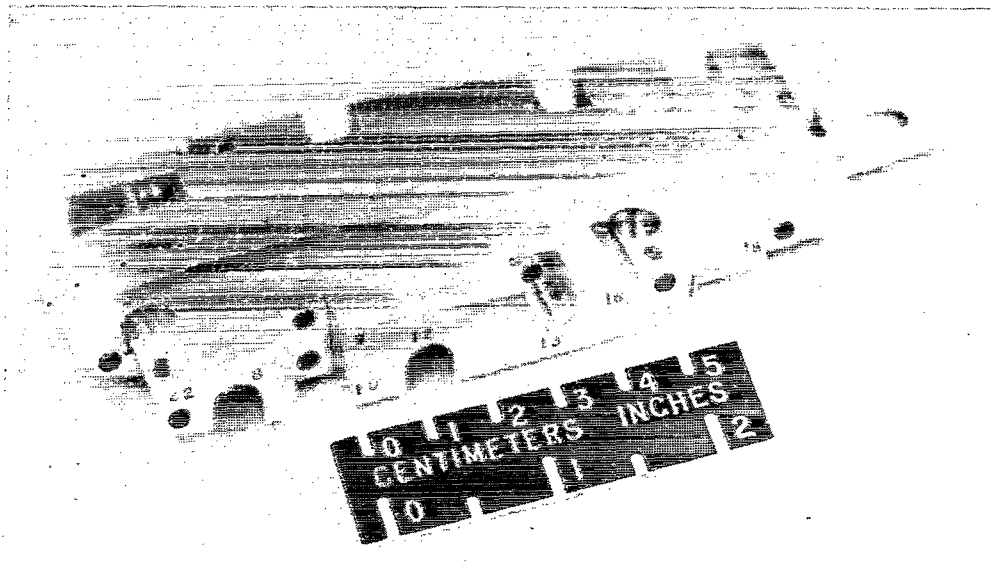


Figure 6.- Particle size measurement system diagram.



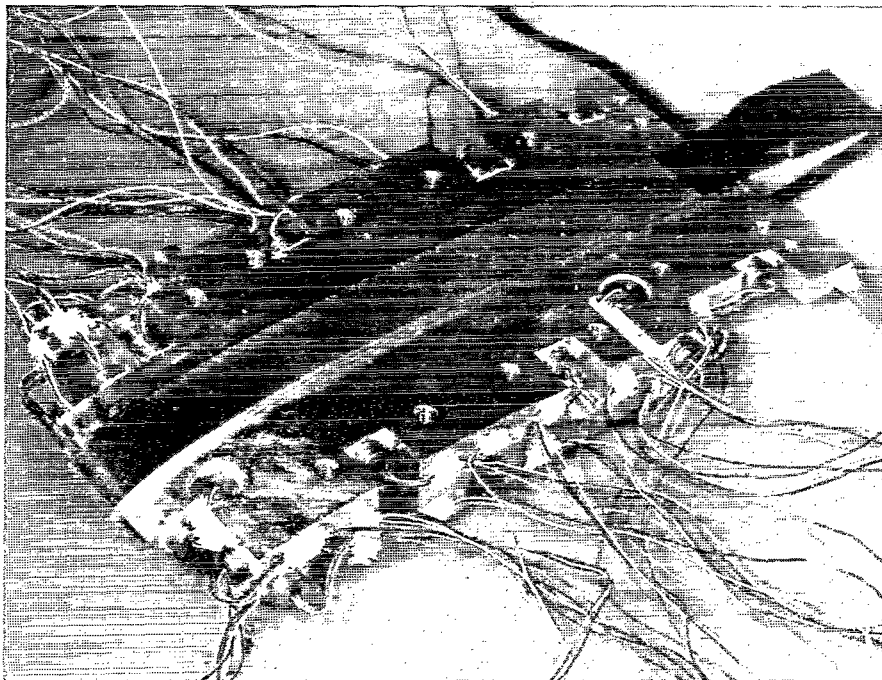
L-76-1348

Figure 7.- Model wing mounted in Langley high-speed 7- by 10-foot tunnel looking downstream.



L-72-2776

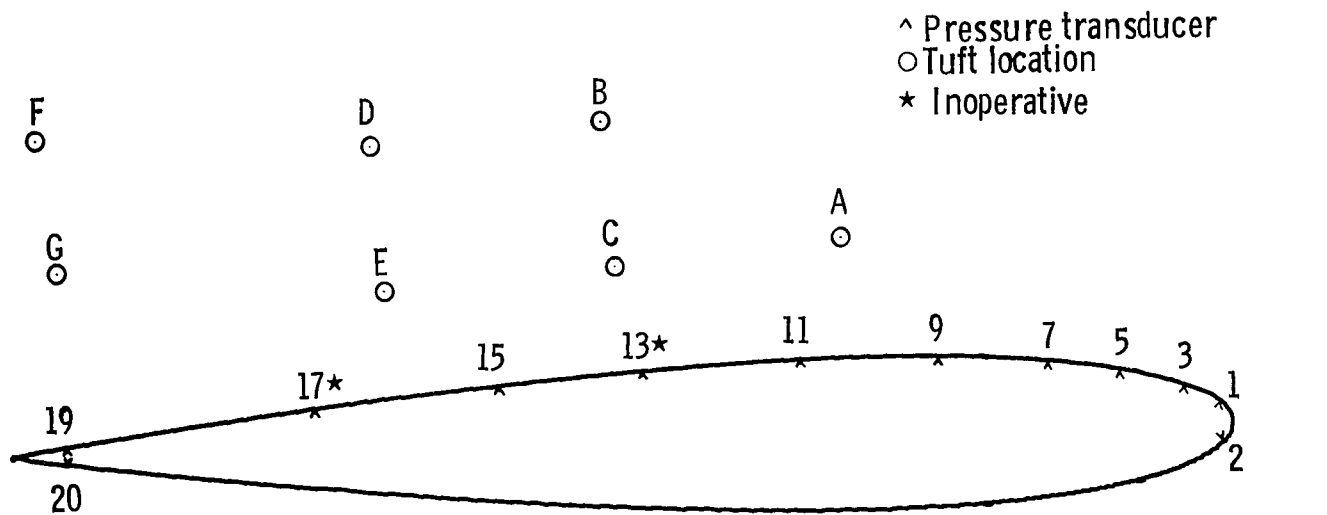
(a) Before transducer installation.



L-72-4186

(b) With pressure transducers in place.

Figure 8.- Instrumentation of center insert of model wing.



TUFT LOCATION

ID	C, % CHORD	N, % CHORD	H, % CHORD
A	30.8	9.4	72.2
B	49.8	19.8	63.6
C	49.8	8.3	63.6
D	68.5	19.8	47.2
E	68.5	8.3	47.2
F	94.8	24.0	30.6
G	94.8	13.5	30.6

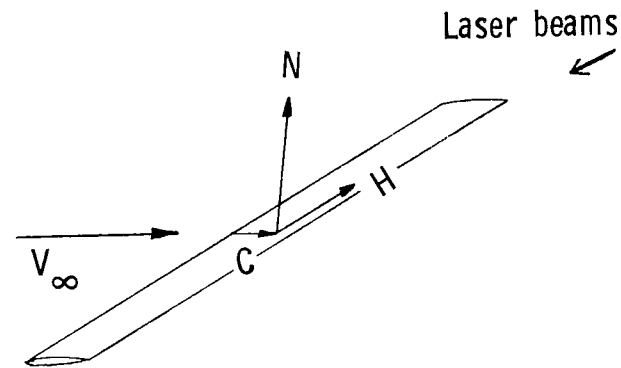


Figure 9. - Locations of pressure transducers and tufts. ID denotes identification.

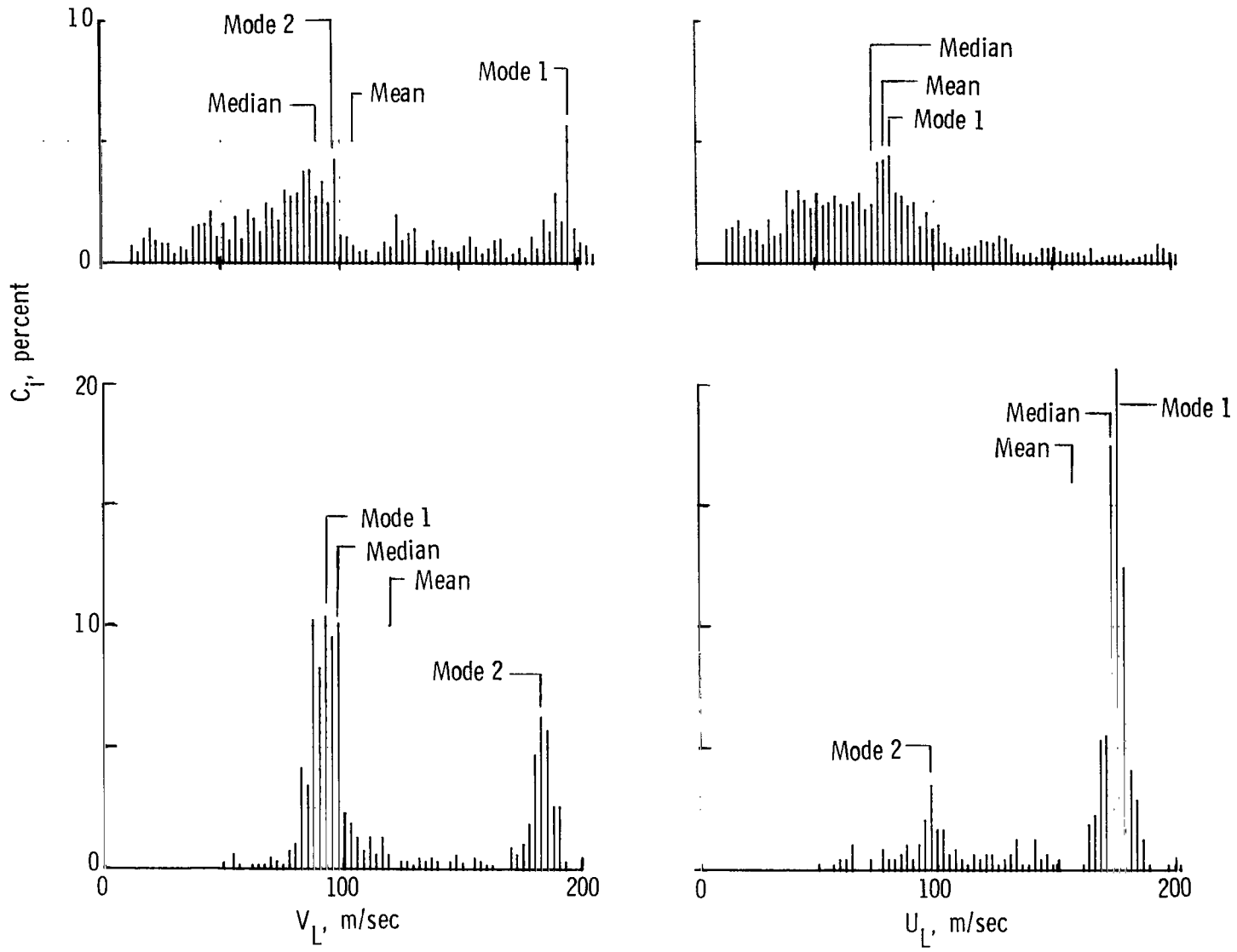


Figure 10.- Examples of mean, median, and mode velocity components from histograms.

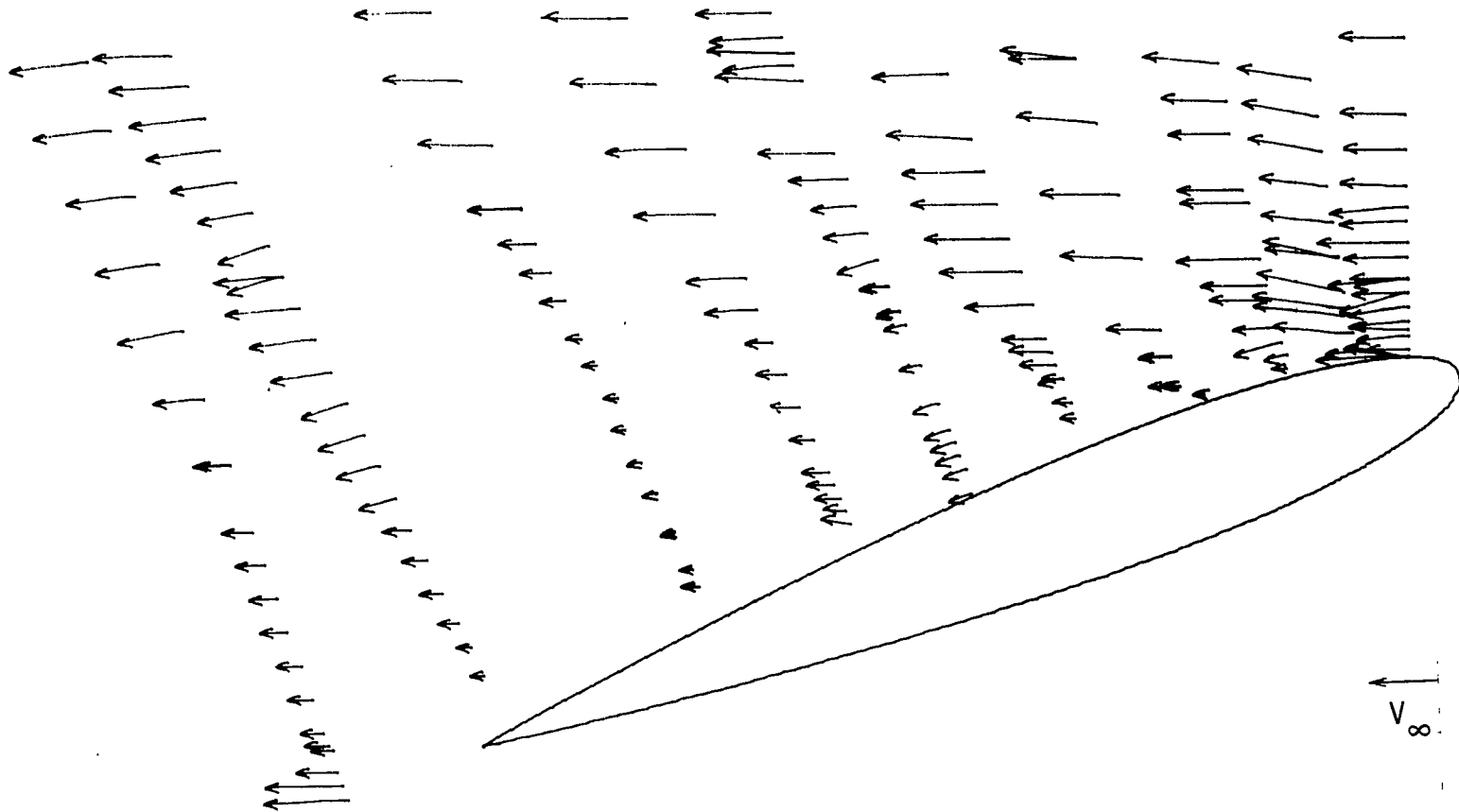


Figure 11. - Mean velocities with all velocities shown in prime direction.

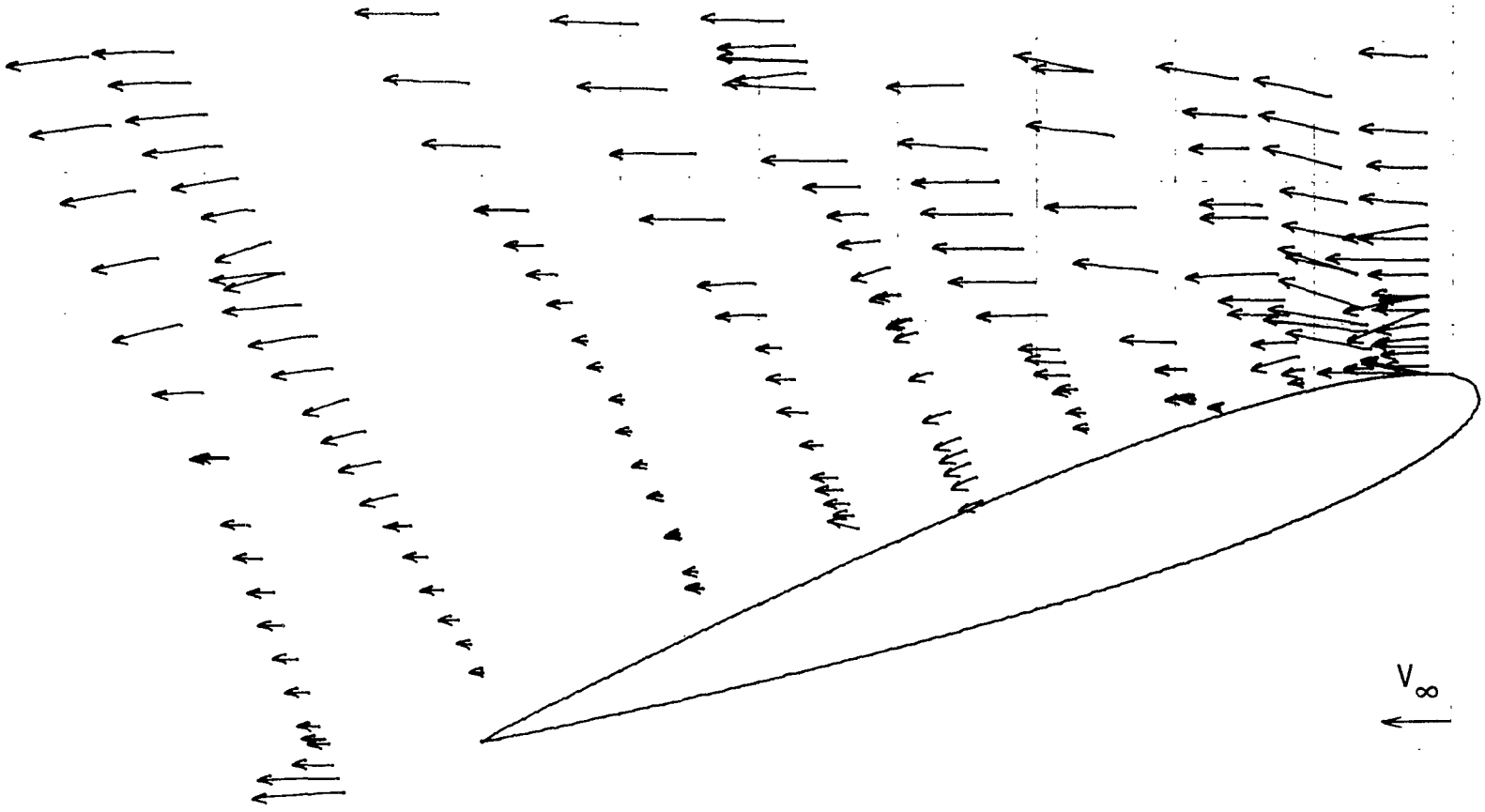


Figure 12.- Median velocities with all velocities shown in prime direction.

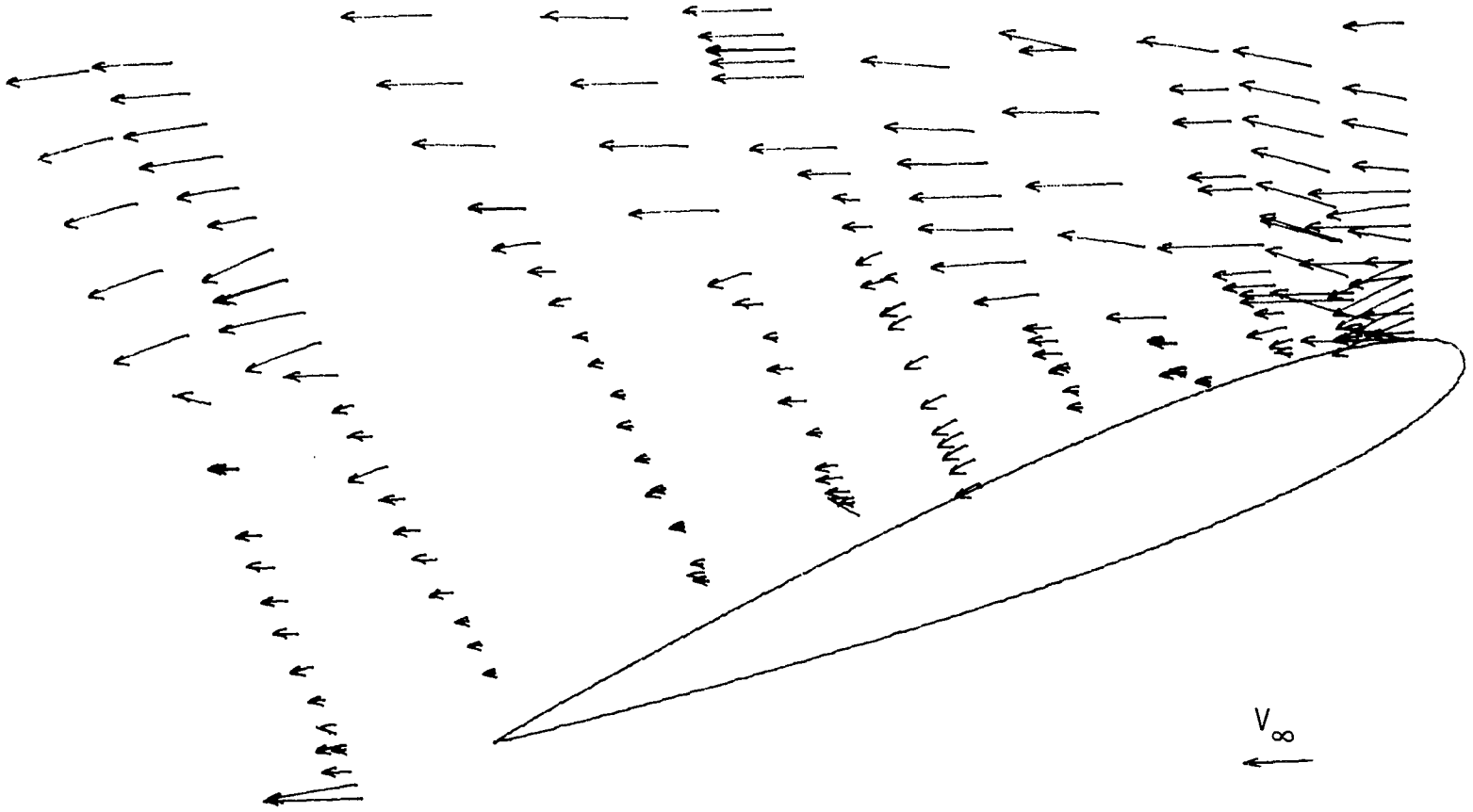


Figure 13.- Mode velocities with all velocities shown in prime direction.

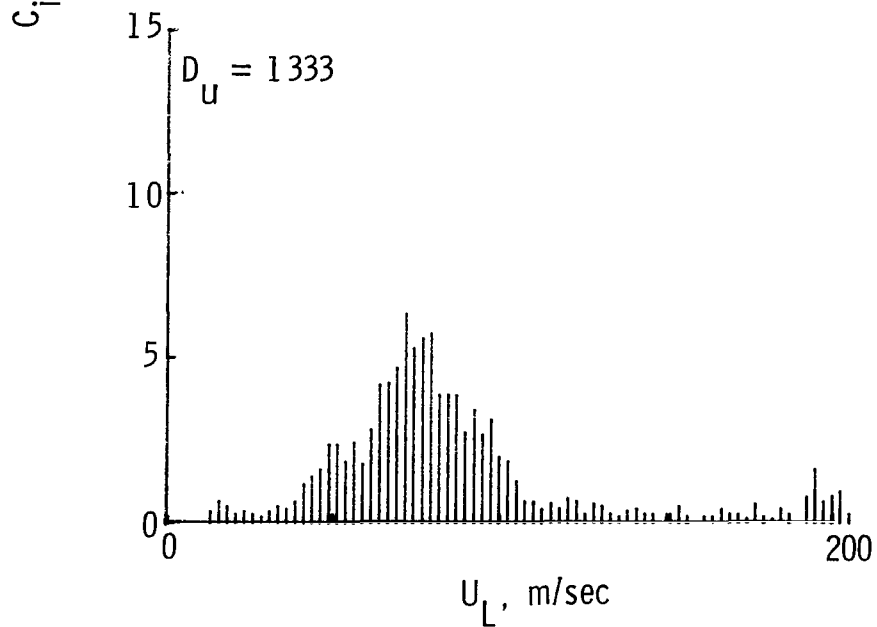
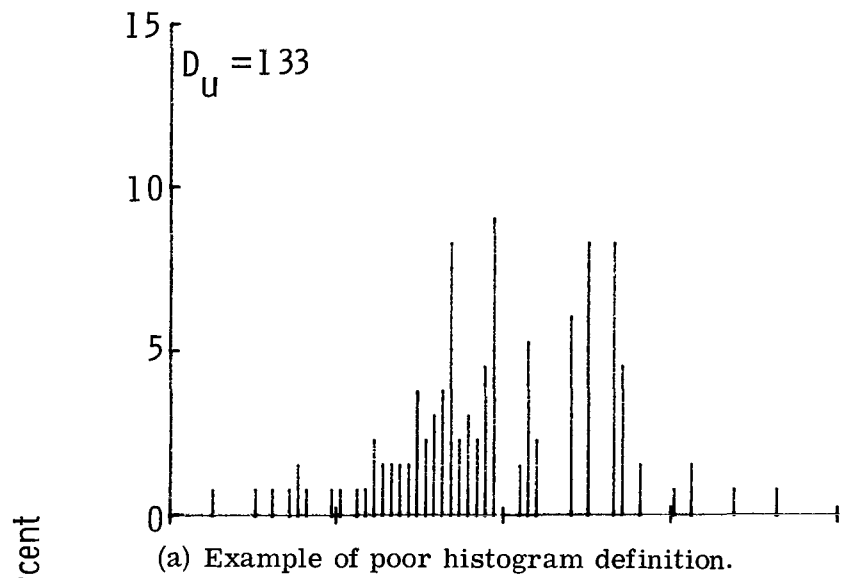


Figure 14.- Comparison of histogram with too few points and histogram with adequate number of points.

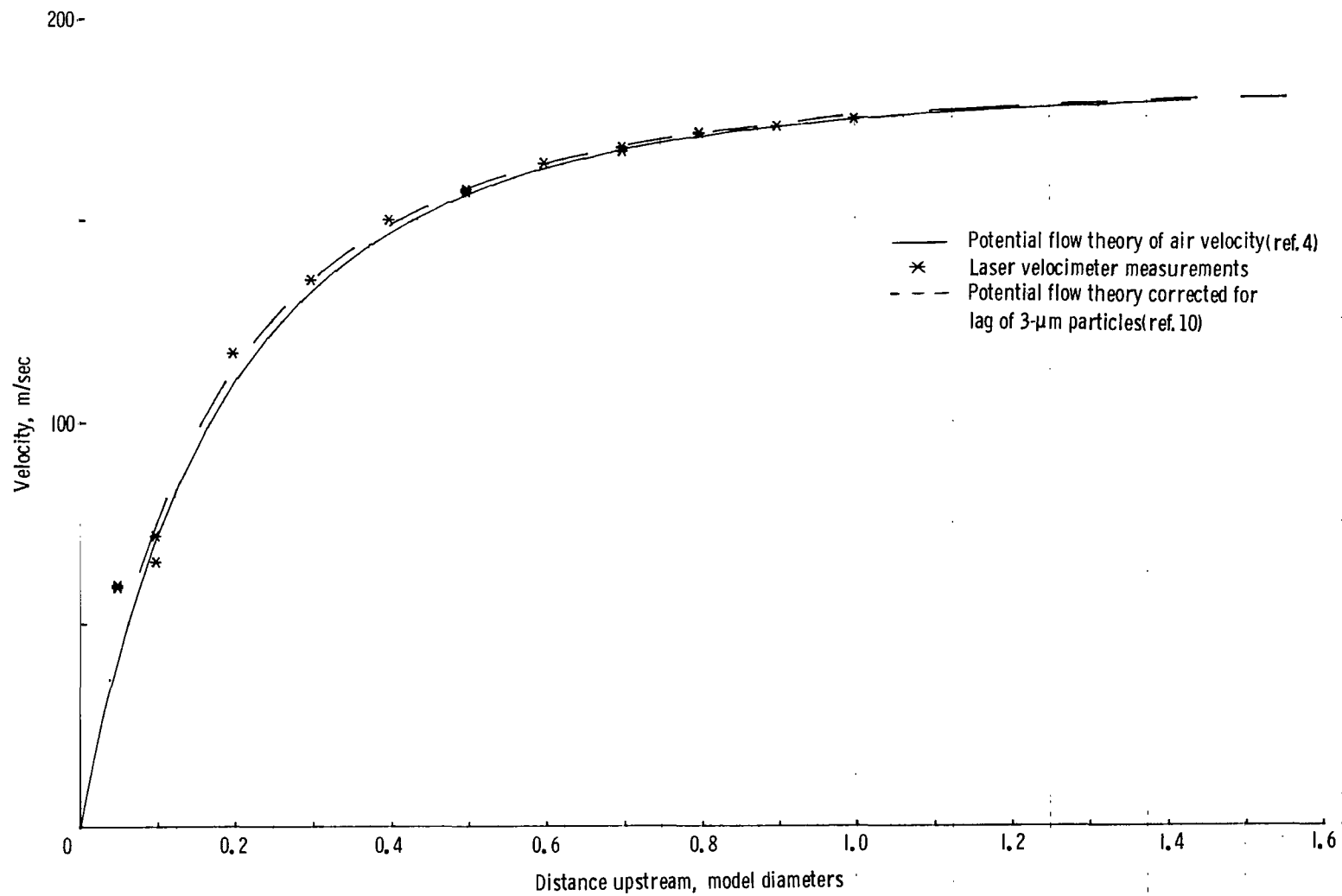


Figure 15.- Velocities upstream of stagnation point of hemisphere at 0° angle of attack, 0.55 Mach number, and Reynolds number of 1.8×10^6 .

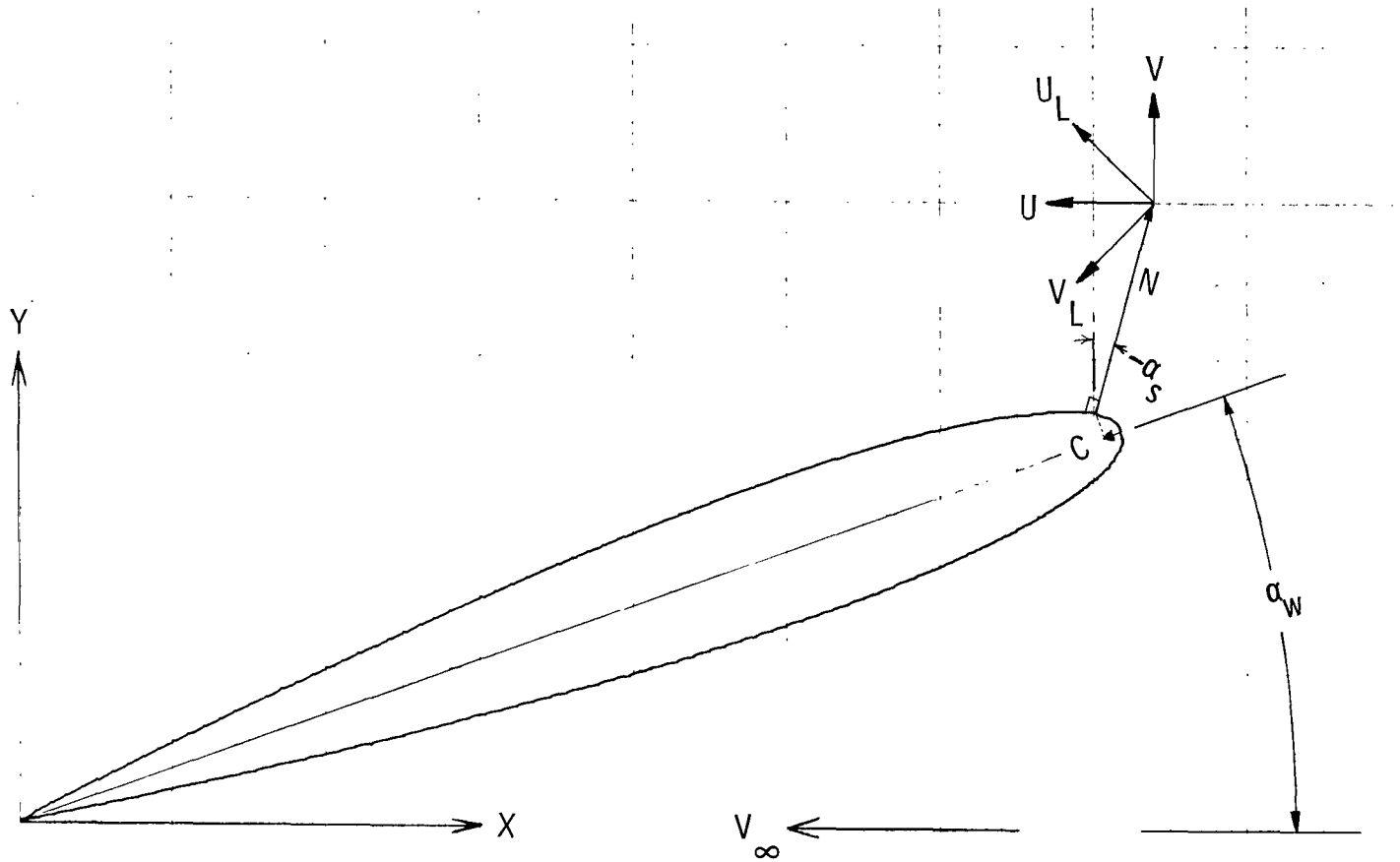


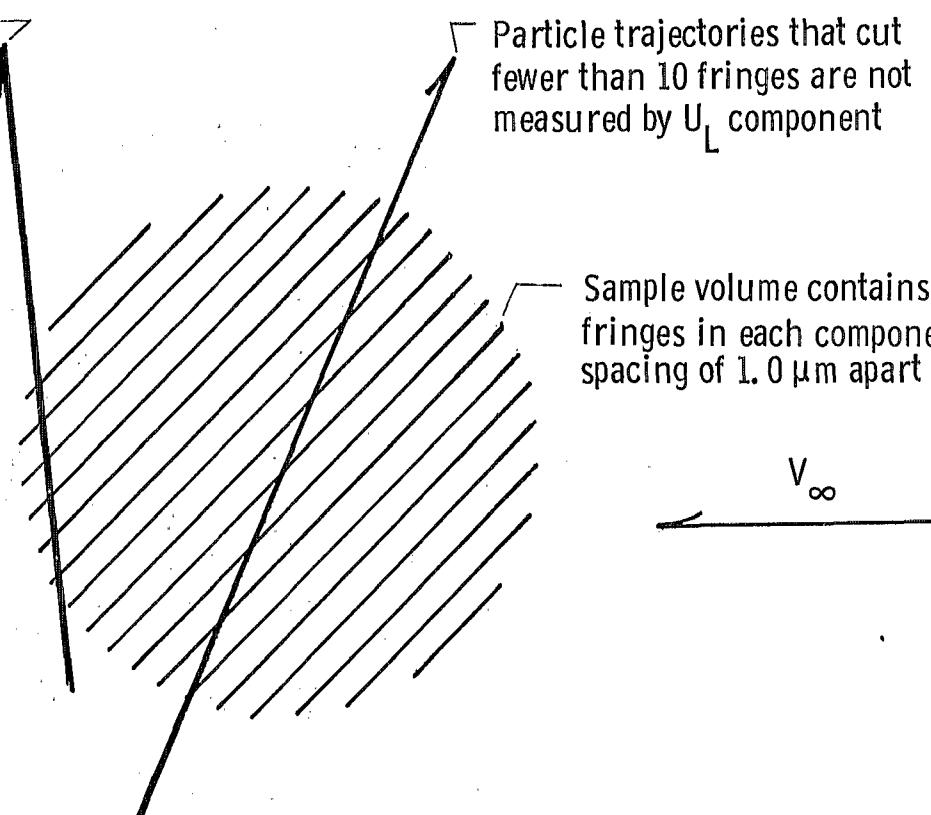
Figure 16.- Wing and laser velocimeter coordinate systems.

Neither component is measured for trajectories too near edge of sample volume

Particle trajectories that cut fewer than 10 fringes are not measured by U_L component

Sample volume contains 18 to 20 fringes in each component with spacing of $1.0 \mu\text{m}$ apart

V_∞



The diagram shows a central rectangular area filled with diagonal hatching, representing a sample volume. Two straight lines with arrowheads at their top ends cross the hatched area from the bottom-left towards the top-right. These lines represent particle trajectories. To the right of the hatched area, there is a horizontal line with an arrowhead pointing to the left, labeled with the symbol V_∞ . Three text annotations with leader lines point to specific features: one points to the left edge of the hatched area, another points to the top-right corner of the hatched area, and a third points to the hatched area itself.

Figure 17.- Diagram of U_L component fringe pattern in sample volume.

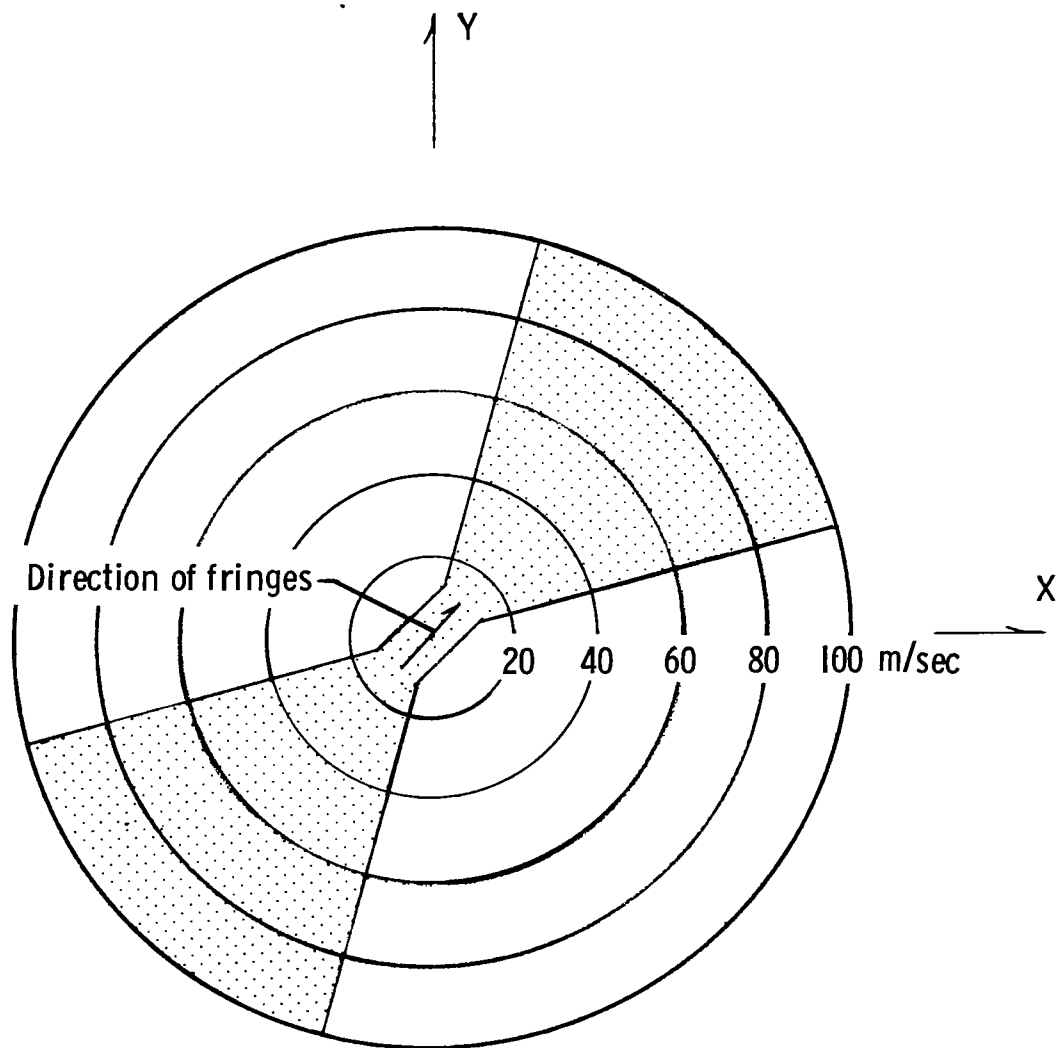


Figure 18.- Dropout zones for U_L component on 1.28-m/sec bin-size scale.

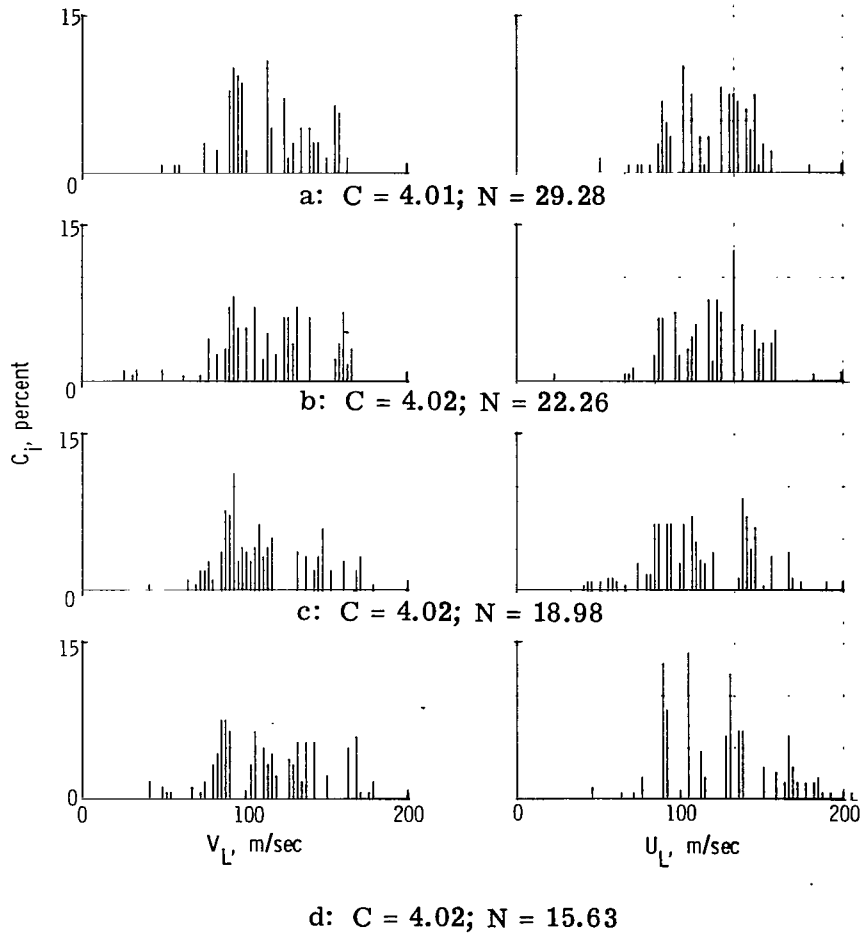
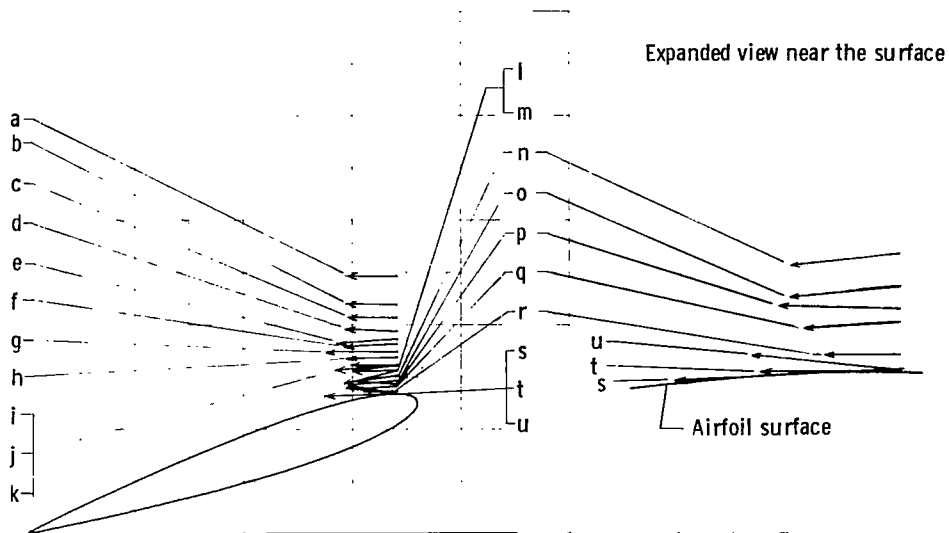


Figure 19.- Histograms above transducer 3.

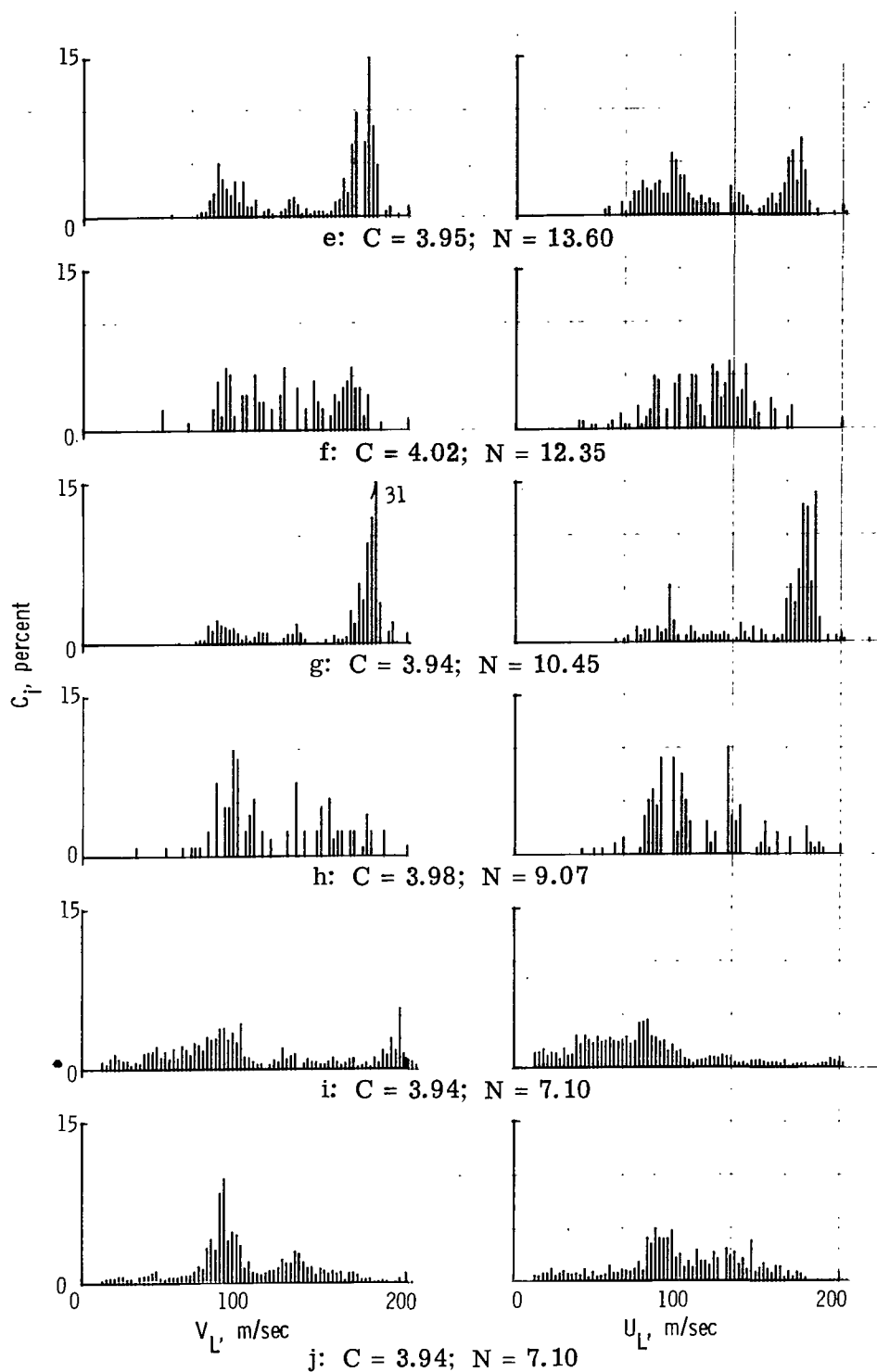


Figure 19.- Histograms above transducer 3. Continued.

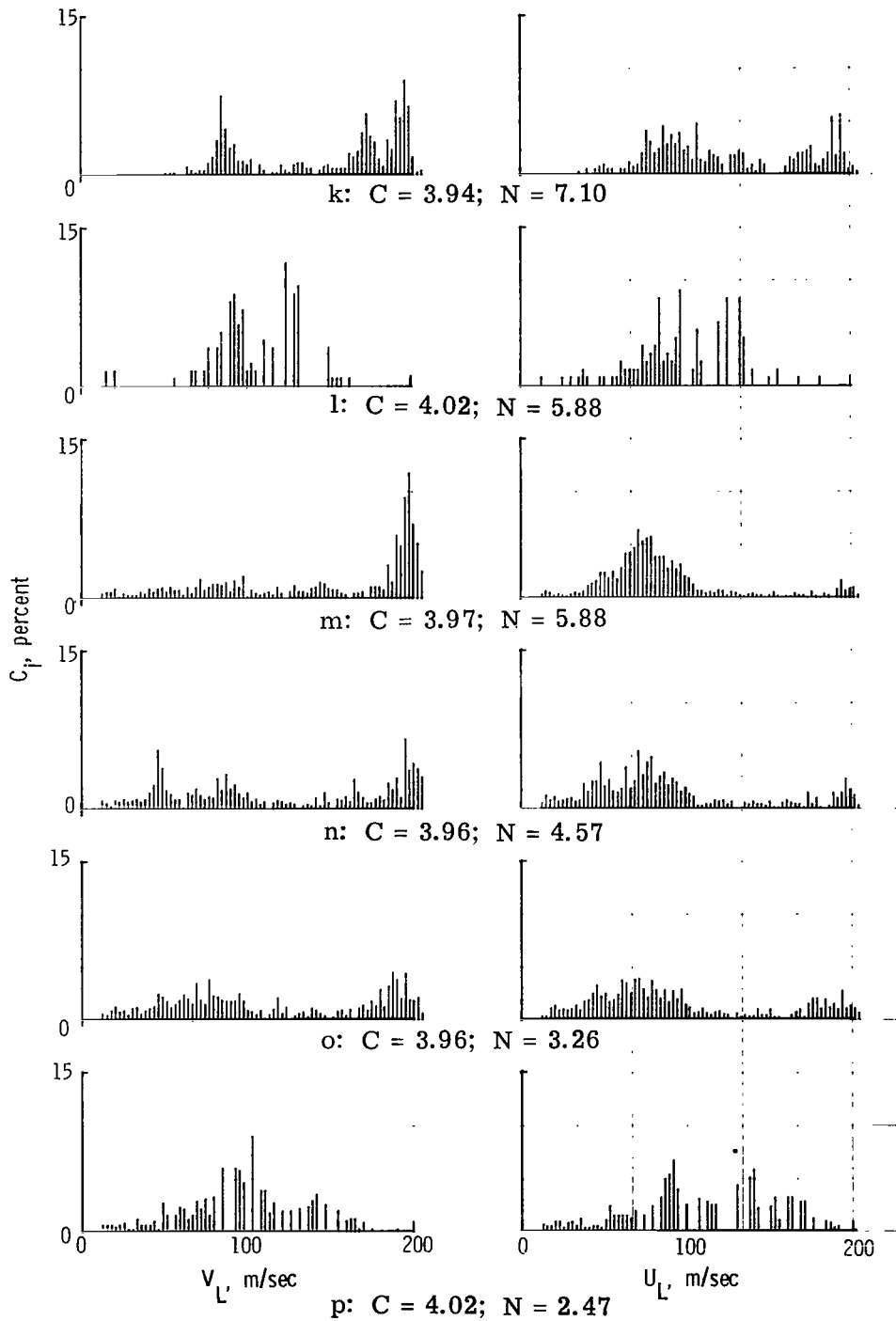


Figure 19.- Histograms above transducer 3. Continued.

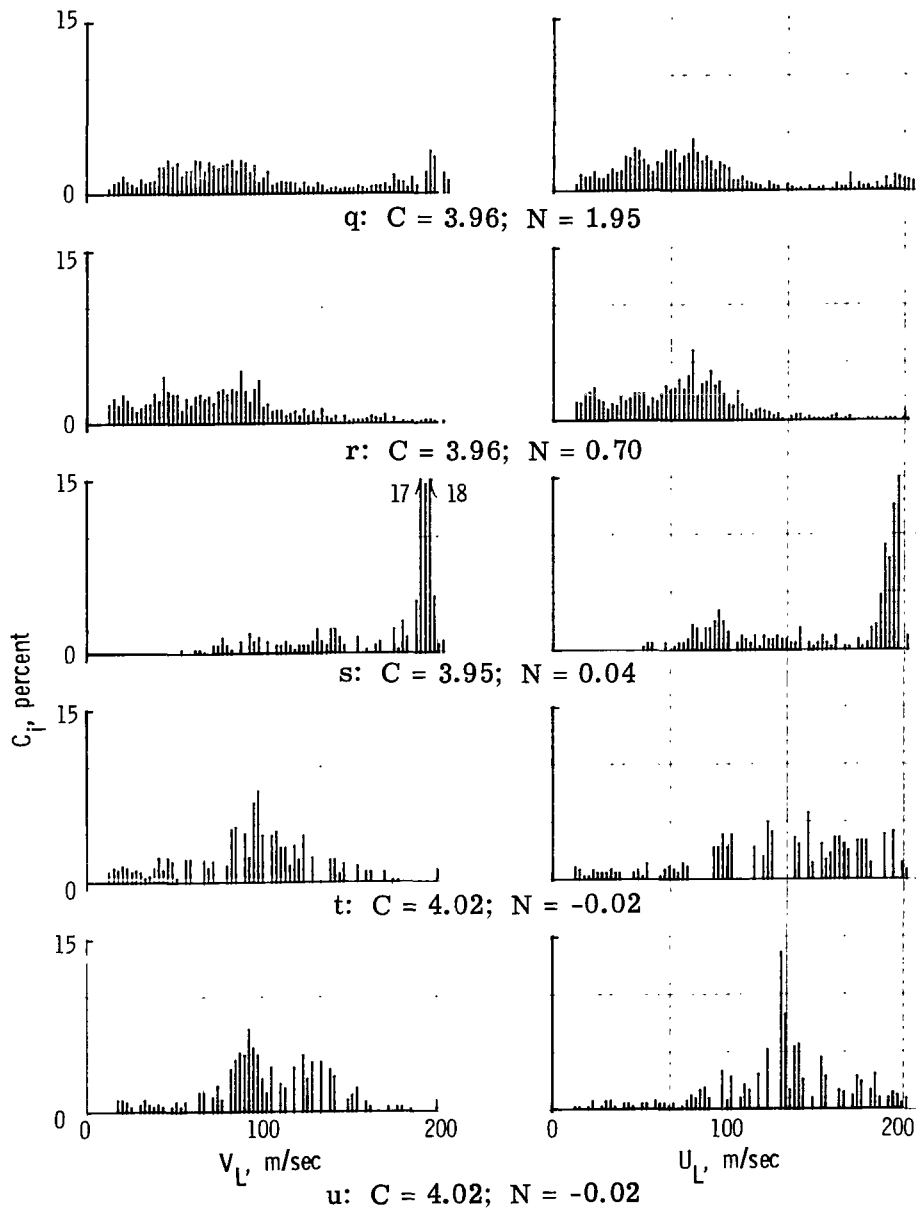


Figure 19.- Histograms above transducer 3. Concluded.

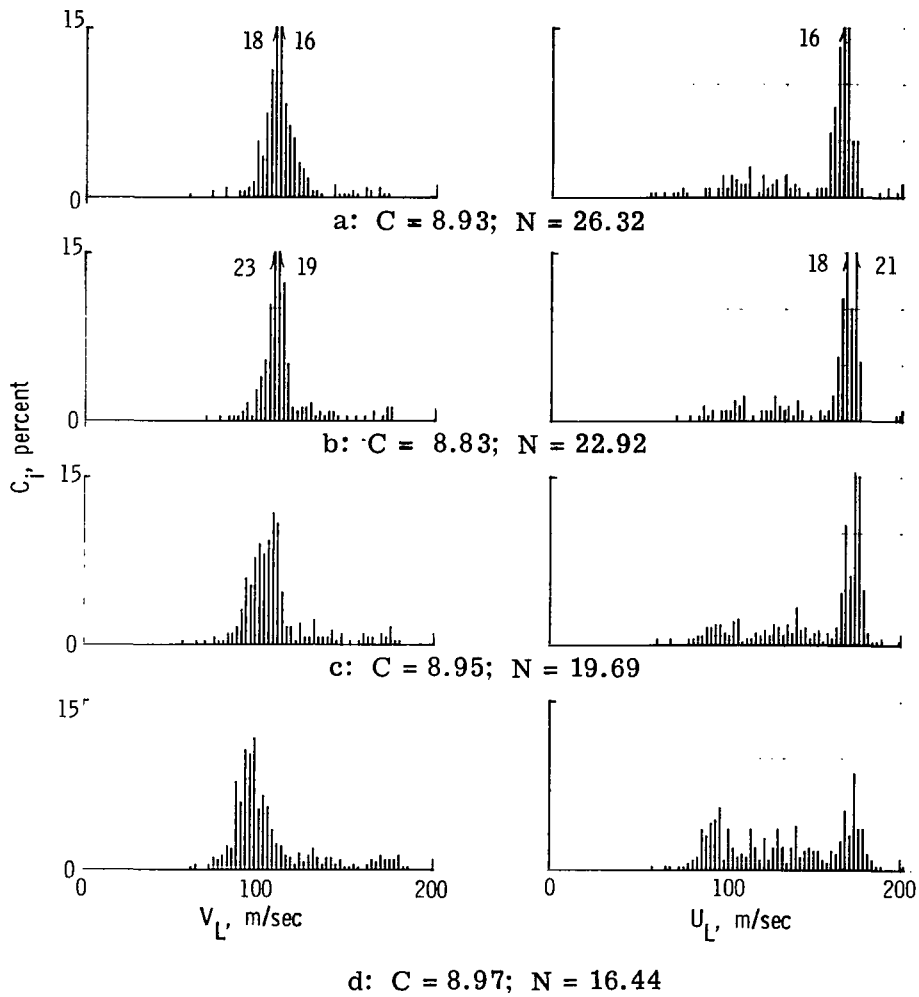
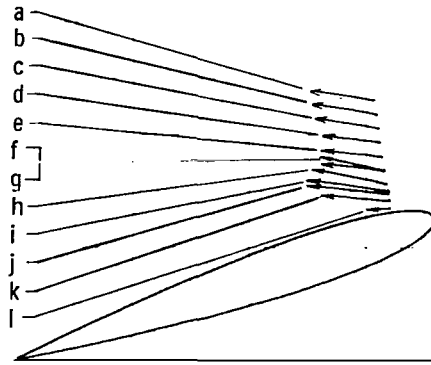


Figure 20.- Histograms above transducer 5.

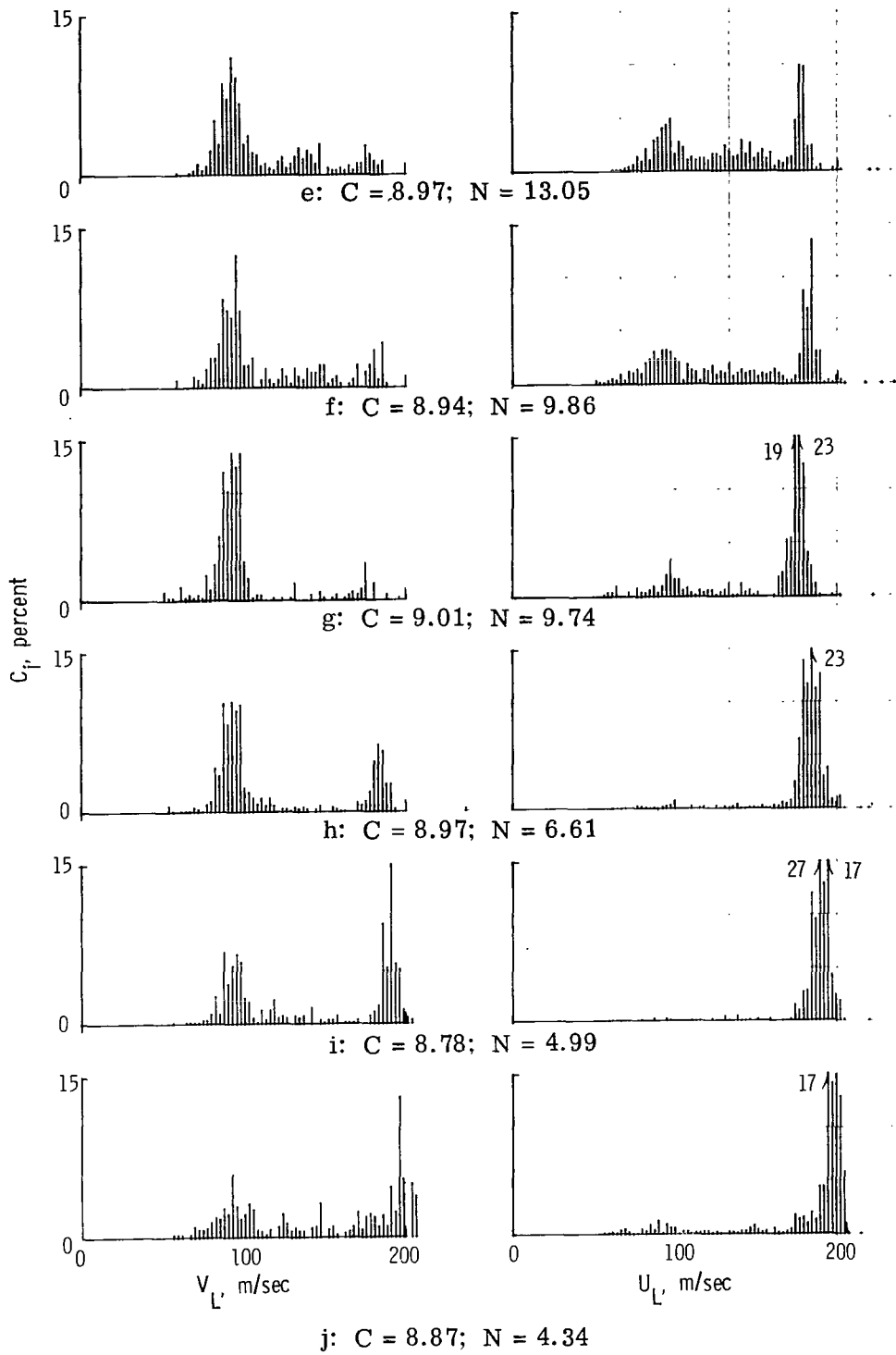


Figure 20.- Histograms above transducer 5. Continued.

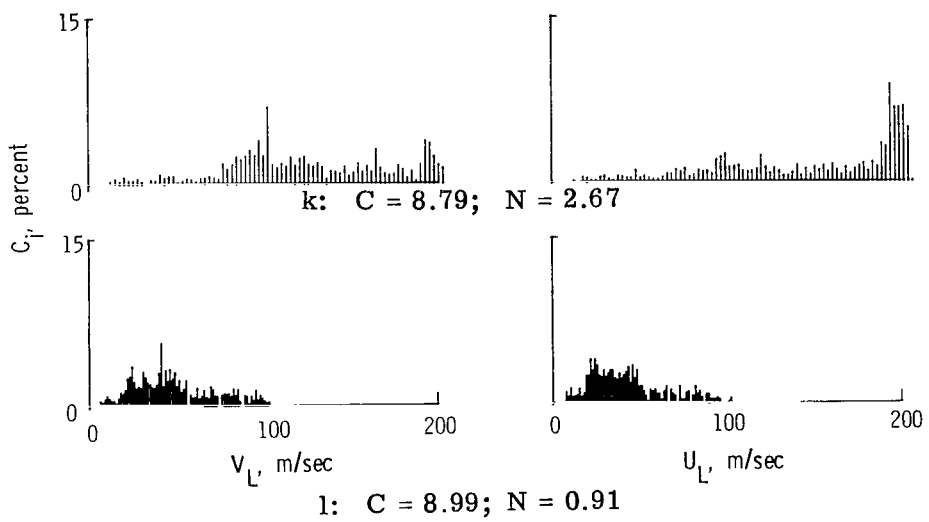


Figure 20.- Histograms above transducer 5. Concluded.

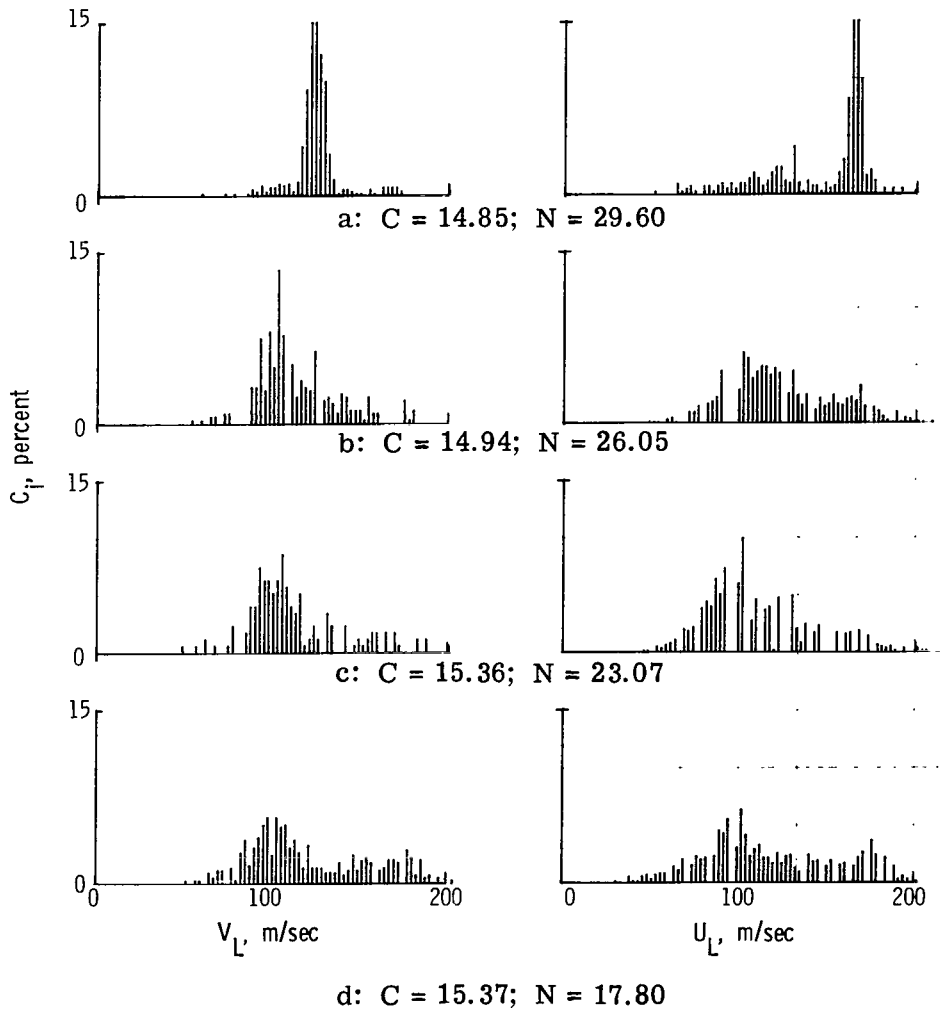
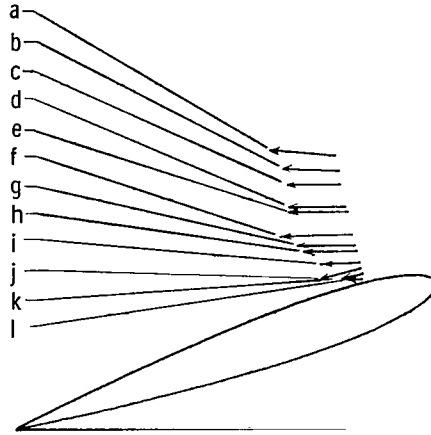


Figure 21. - Histograms above transducer 7.

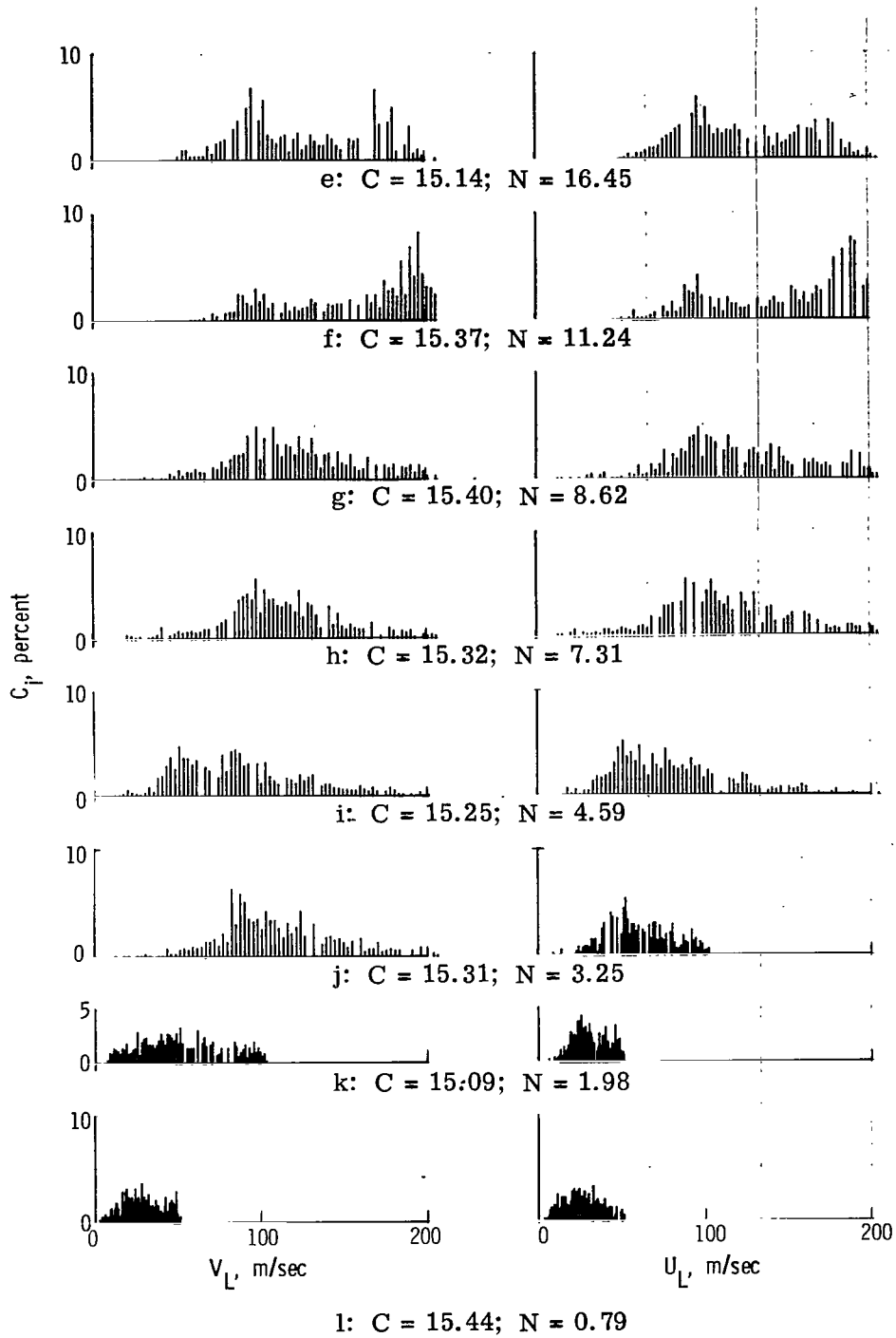


Figure 21.- Histograms above transducer 7. Concluded.

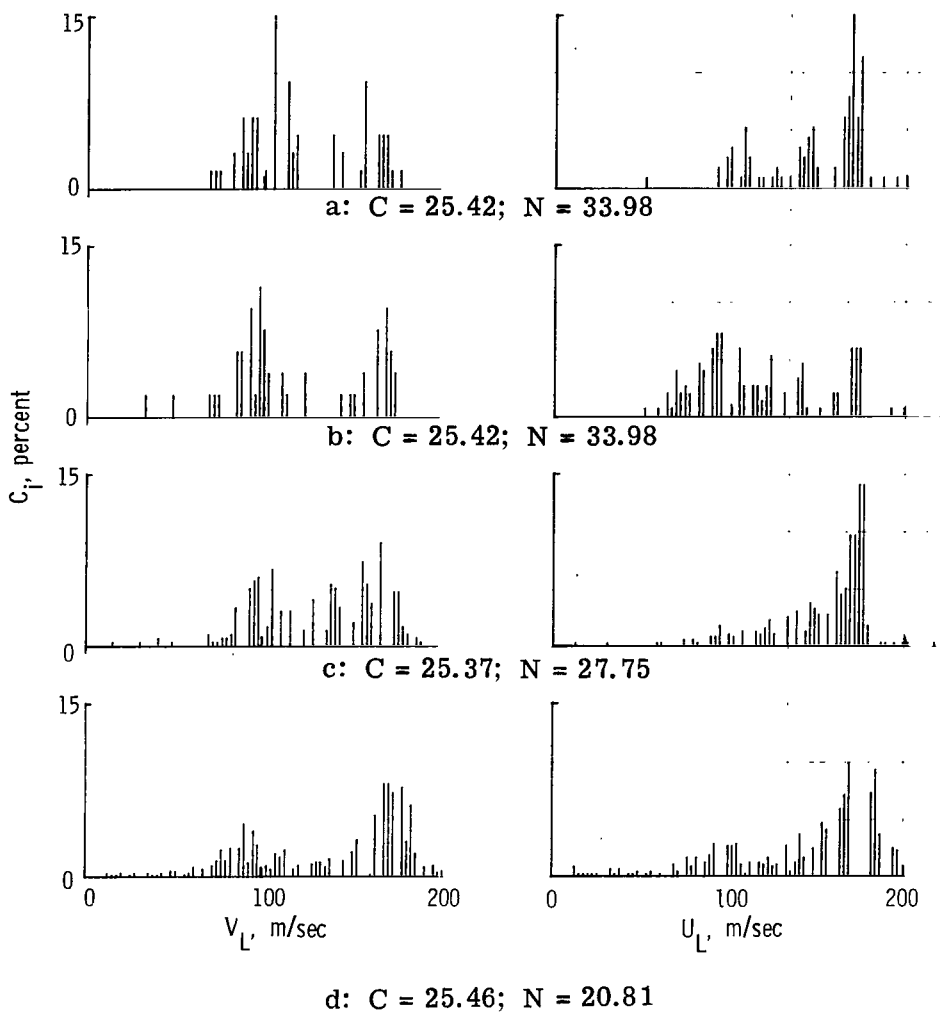
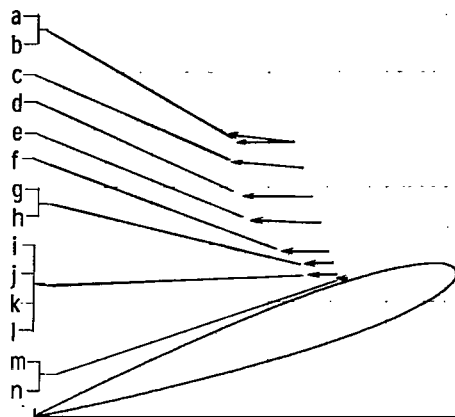


Figure 22. - Histograms above transducer 9.

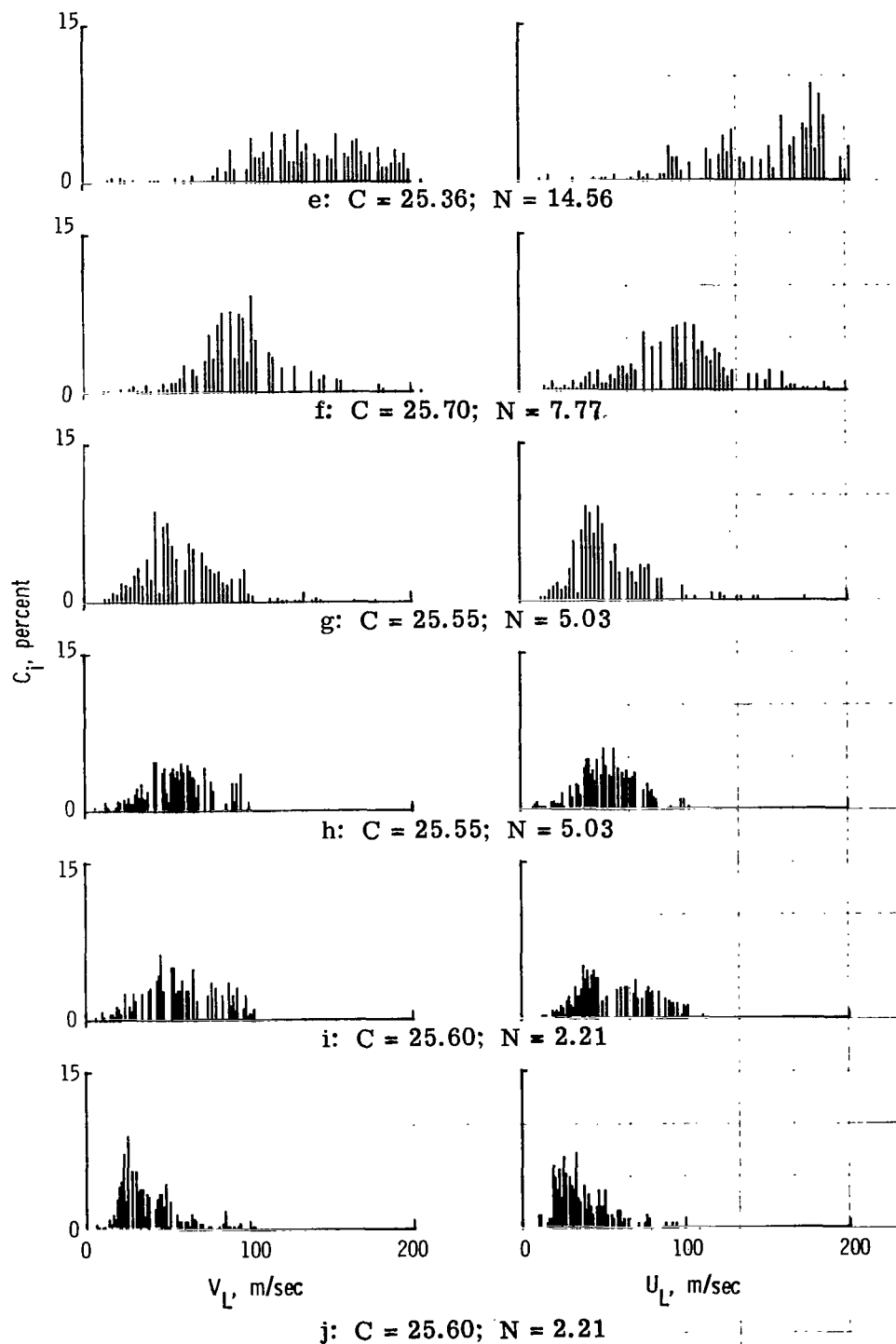


Figure 22.- Histograms above transducer 9. Continued.

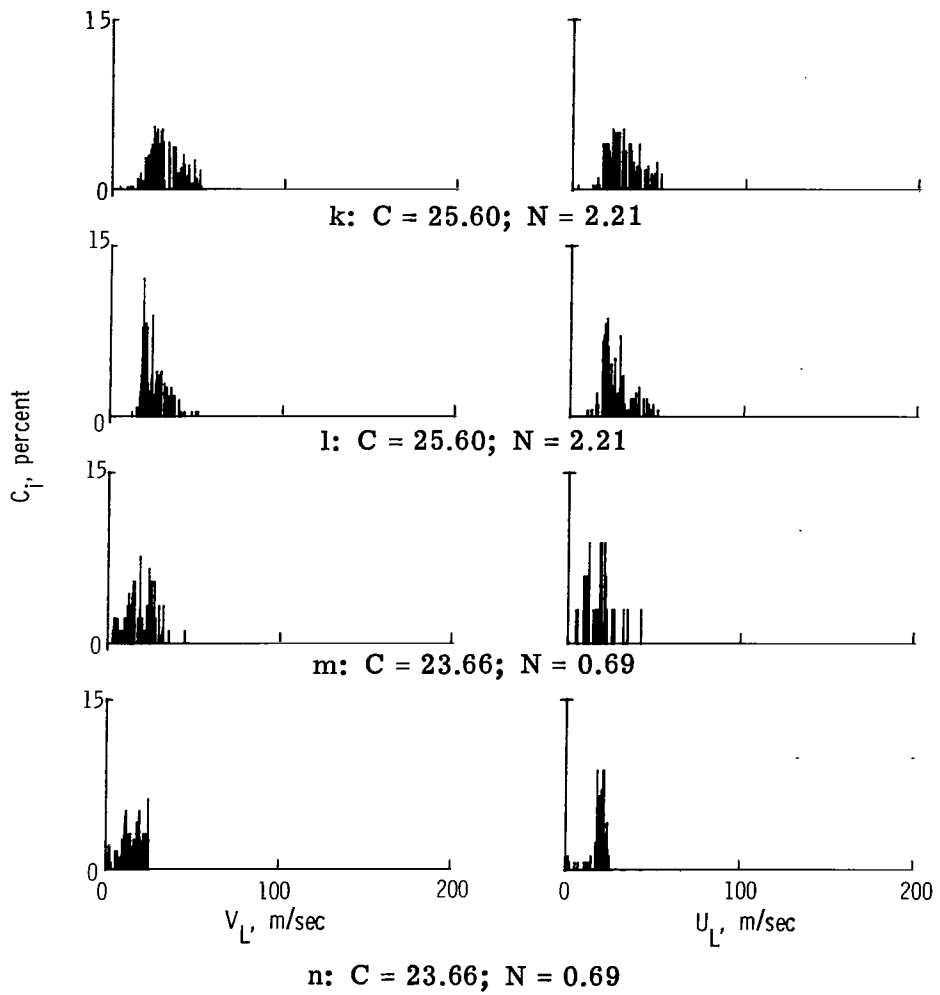


Figure 22.- Histograms above transducer 9. Concluded.

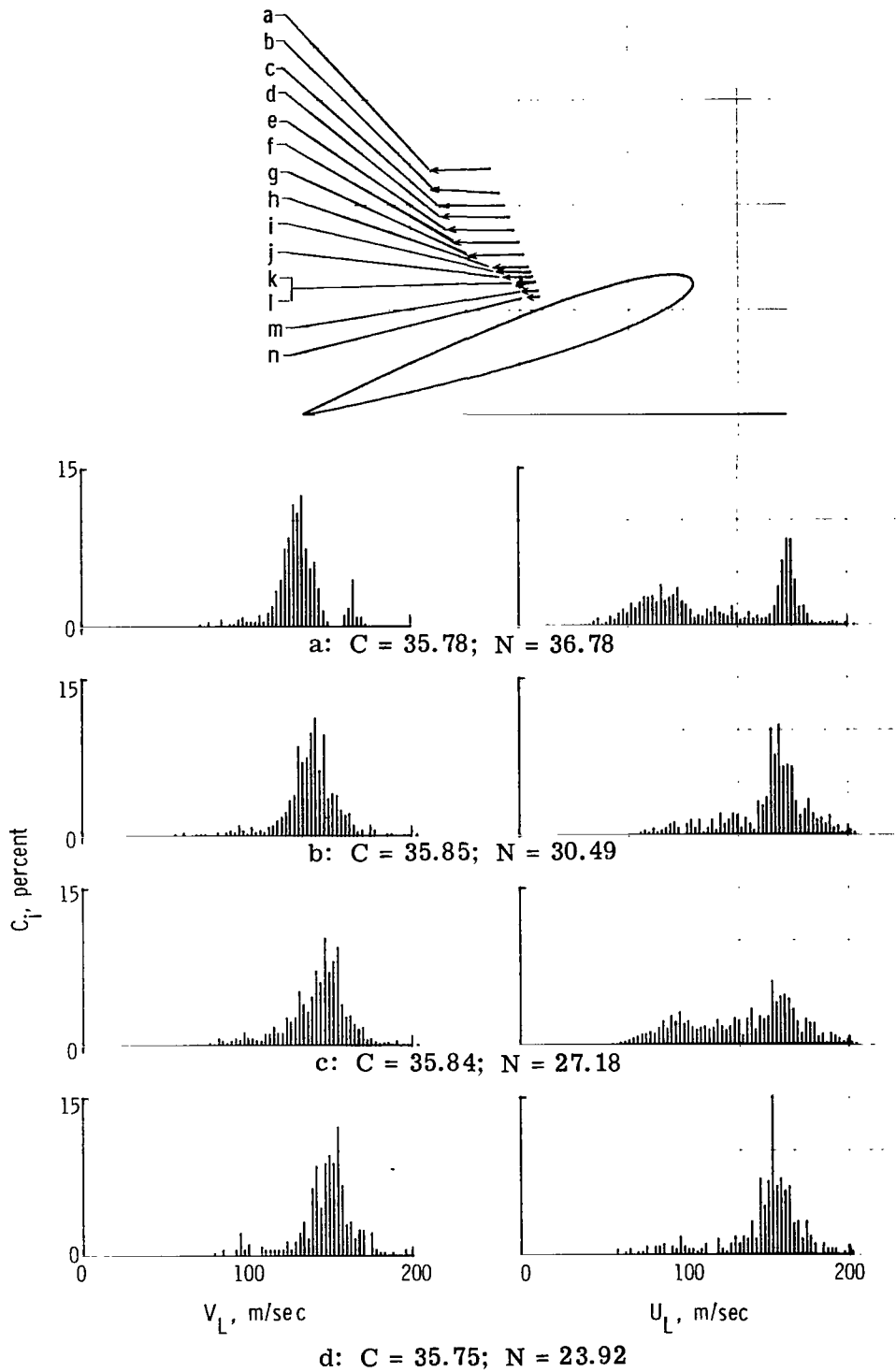


Figure 23.- Histograms above transducer 11.

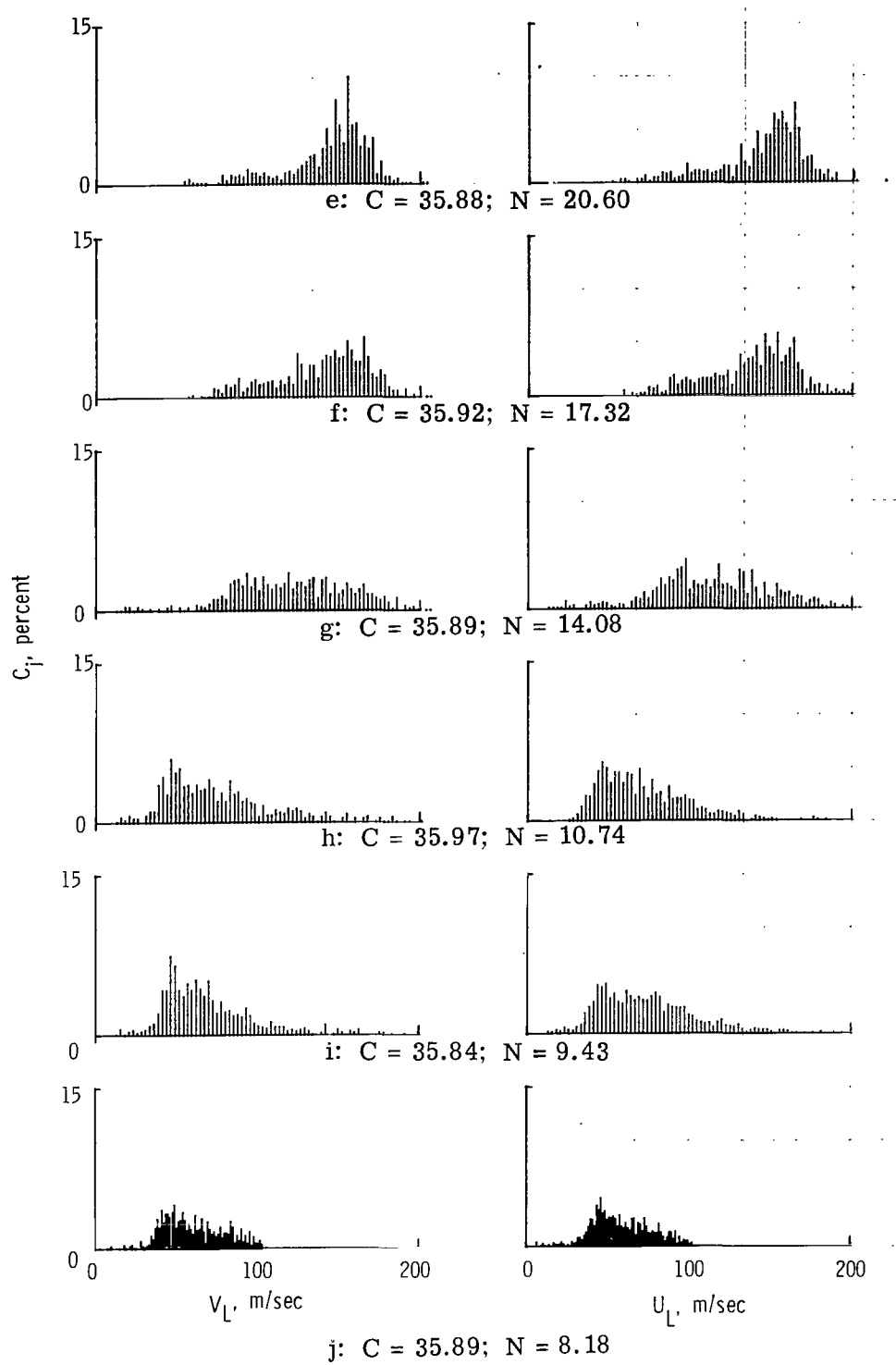


Figure 23.- Histograms above transducer 11. Continued.

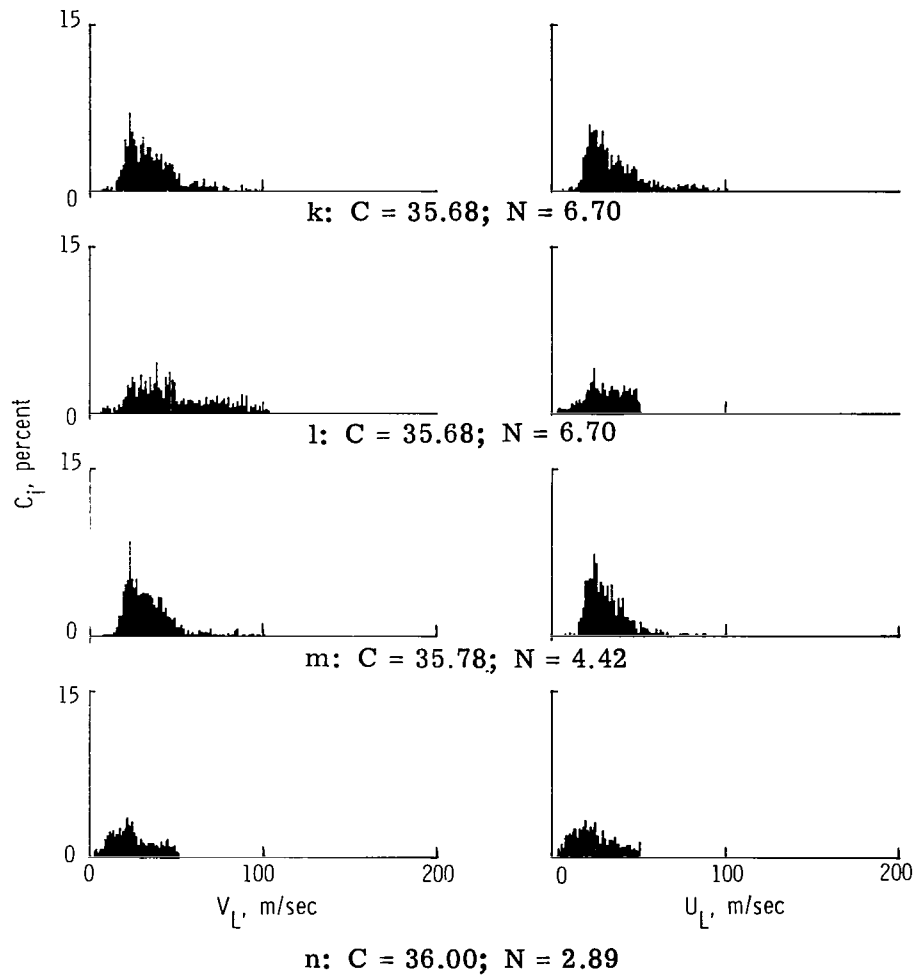


Figure 23.- Histograms above transducer 11. Concluded.

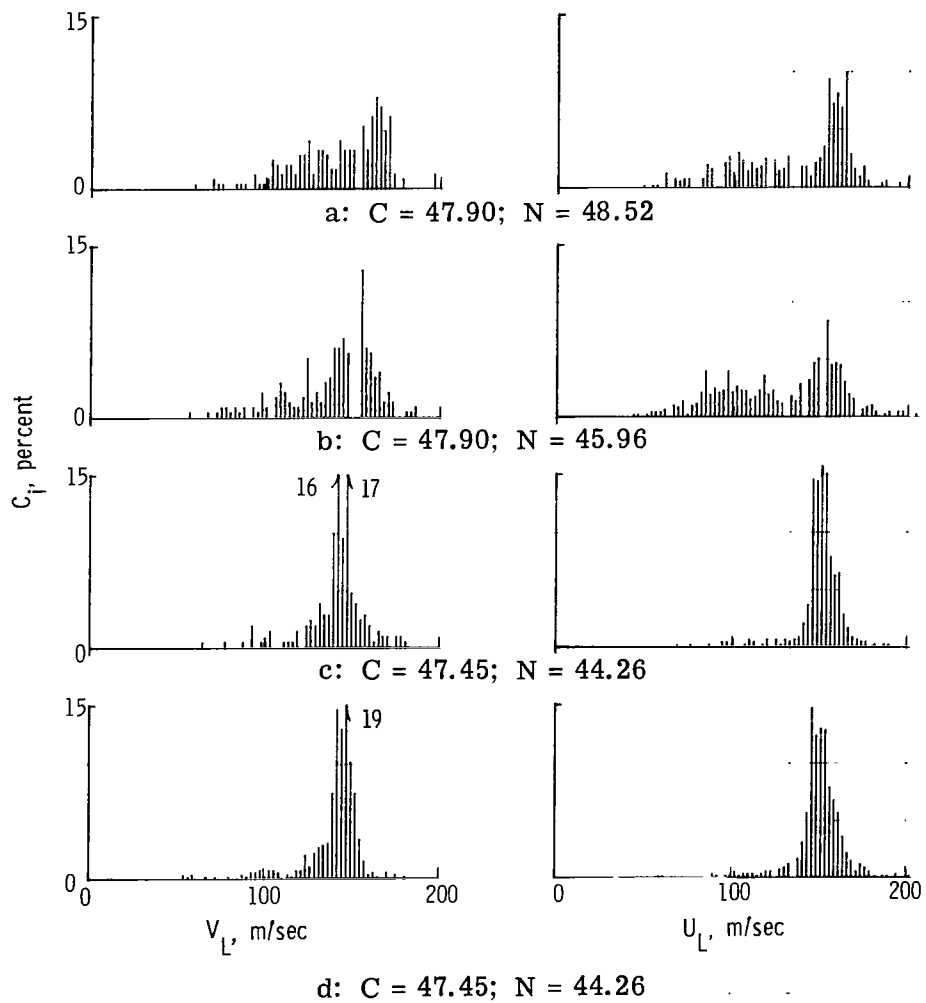
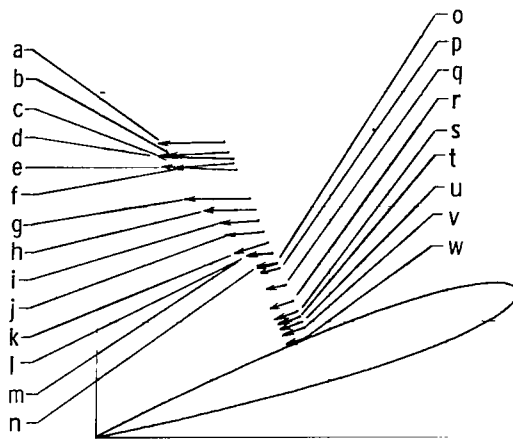


Figure 24.- Histograms above transducer 13.

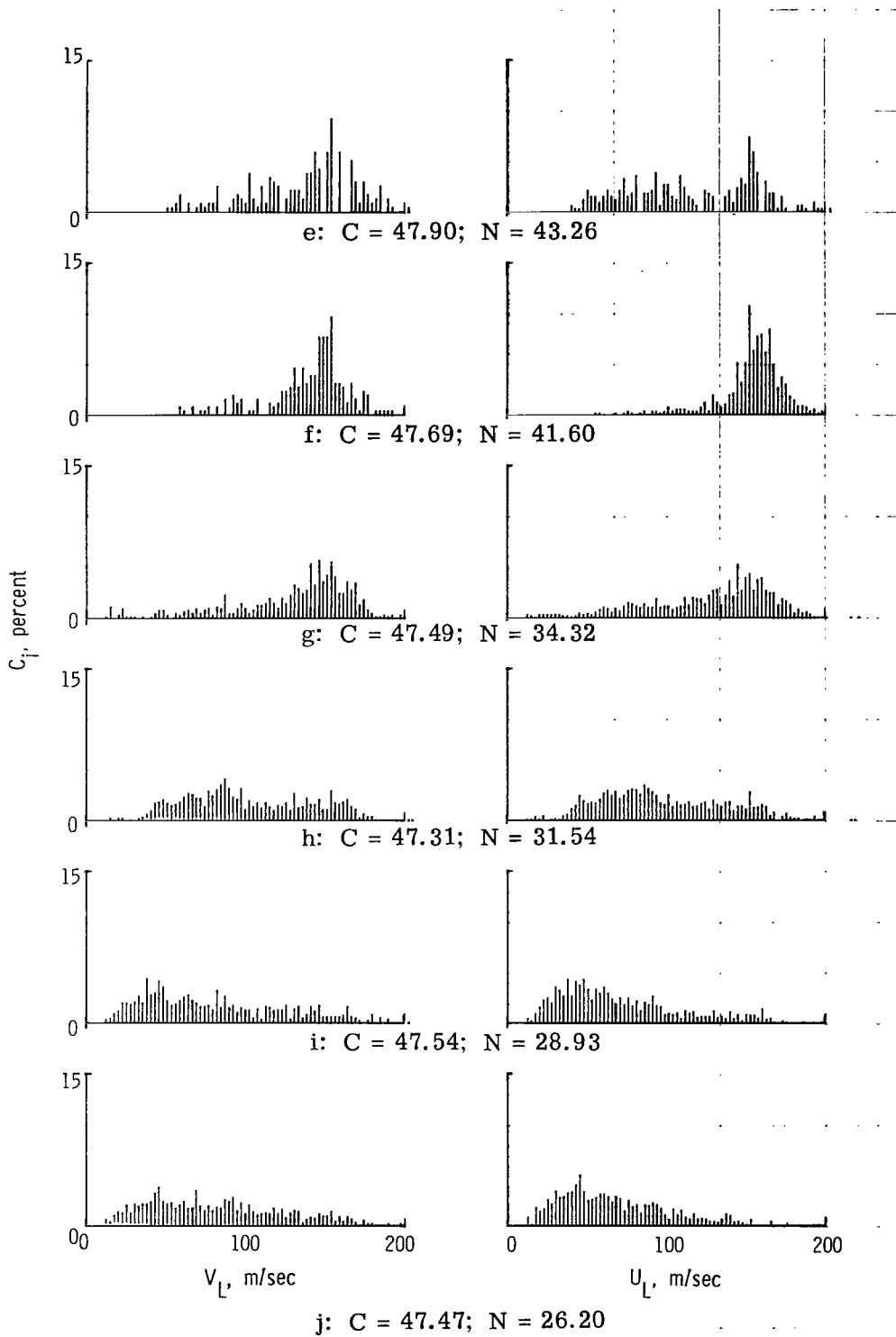


Figure 24.- Histograms above transducer 13. Continued.

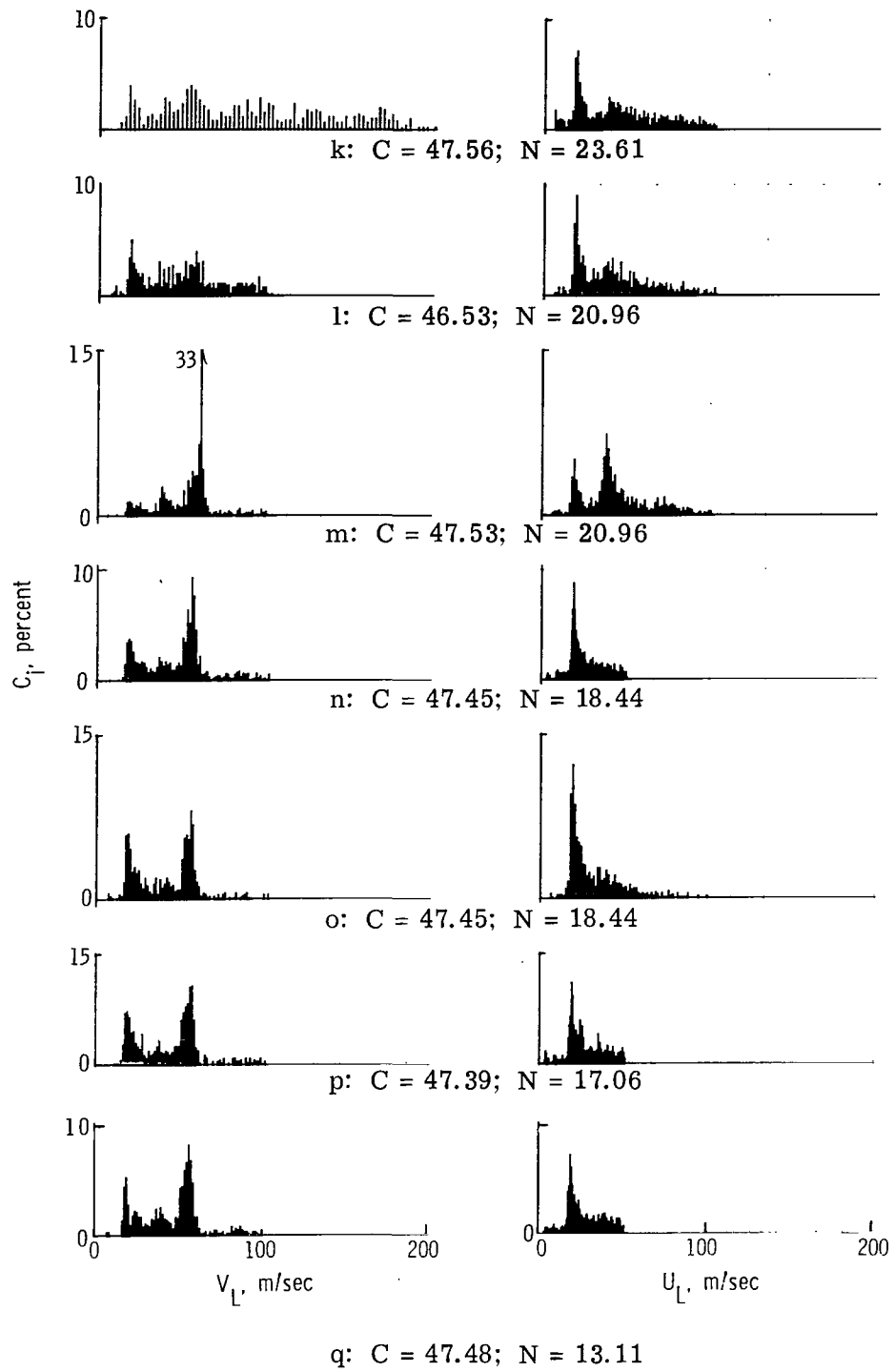


Figure 24.- Histograms above transducer 13. Continued.

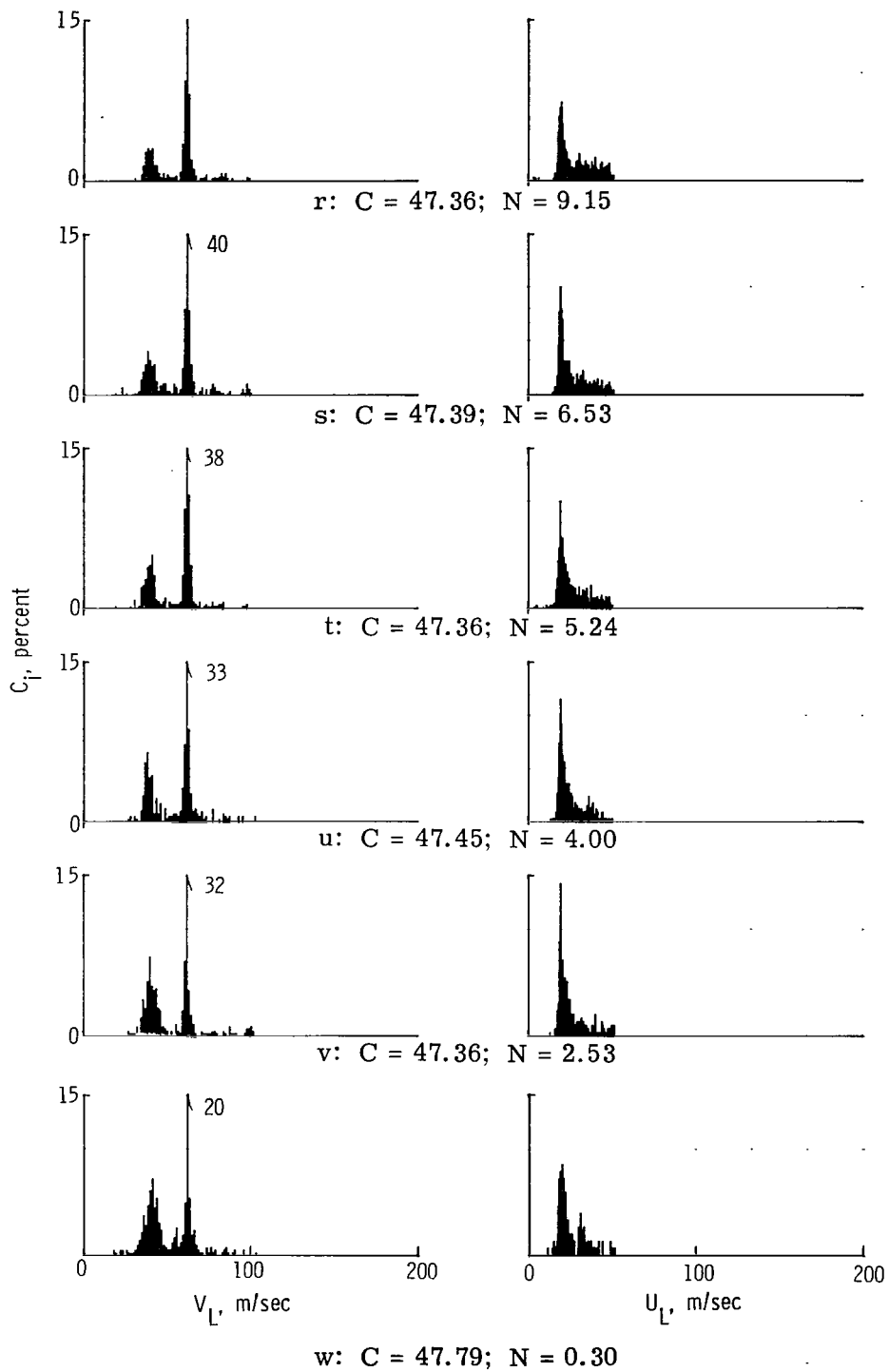


Figure 24.- Histograms above transducer 13. Concluded.

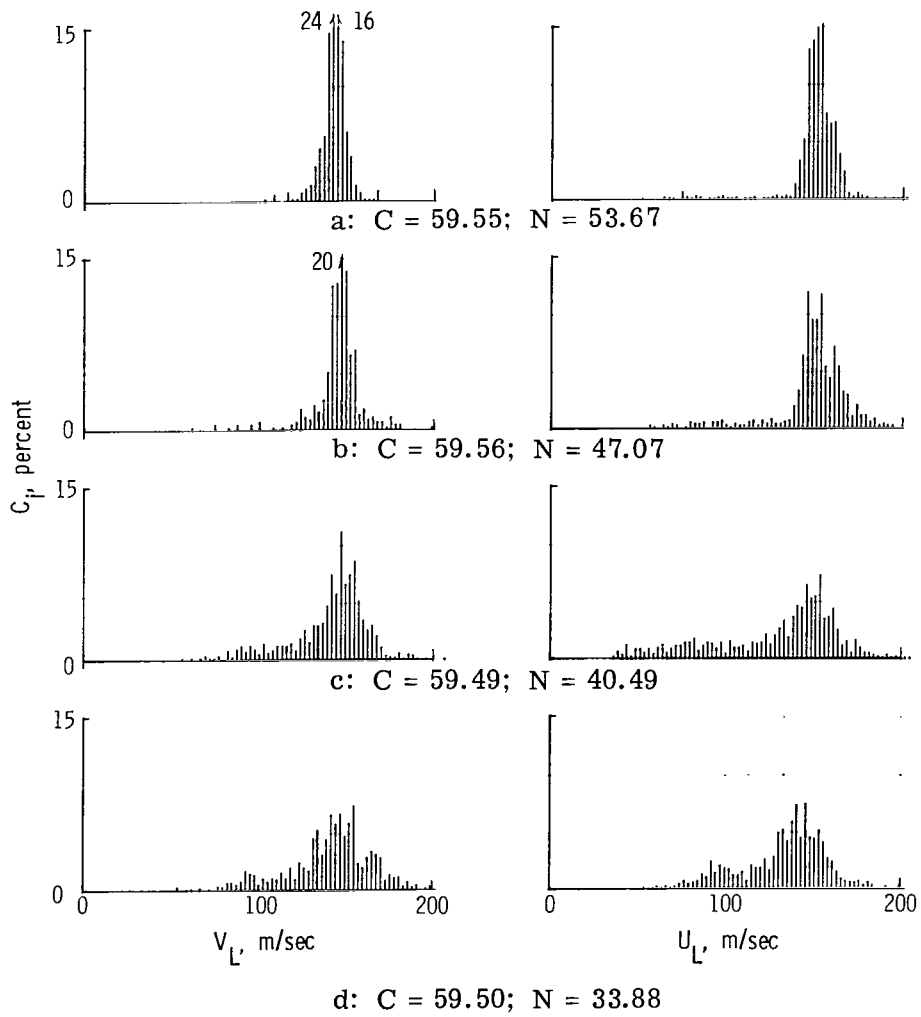
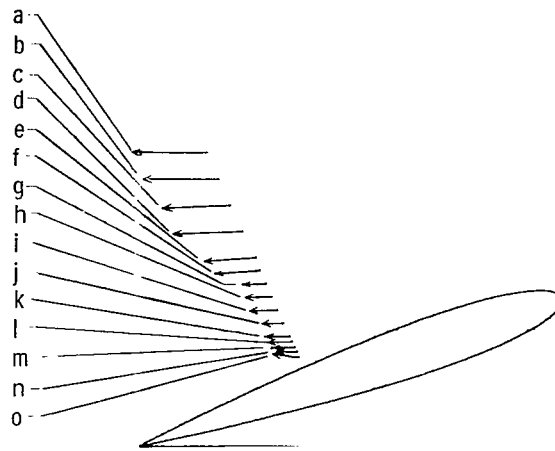


Figure 25.- Histograms above transducer 15.

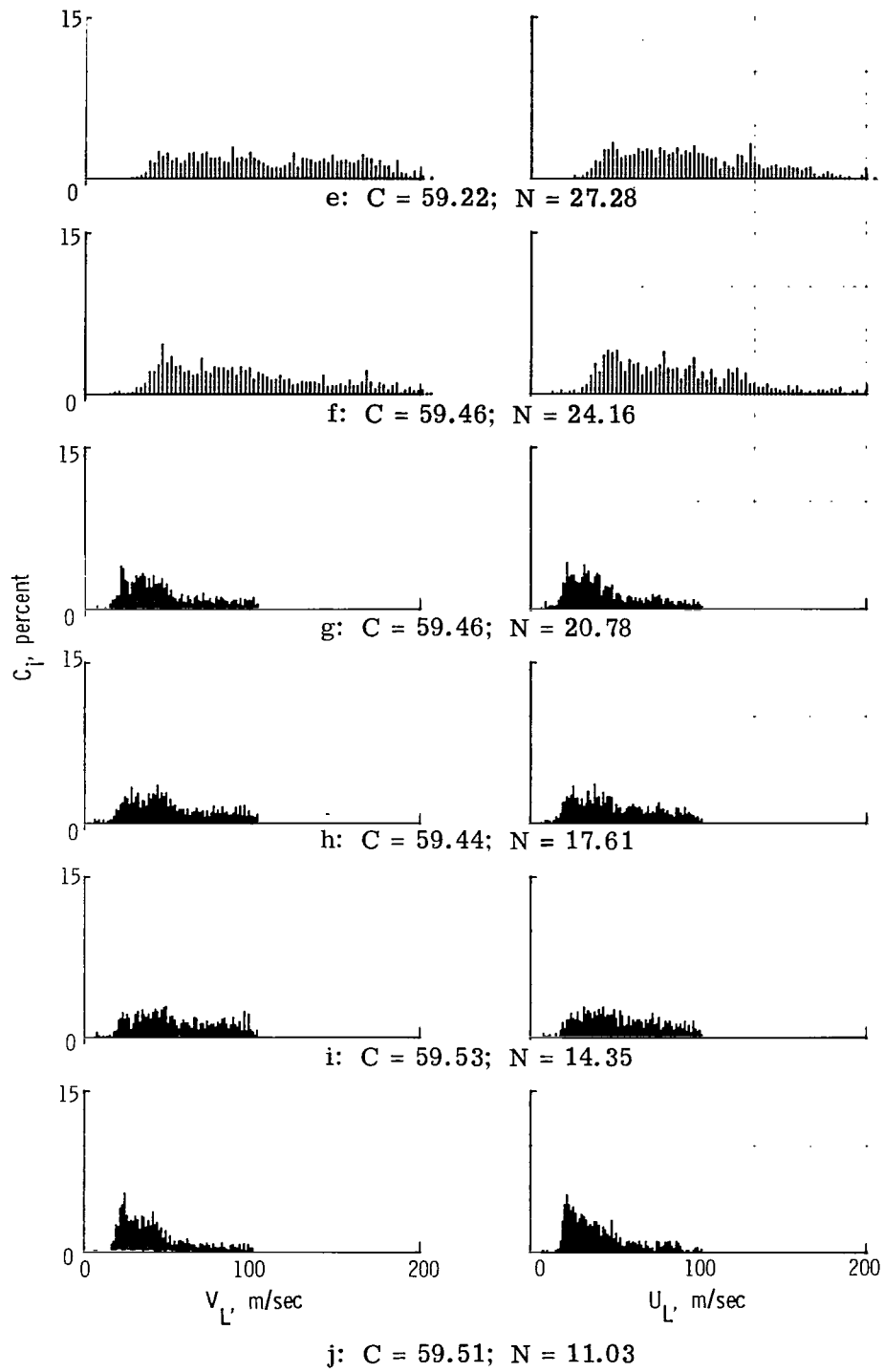


Figure 25.- Histograms above transducer 15. Continued.

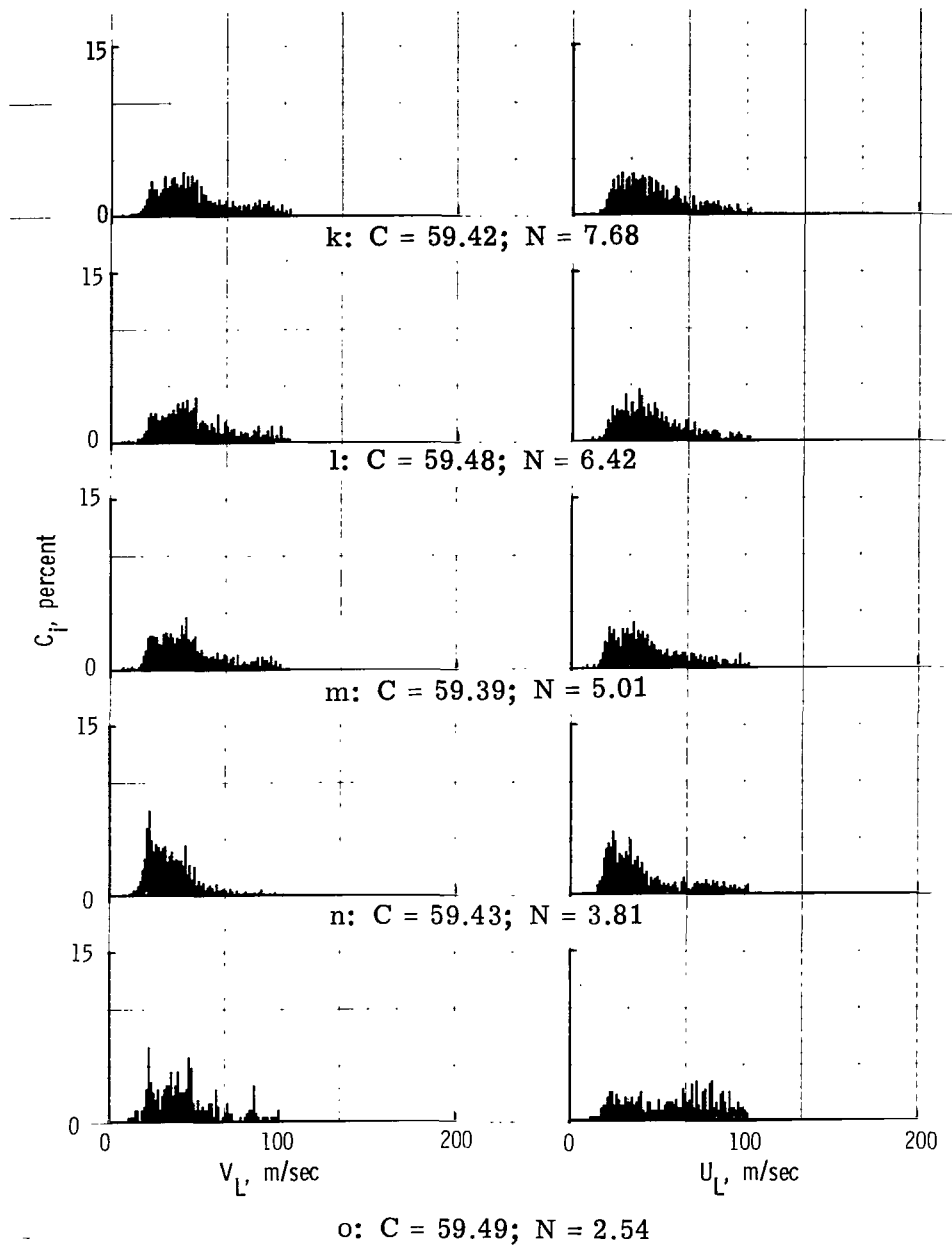


Figure 25.- Histograms above transducer 15. Concluded.

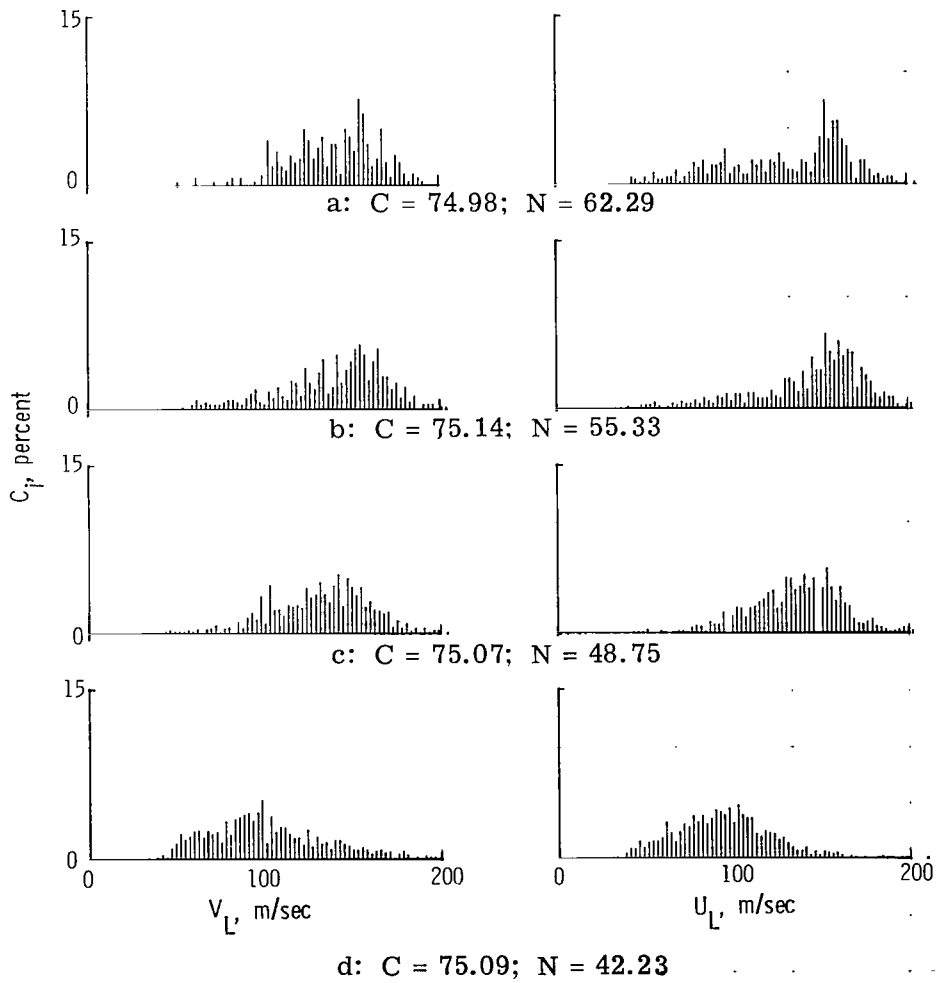
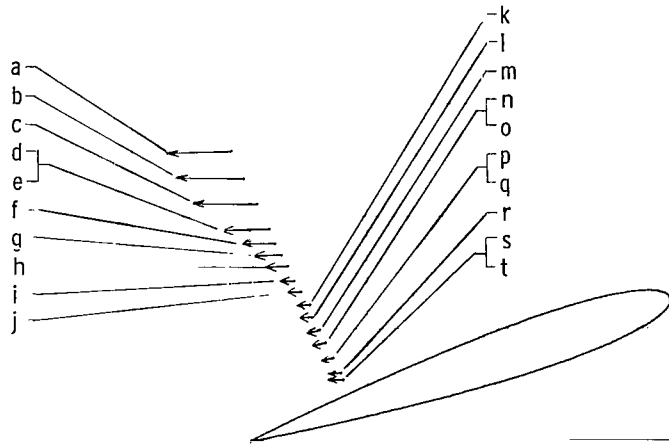


Figure 26.- Histograms above transducer 17.

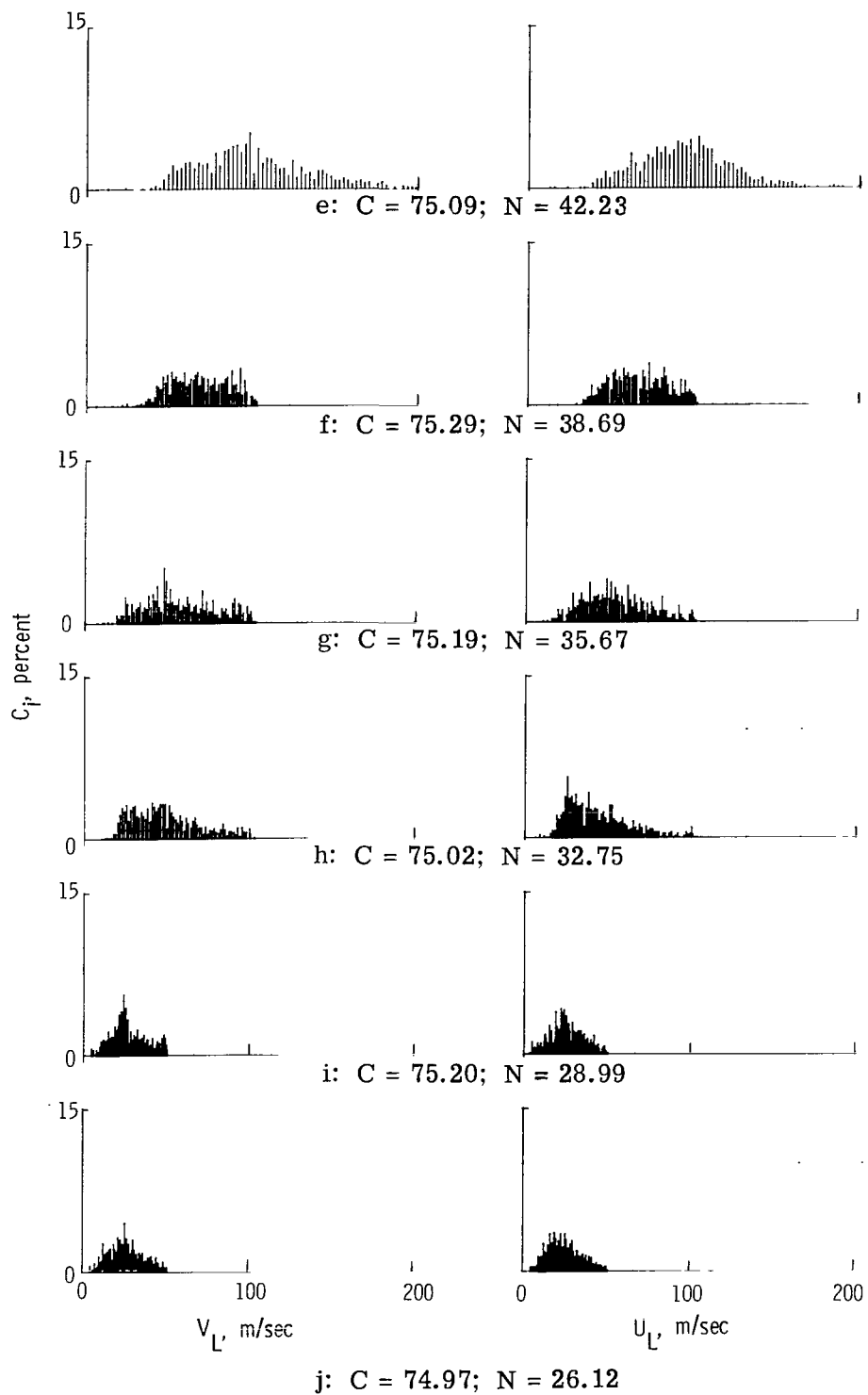


Figure 26.- Histograms above transducer 17. Continued.

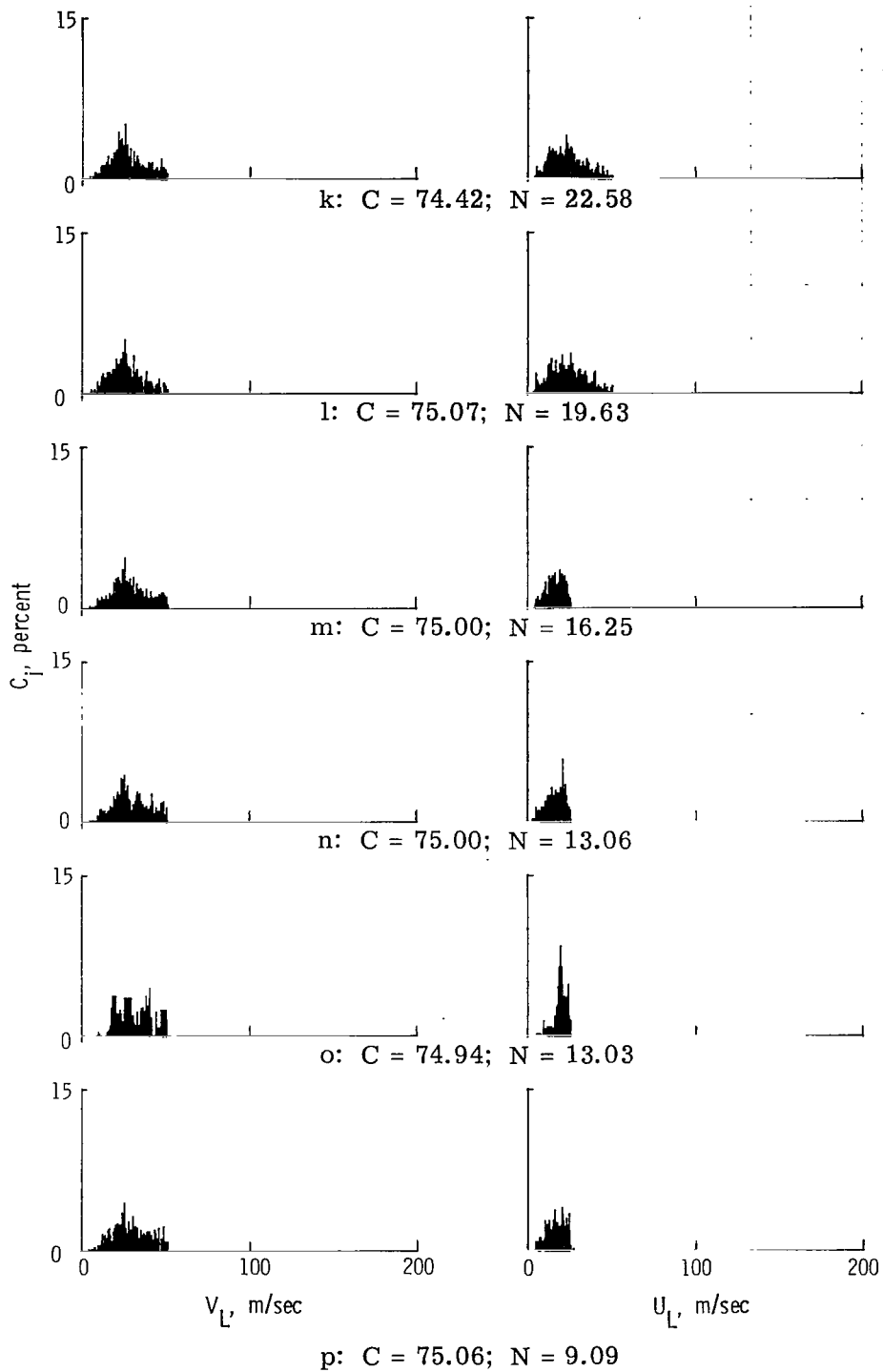


Figure 26.- Histograms above transducer 17. Continued.

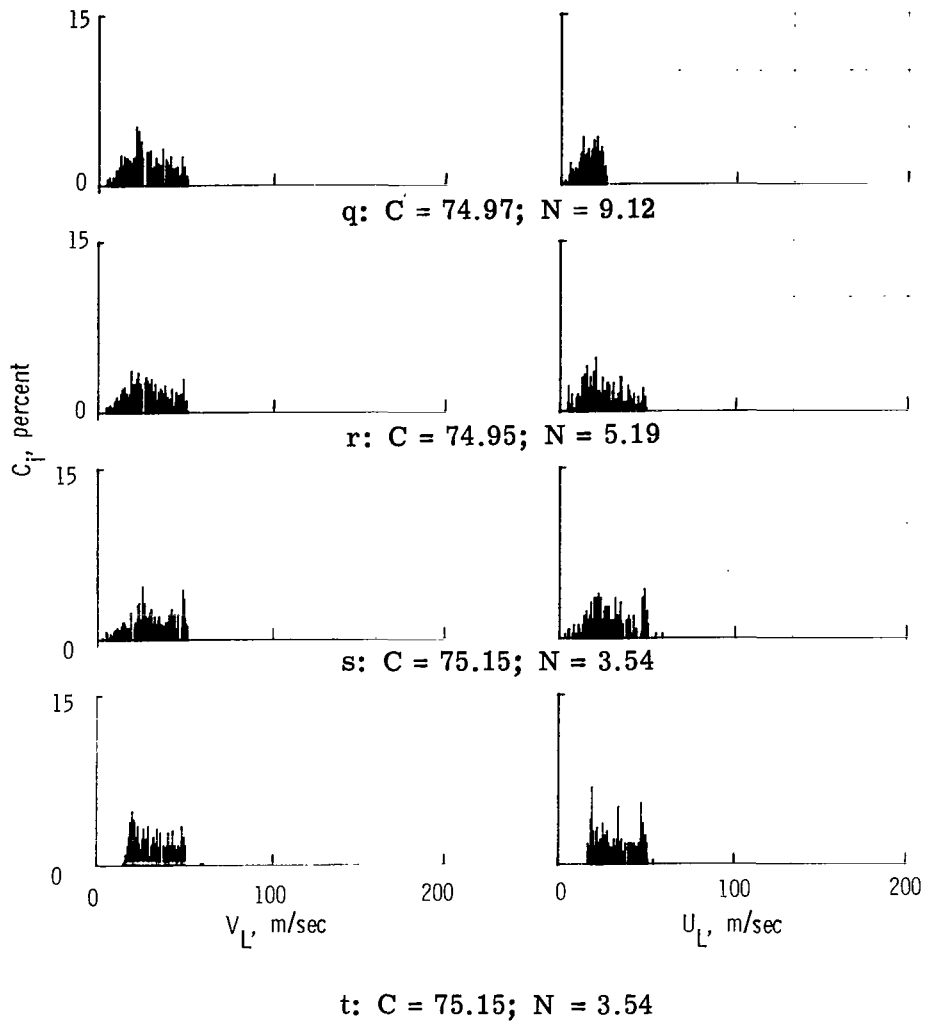


Figure 26.- Histograms above transducer 17. Concluded.

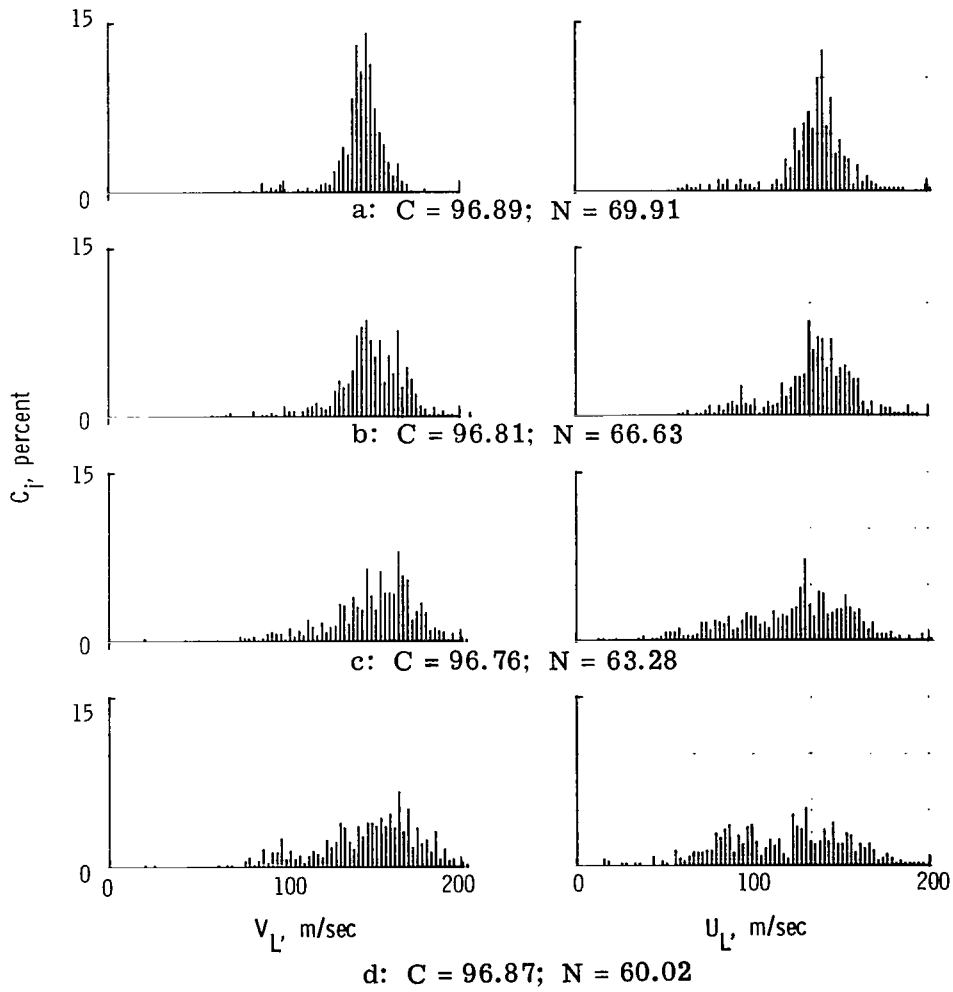
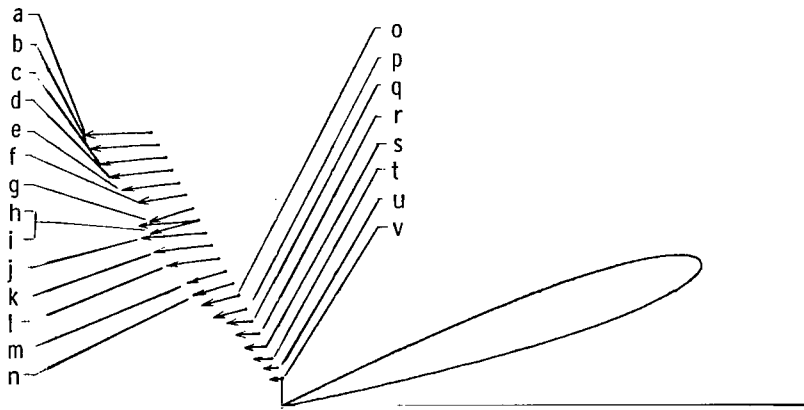


Figure 27.- Histograms above transducer 19.

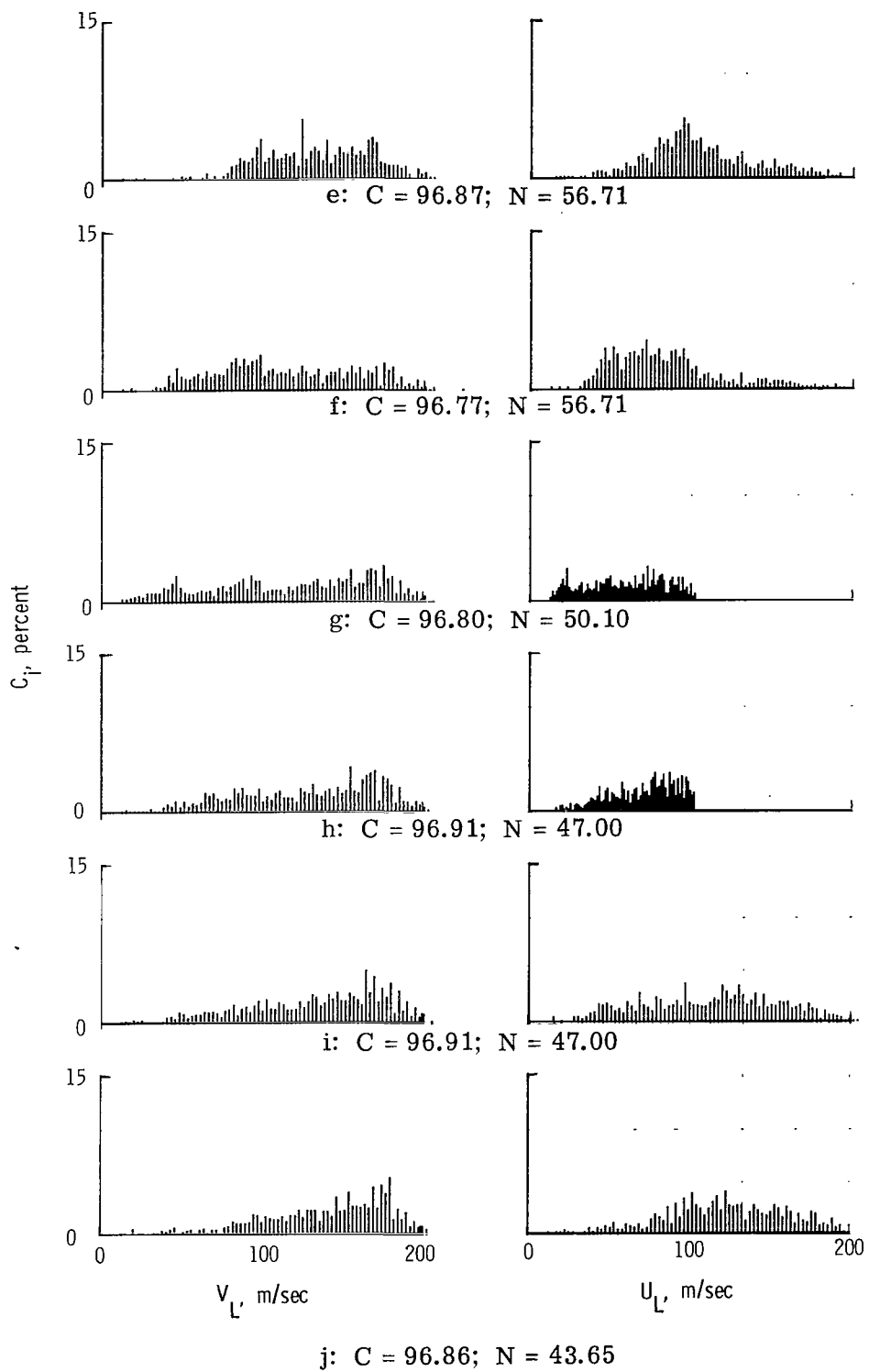


Figure 27.- Histograms above transducer 19. Continued.

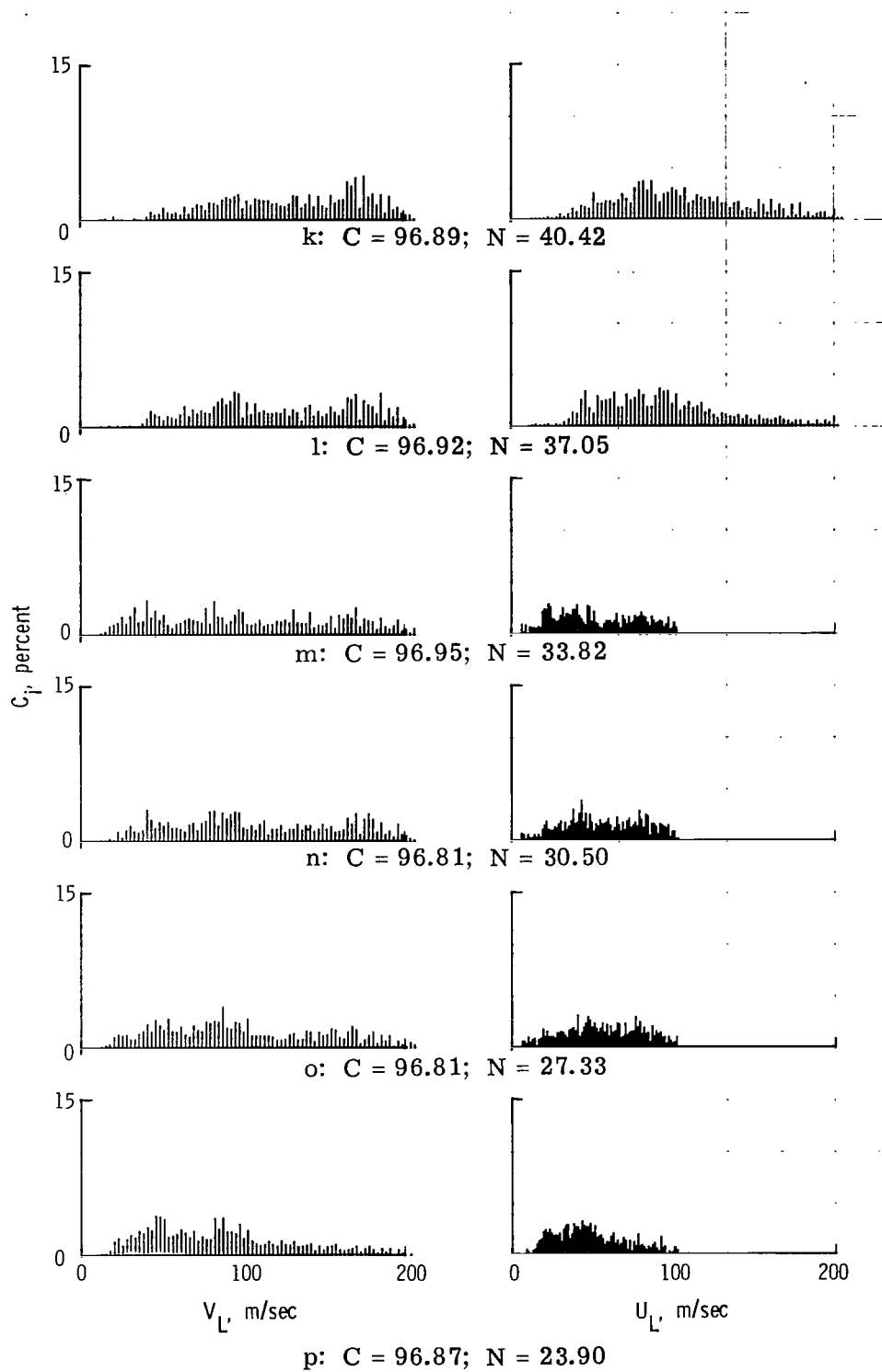


Figure 27.- Histograms above transducer 19. Continued.

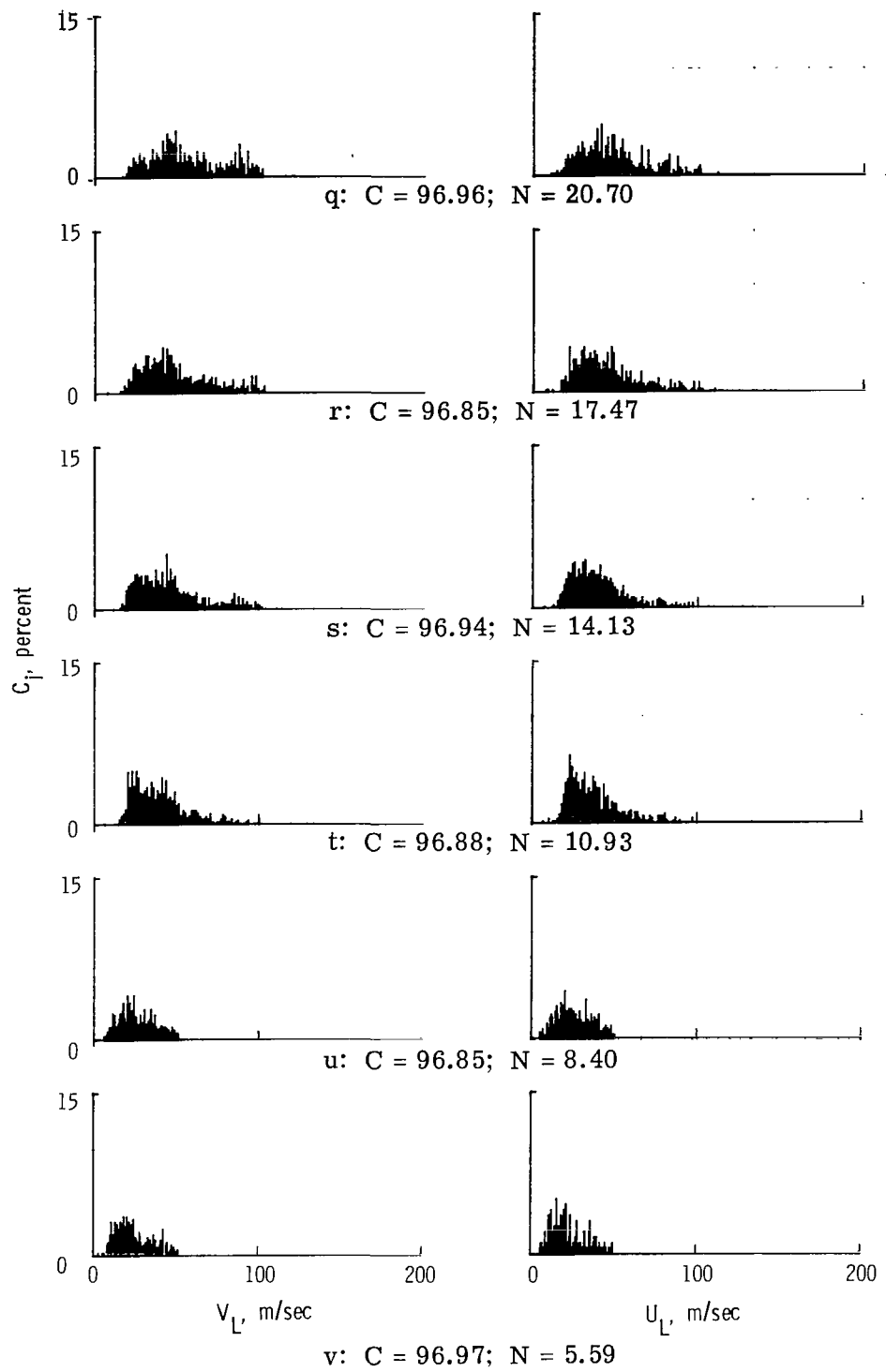


Figure 27.- Histograms above transducer 19. Concluded.

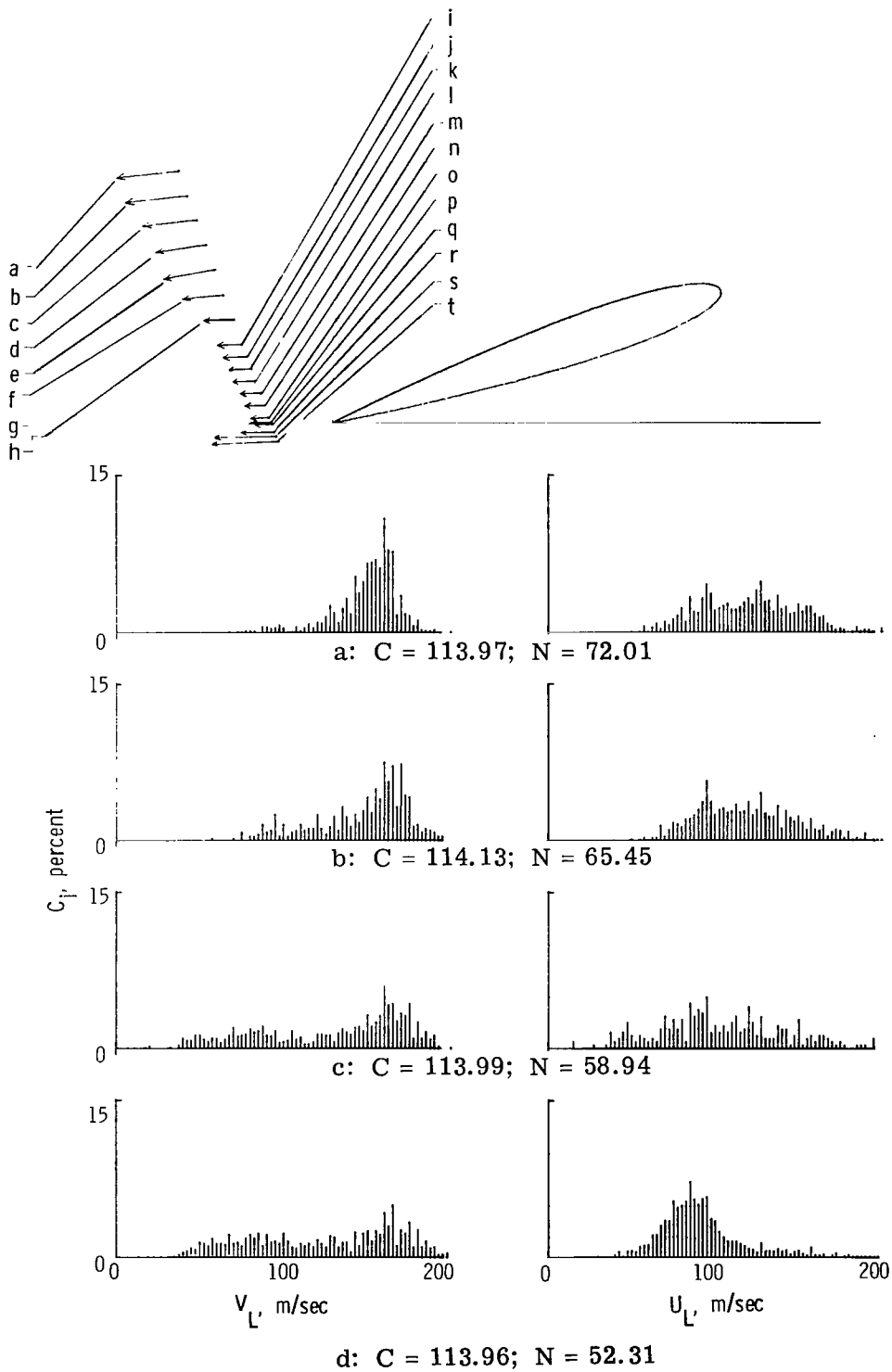


Figure 28.- Histograms behind trailing edge.

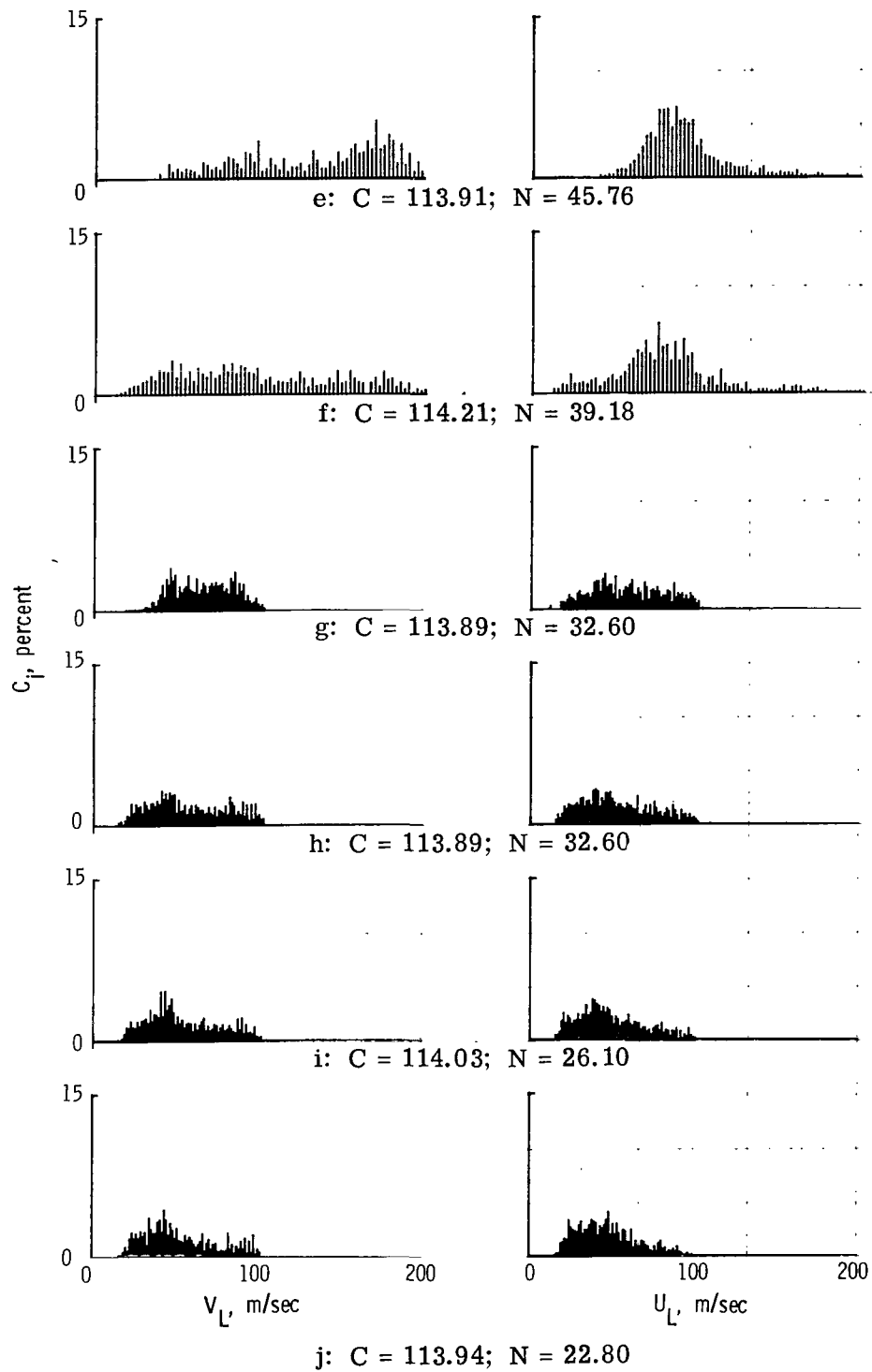


Figure 28.- Histograms behind trailing edge. Continued.

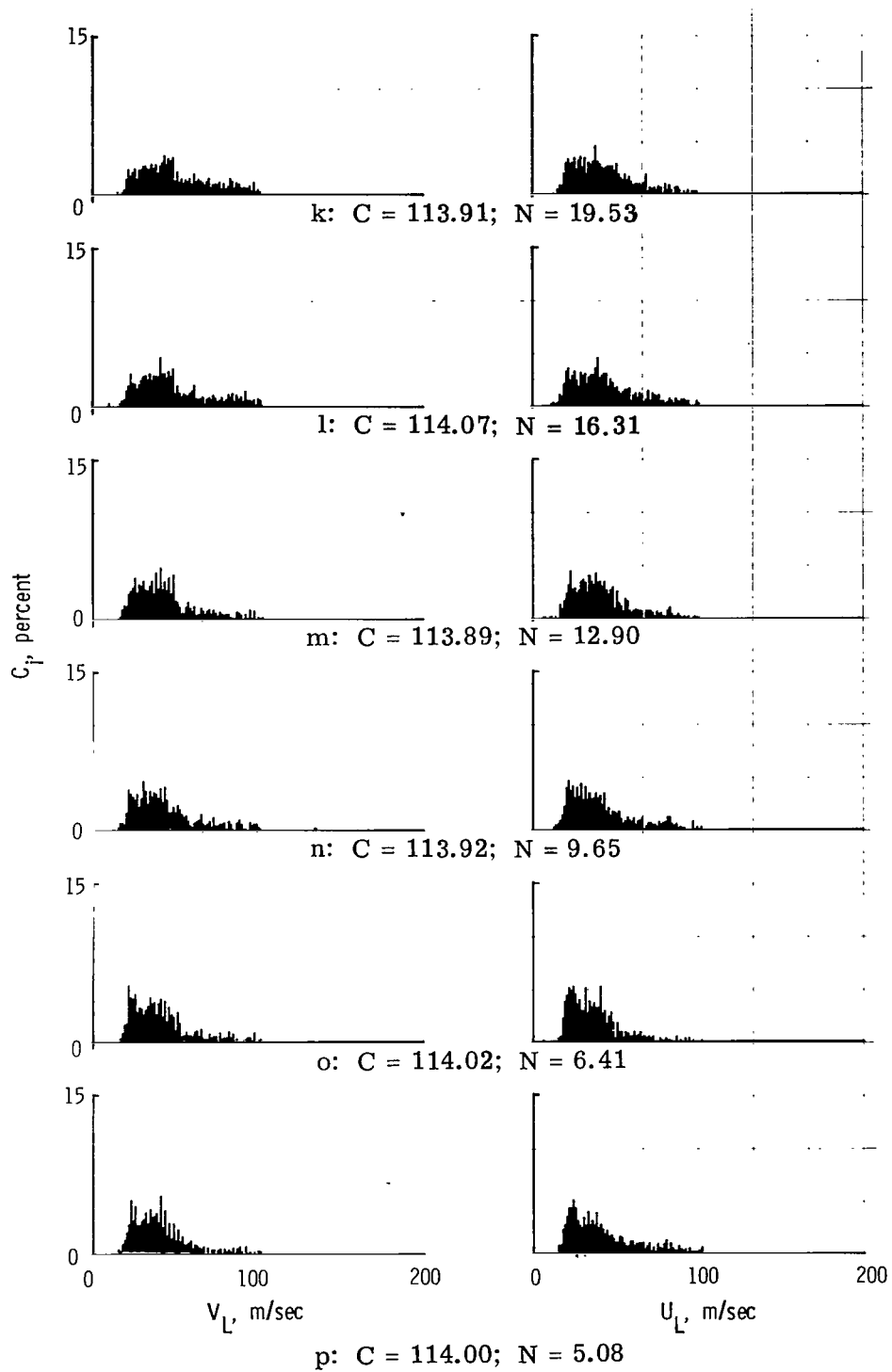


Figure 28.- Histograms behind trailing edge. Continued.

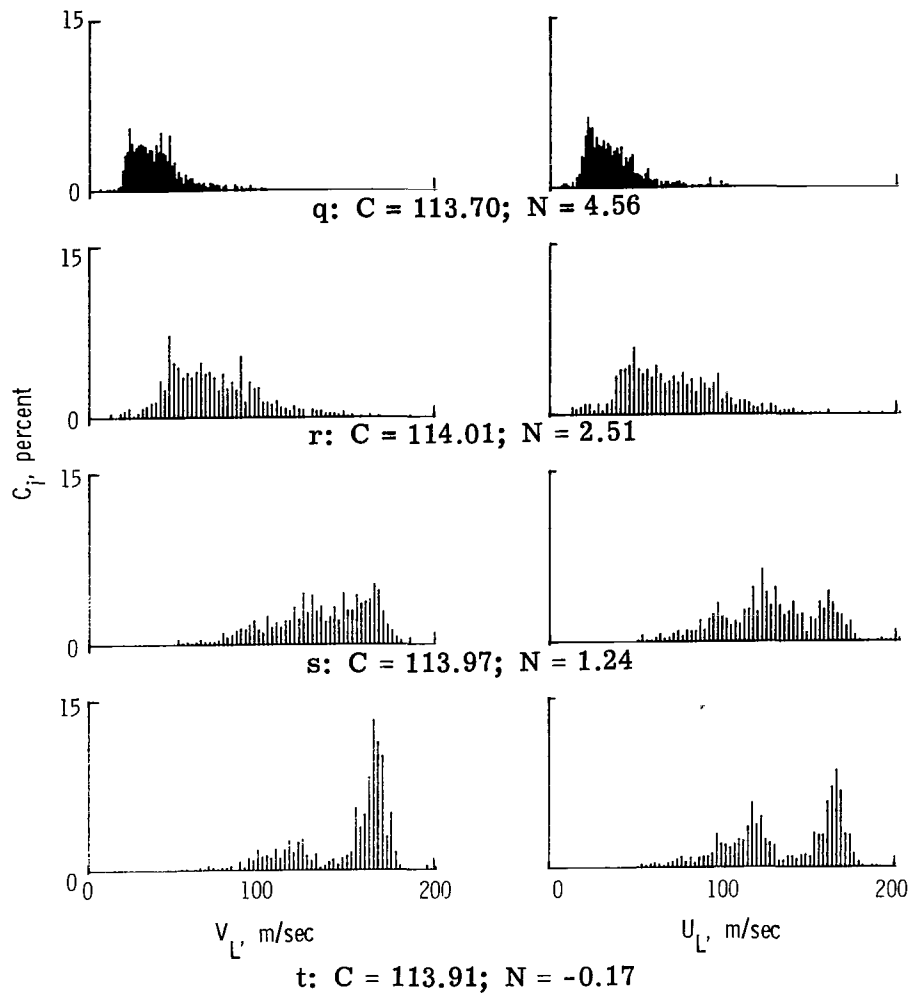


Figure 28.- Histograms behind trailing edge. Concluded.

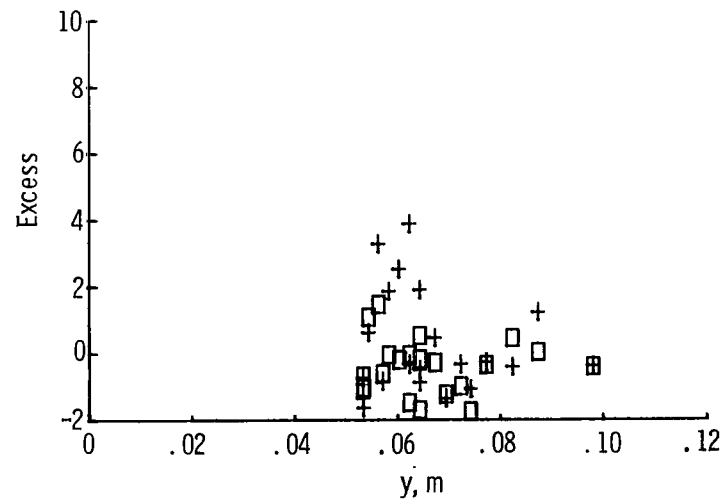
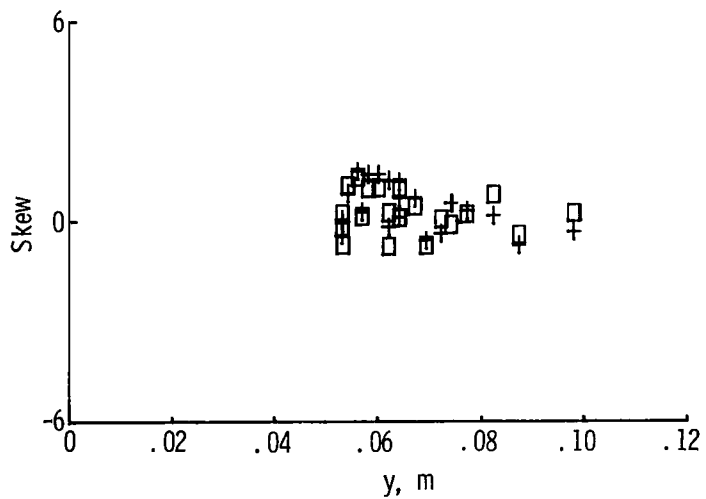
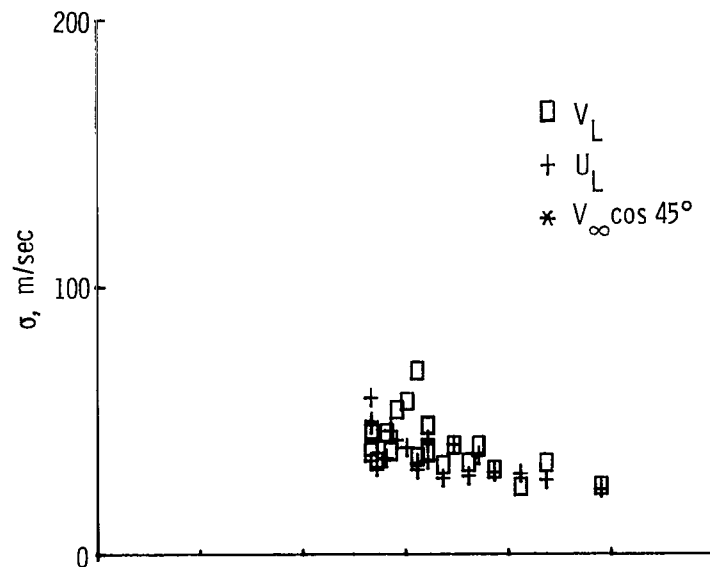
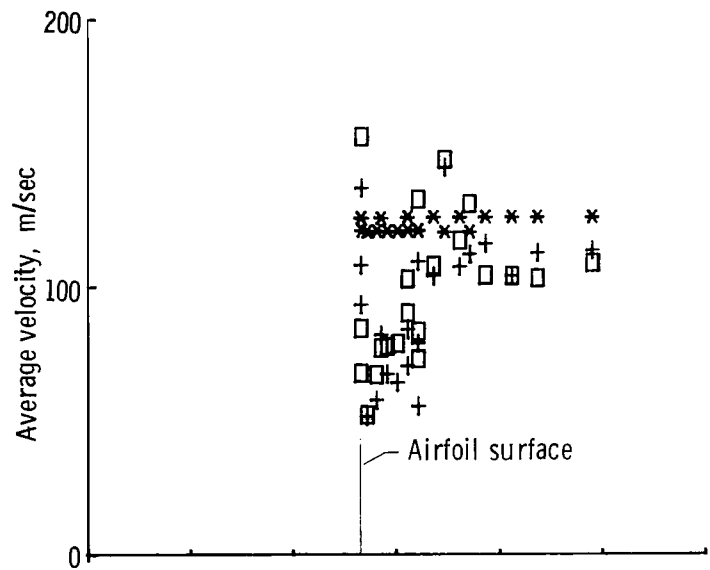


Figure 29.- Histogram moments for scan above transducer 3.

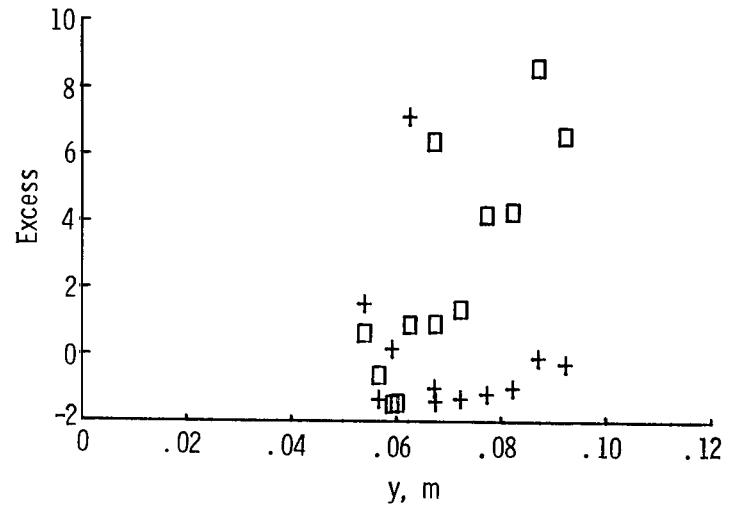
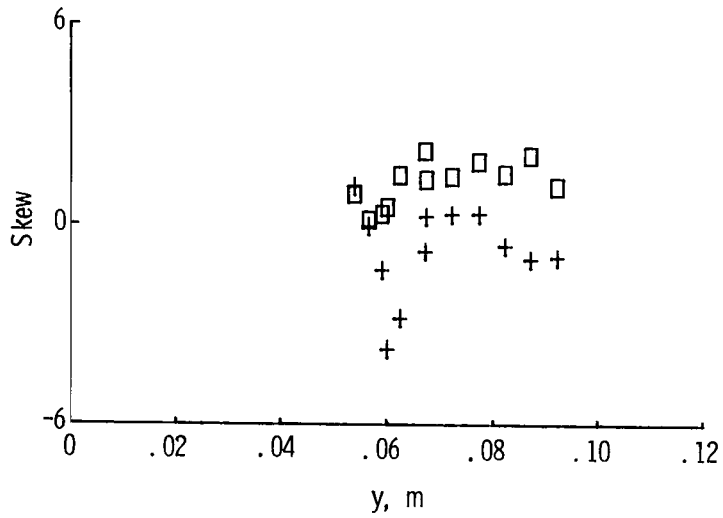
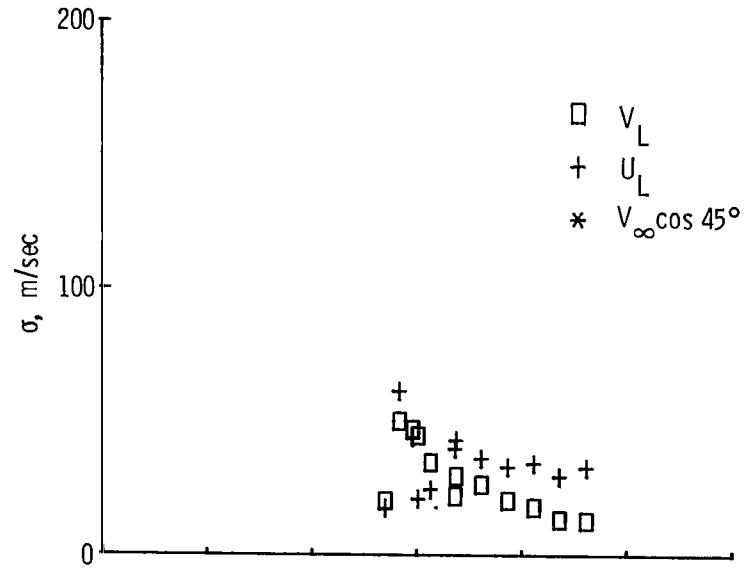
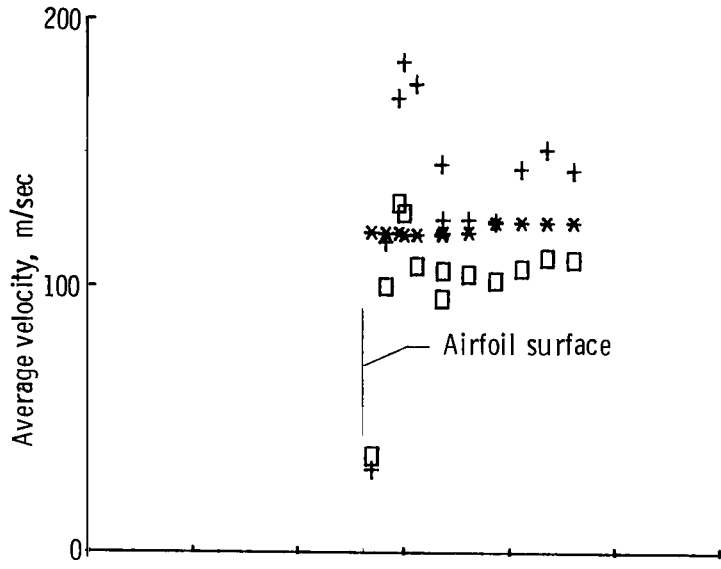


Figure 30.- Histogram moments for scan above transducer 5.

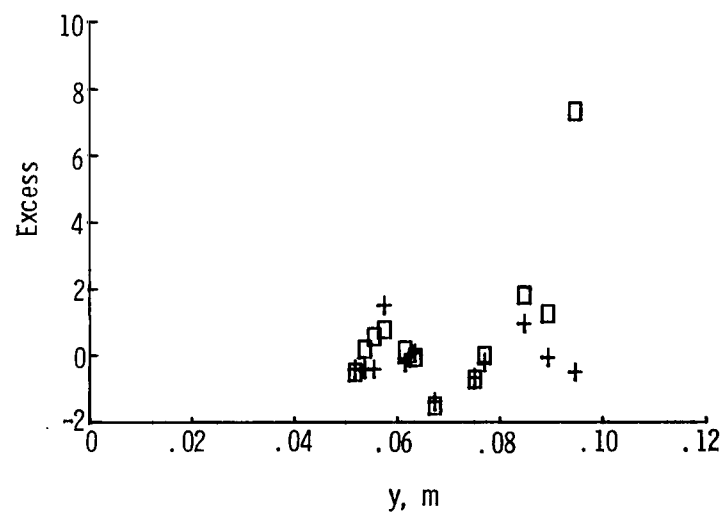
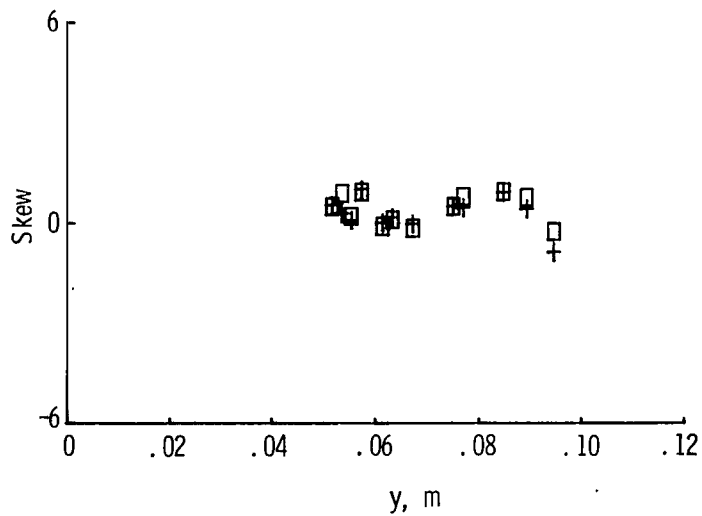
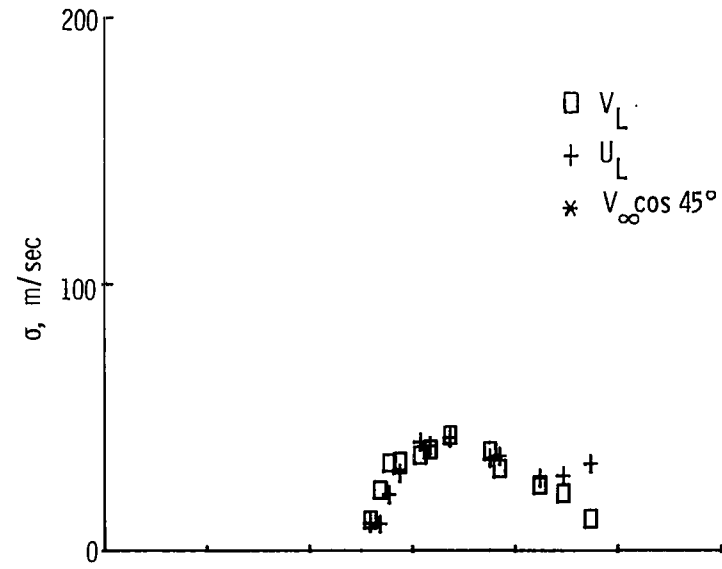
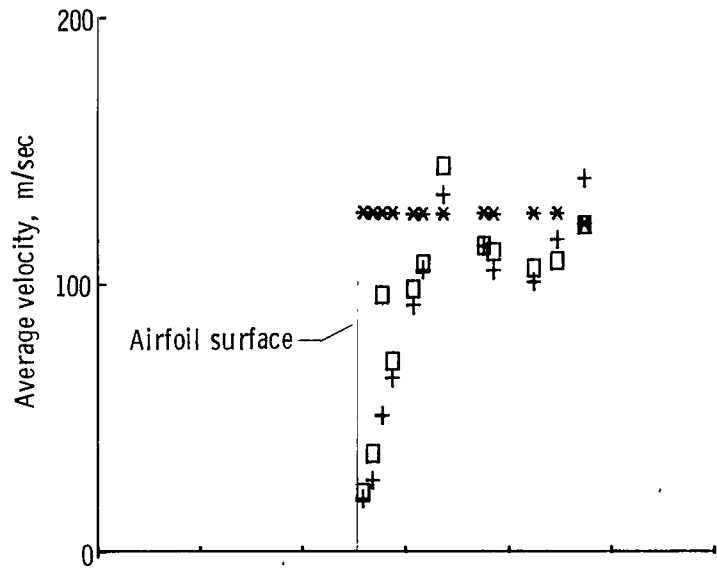


Figure 31.- Histogram moments for scan above transducer 7.

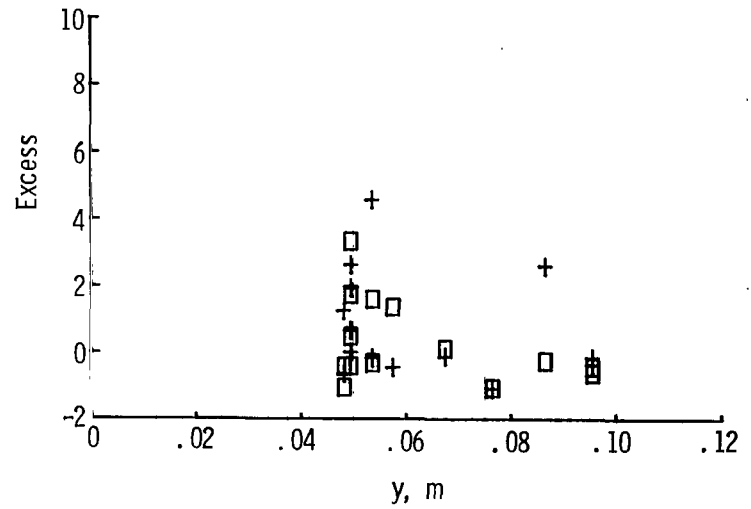
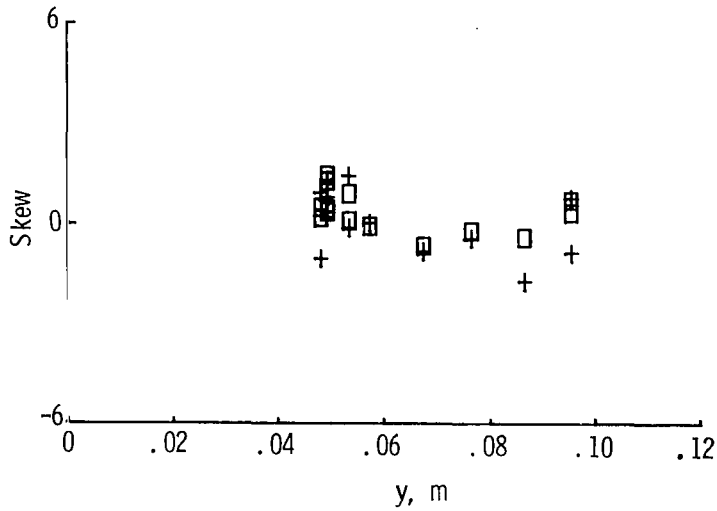
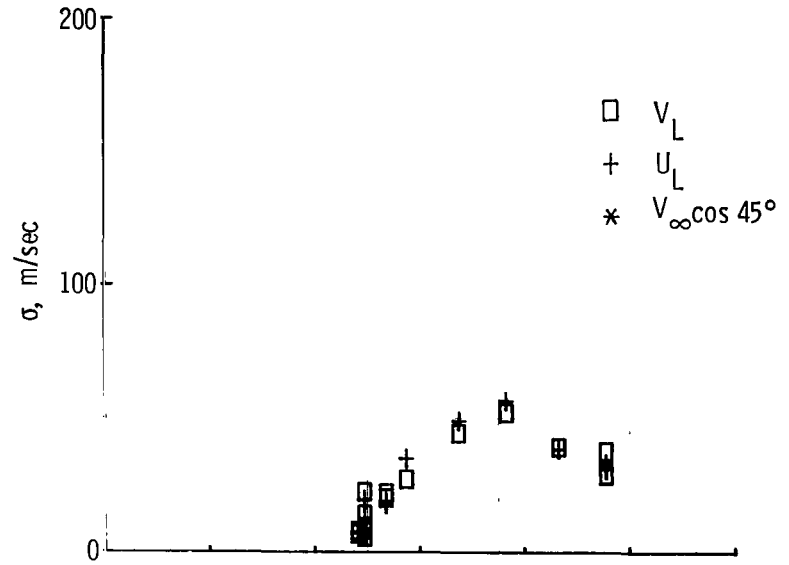
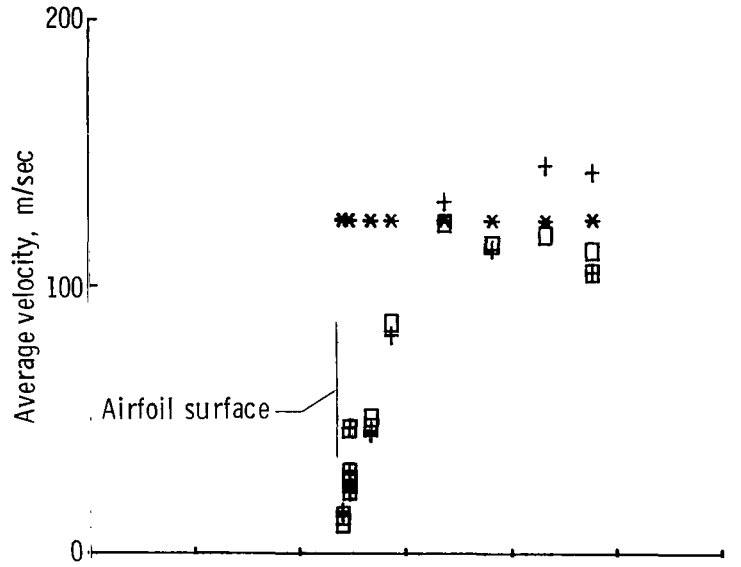


Figure 32.- Histogram moments for scan above transducer 9.

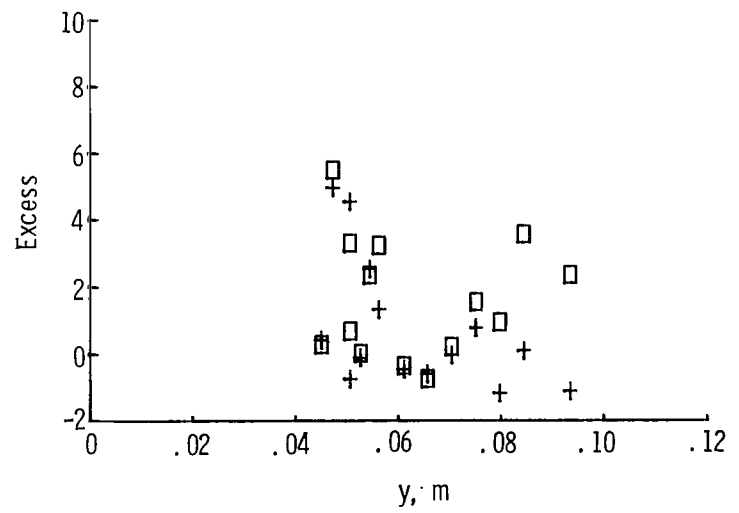
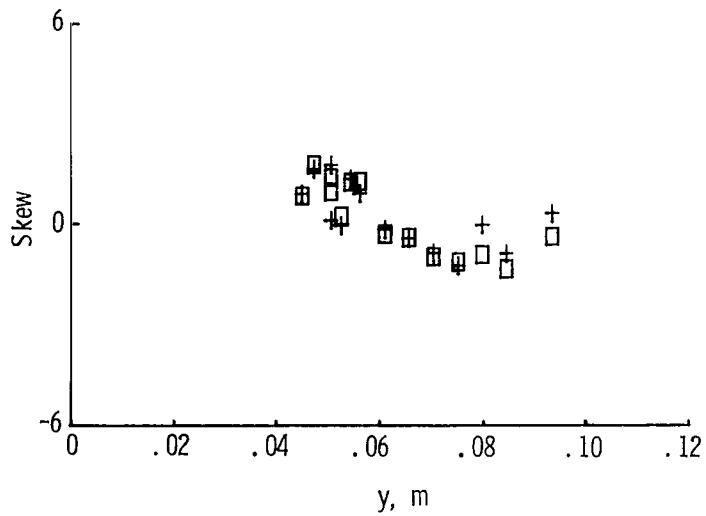
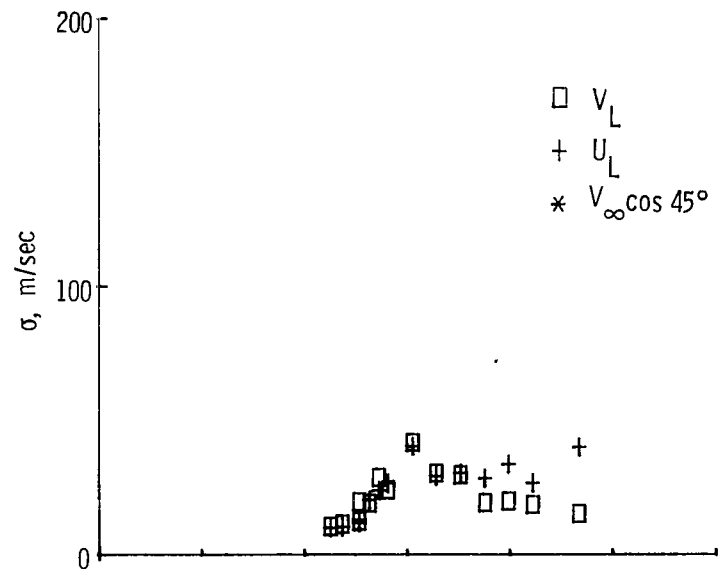
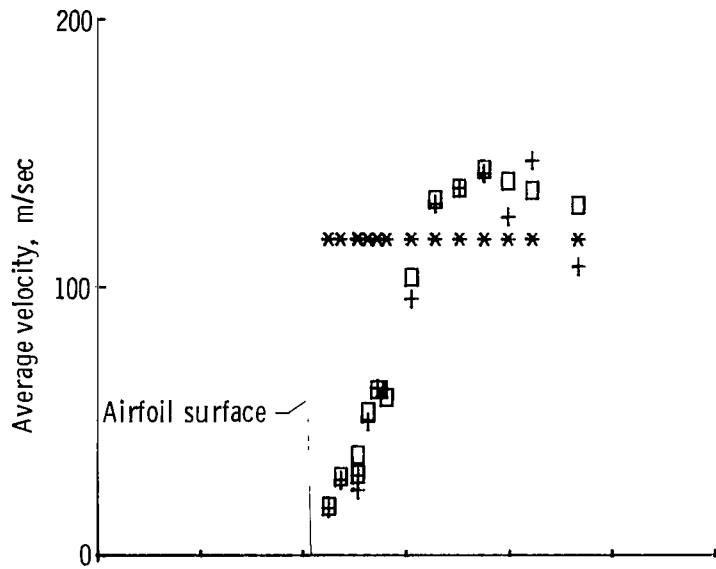


Figure 33.- Histogram moments for scan above transducer 11.

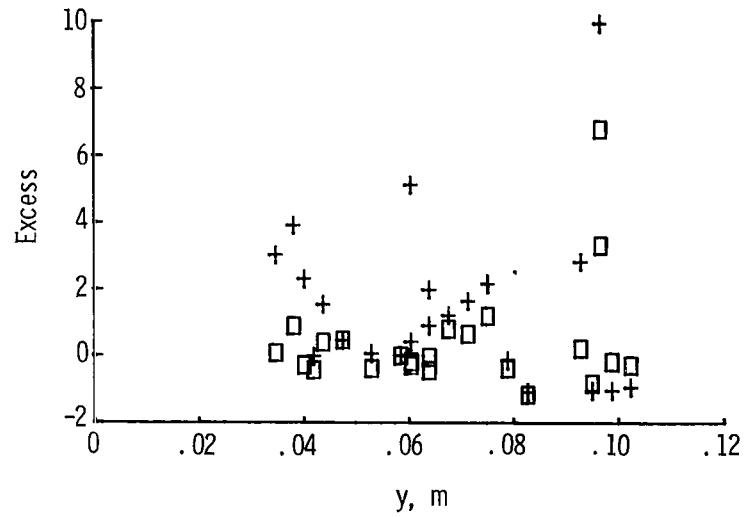
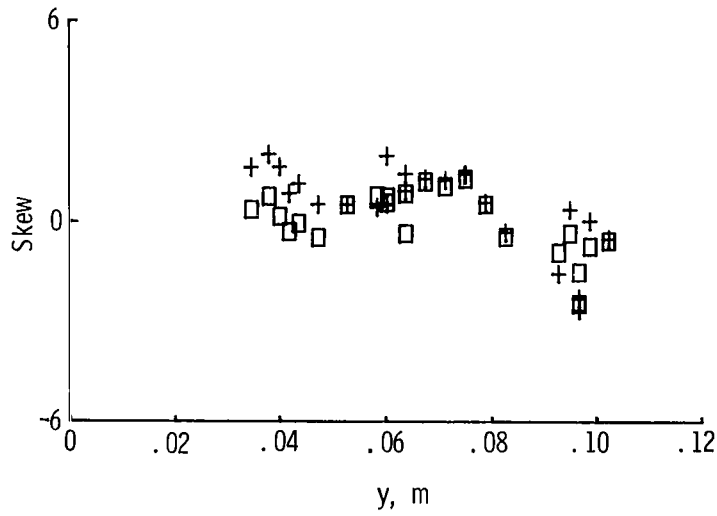
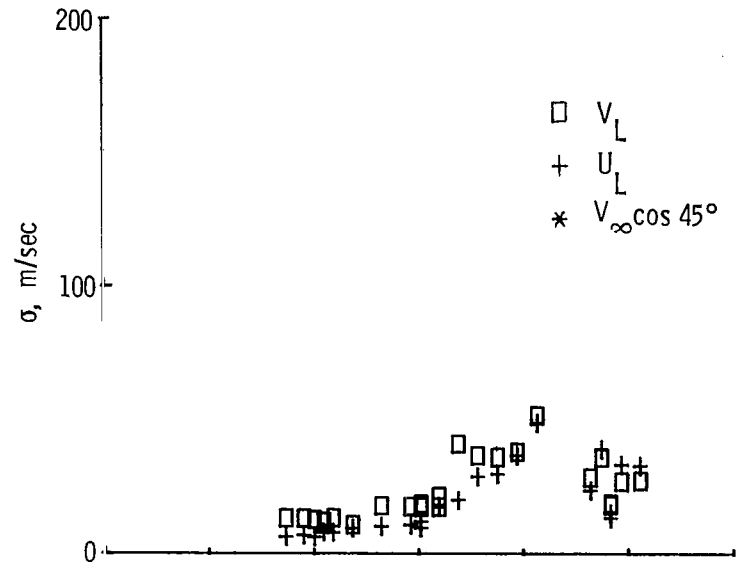
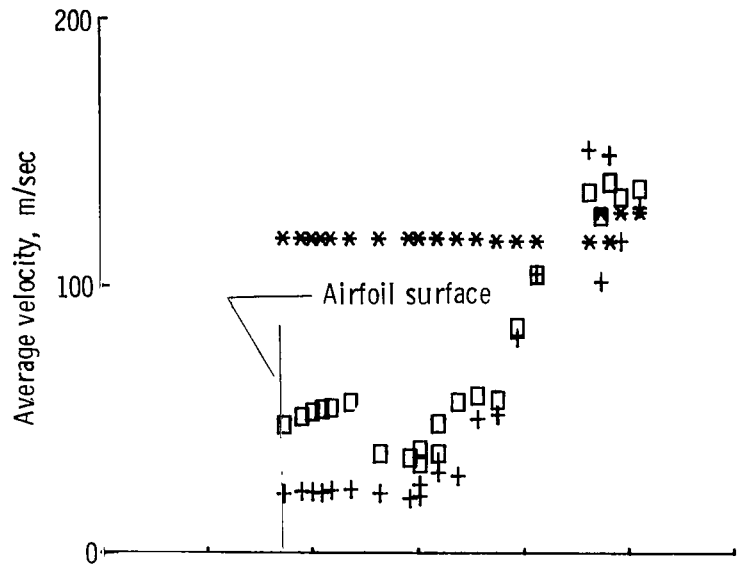


Figure 34.- Histogram moments for scan above transducer 13.

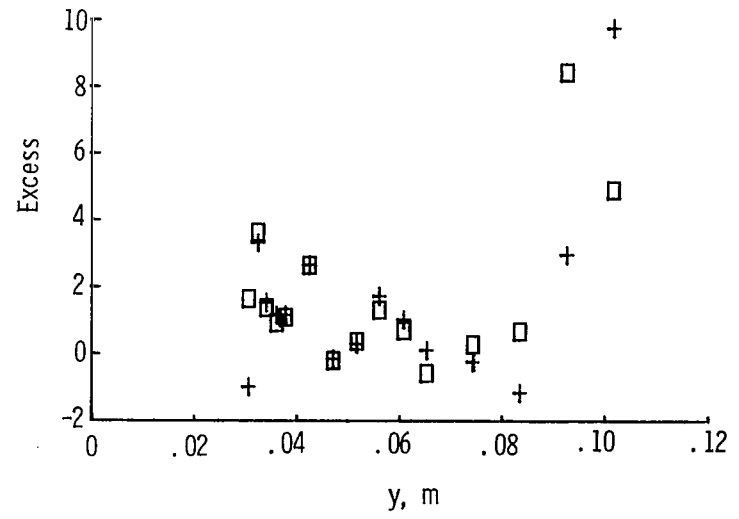
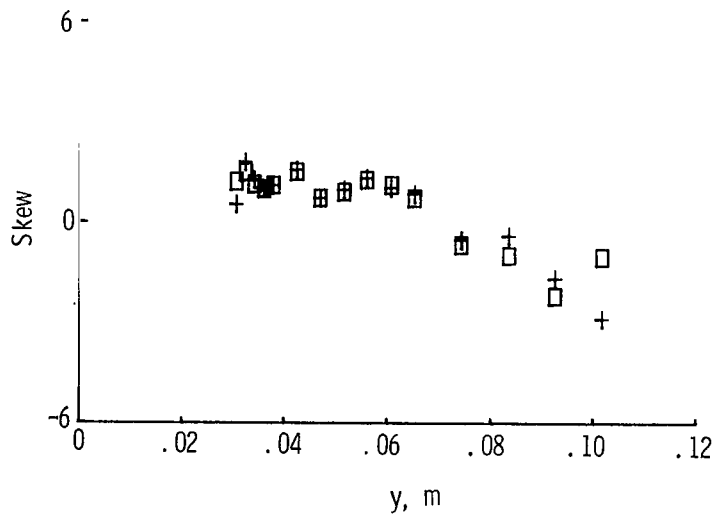
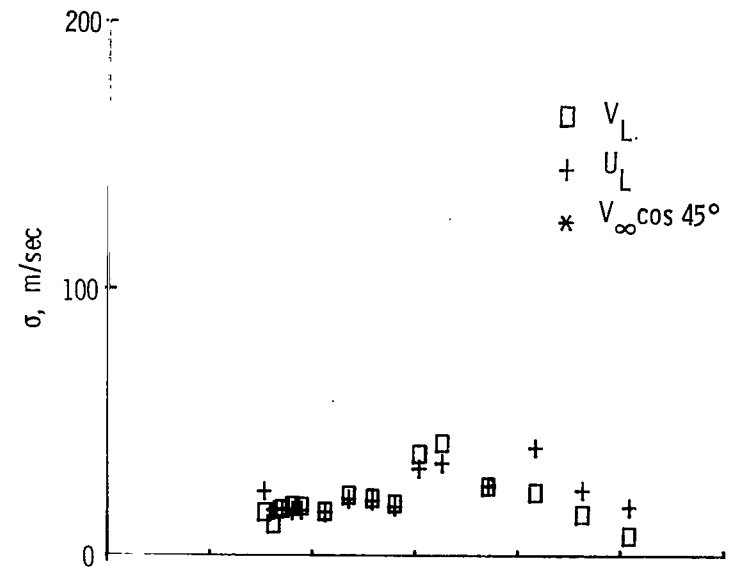
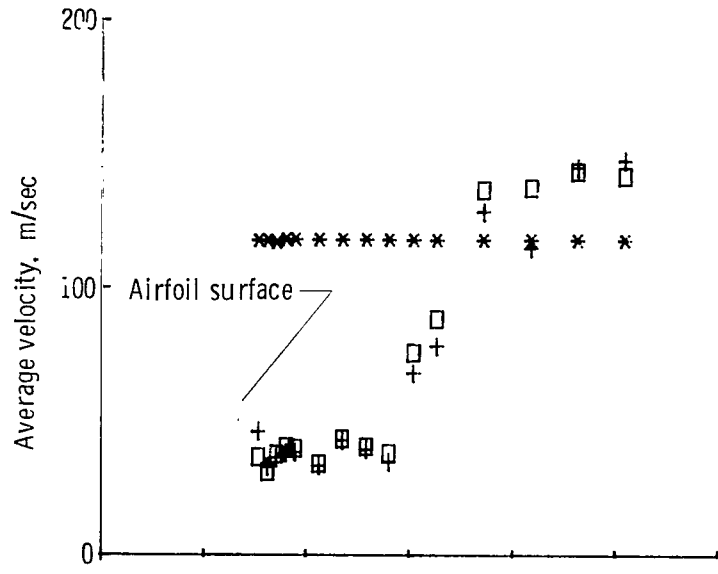


Figure 35.- Histogram moments for scan above transducer 15.

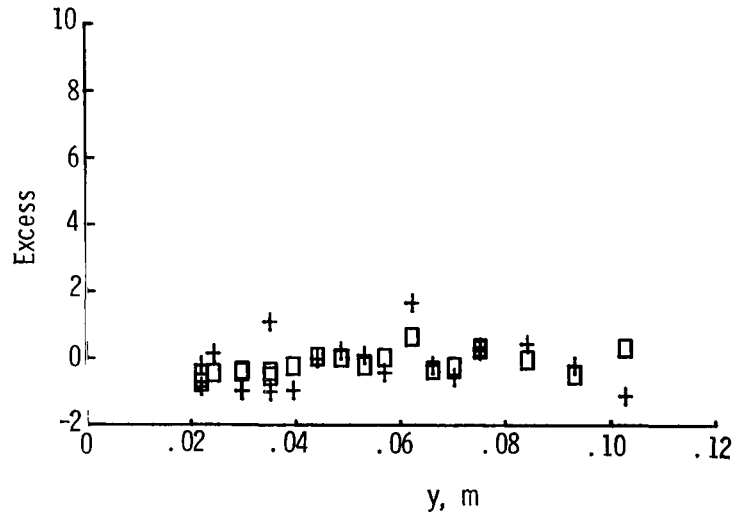
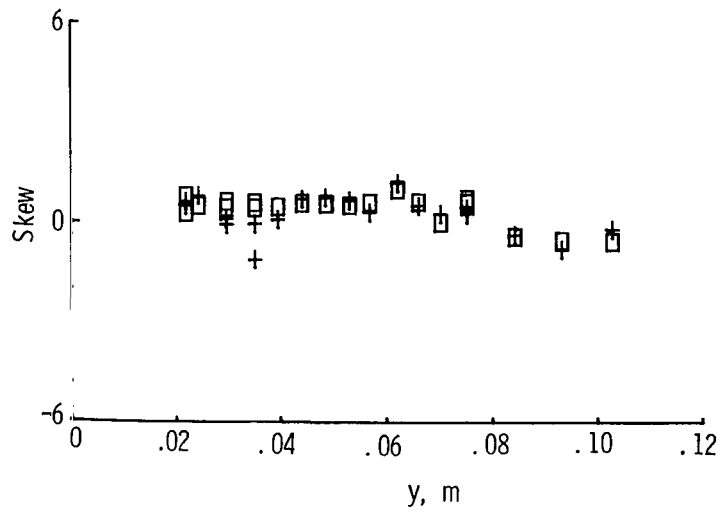
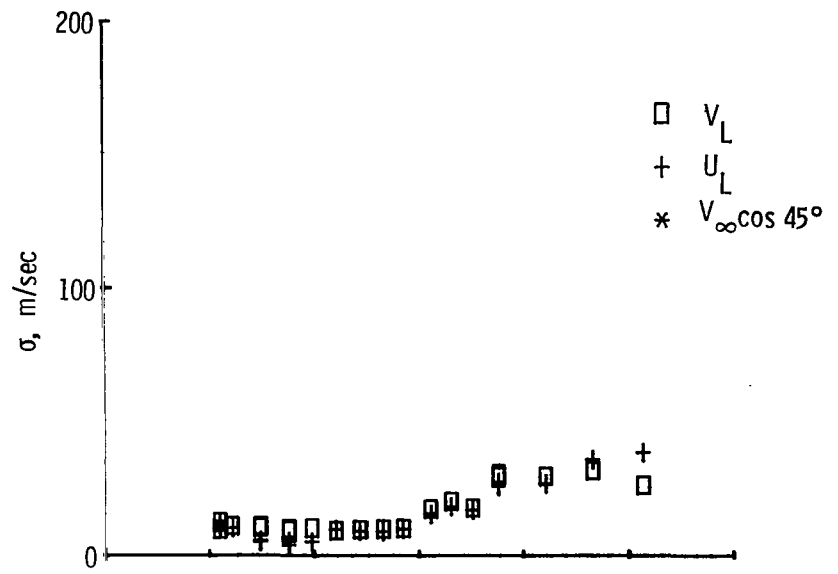
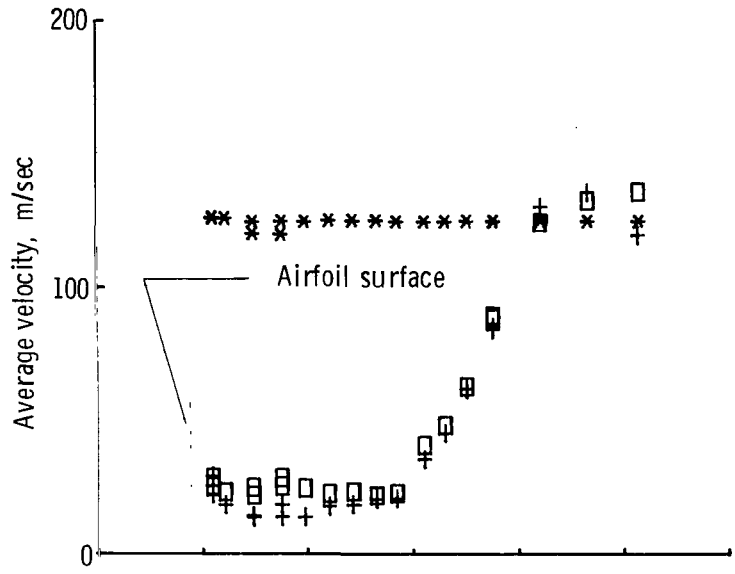


Figure 36.- Histogram moments for scan above transducer 17.

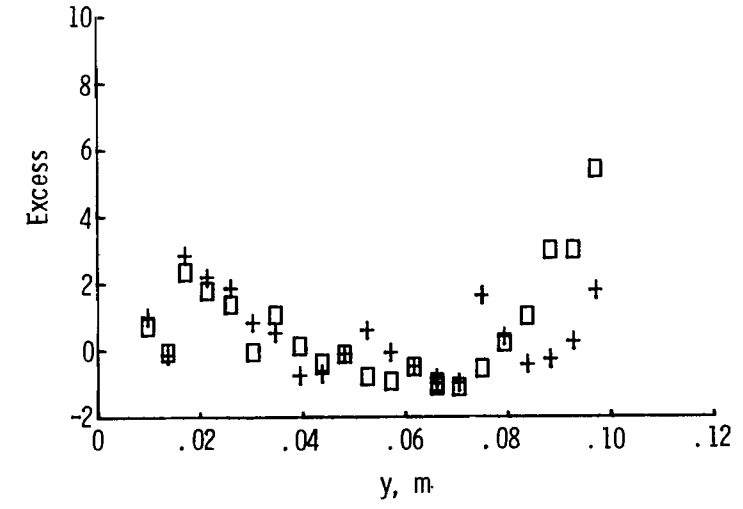
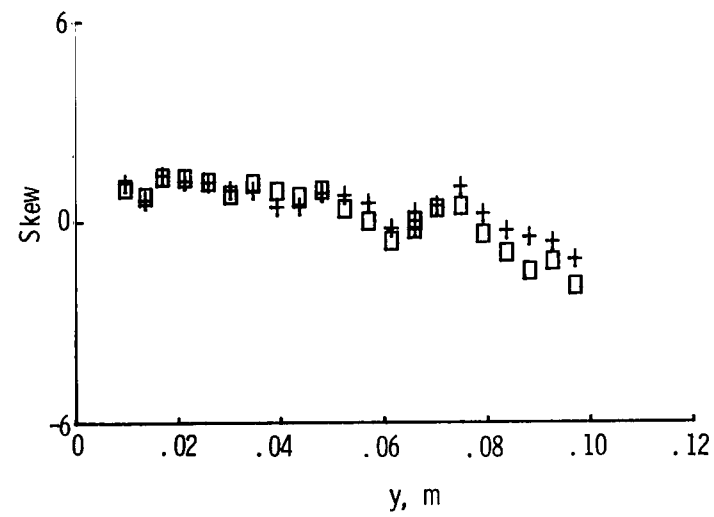
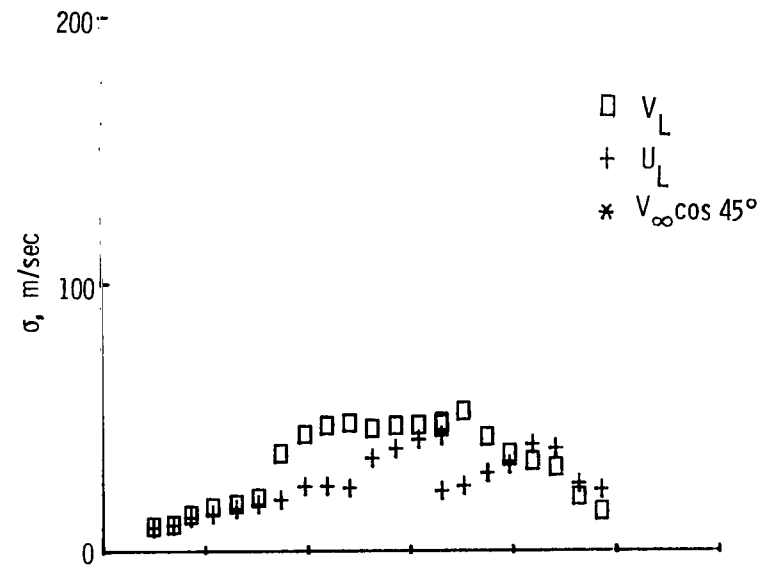
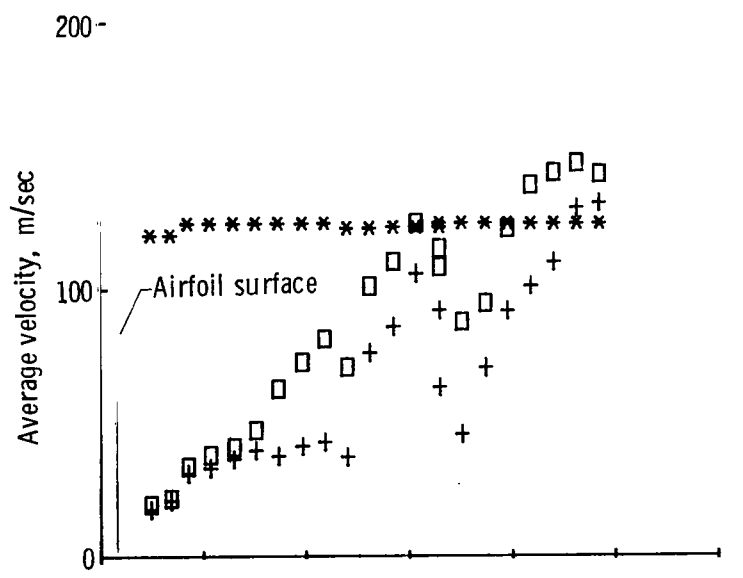


Figure 37. - Histogram moments for scan above transducer 19.

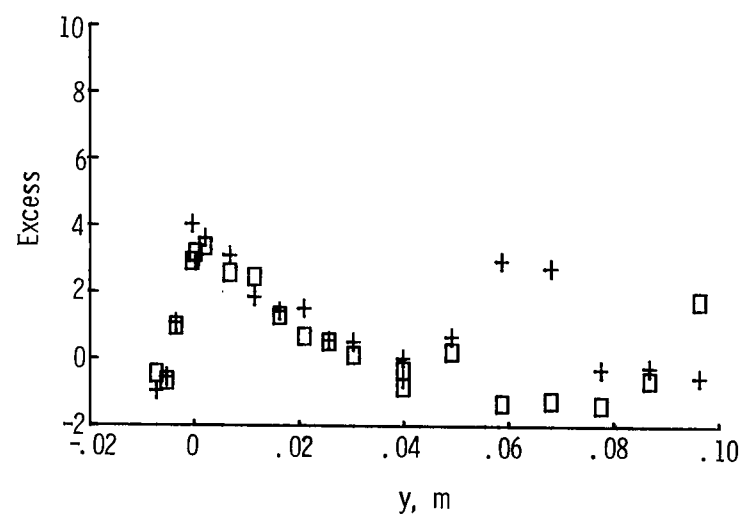
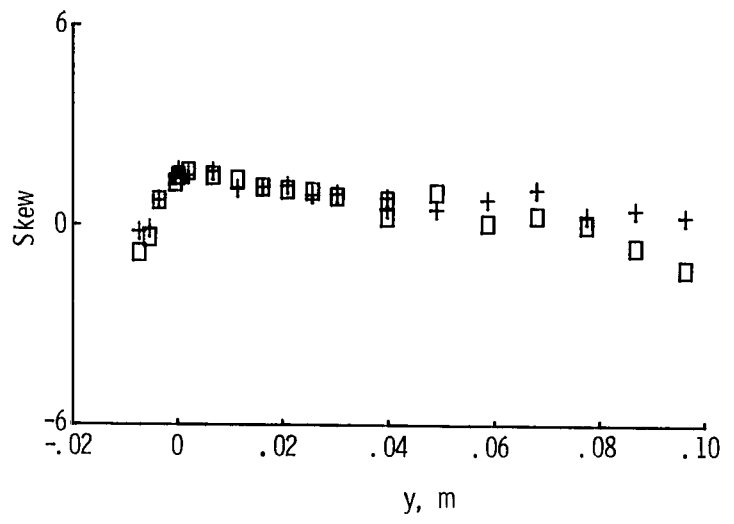
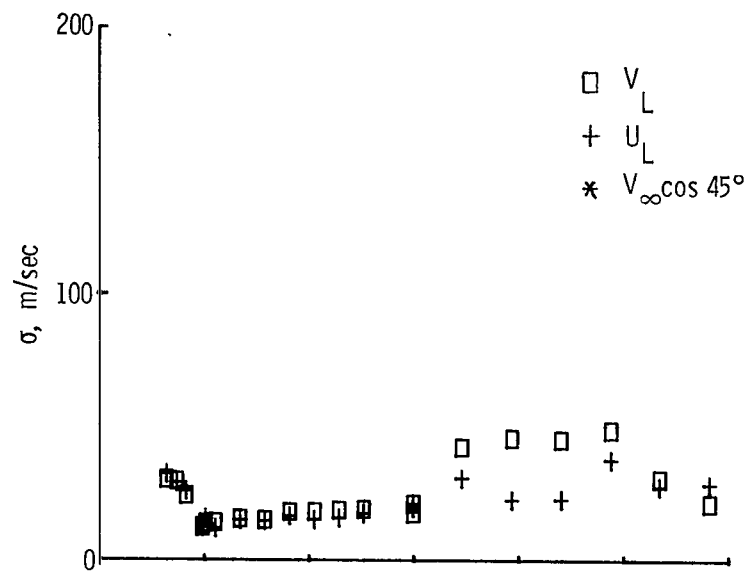
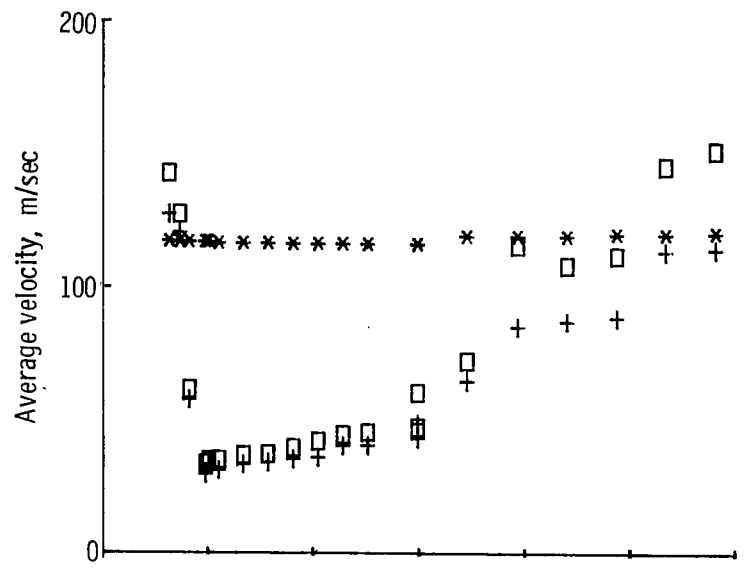
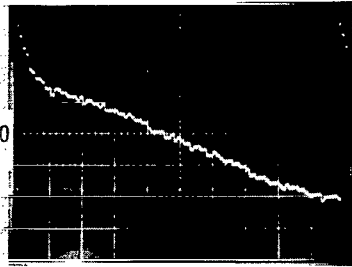
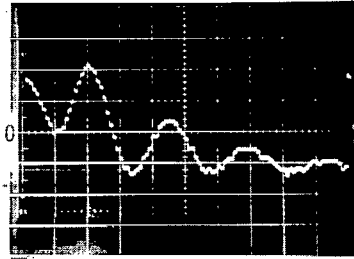


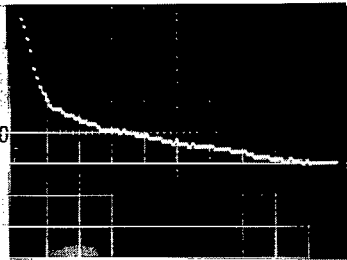
Figure 38.- Histogram moments for scan behind trailing edge.



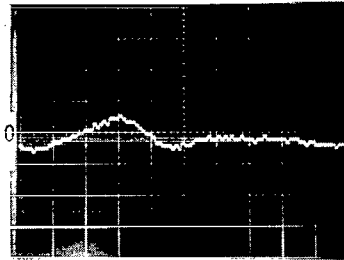
(a) 3D1.



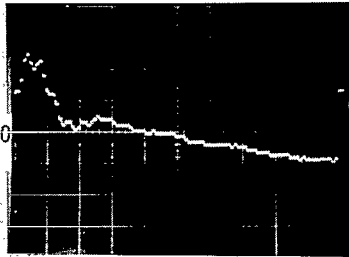
(e) 9D3.



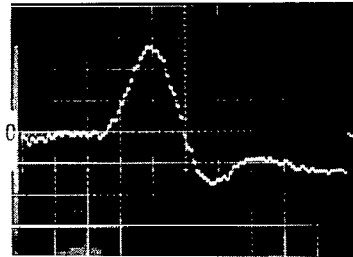
(b) 3D3.



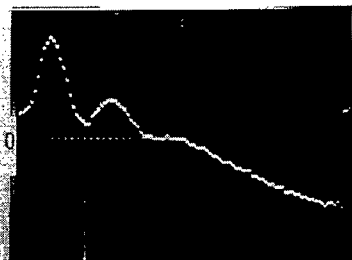
(f) 11D3.



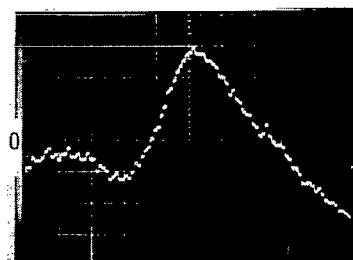
(c) 5D3.



(g) 15D3.



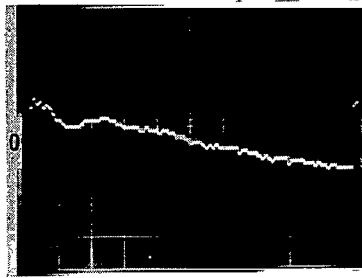
(d) 7D3.



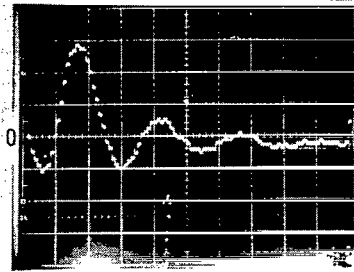
(h) 19D3.

L-77-151

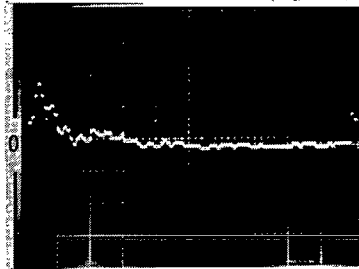
Figure 39. - Crosscorrelations and autocorrelations with respect to transducer 3. (For example, 3D9 denotes crosscorrelation of transducer 9 with delay on transducer 3.)



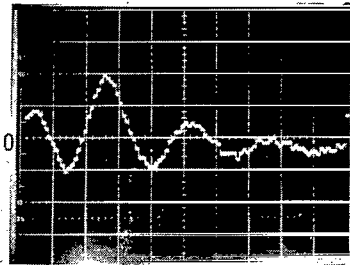
(a) 5D1.



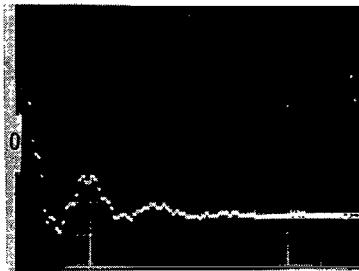
(e) 9D5.



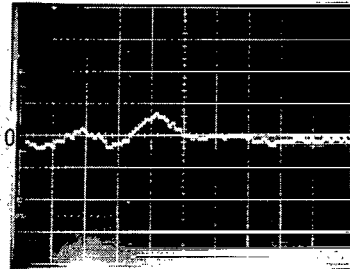
(b) 5D3.



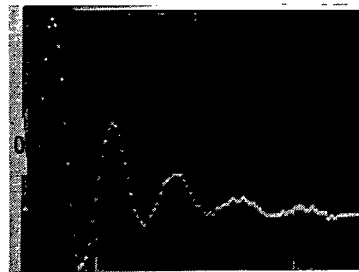
(f) 11D5.



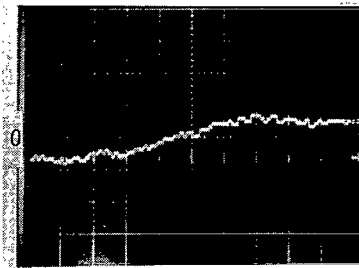
(c) 5D5.



(g) 15D5.



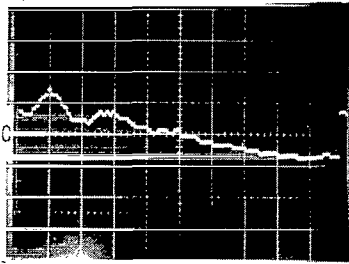
(d) 7D5.



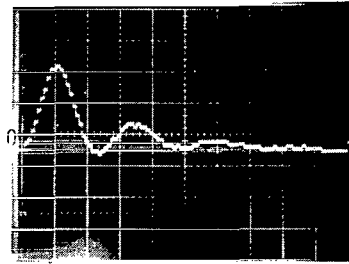
(h) 19D5.

L-77-152

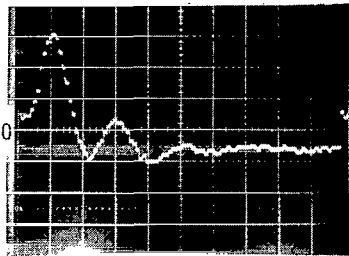
Figure 40.- Crosscorrelations and autocorrelations with respect to transducer 5.



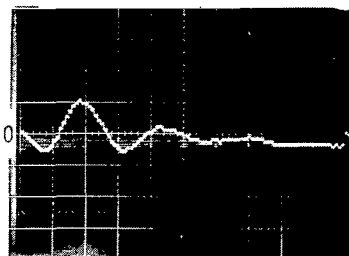
(a) 7D1.



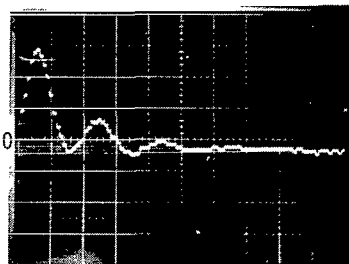
(e) 9D7.



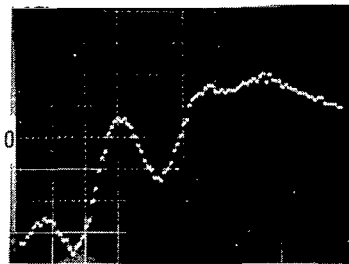
(b) 7D3.



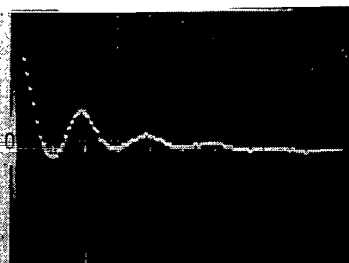
(f) 11D7.



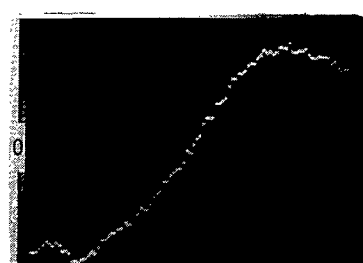
(c) 7D5.



(g) 15D7.

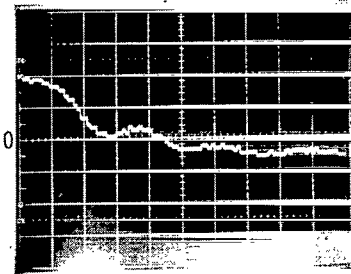


(d) 7D7.

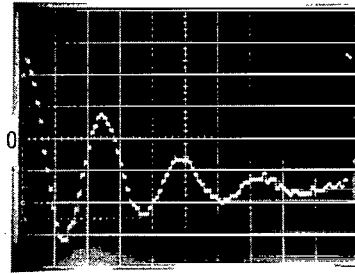


(h) 19D7.

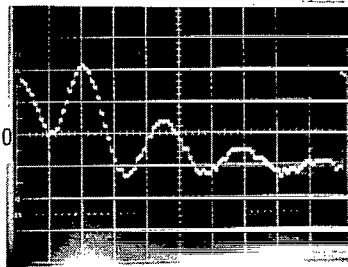
Figure 41.- Crosscorrelations and autocorrelations with respect
L-77-153
to transducer 7.



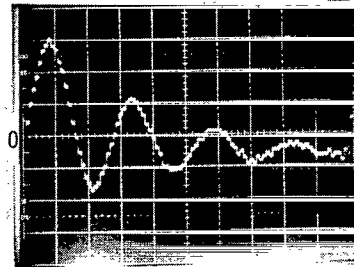
(a) 9D1.



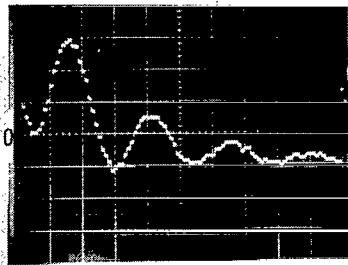
(e) 9D9.



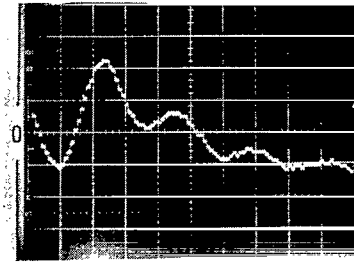
(b) 9D3.



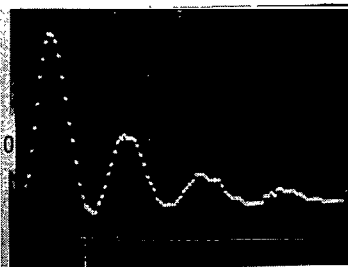
(f) 11D9.



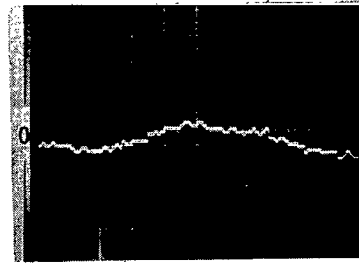
(c) 9D5.



(g) 15D9.



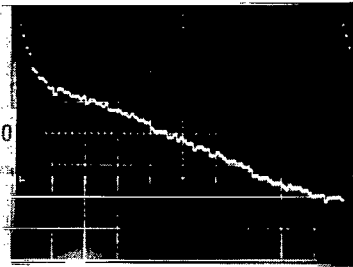
(d) 9D7.



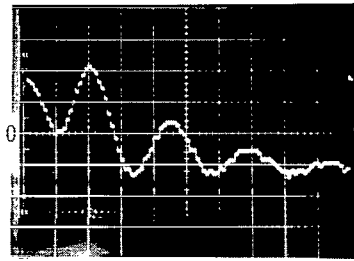
(h) 19D9.

L-77-154

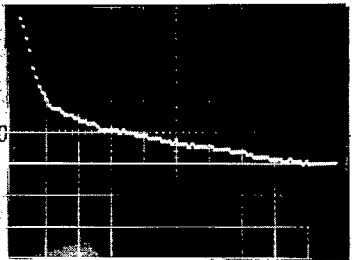
Figure 42.- Crosscorrelations and autocorrelations with respect to transducer 9.



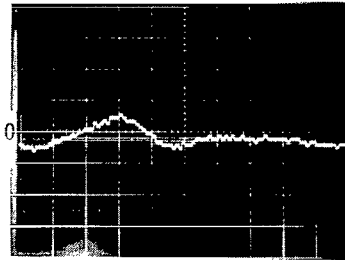
(a) 3D1.



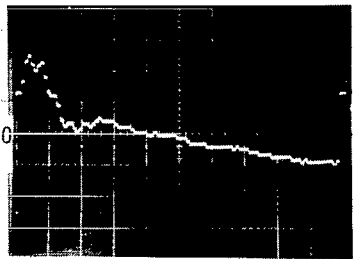
(e) 9D3.



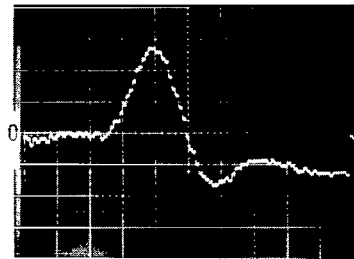
(b) 3D3.



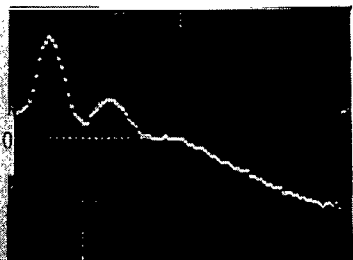
(f) 11D3.



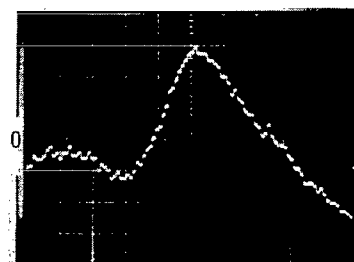
(c) 5D3.



(g) 15D3.



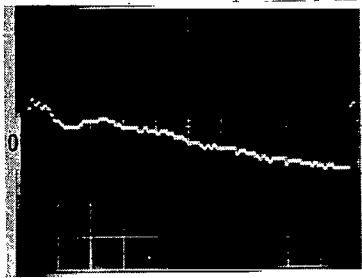
(d) 7D3.



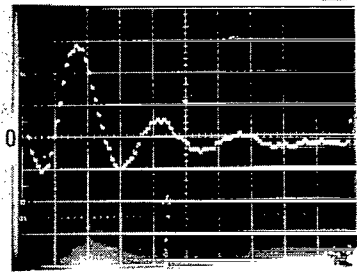
(h) 19D3.

Figure 39.- Crosscorrelations and autocorrelations with respect to transducer 3. (For example, 3D9 denotes crosscorrelation of transducer 9 with delay on transducer 3.)

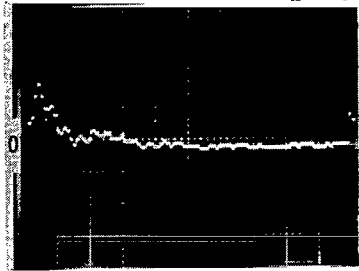
L-77-151



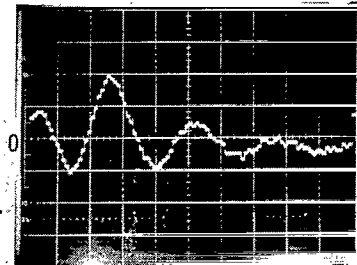
(a) 5D1.



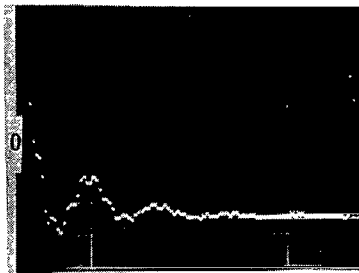
(e) 9D5.



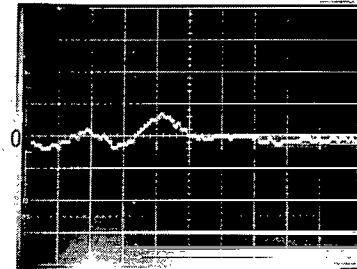
(b) 5D3.



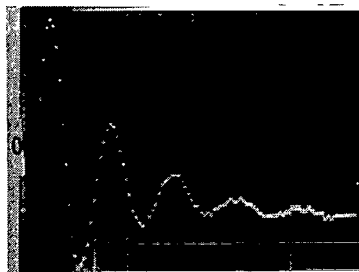
(f) 11D5.



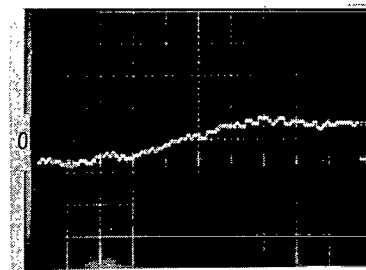
(c) 5D5.



(g) 15D5.



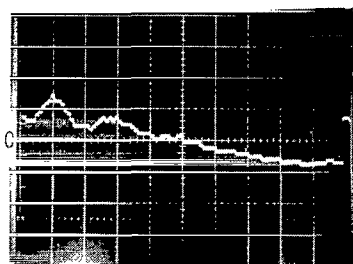
(d) 7D5.



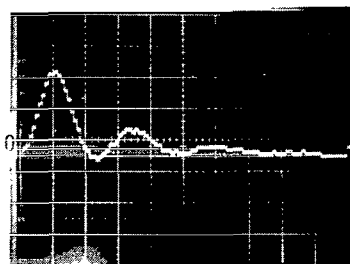
(h) 19D5.

L-77-152

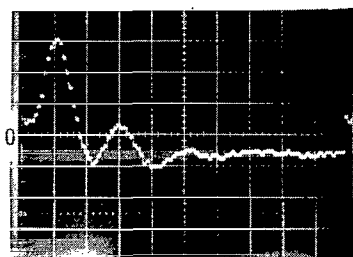
Figure 40.- Crosscorrelations and autocorrelations with respect to transducer 5.



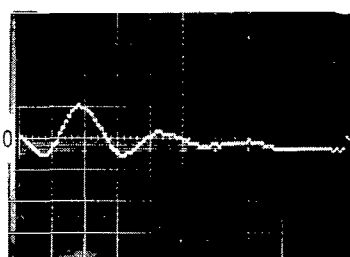
(a) 7D1.



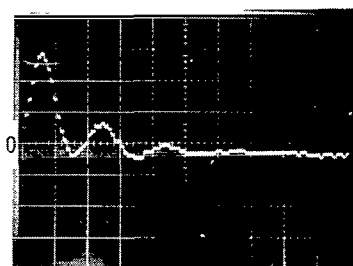
(e) 9D7.



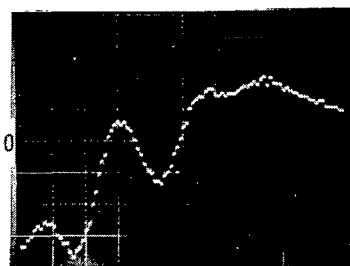
(b) 7D3.



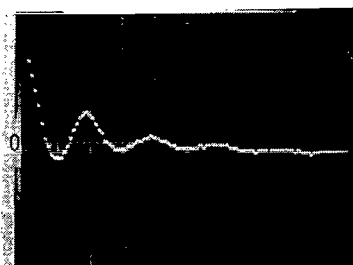
(f) 11D7.



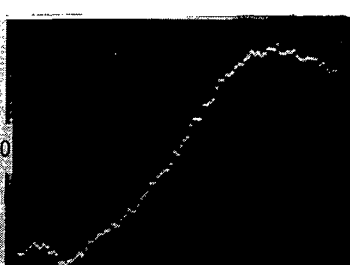
(c) 7D5.



(g) 15D7.

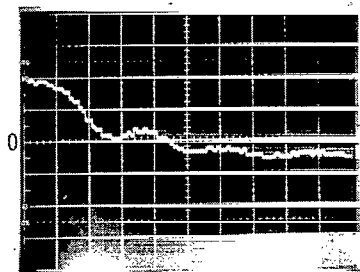


(d) 7D7.

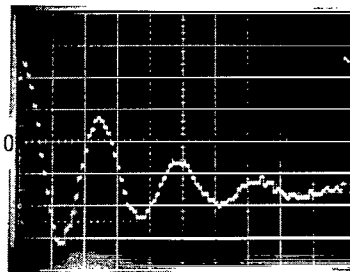


(h) 19D7.

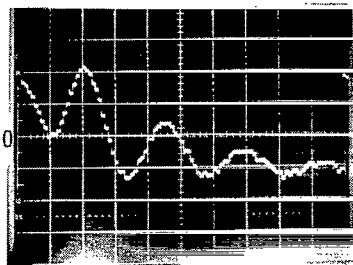
Figure 41.- Crosscorrelations and autocorrelations with respect to transducer 7. L-77-153



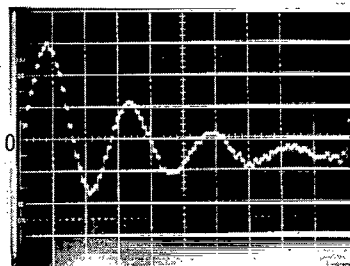
(a) 9D1.



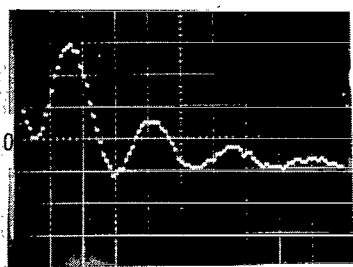
(e) 9D9.



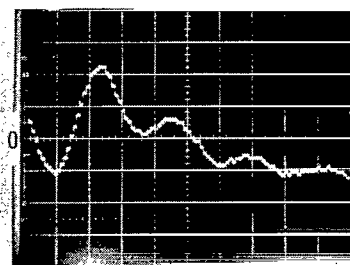
(b) 9D3.



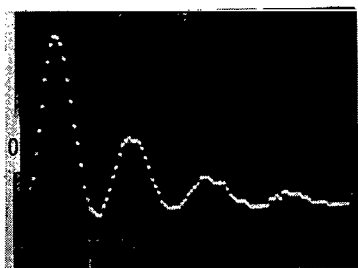
(f) 11D9.



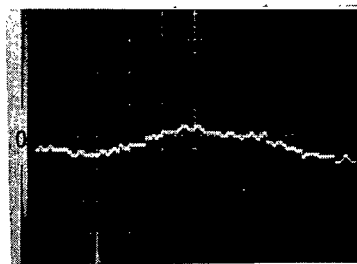
(c) 9D5.



(g) 15D9.



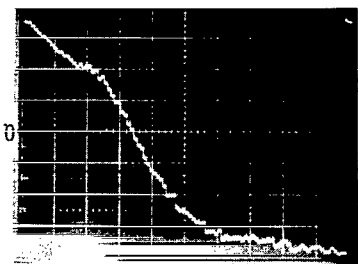
(d) 9D7.



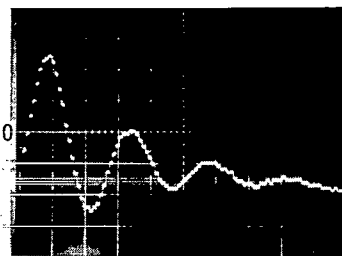
(h) 19D9.

L-77-154

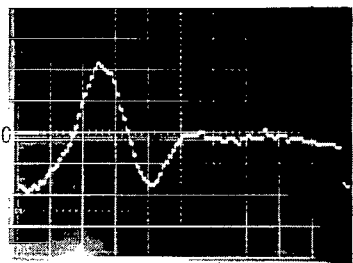
Figure 42.- Crosscorrelations and autocorrelations with respect to transducer 9.



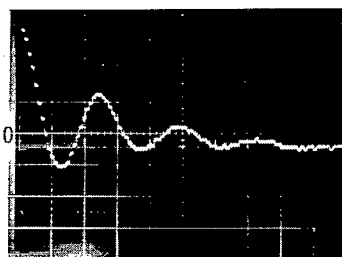
(a) 11D1.



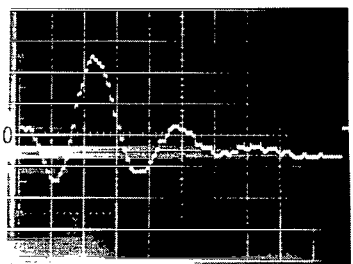
(e) 11D9.



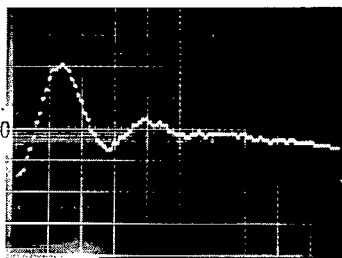
(b) 11D3.



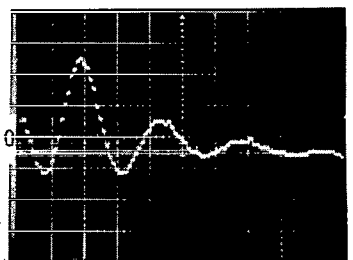
(f) 11D11.



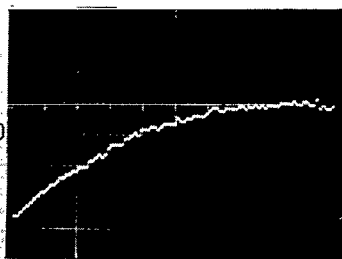
(c) 11D5.



(g) 15D11.

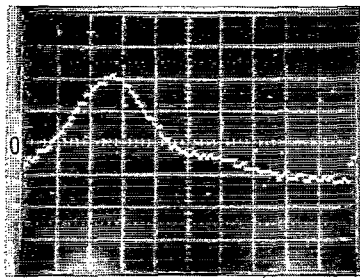


(d) 11D7.

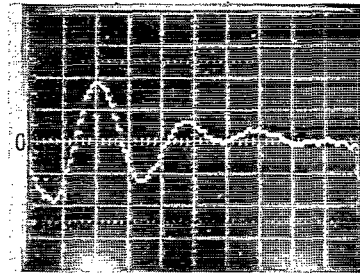


(h) 19D11.

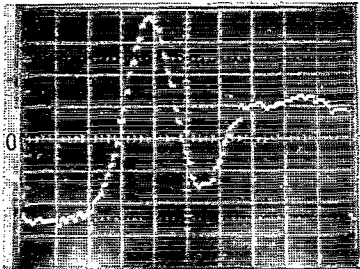
Figure 43. - Crosscorrelations and autocorrelations with respect to transducer 11.
L-77-155



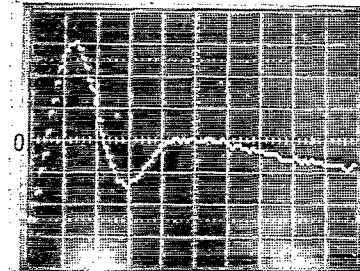
(a) 15D1.



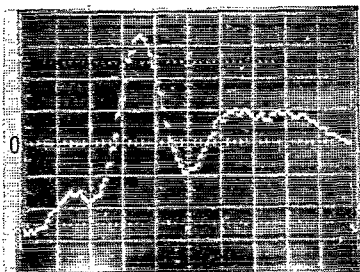
(e) 15D9.



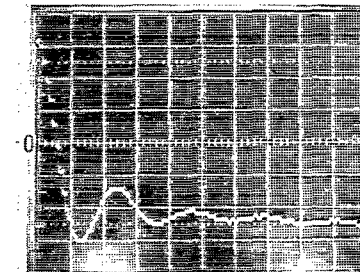
(b) 15D3.



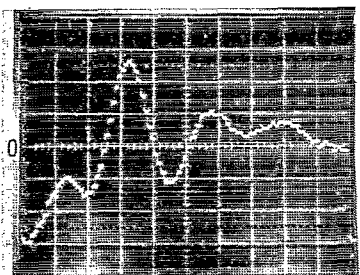
(f) 15D11.



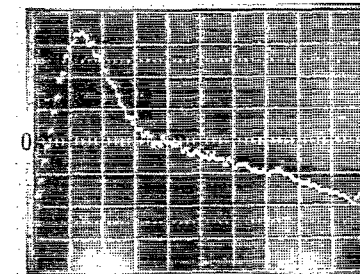
(c) 15D5.



(g) 15D15.

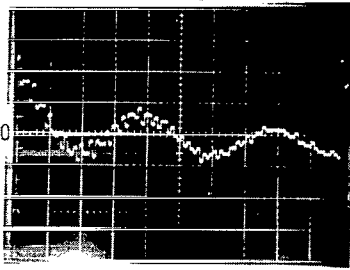


(d) 15D7.

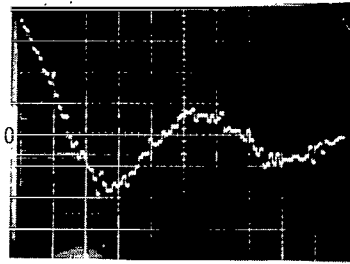


(h) 19D15.

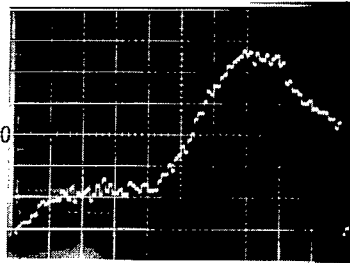
Figure 44.- Crosscorrelations and autocorrelations with respect
L-77-156
to transducer 15.



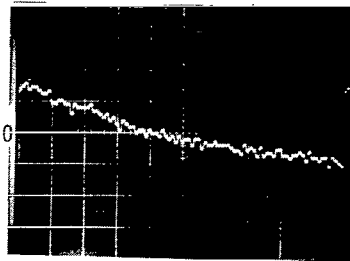
(a) 20D20.



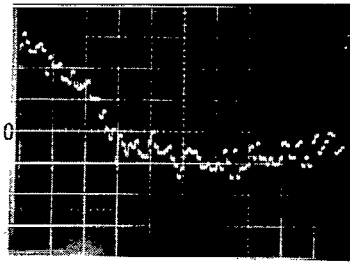
(e) 2D2.



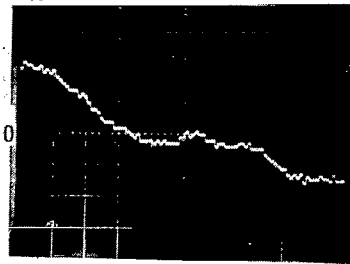
(b) 20D3.



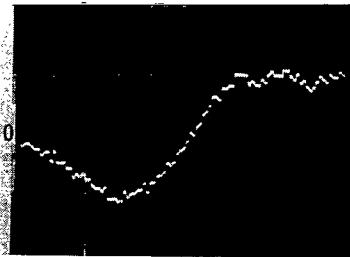
(f) 7D2.



(c) 7D20.



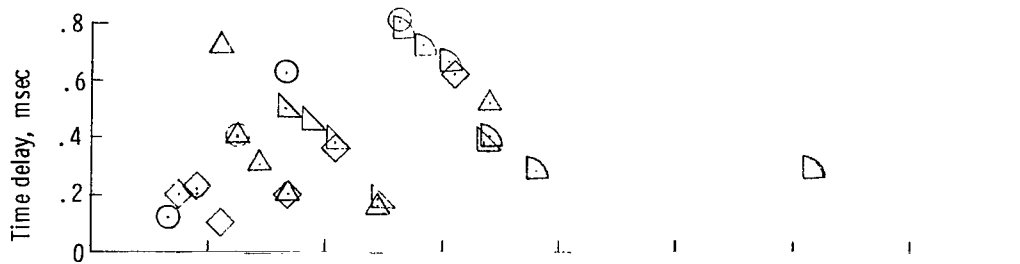
(g) 2D7.



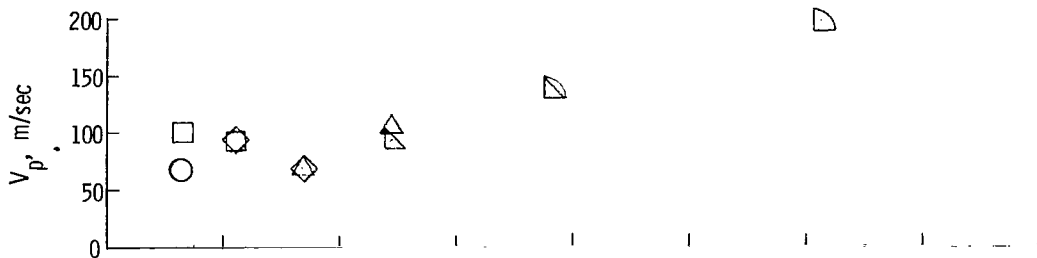
(d) 20D7.

L-77-157

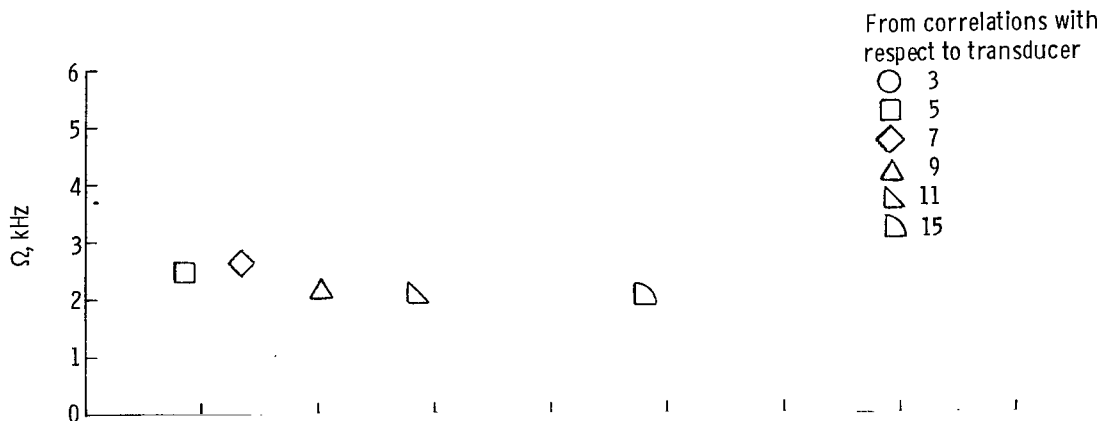
Figure 45.- Crosscorrelations and autocorrelations with respect
to transducers 2 and 20.



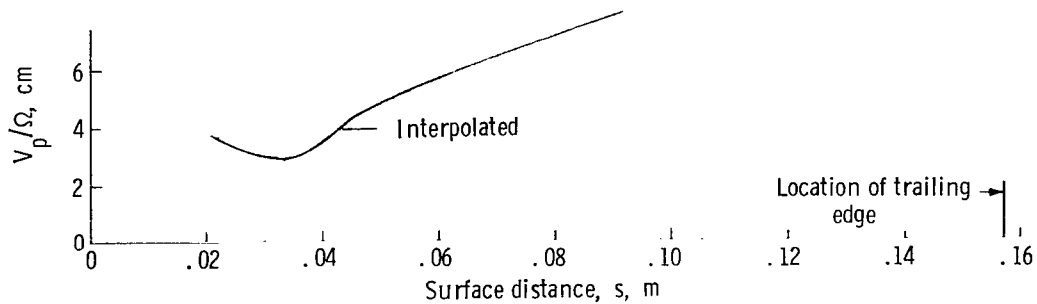
(a) Measured delay times between various pairs of transducers.



(b) Pressure pulse velocity found from delay times of adjacent transducers.



(c) Frequency of pressure pulse passage found from autocorrelations.



(d) Spacing of pressure pulses from ratio of V_p to Ω .

Figure 46.- Correlation summary from online measurement of first positive correlation peak.

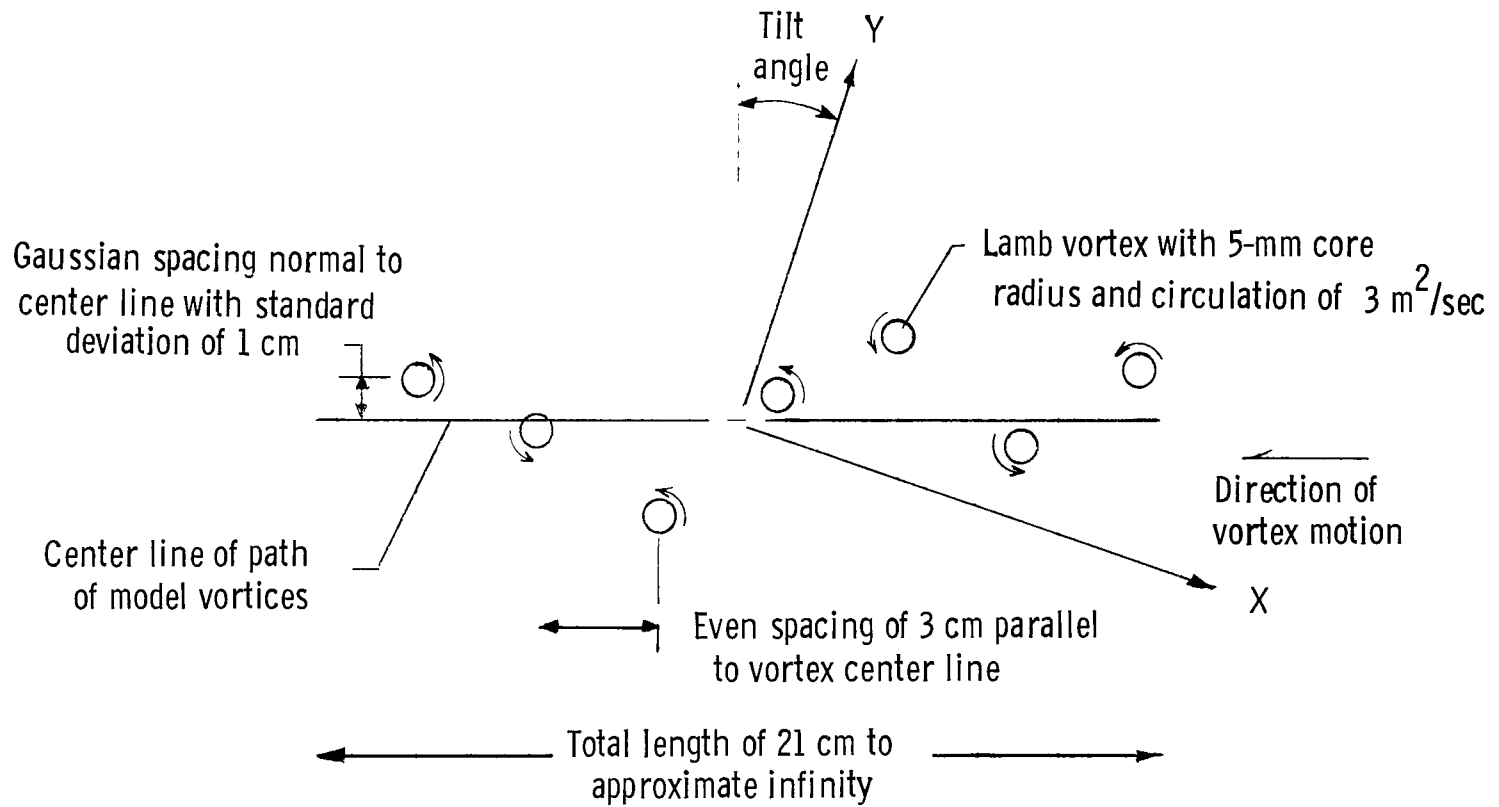


Figure 47.- Model of vortex stream used to generate simulated histograms.

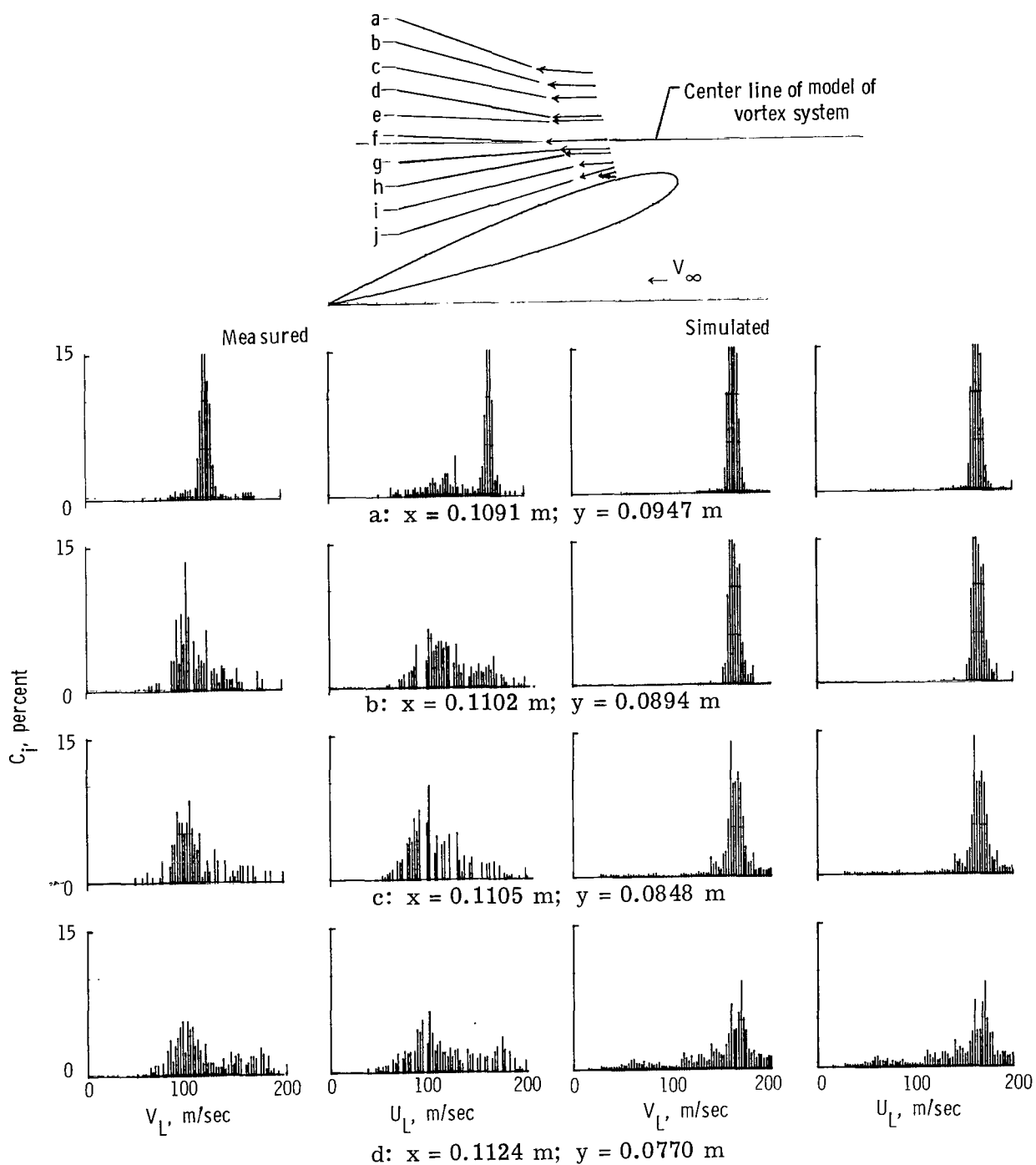


Figure 48.- Measured (left 2 columns) and simulated (right 2 columns) histograms above transducer 7.

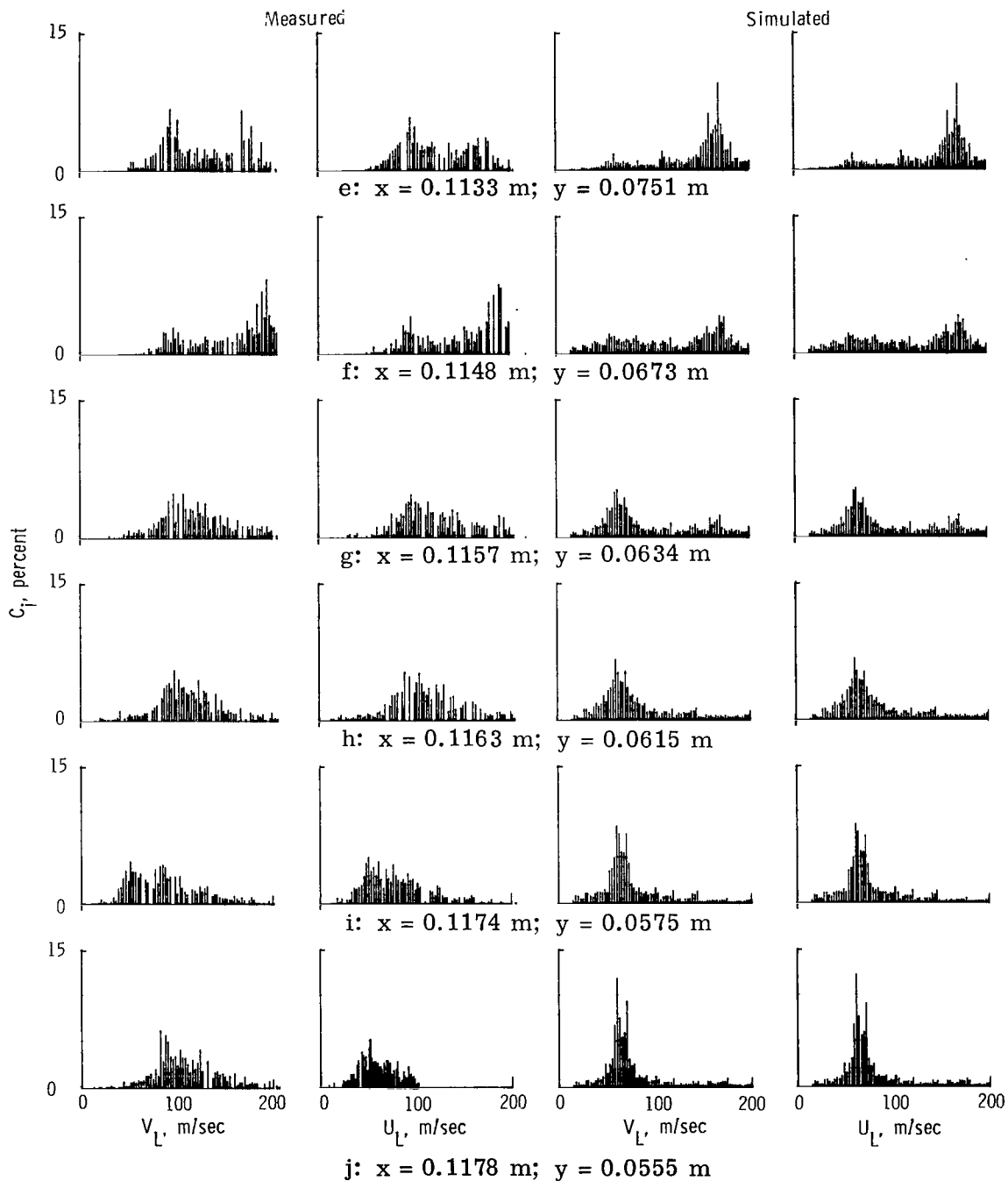


Figure 48.- Measured (left 2 columns) and simulated (right 2 columns) histograms above transducer 7. Concluded.

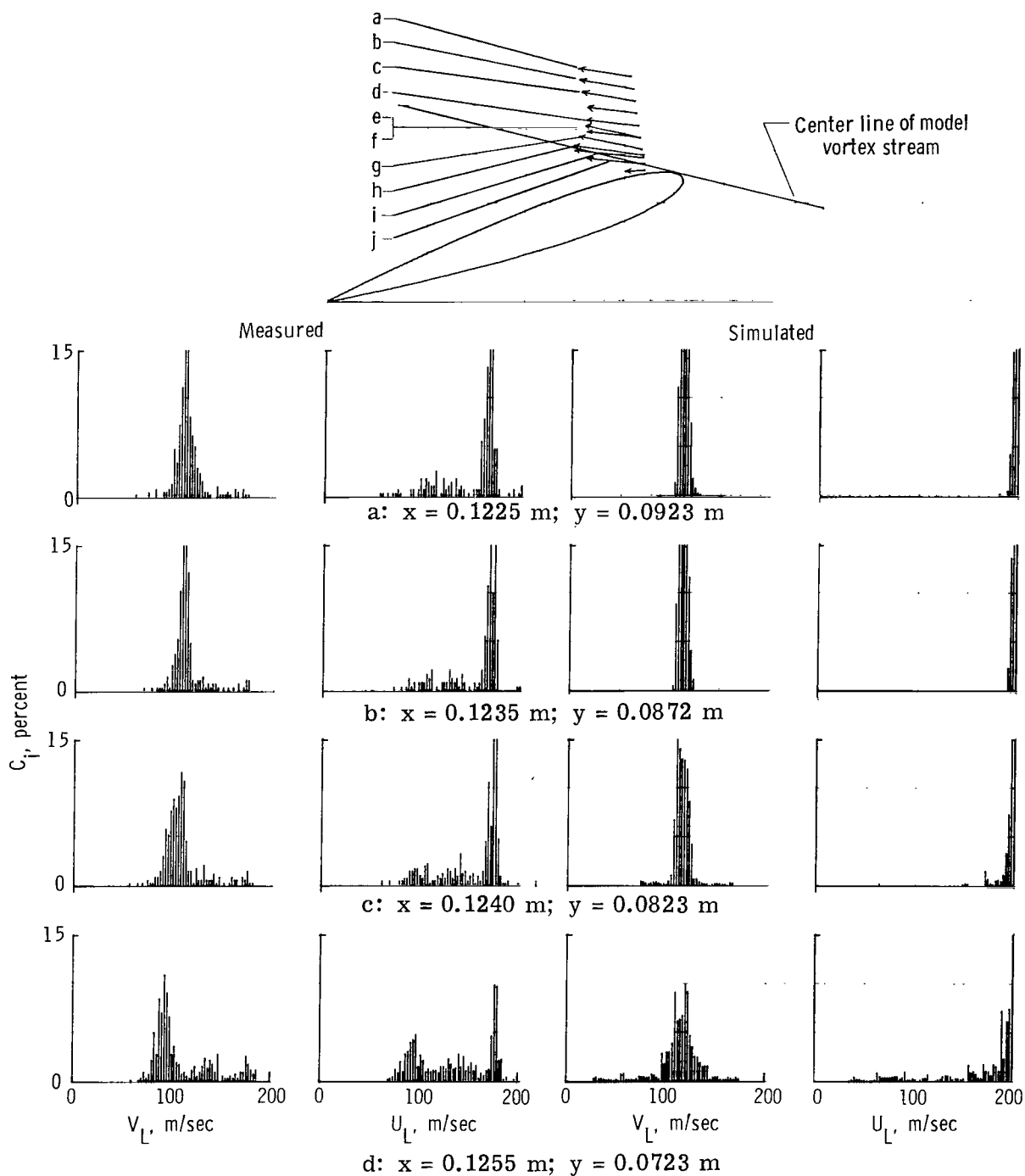


Figure 49.- Measured (left 2 columns) and simulated (right 2 columns) histograms above transducer 5.

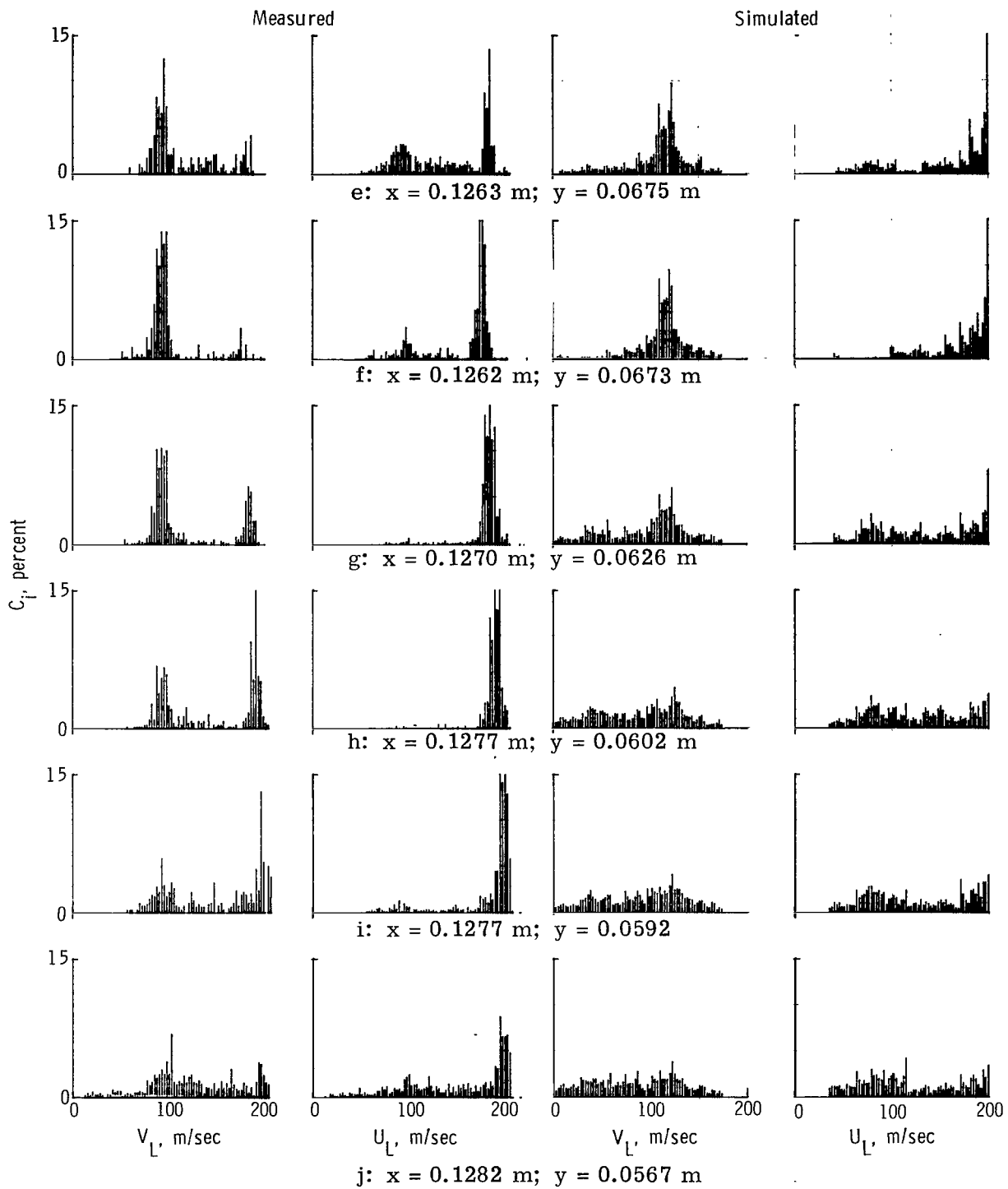


Figure 49.- Measured (left 2 columns) and simulated (right 2 columns) histograms above transducer 5. Concluded.

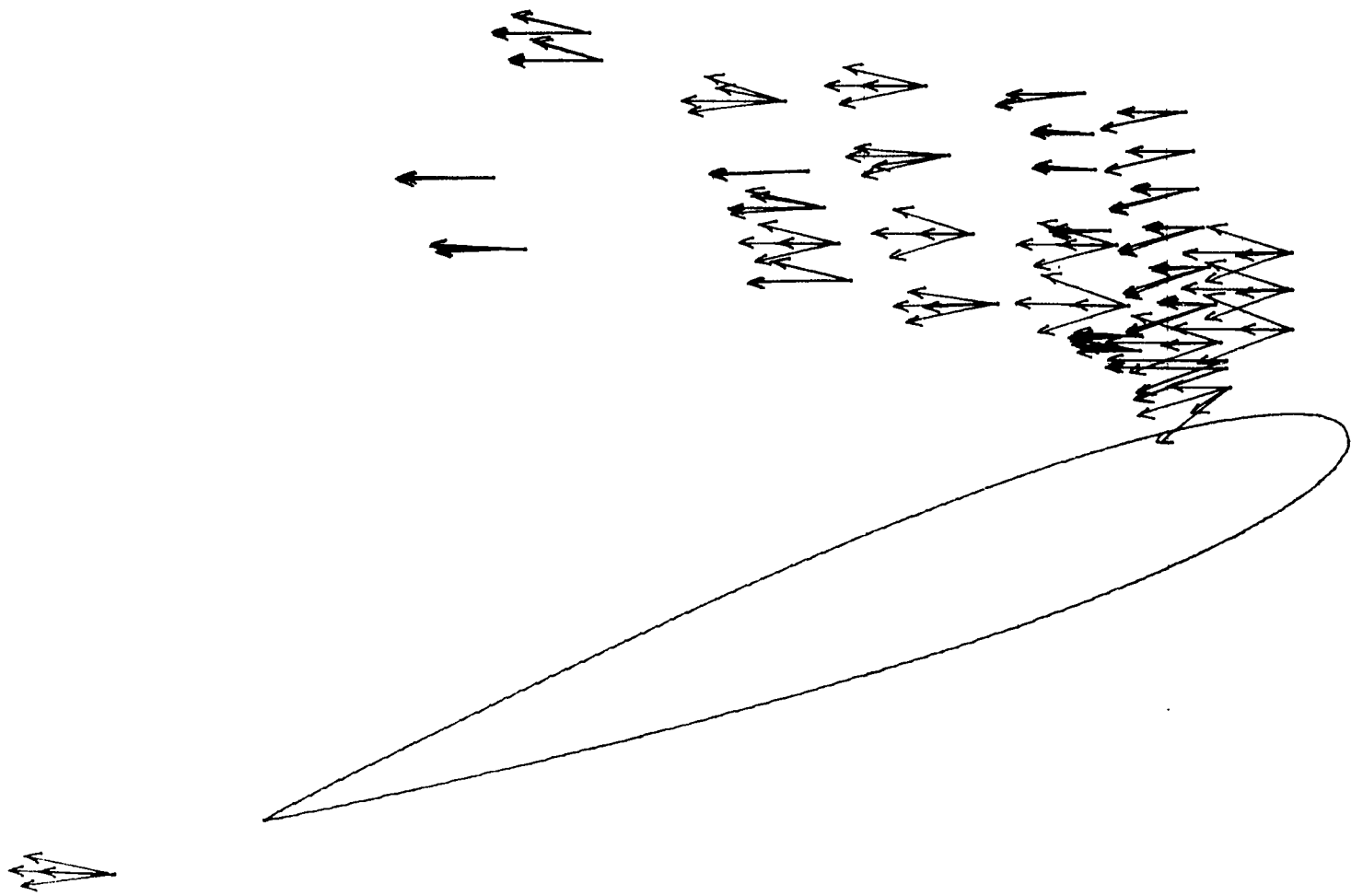


Figure 50. - Possible velocity vectors resulting from combinations of mode 1 and mode 2 velocities.

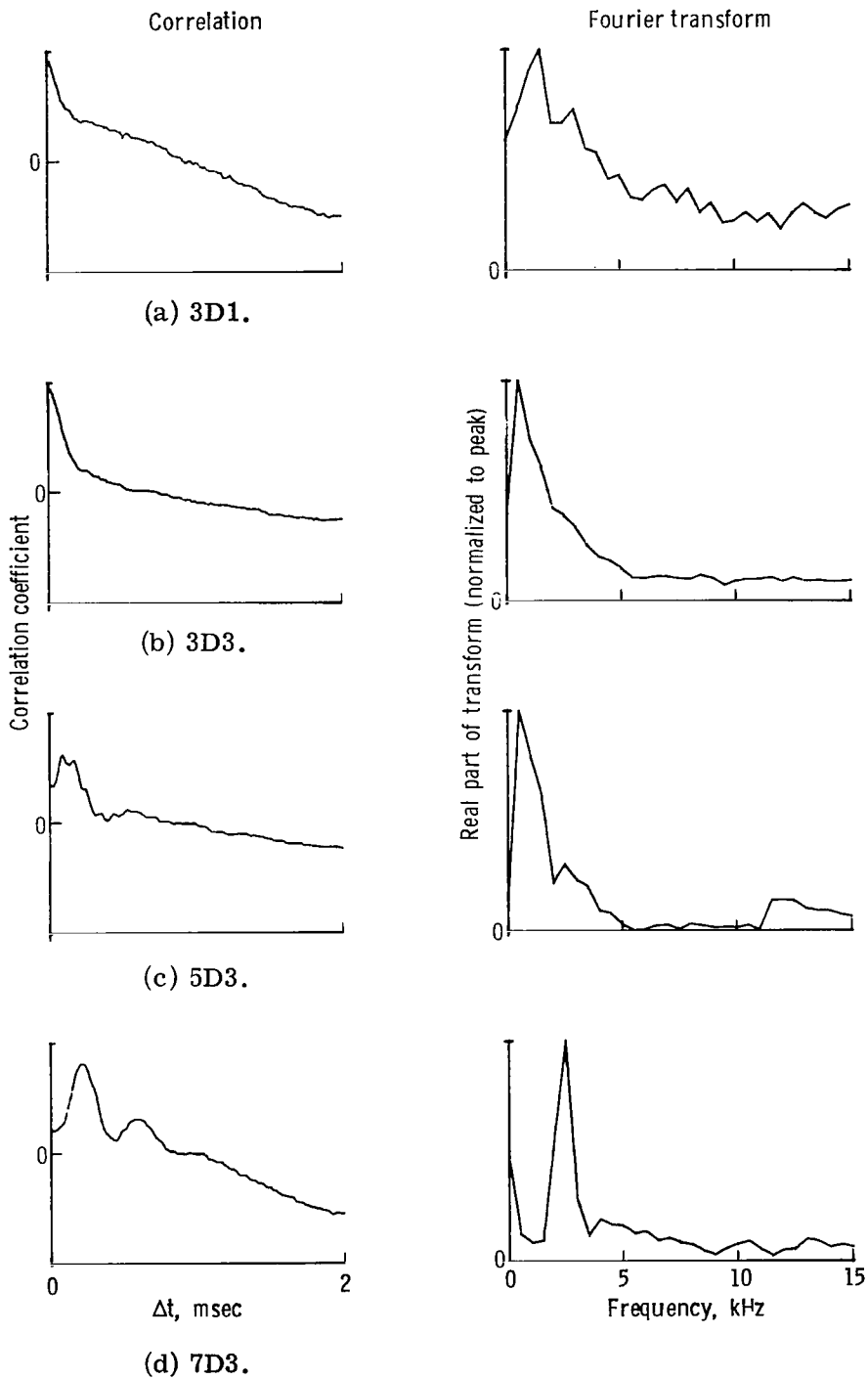


Figure 51.- Correlations and Fourier transforms of correlations for pressure at transducer 3.

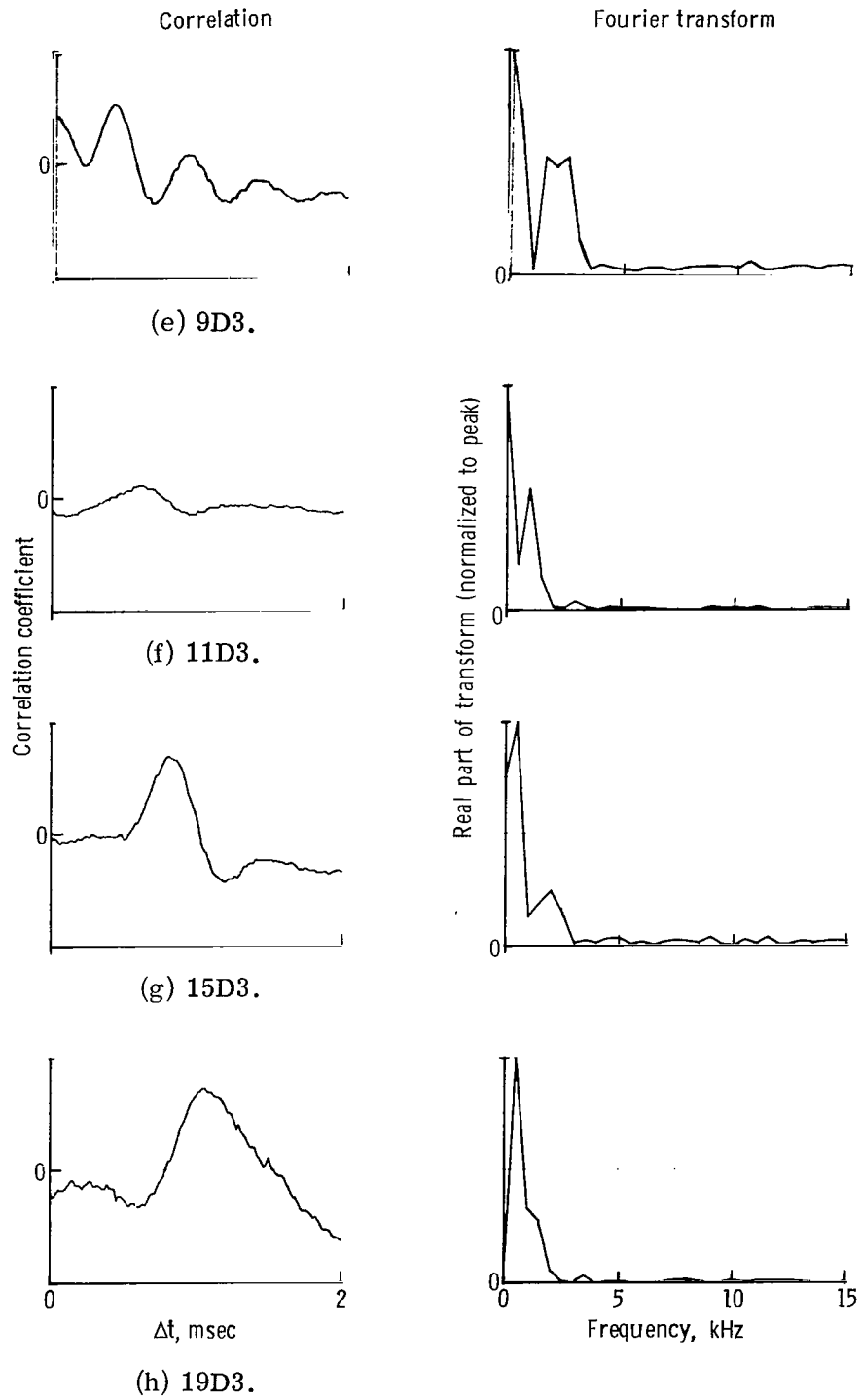


Figure 51.- Correlations and Fourier transforms of correlations for pressure at transducer 3. Concluded.

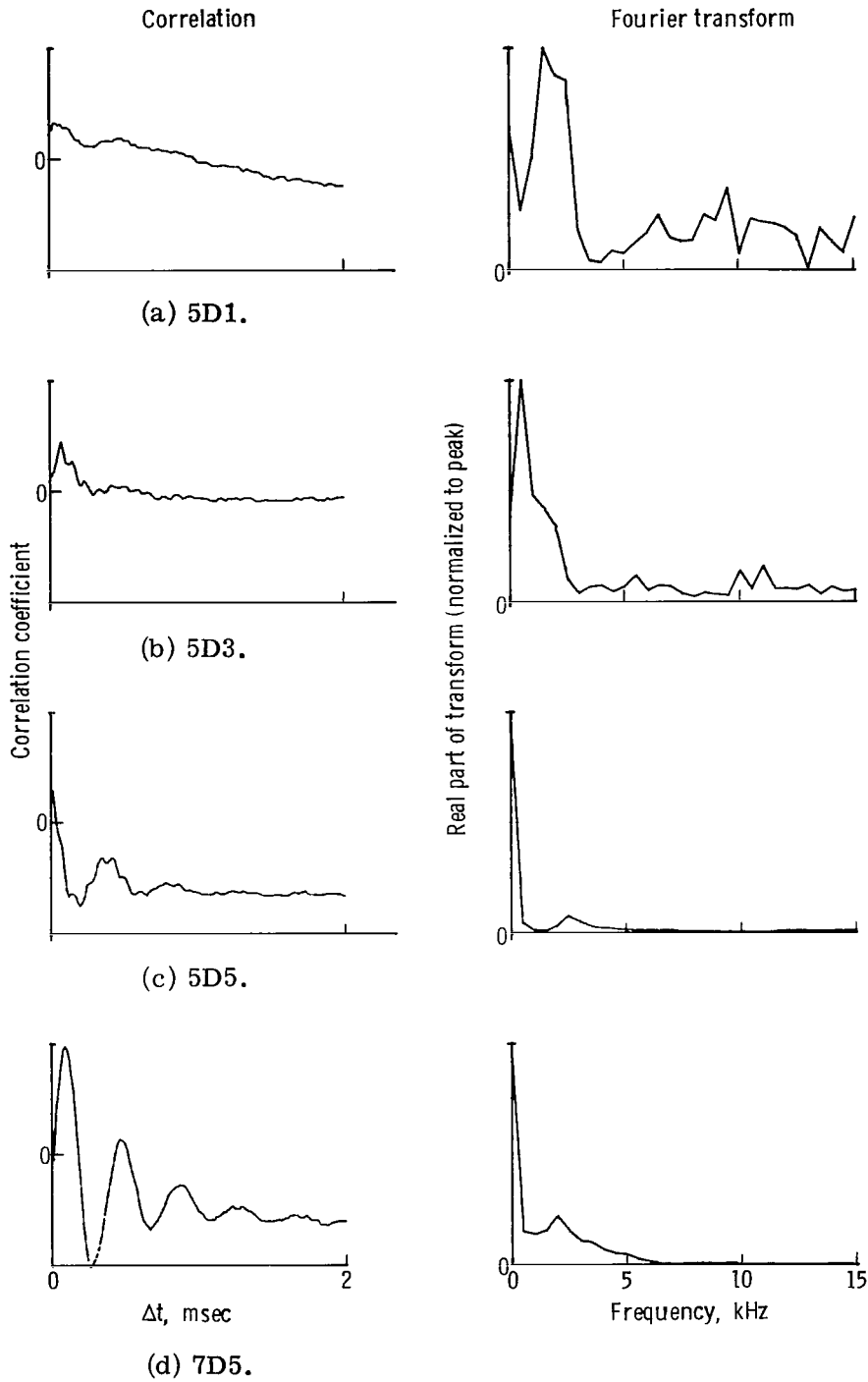


Figure 52.- Correlations and Fourier transforms of correlations for pressure at transducer 5.

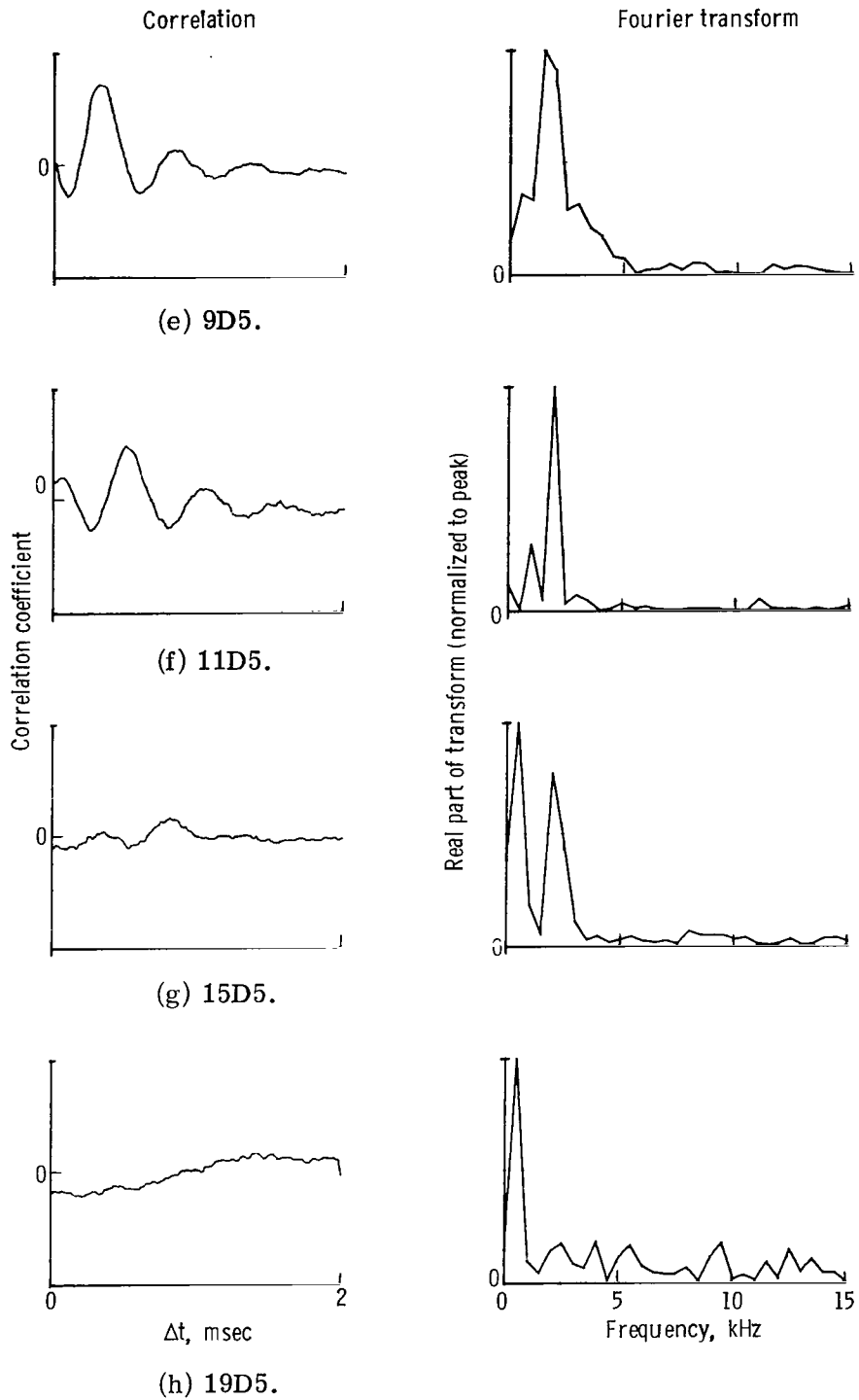


Figure 52.- Correlations and Fourier transforms of correlations for pressure at transducer 5. Concluded.

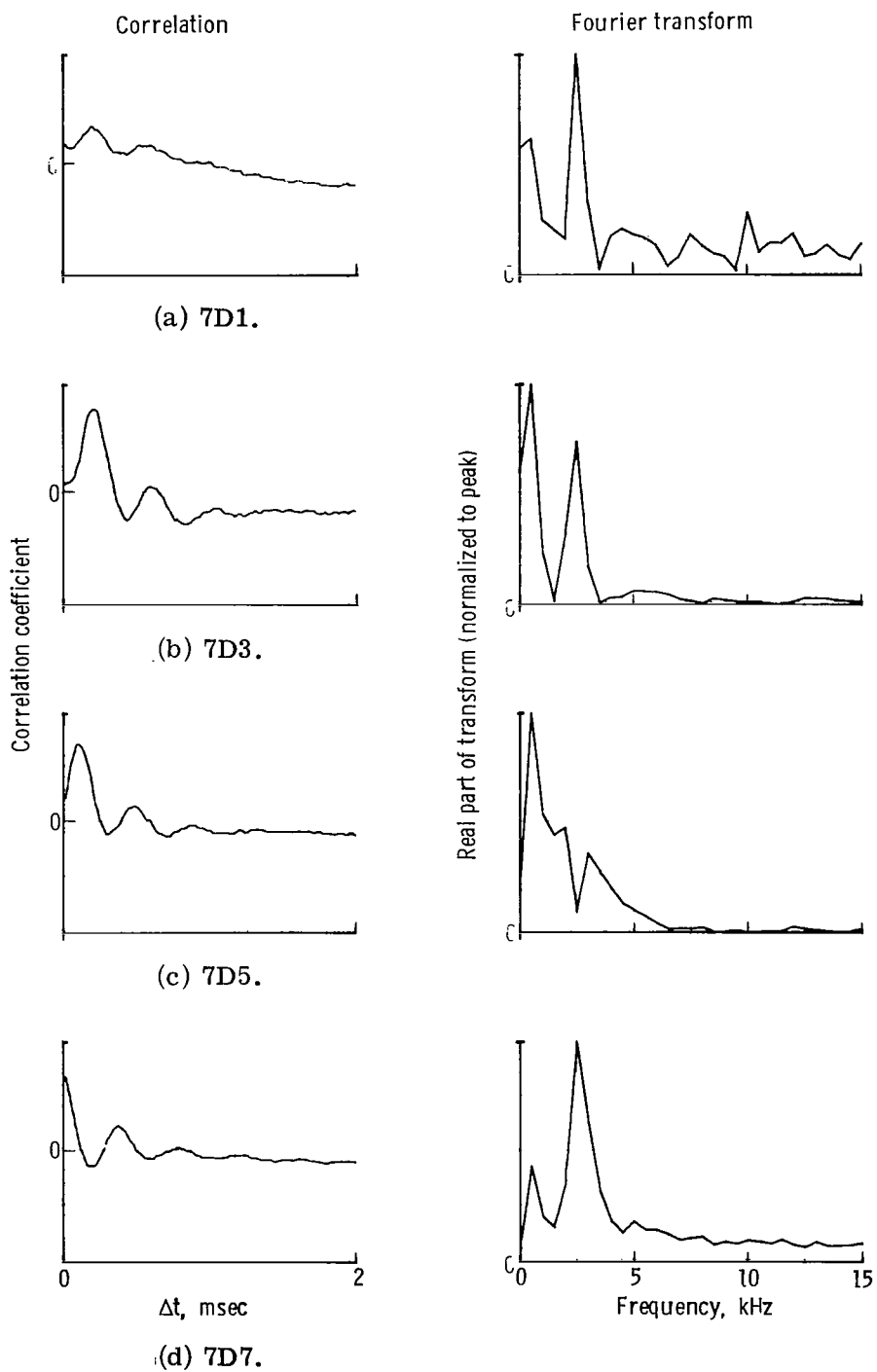


Figure 53.- Correlations and Fourier transforms of correlations for pressure at transducer 7.

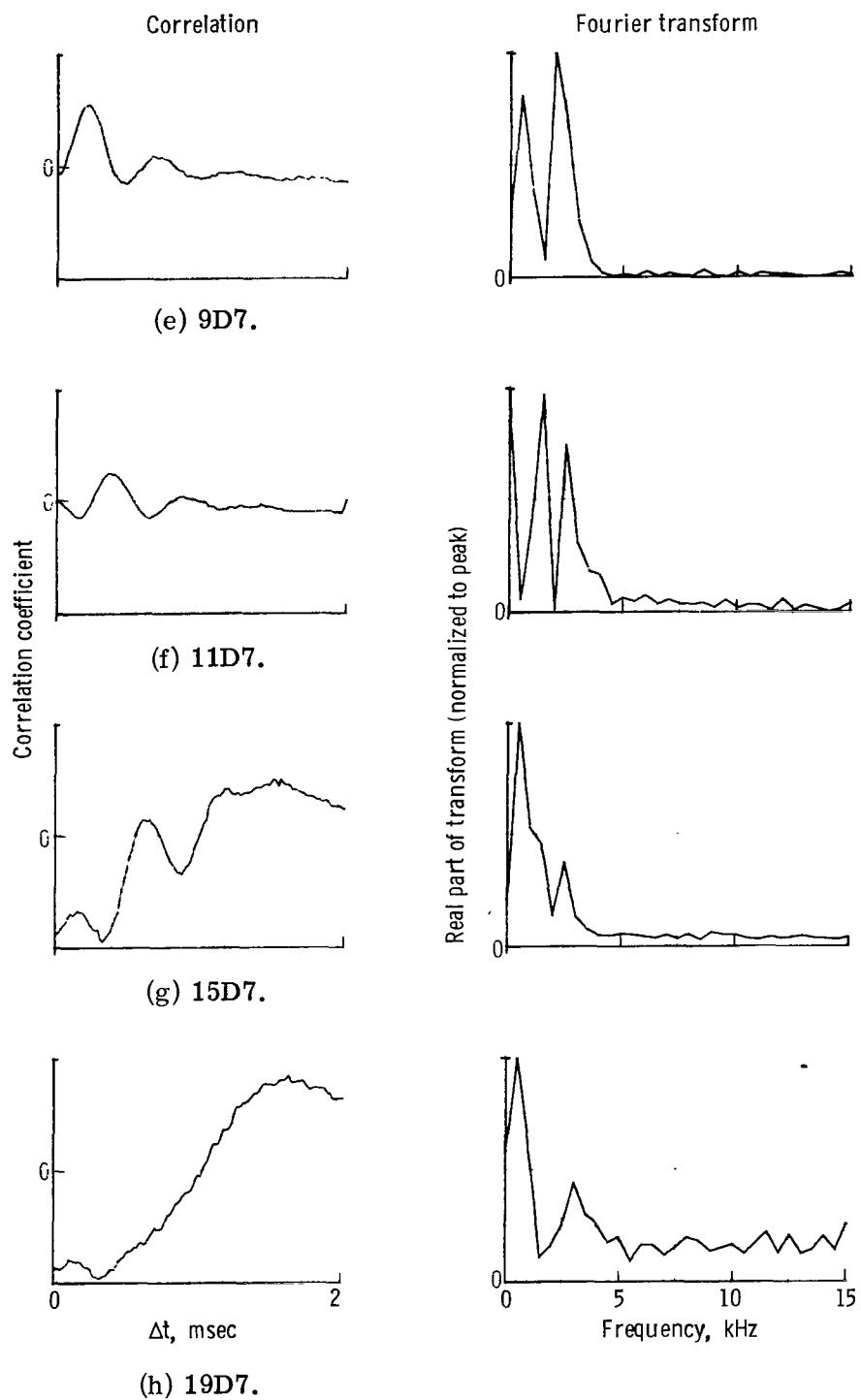


Figure 53.- Correlations and Fourier transforms of correlations for pressure at transducer 7. Concluded.

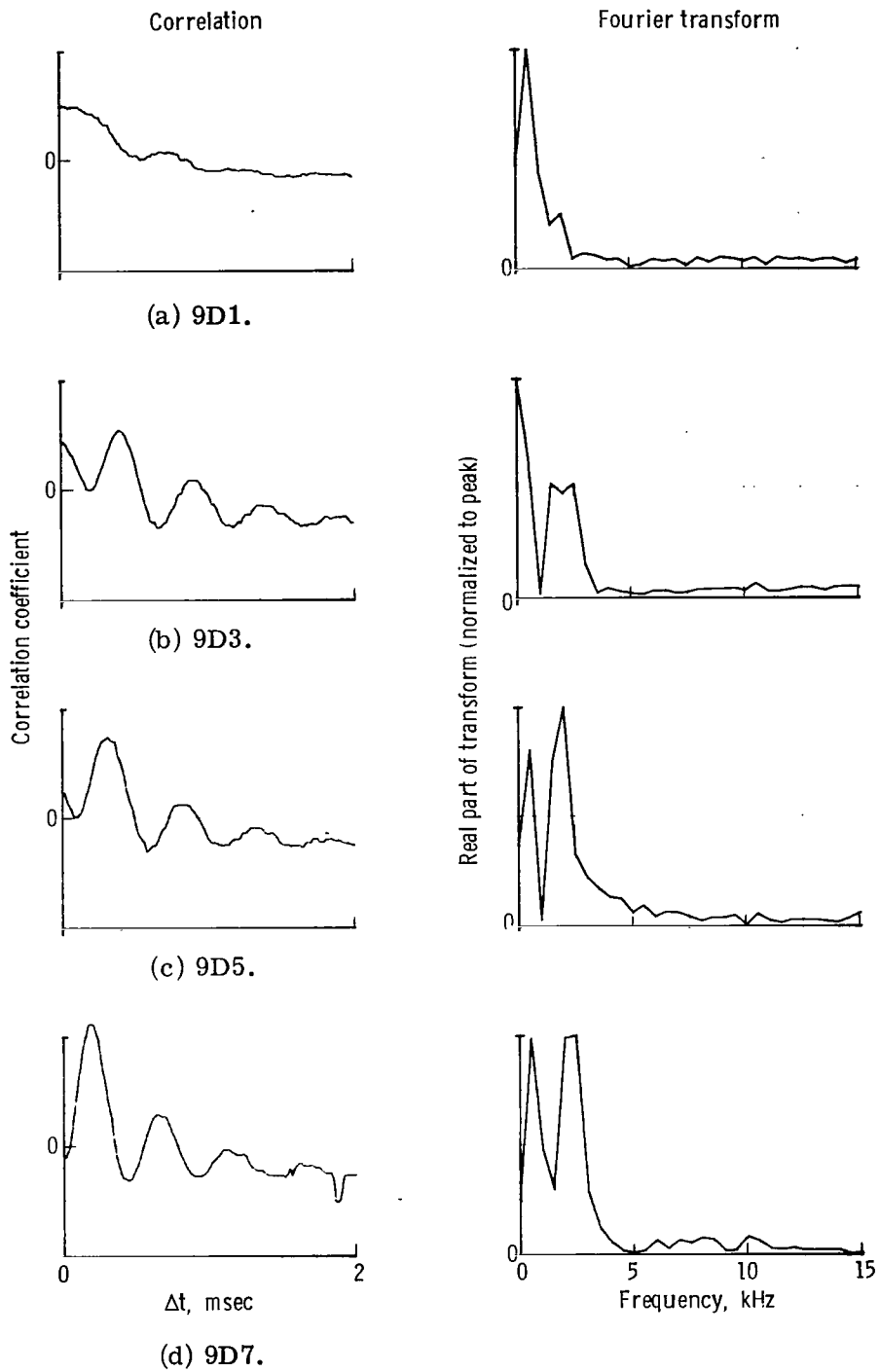


Figure 54.- Correlations and Fourier transforms of correlations for pressure at transducer 9.

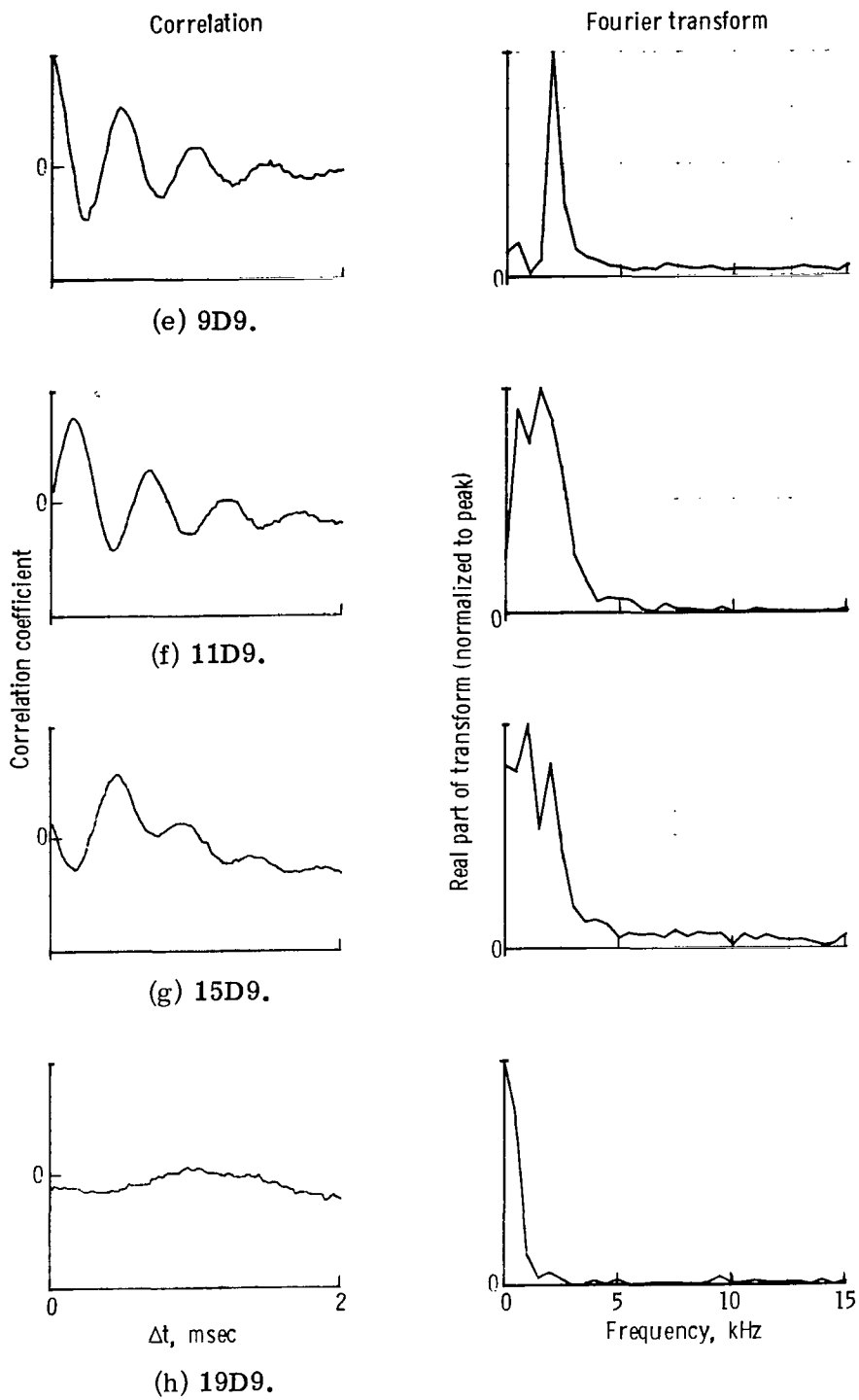


Figure 54.- Correlations and Fourier transforms of correlations for pressure at transducer 9. Concluded.

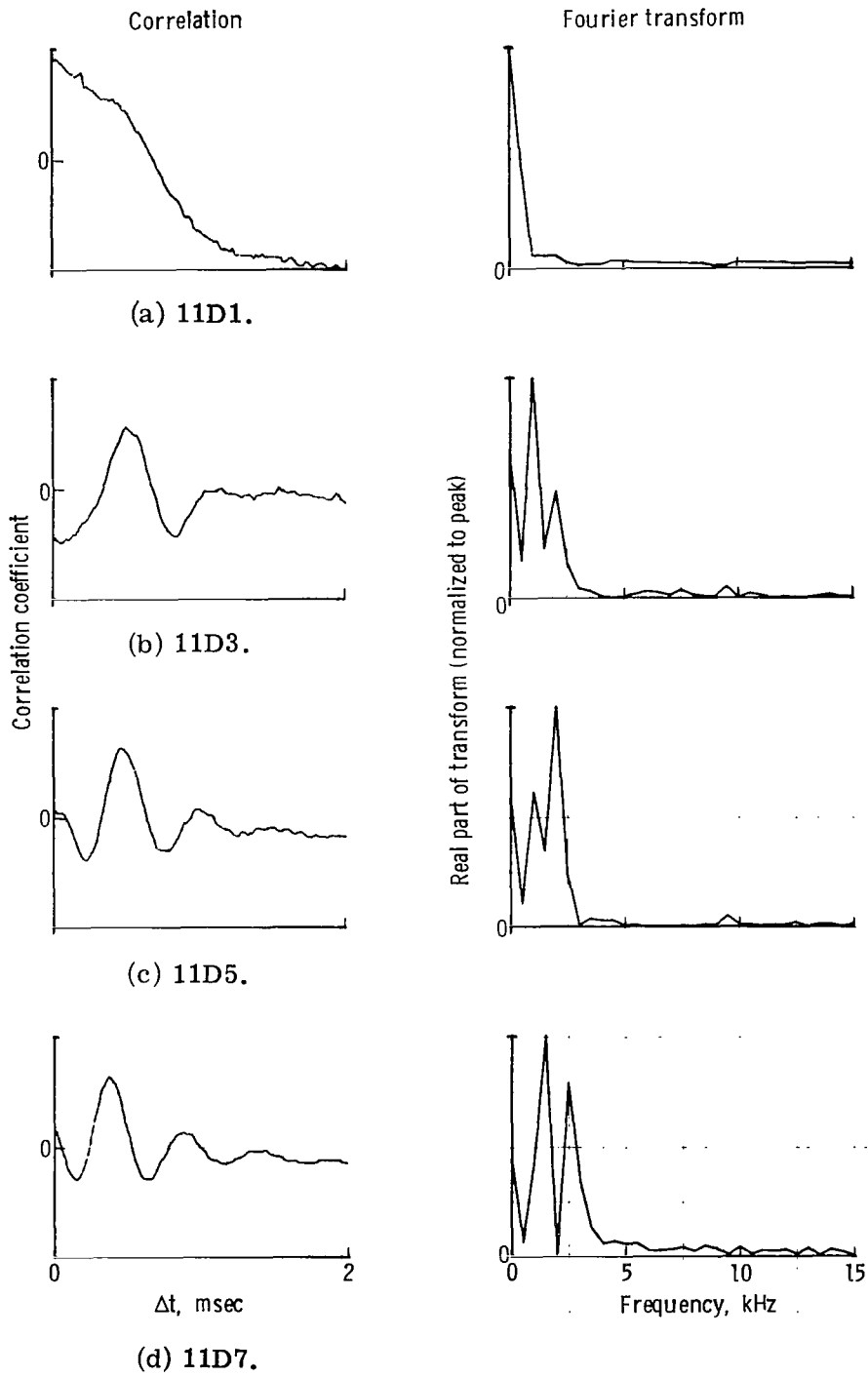


Figure 55.- Correlations and Fourier transforms of correlations for pressure at transducer 11.

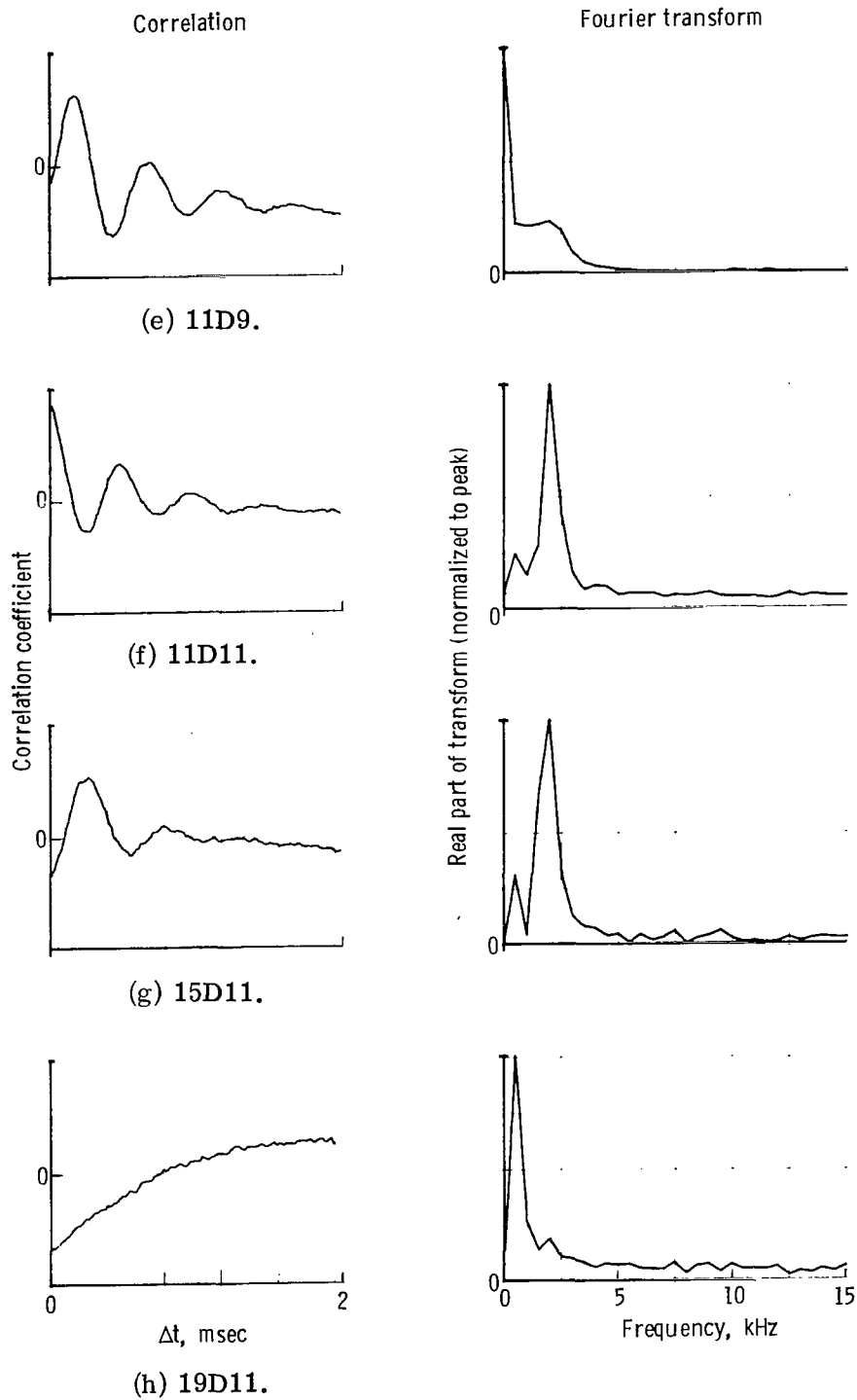


Figure 55.- Correlations and Fourier transforms of correlations for pressure at transducer 11. Concluded.

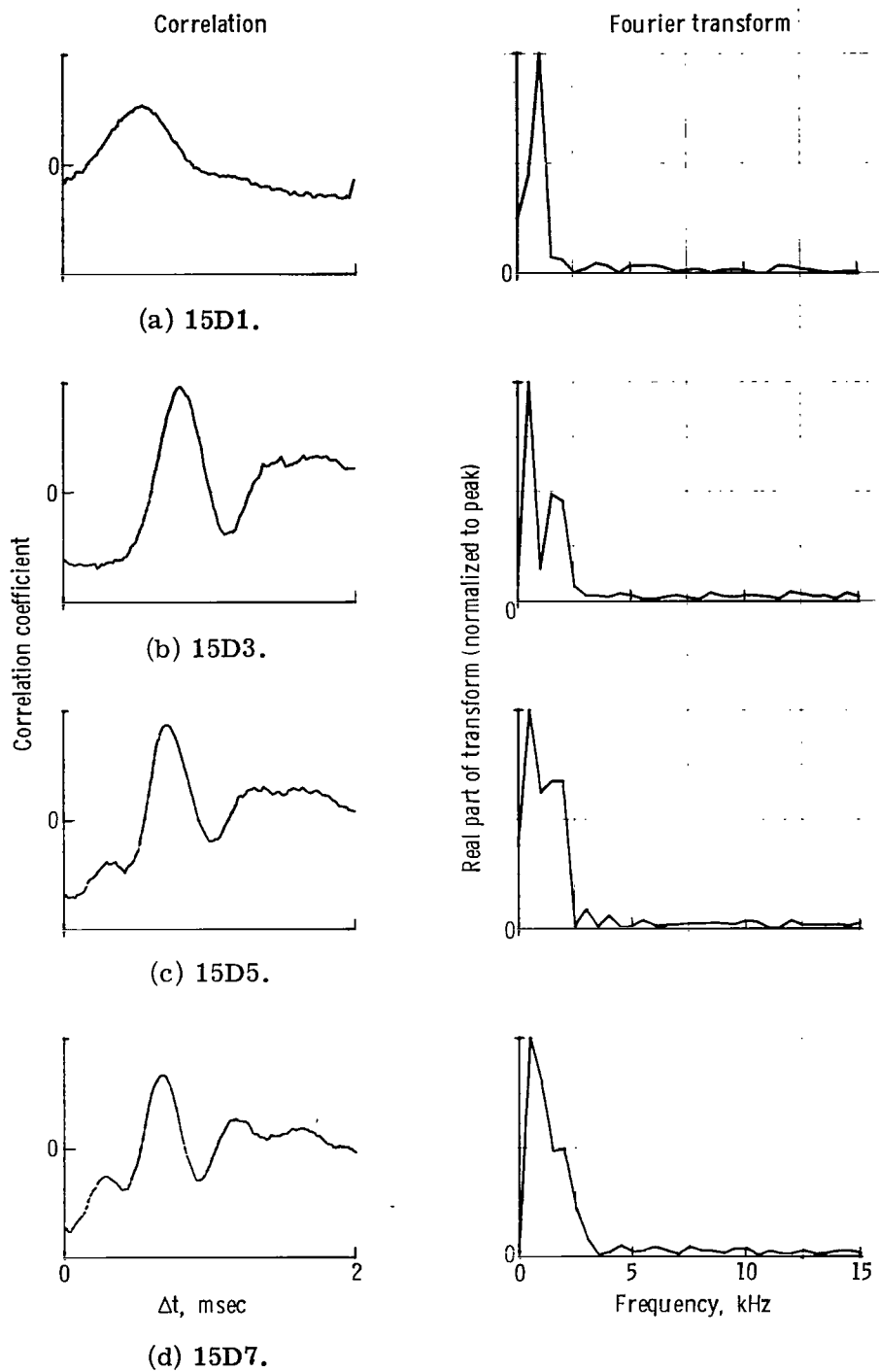


Figure 56.- Correlations and Fourier transforms of correlations for pressure at transducer 15.

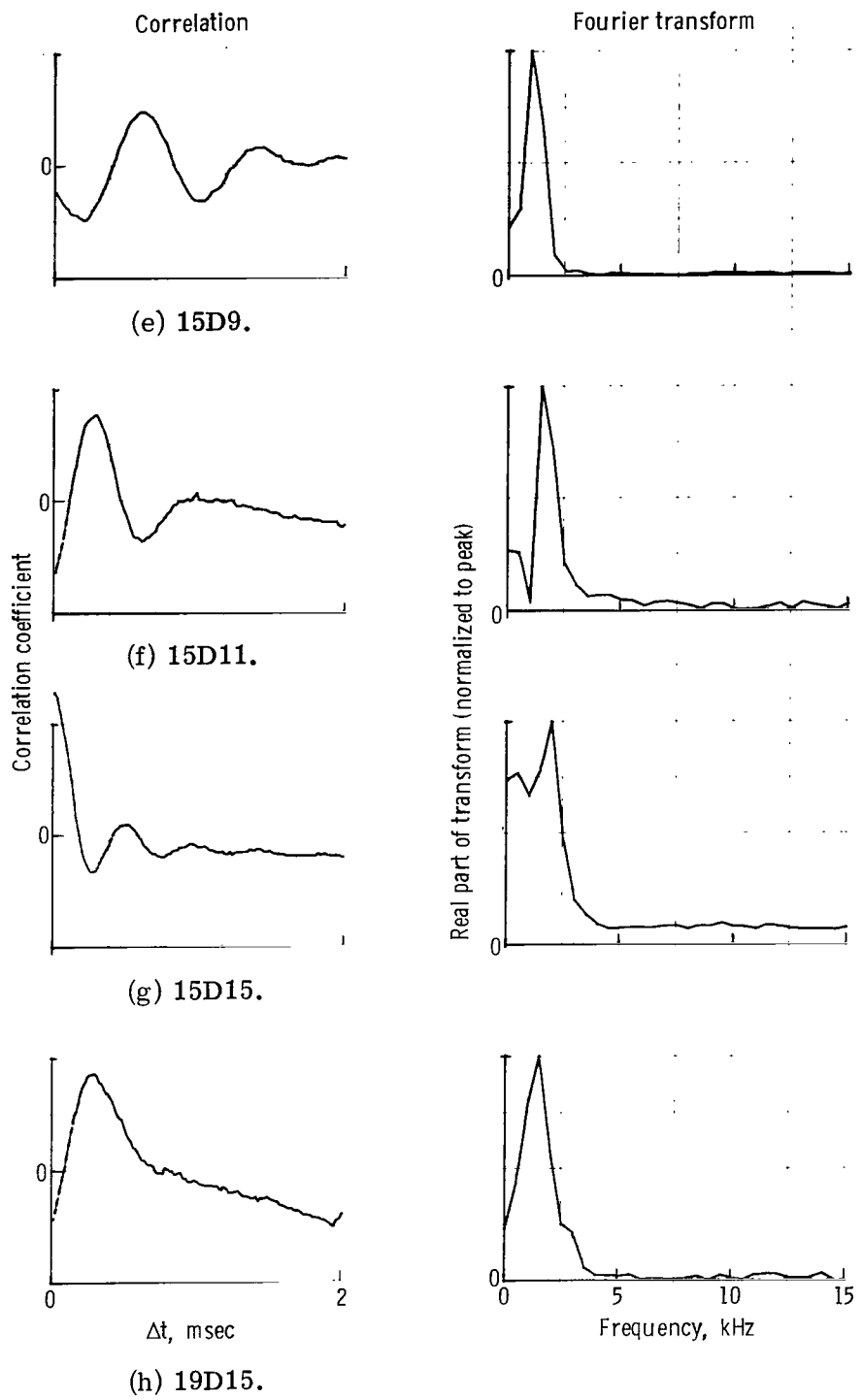


Figure 56.- Correlations and Fourier transforms of correlations for pressure at transducer 15. Concluded.

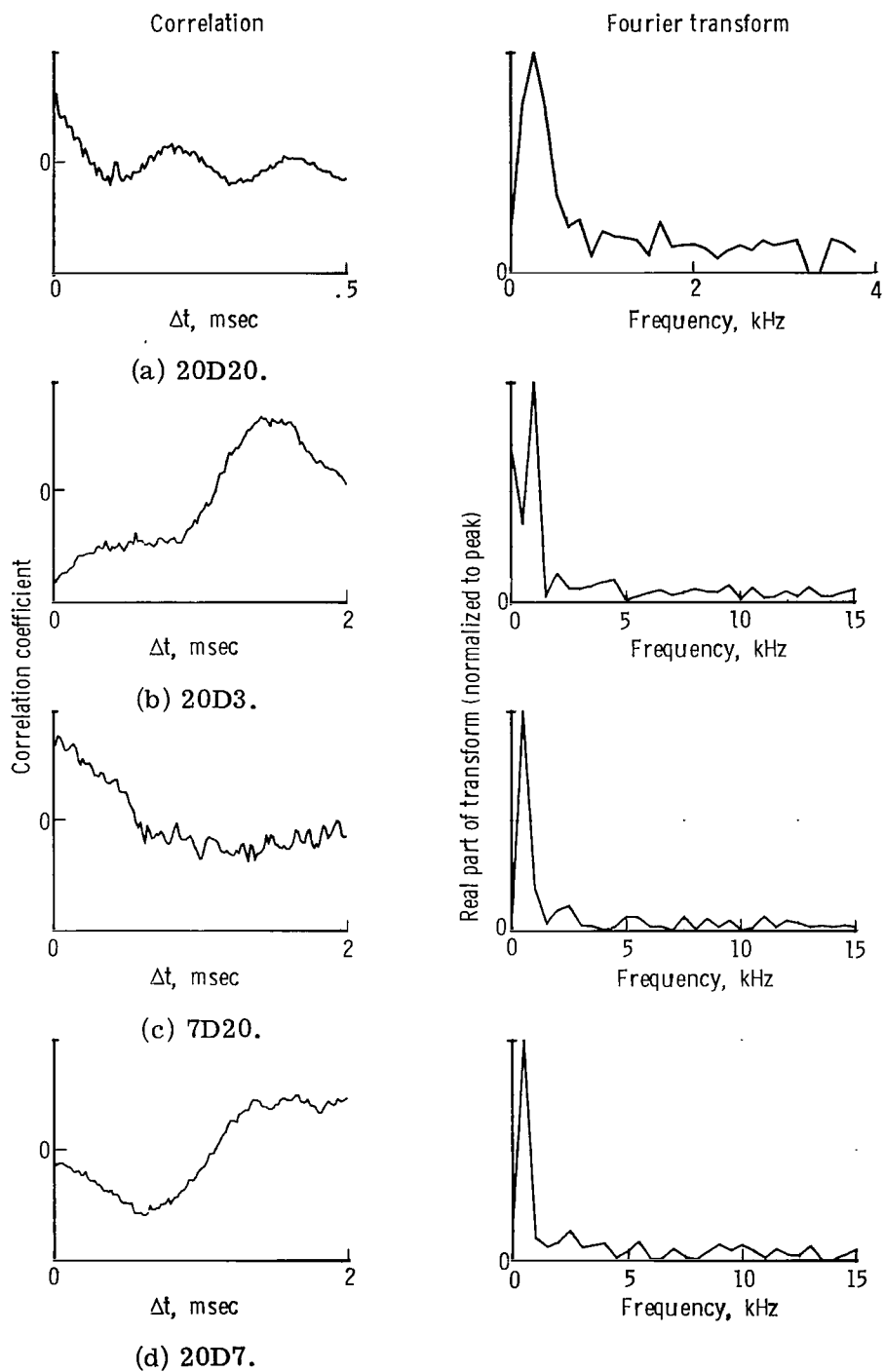


Figure 57.- Correlations and Fourier transforms of correlations for pressure at transducers 20 and 2.

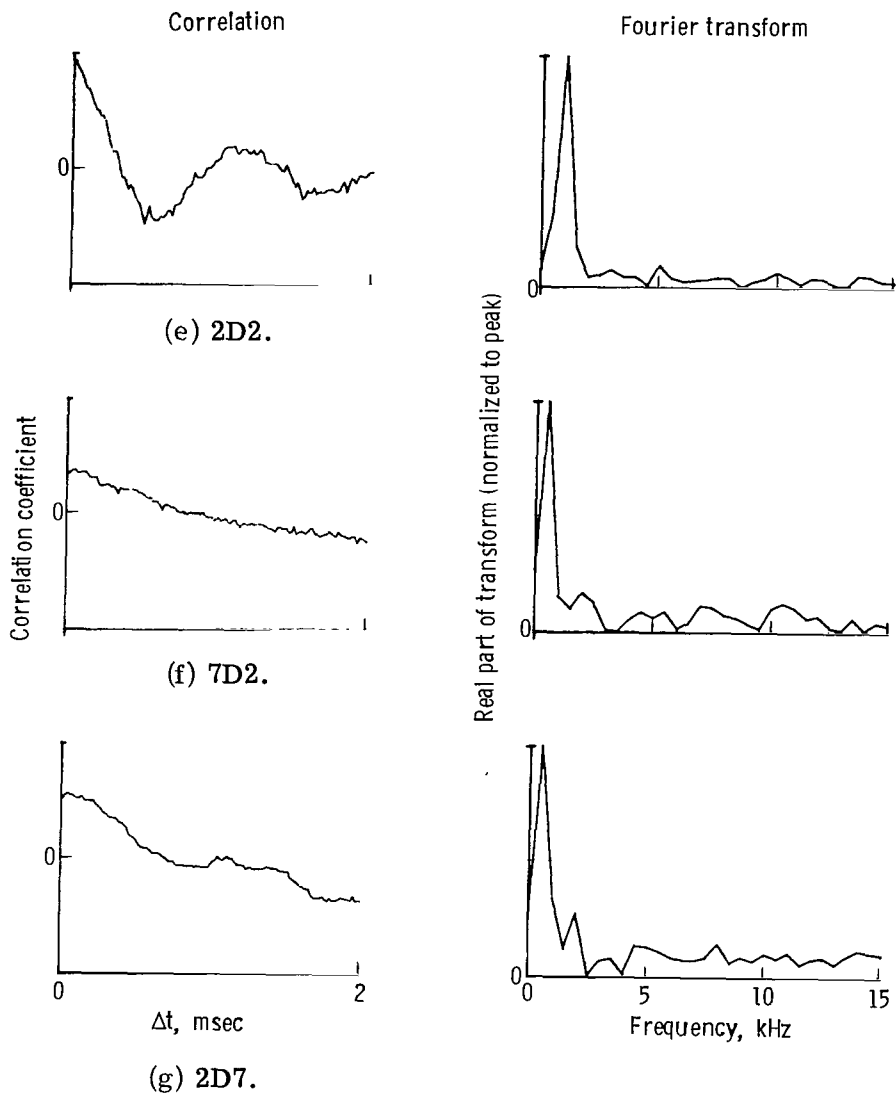
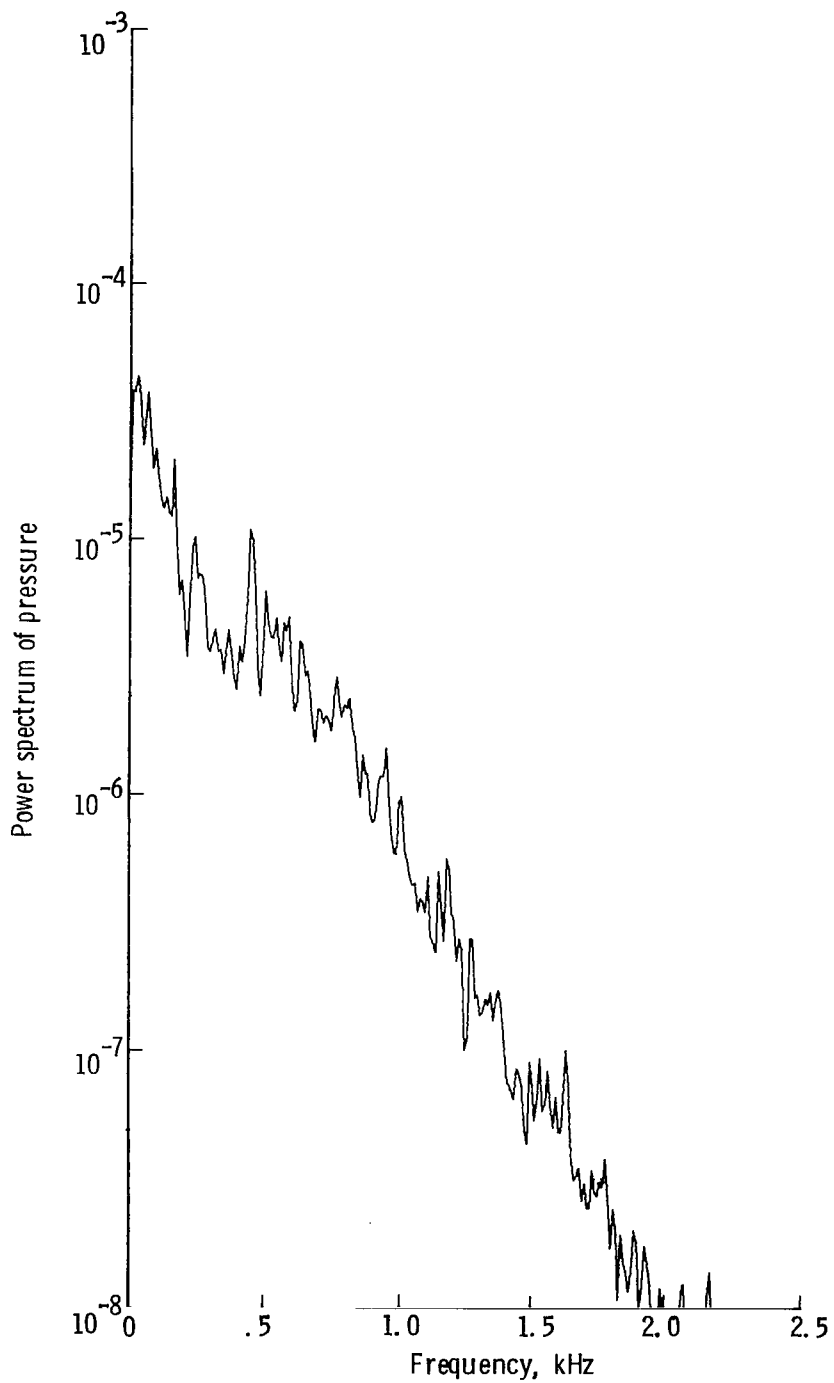
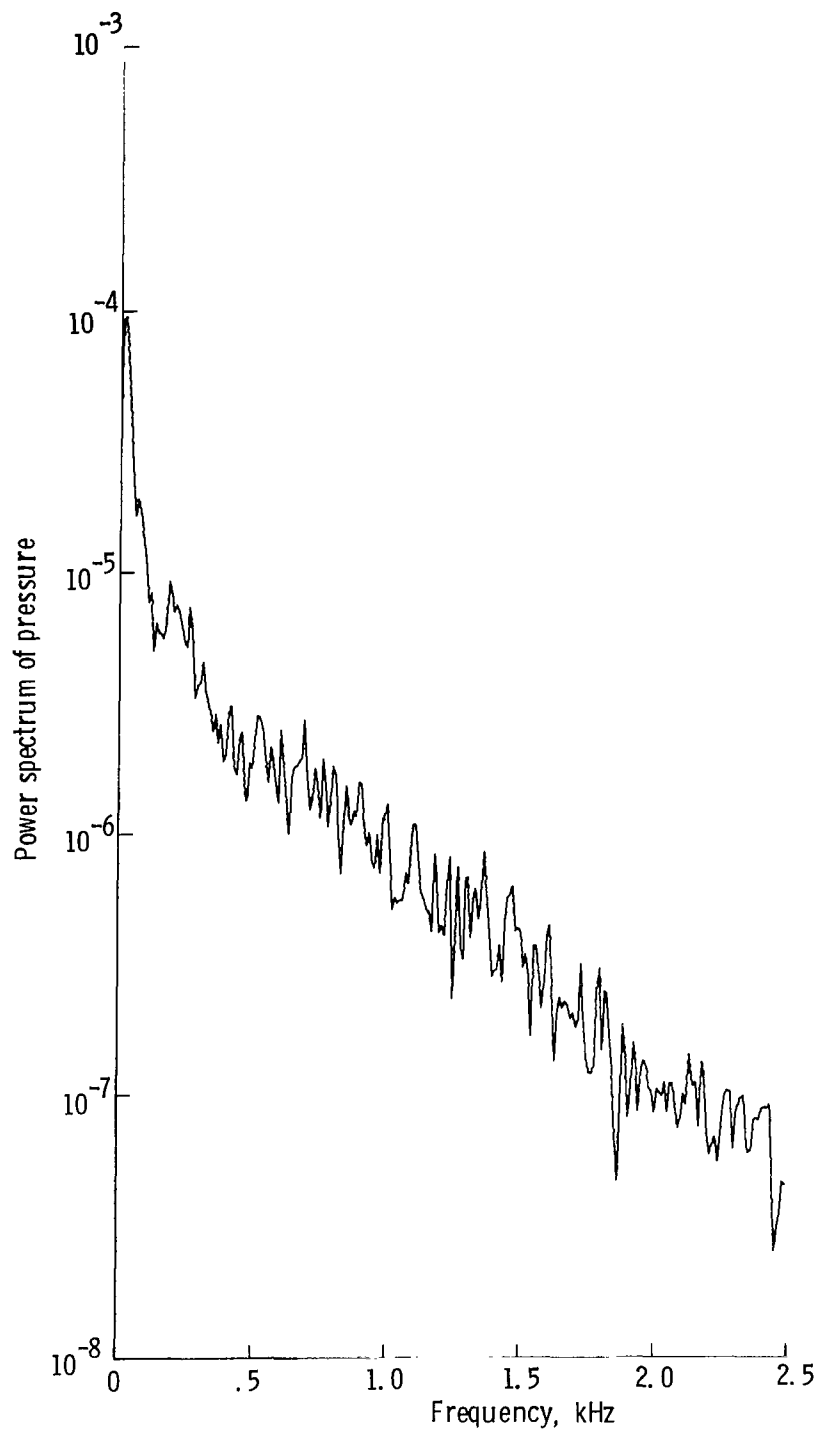


Figure 57. - Correlations and Fourier transforms of correlations for pressure at transducers 20 and 2. Concluded.



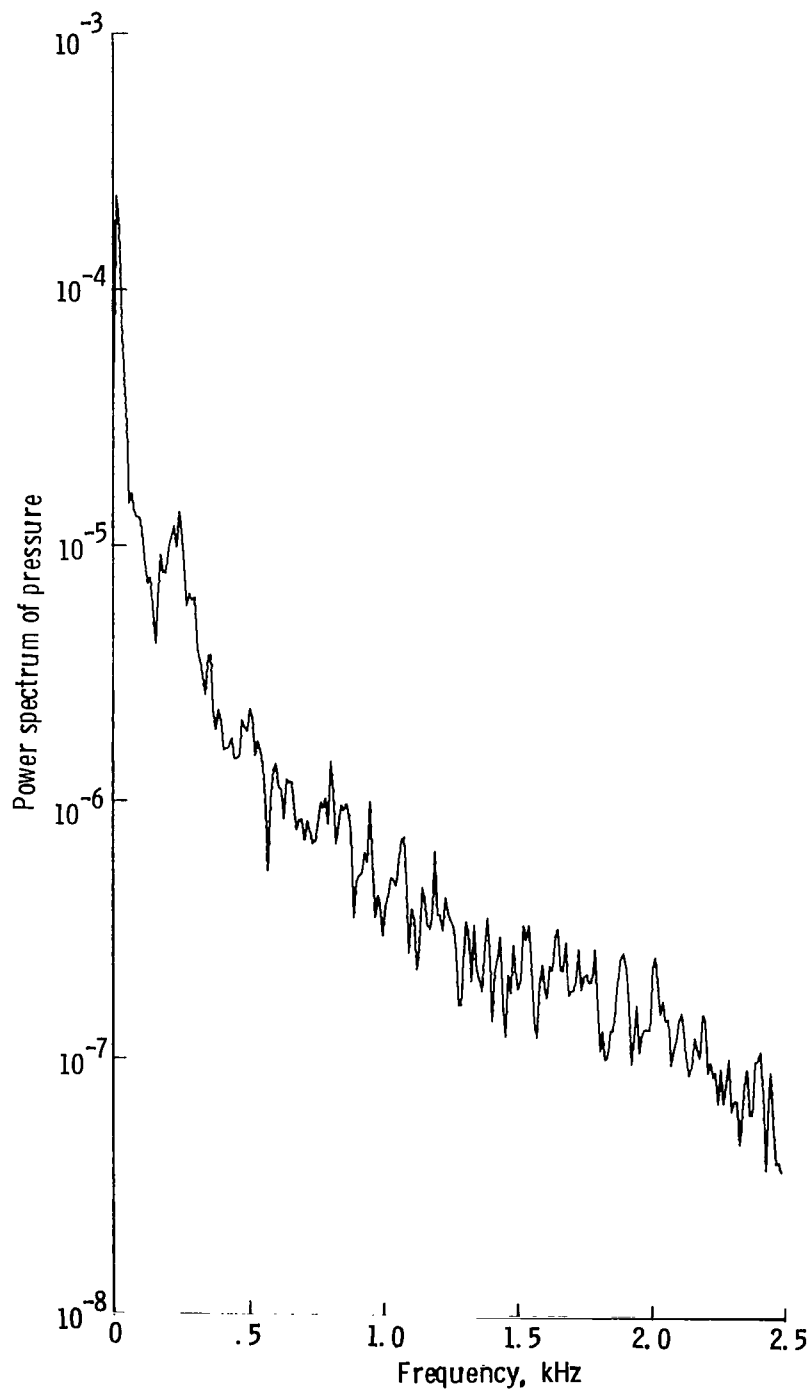
(a) Transducer 1.

Figure 58.- Power spectral density of recorded pressures.



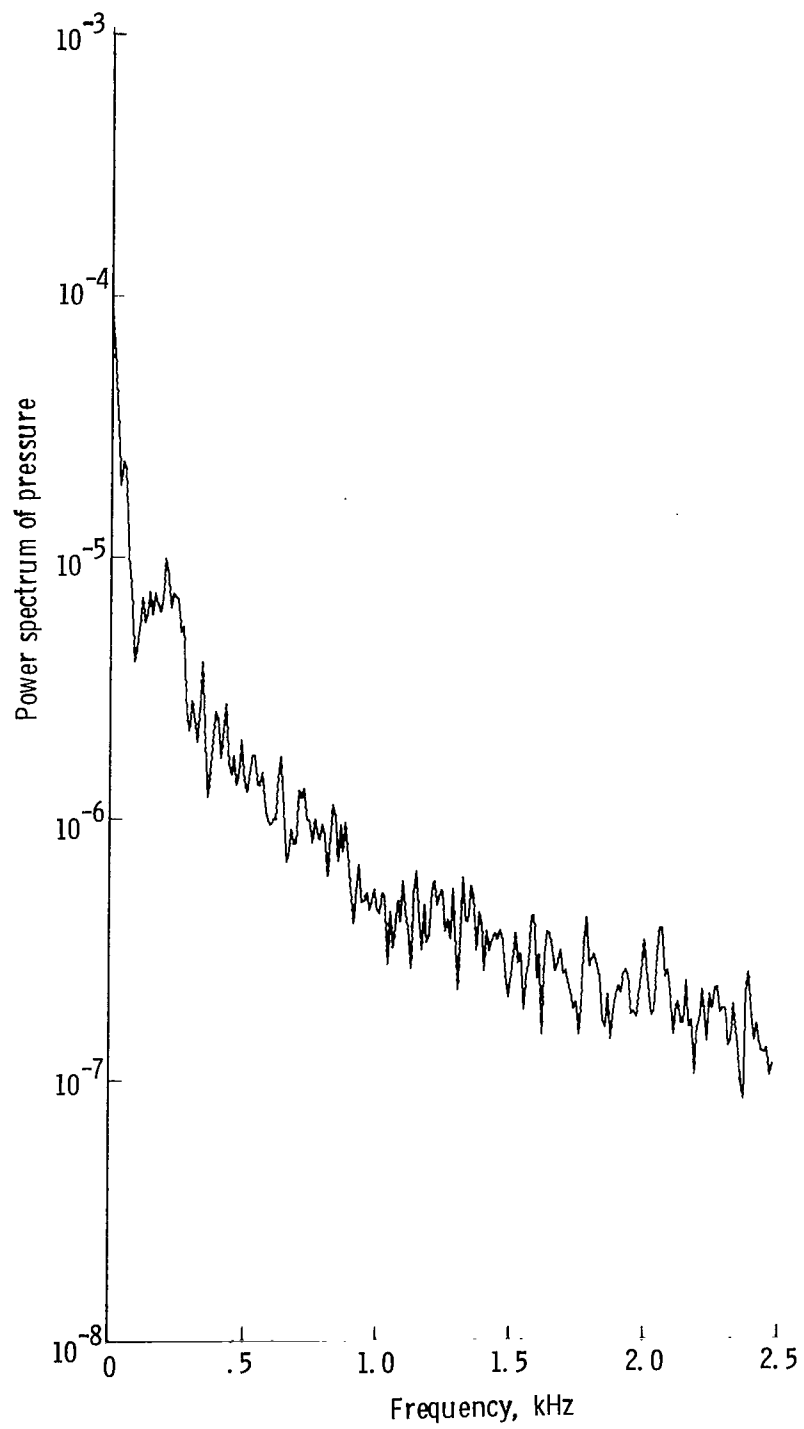
(b) Transducer 3.

Figure 58. - Continued.



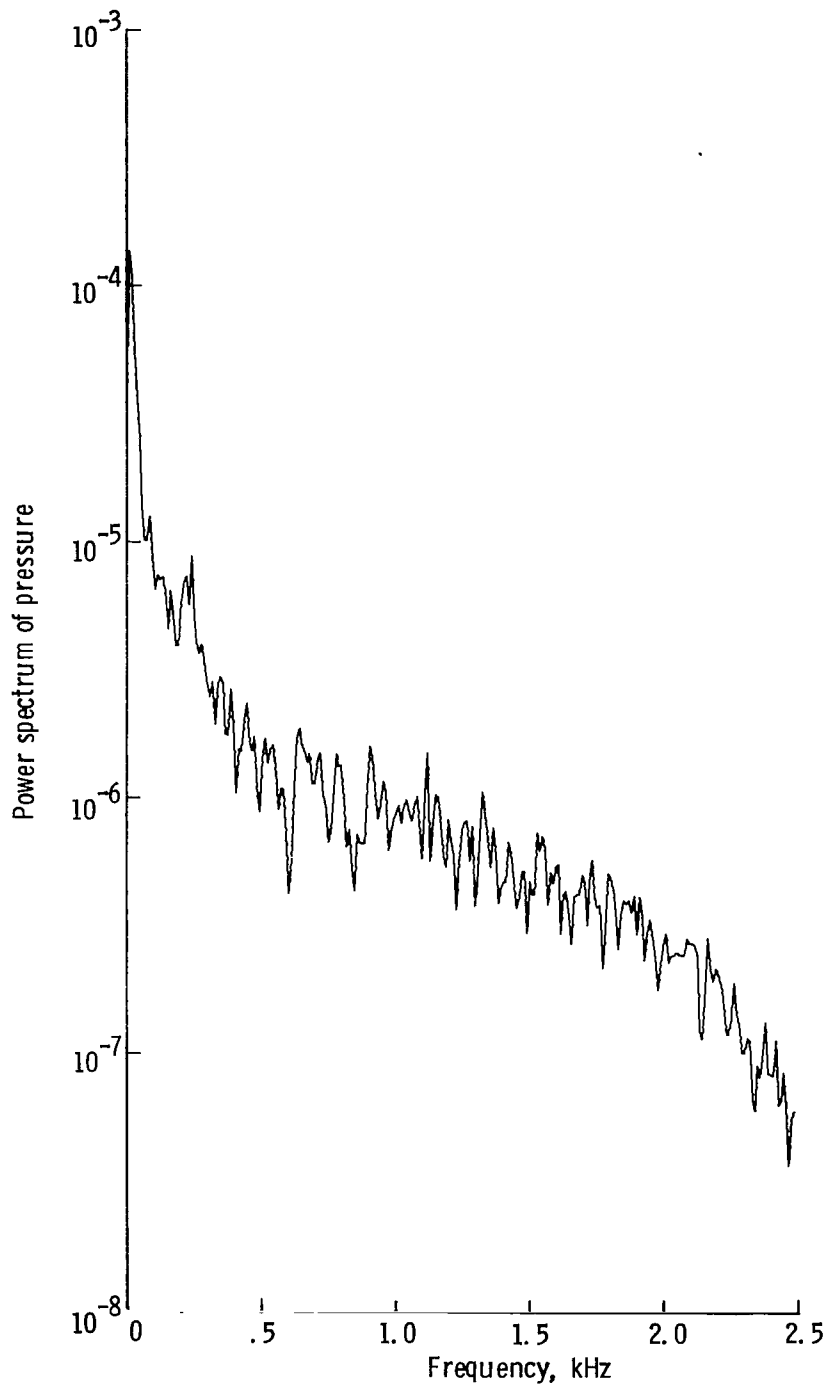
(c) Transducer 5.

Figure 58.- Continued.



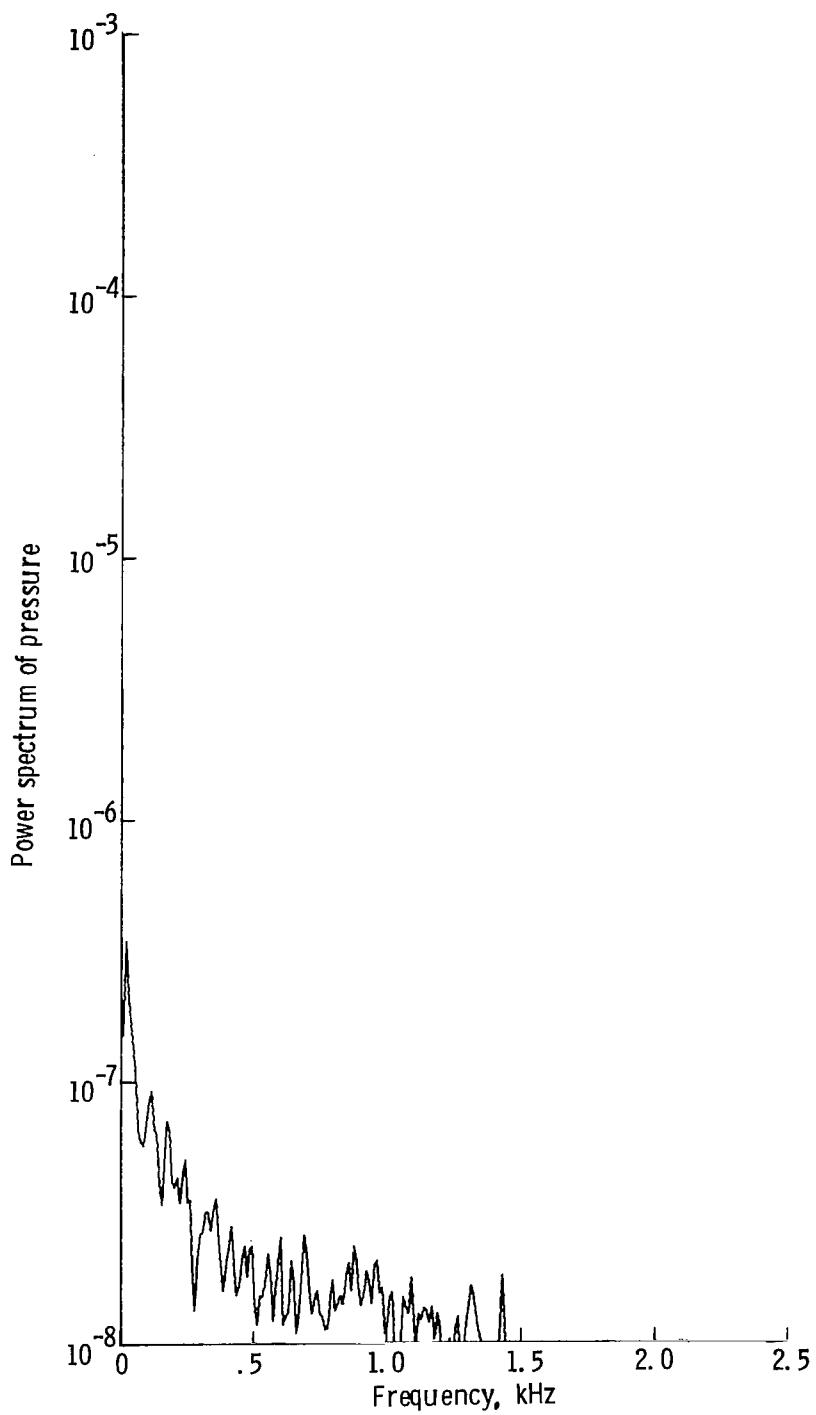
(d) Transducer 7.

Figure 58.- Continued.



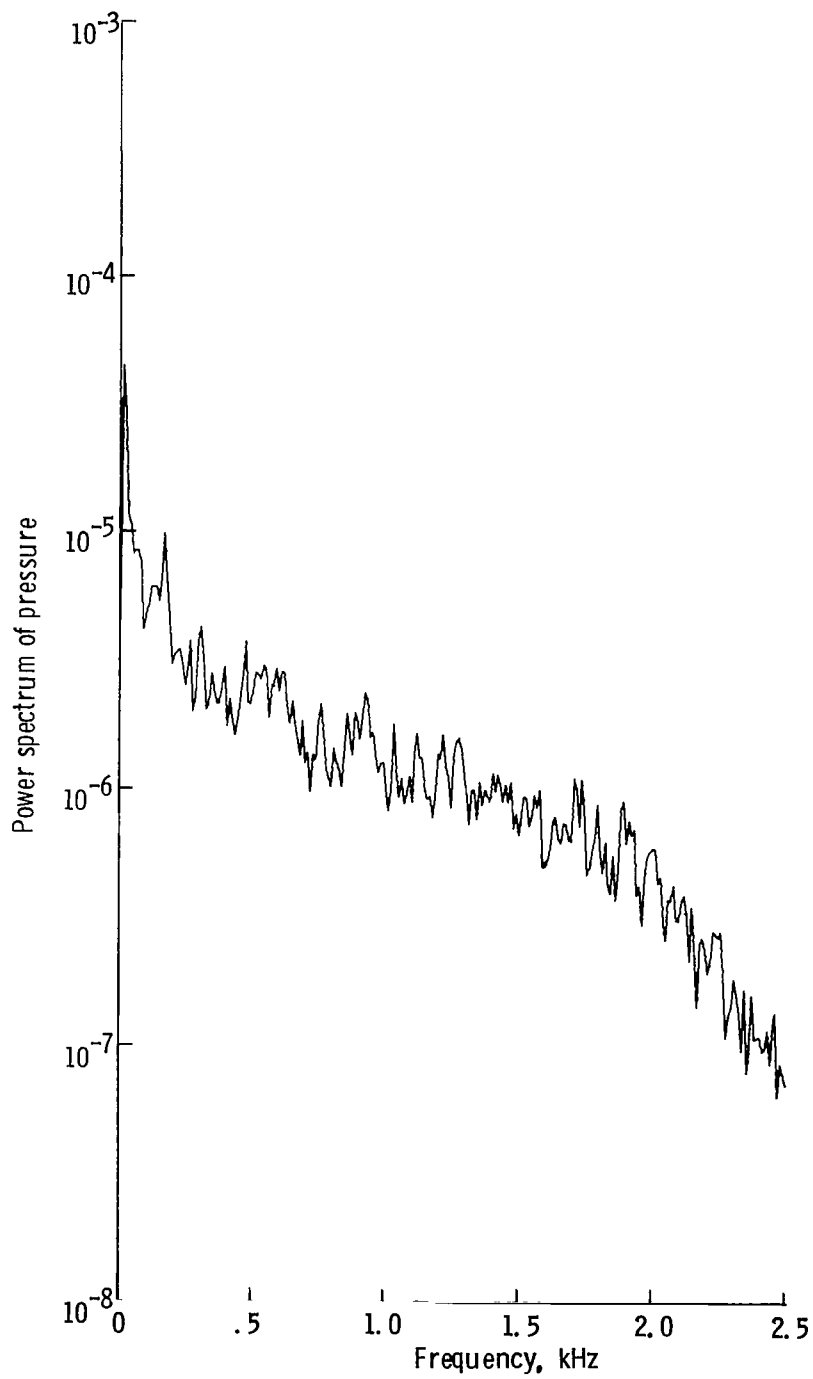
(e) Transducer 9.

Figure 58.- Continued.



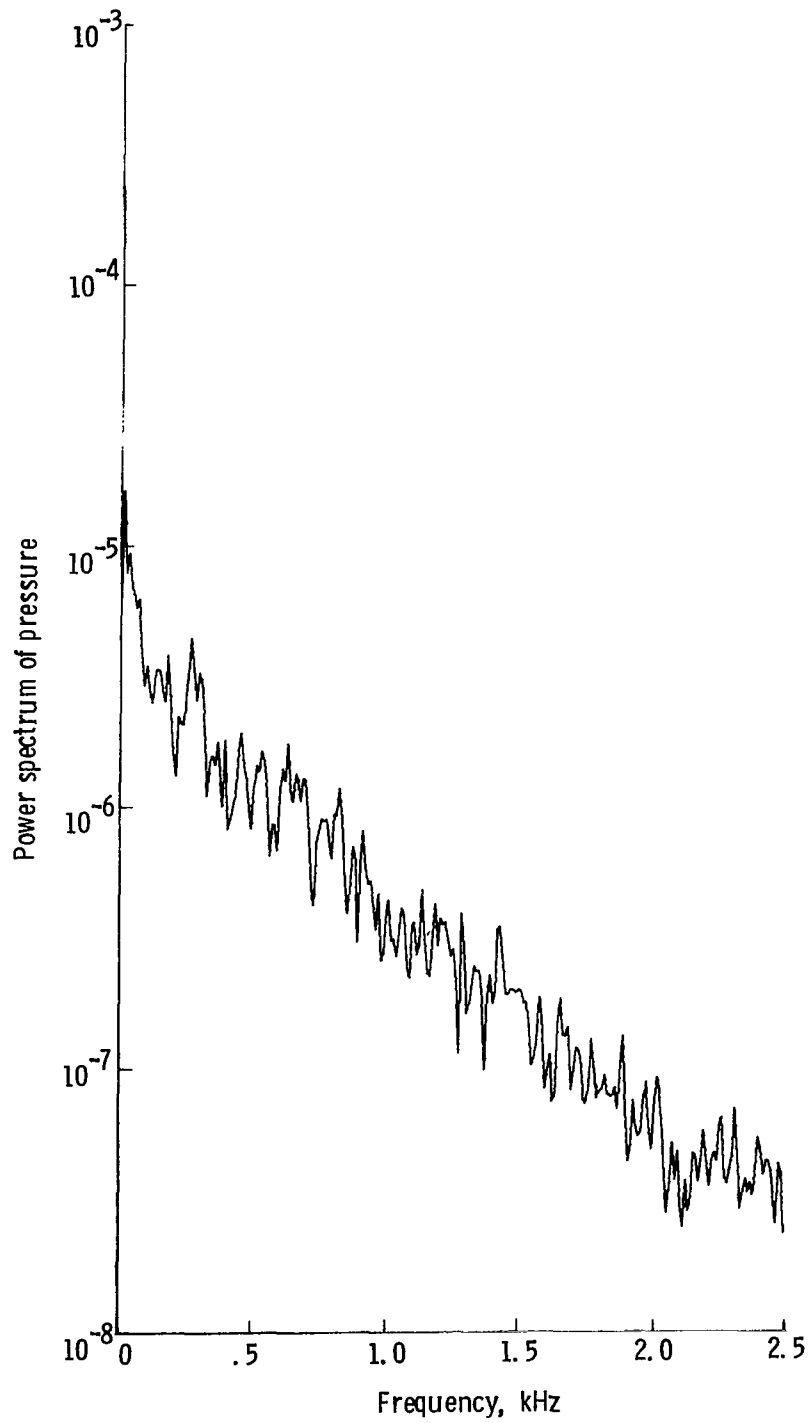
(f) Transducer 11.

Figure 58. - Continued.



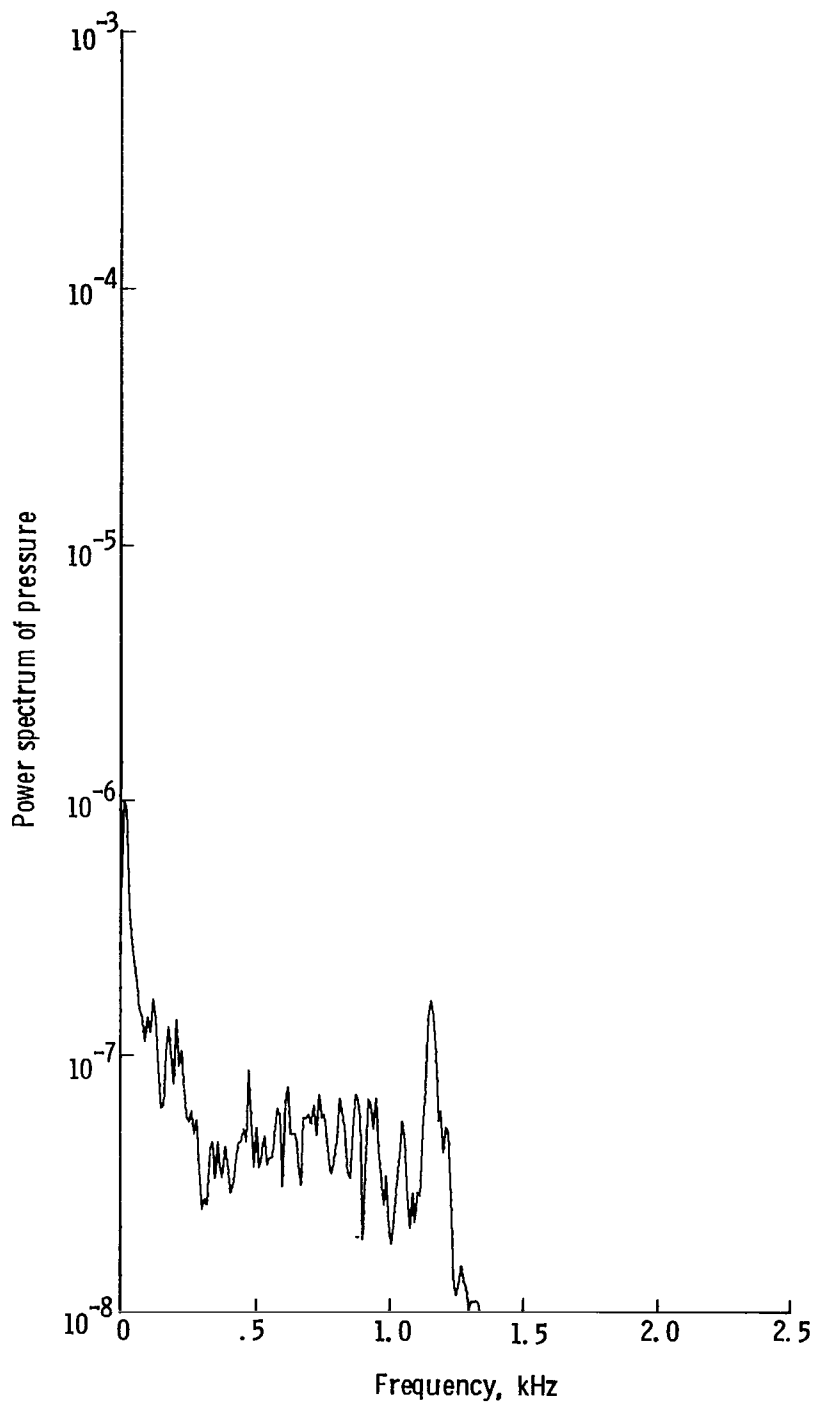
(g) Transducer 15.

Figure 58.- Continued.



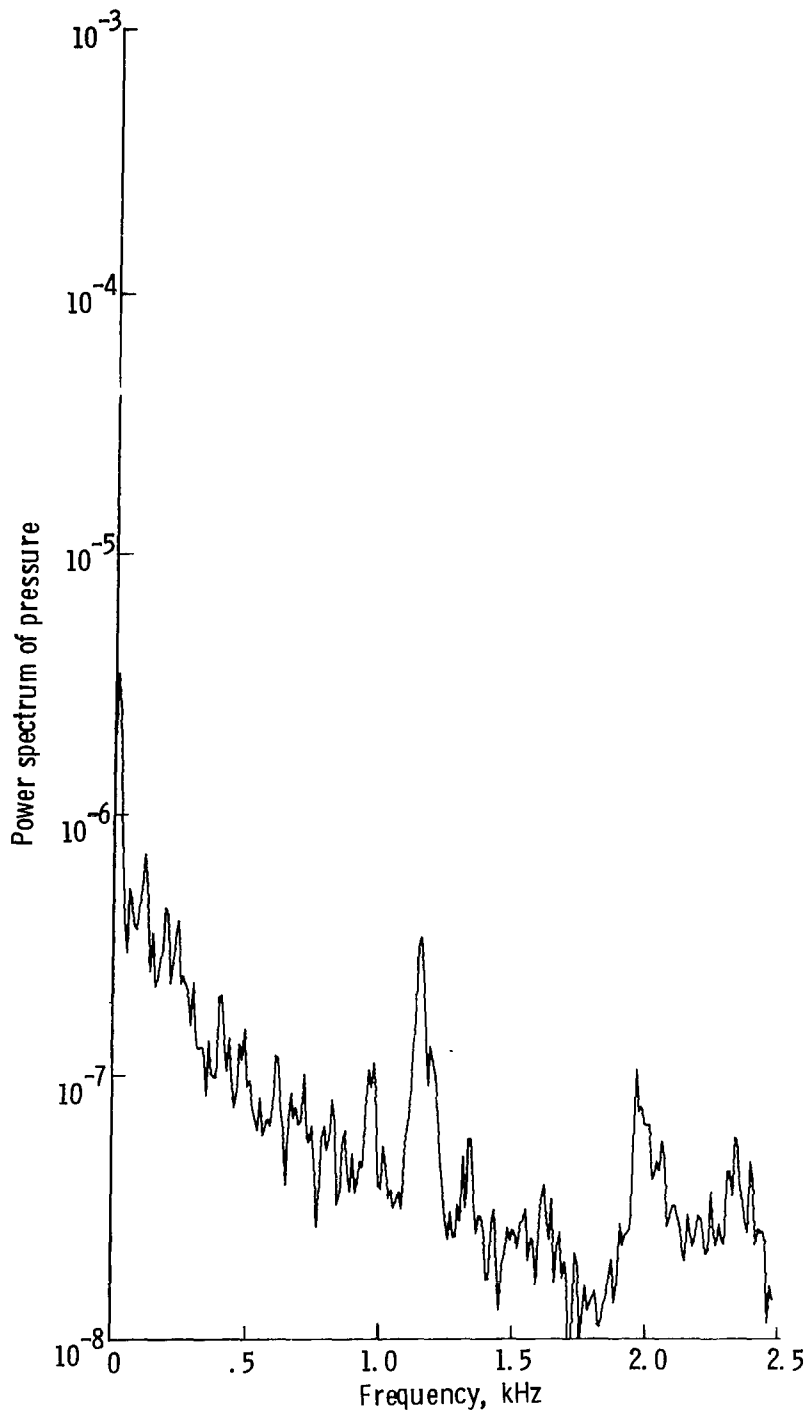
(h) Transducer 19.

Figure 58.- Continued.



(i) Transducer 2.

Figure 58. - Continued.



(j) Transducer 20.

Figure 58. - Concluded.

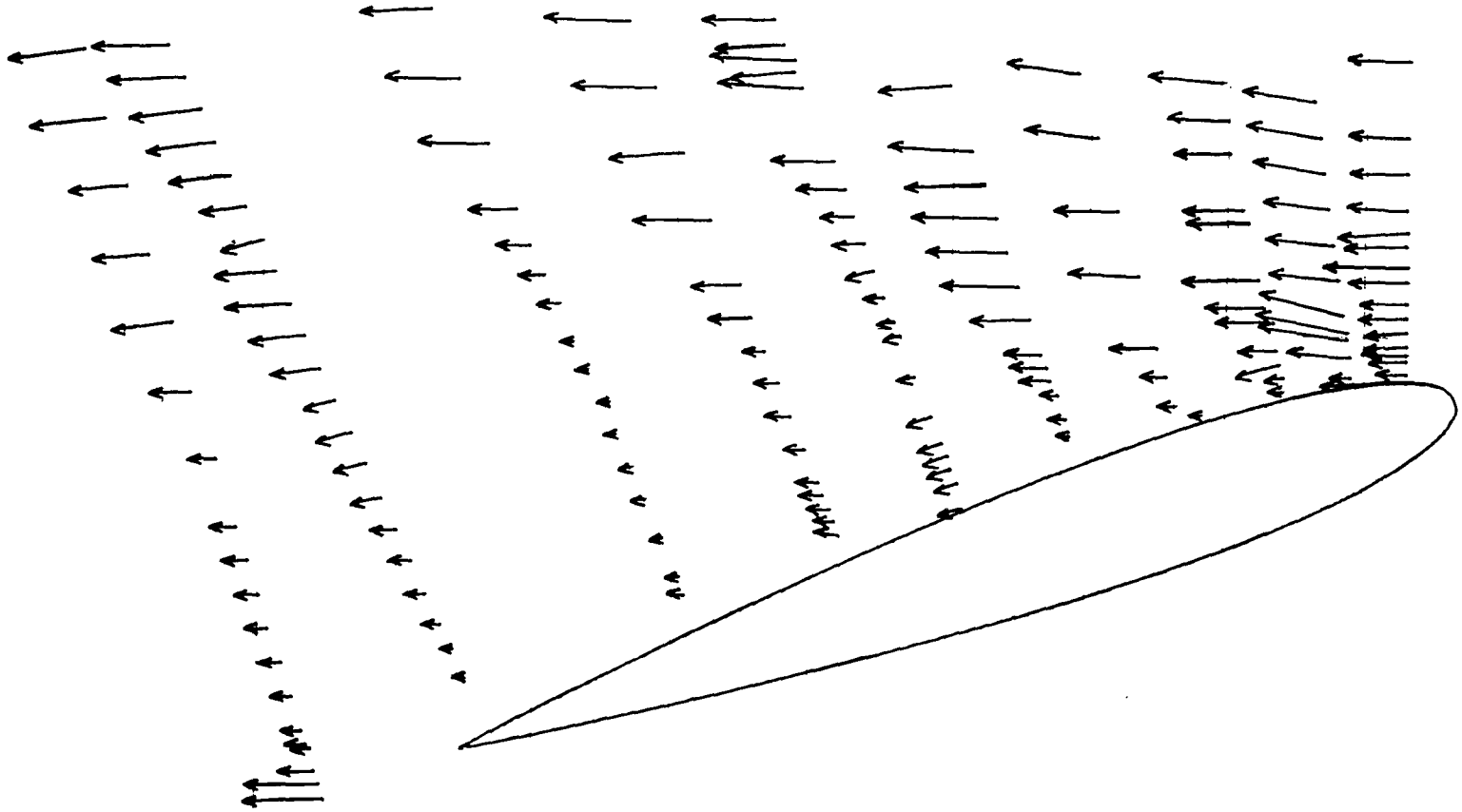


Figure 59. - Resultant average velocity vectors in prime direction normalized to free stream and corrected for velocity bias.

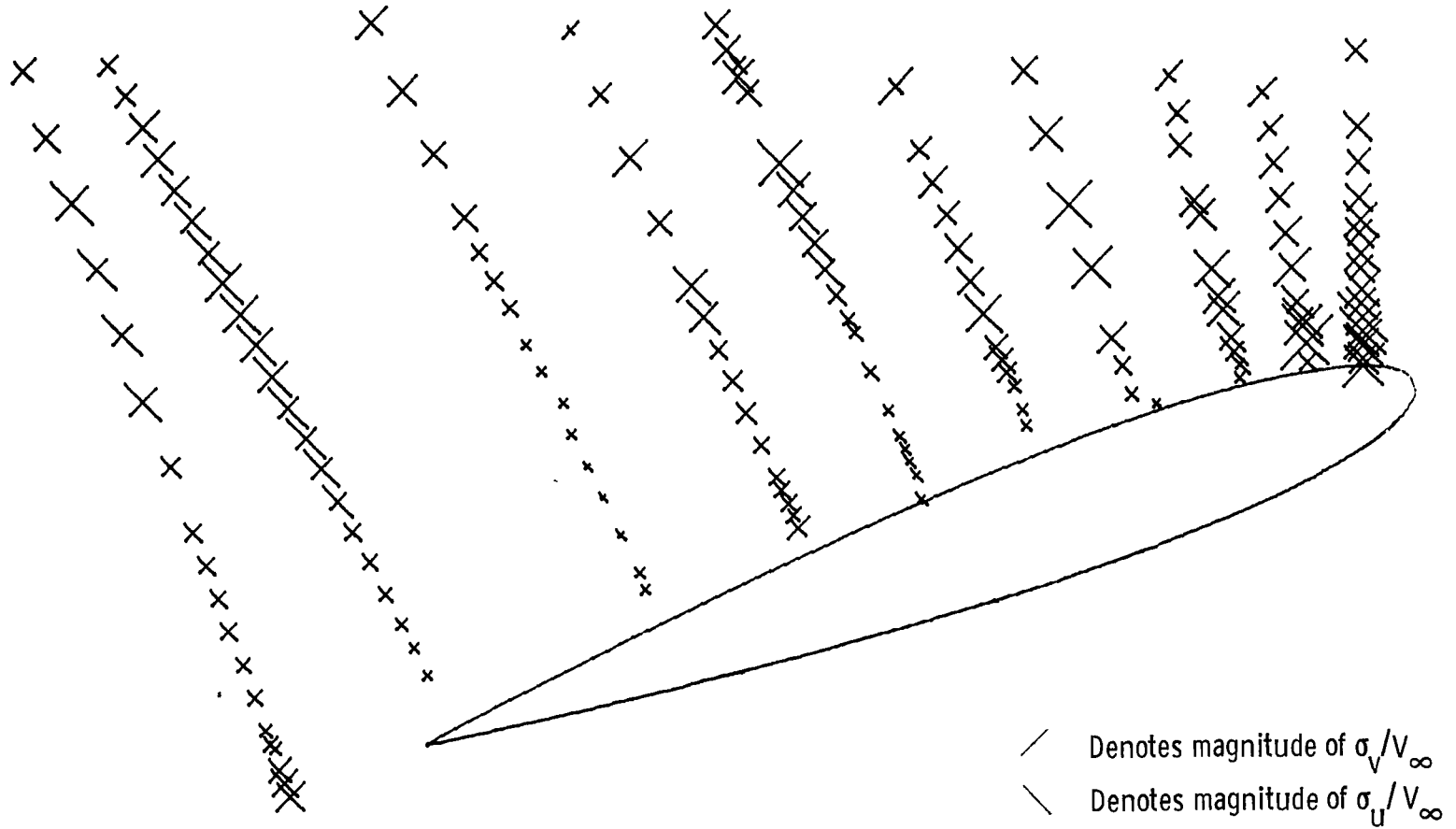


Figure 60. - Map of two components of standard deviation of velocity corrected for velocity bias and scaled by tunnel velocity.

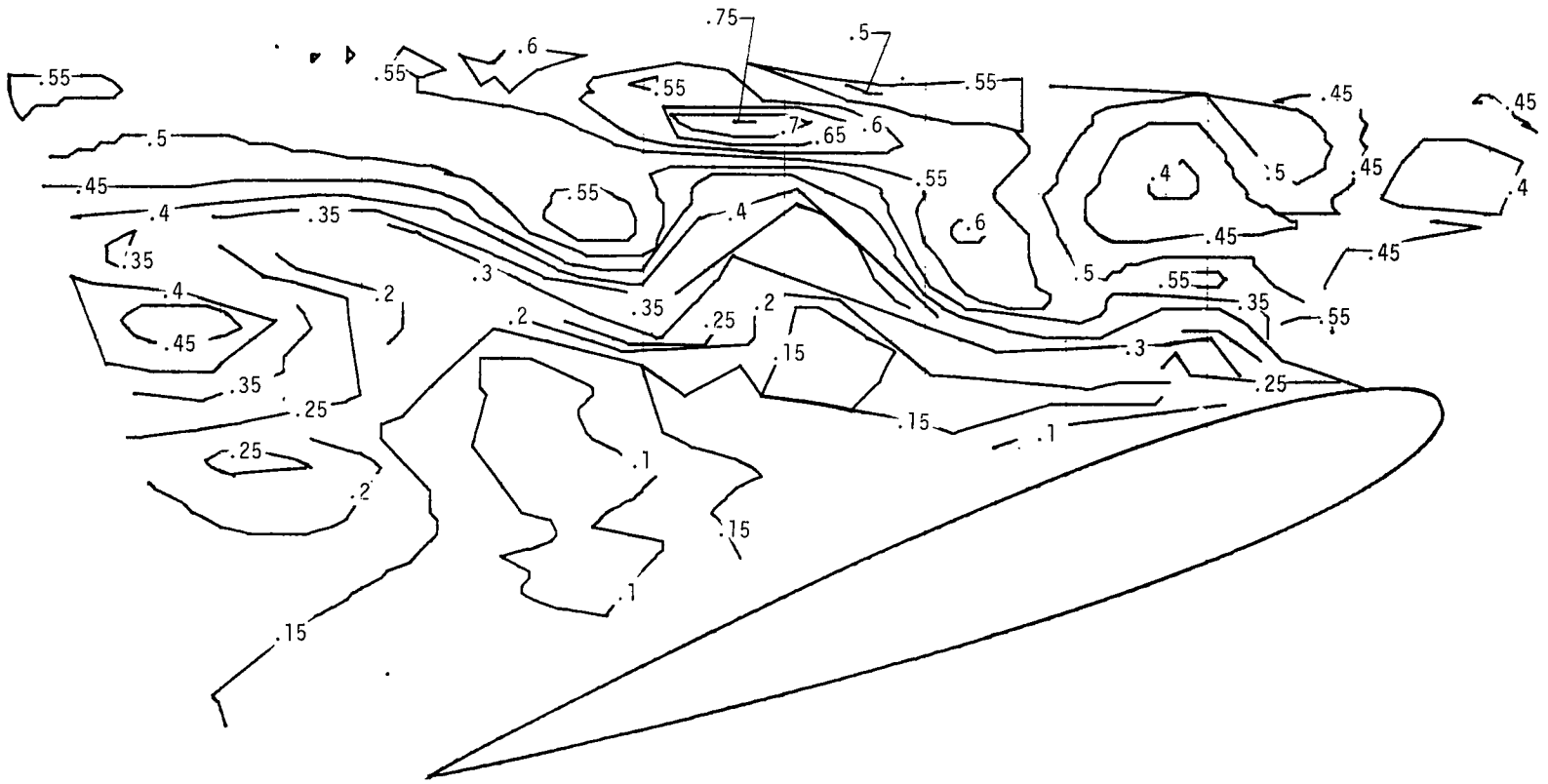


Figure 61.- Contours of constant Mach number based on average resultant velocity corrected for velocity bias.

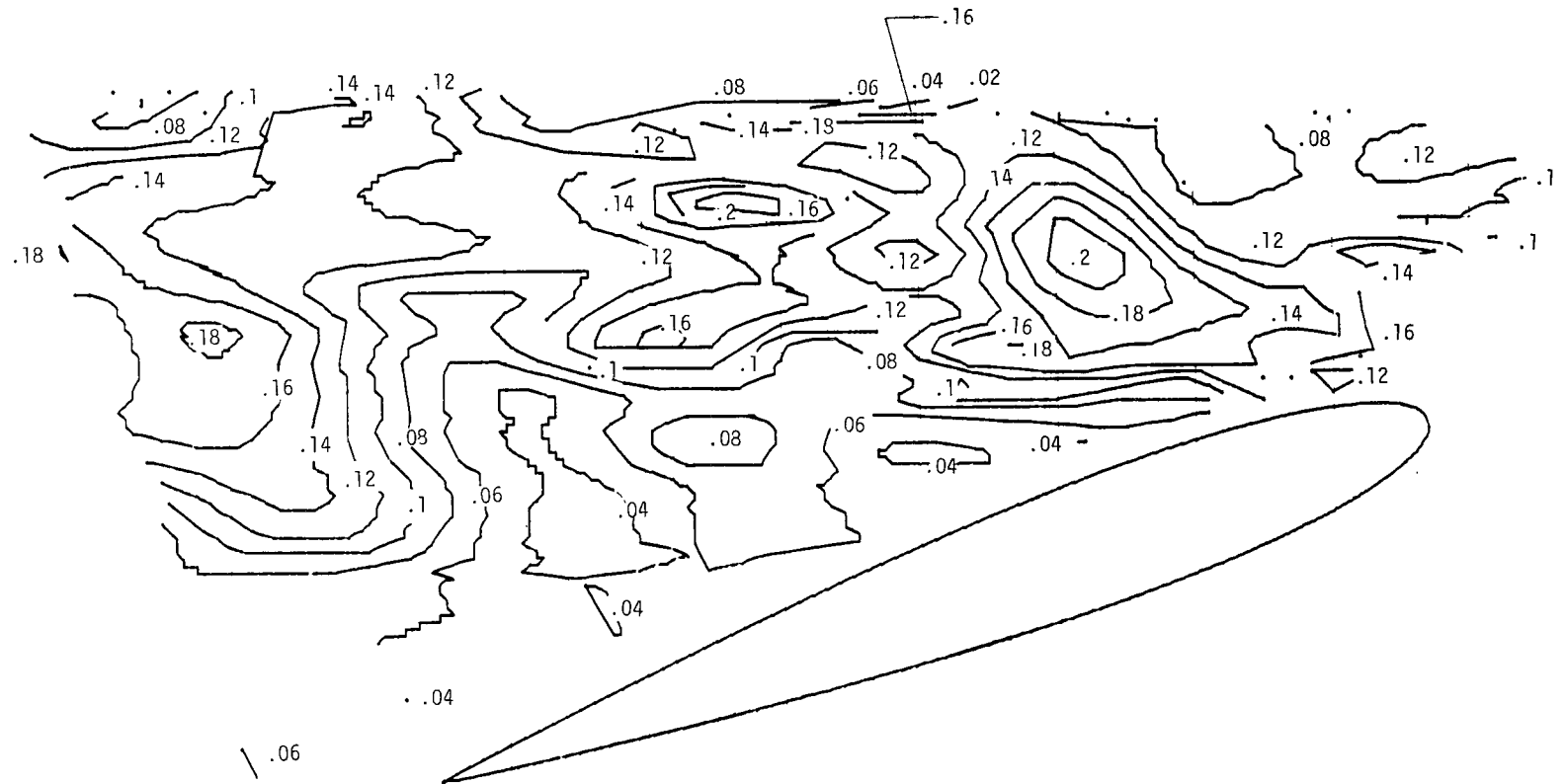


Figure 62.- Contours of constant resultant standard deviation corrected for velocity bias and converted to Mach number.

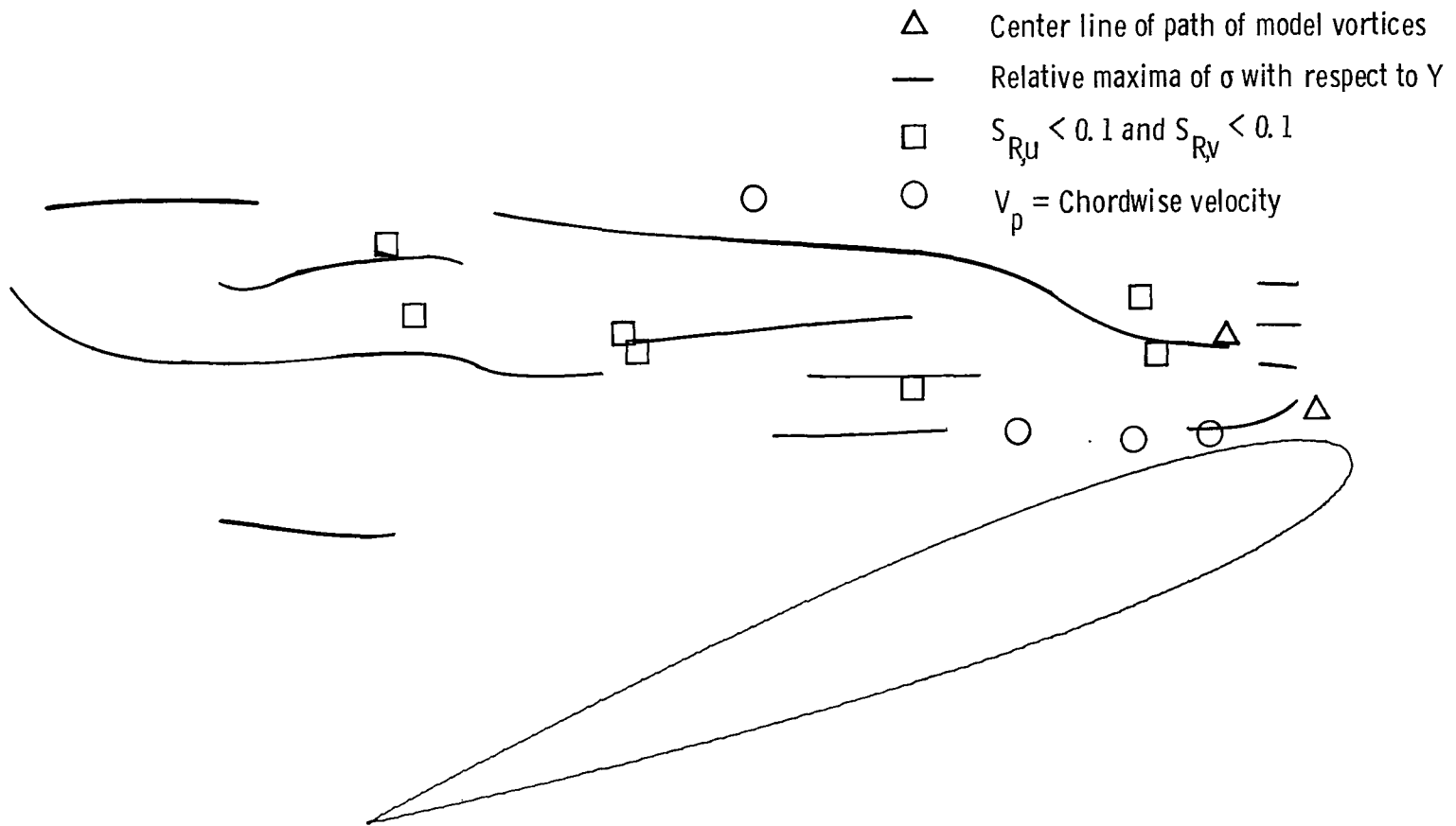
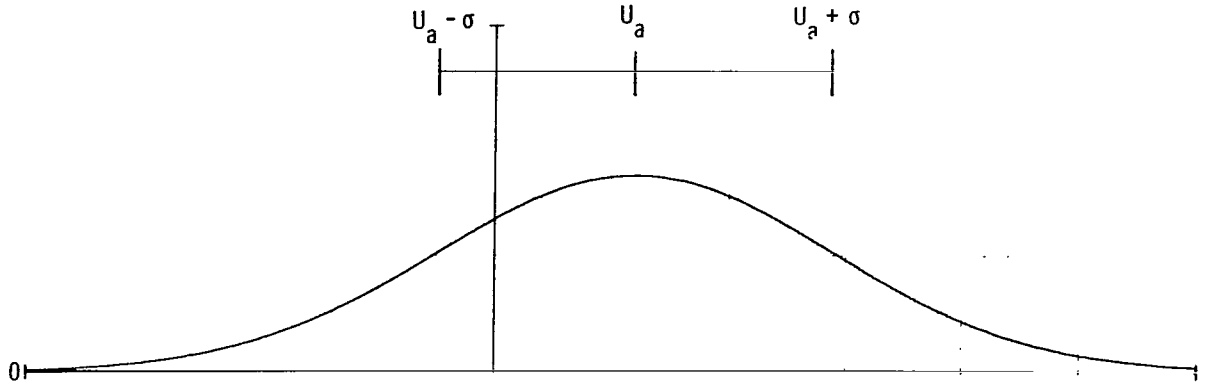
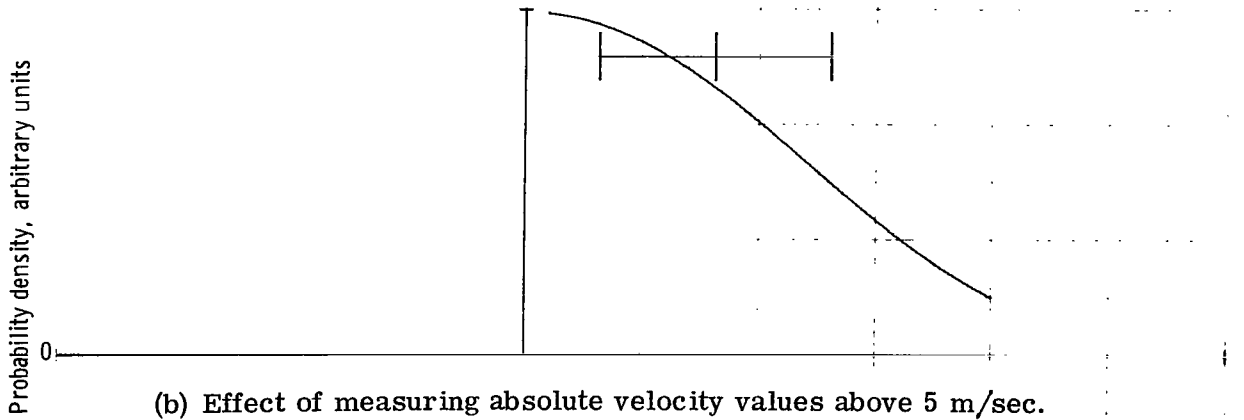


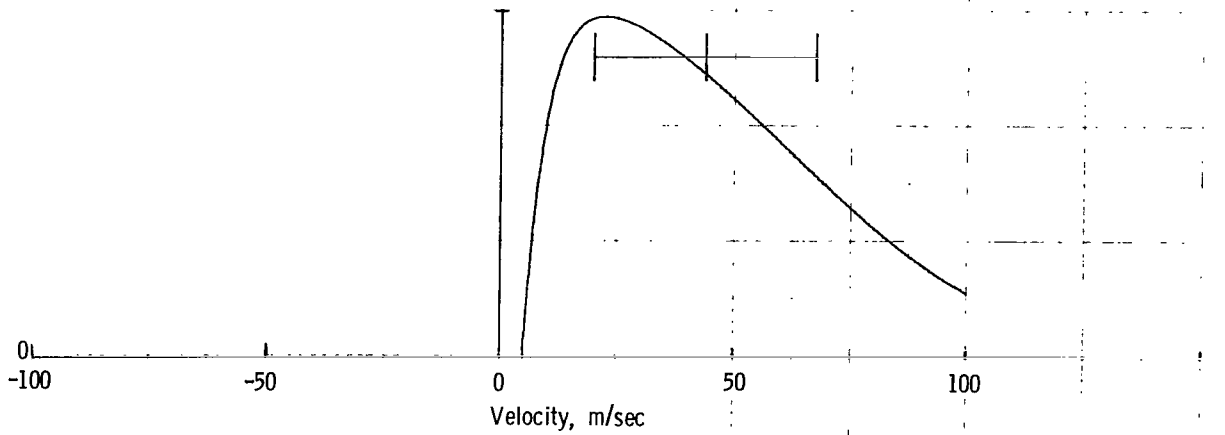
Figure 63.- Summary of indicators of center line of vortex paths.



(a) Theoretical histogram of Gaussian distribution.

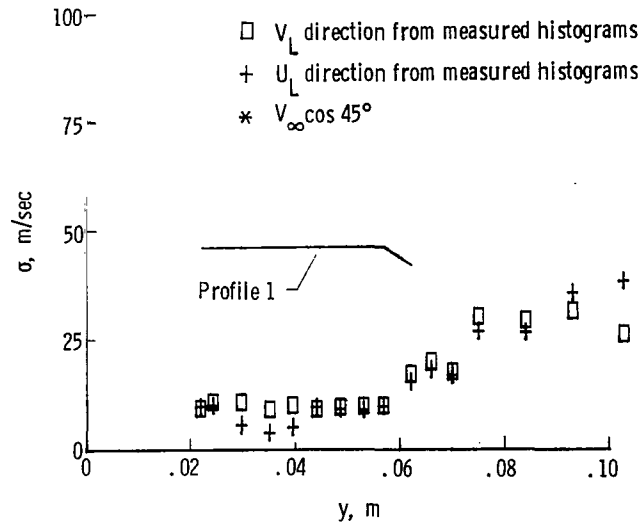
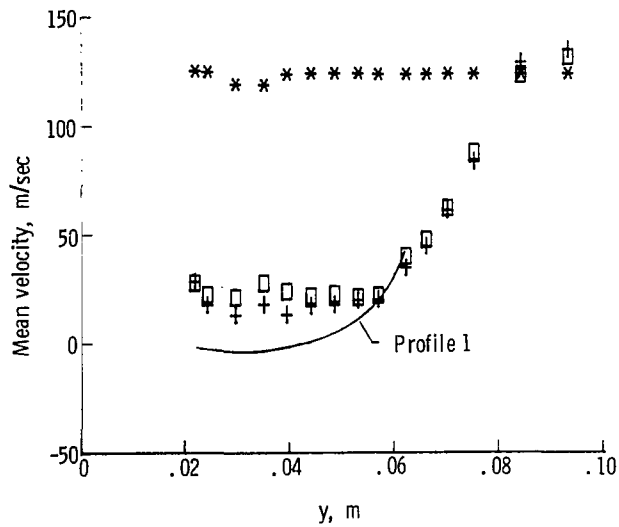


(b) Effect of measuring absolute velocity values above 5 m/sec.

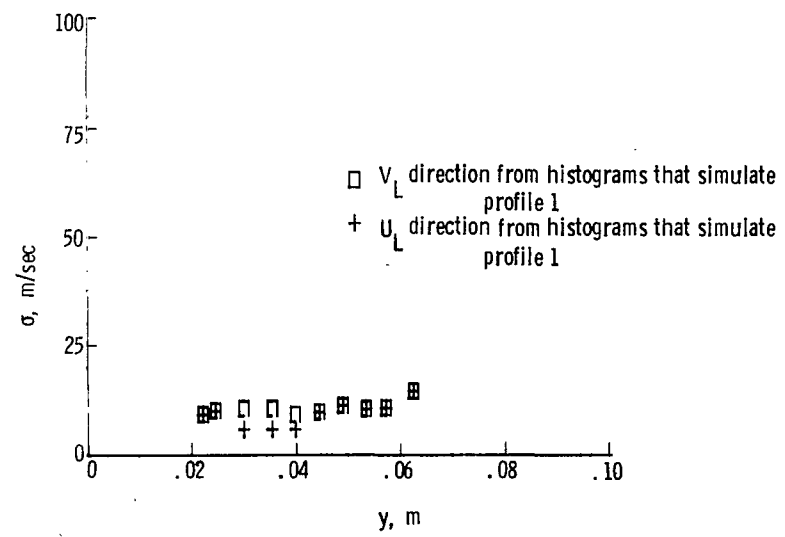
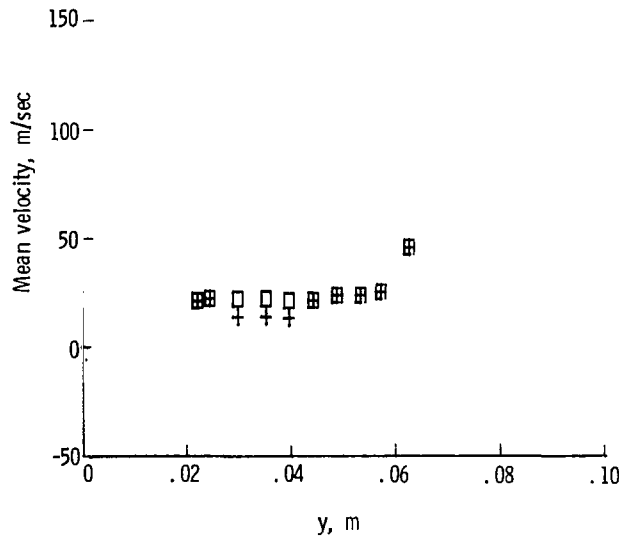


(c) Additional effect of high-pass filter.

Figure 64. - Effect of data processing on mean velocity and standard deviation.



(a) Comparison of values calculated from measured histograms at transducer 17 with arbitrarily chosen profile 1.



(b) Values calculated from histograms generated from profile 1.

Figure 65.- Comparison of measured histogram moments to moments simulated from hypothetical profile 1.

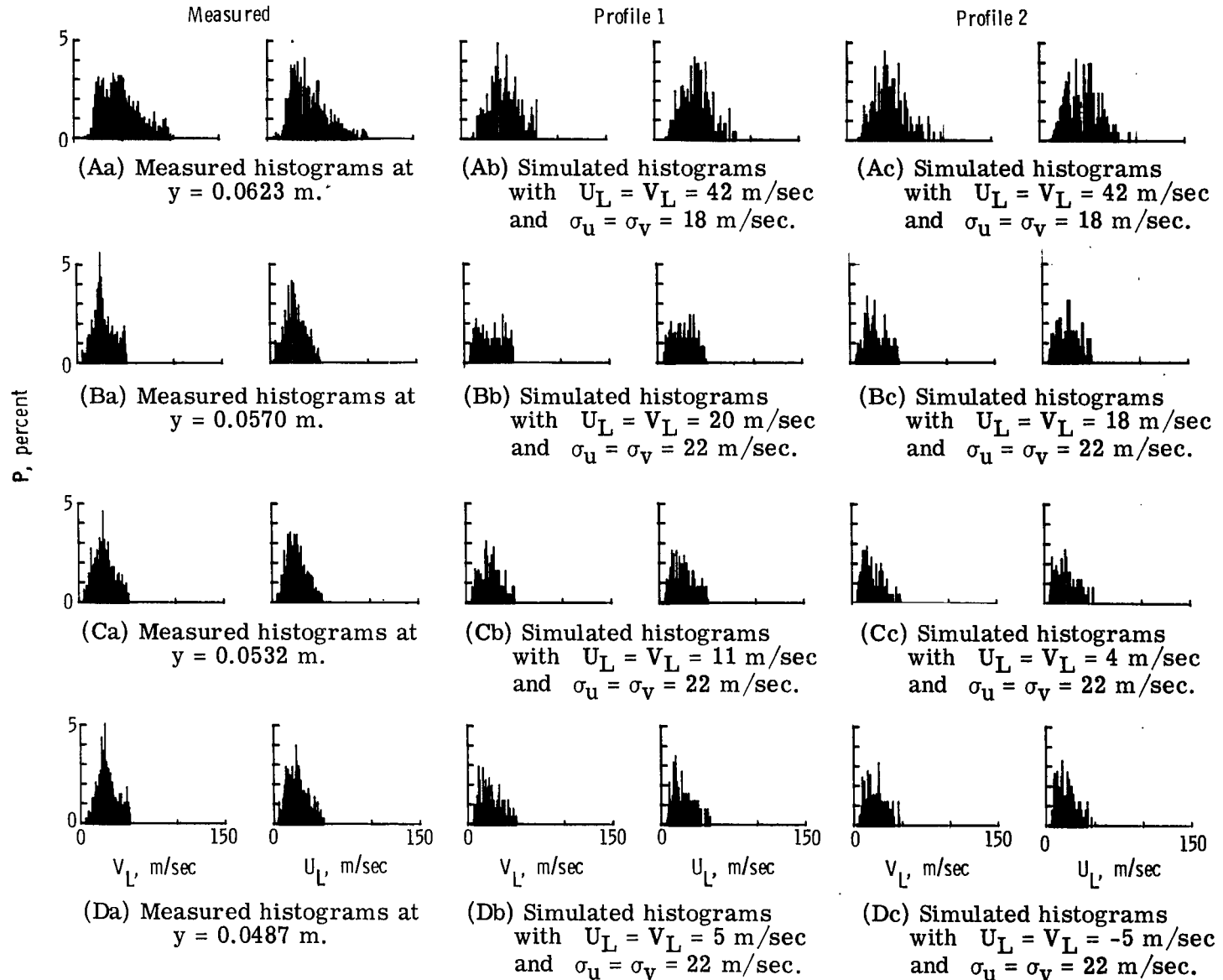


Figure 66.- Measured and simulated histograms above transducer 17.

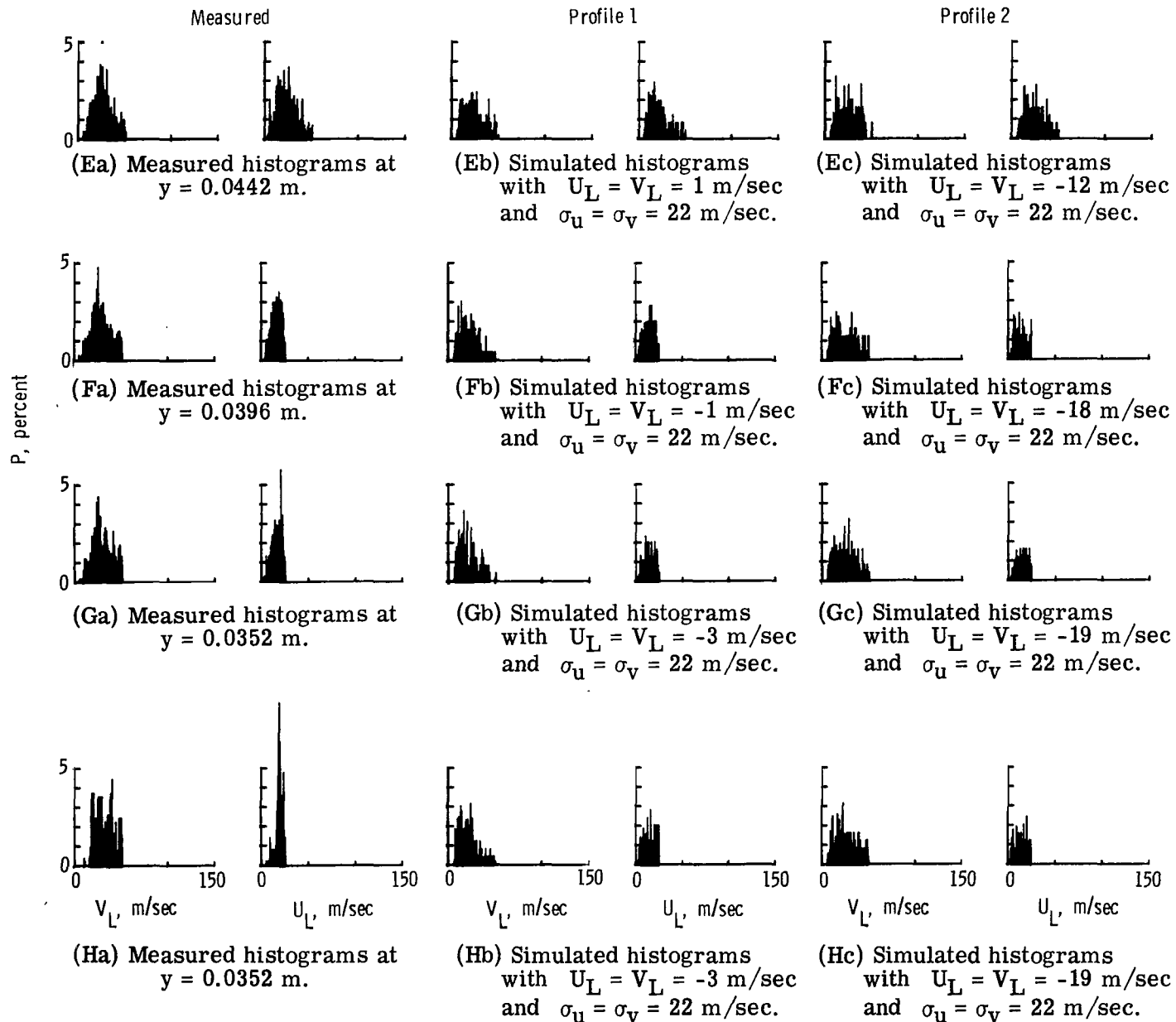


Figure 66.- Continued.

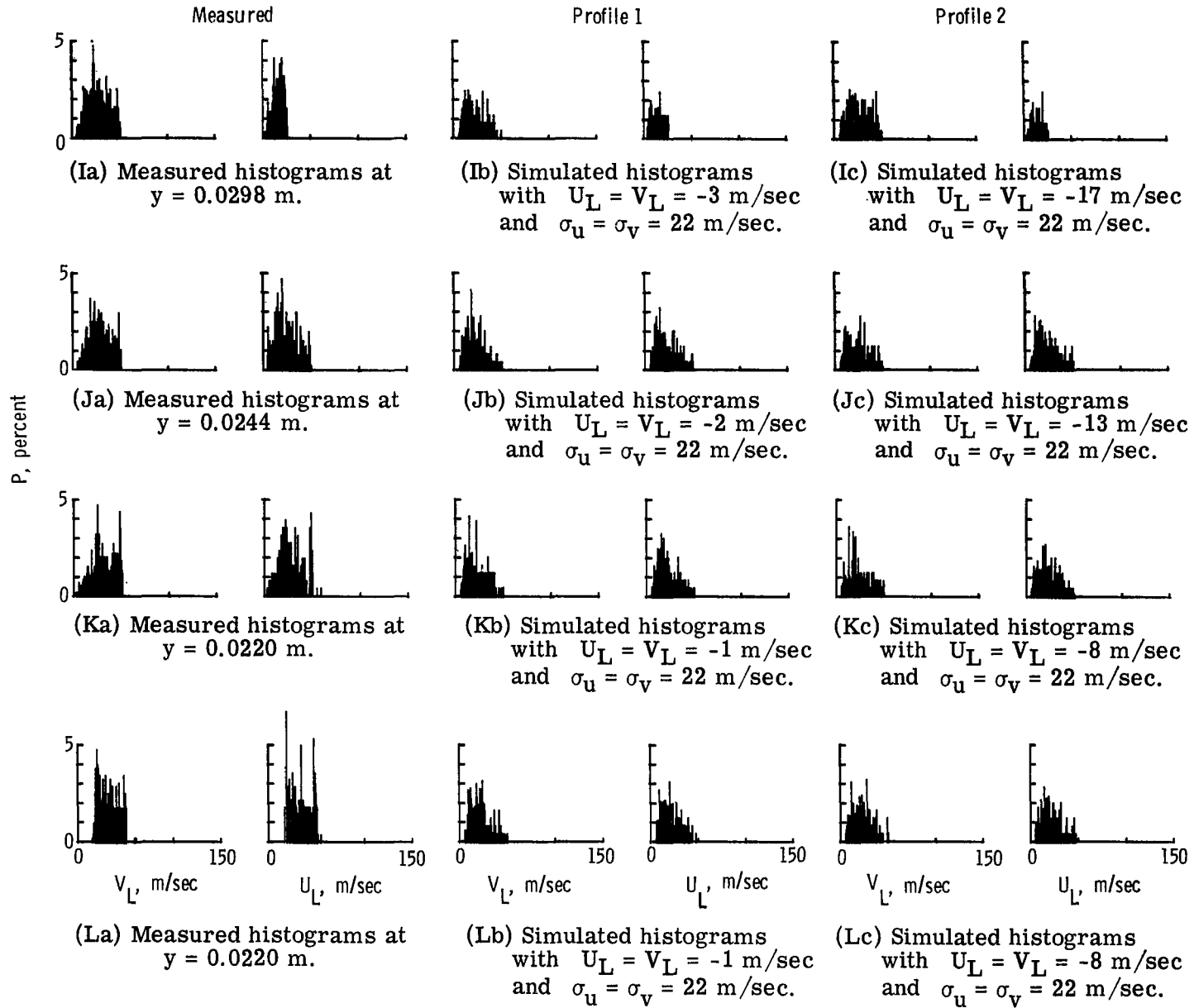
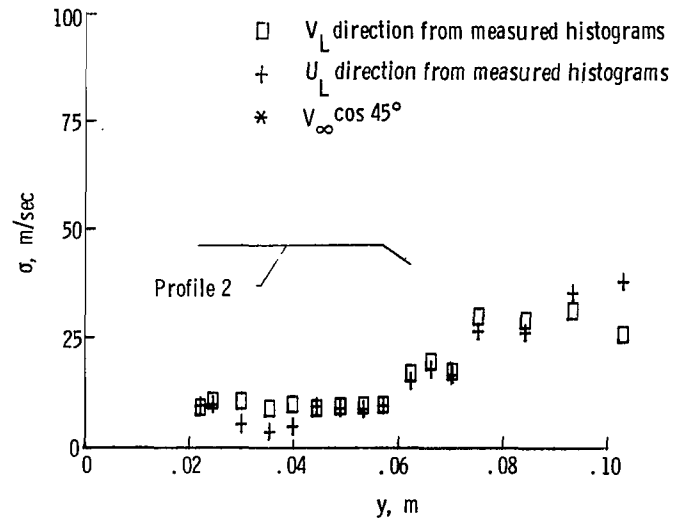
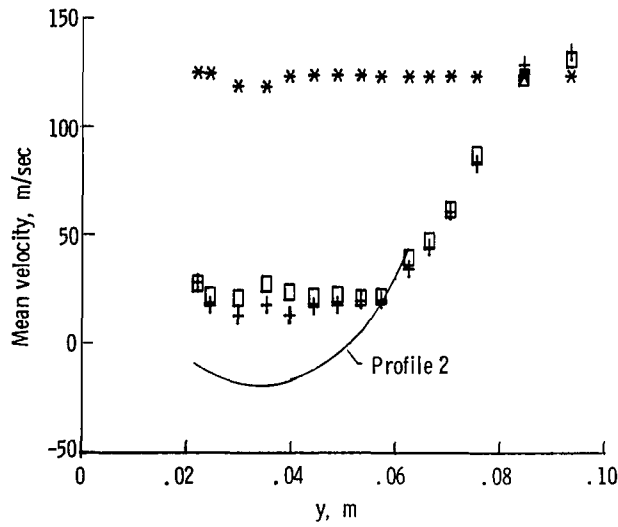
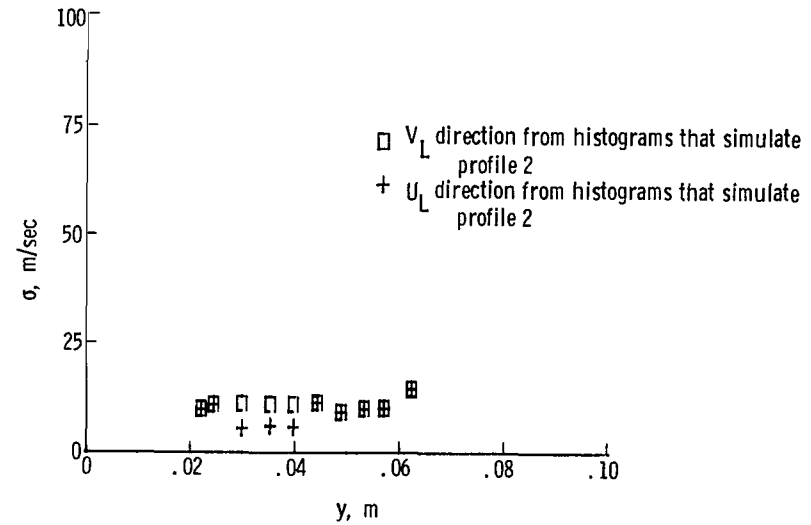
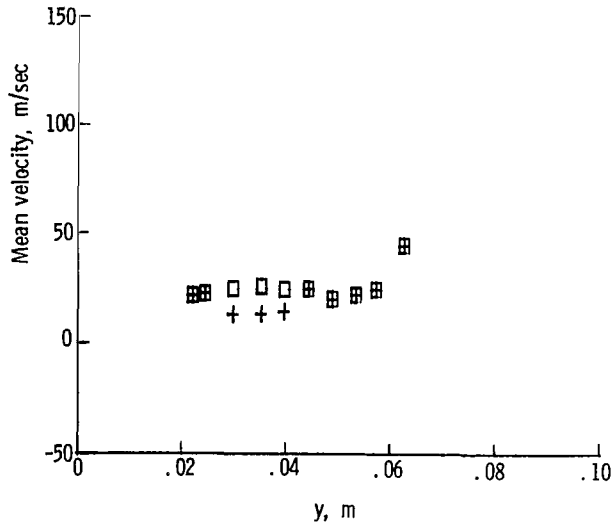


Figure 66.- Concluded.



(a) Comparison of values calculated from measured histograms at transducer 17 with arbitrarily chosen profile 2.



(b) Values calculated from histograms generated from profile 2.

Figure 67.- Comparison of measured histogram moments to moments simulated from hypothetical profile 2.



456 001 C1 U A 770701 S00903DS
DEPT OF THE AIR FORCE
AF WEAPONS LABORATORY
ATTN: TECHNICAL LIBRARY (SUL)
KIRTLAND AFB NM 87117

POSTMASTER: If Undeliverable (Section 158
Postal Manual) Do Not Return

"The aeronautical and space activities of the United States shall be conducted so as to contribute . . . to the expansion of human knowledge of phenomena in the atmosphere and space. The Administration shall provide for the widest practicable and appropriate dissemination of information concerning its activities and the results thereof."

—NATIONAL AERONAUTICS AND SPACE ACT OF 1958

NASA SCIENTIFIC AND TECHNICAL PUBLICATIONS

TECHNICAL REPORTS: Scientific and technical information considered important, complete, and a lasting contribution to existing knowledge.

TECHNICAL NOTES: Information less broad in scope but nevertheless of importance as a contribution to existing knowledge.

TECHNICAL MEMORANDUMS: Information receiving limited distribution because of preliminary data, security classification, or other reasons. Also includes conference proceedings with either limited or unlimited distribution.

CONTRACTOR REPORTS: Scientific and technical information generated under a NASA contract or grant and considered an important contribution to existing knowledge.

TECHNICAL TRANSLATIONS: Information published in a foreign language considered to merit NASA distribution in English.

SPECIAL PUBLICATIONS: Information derived from or of value to NASA activities. Publications include final reports of major projects, monographs, data compilations, handbooks, sourcebooks, and special bibliographies.

TECHNOLOGY UTILIZATION PUBLICATIONS: Information on technology used by NASA that may be of particular interest in commercial and other non-aerospace applications. Publications include Tech Briefs, Technology Utilization Reports and Technology Surveys.

Details on the availability of these publications may be obtained from:

SCIENTIFIC AND TECHNICAL INFORMATION OFFICE

NATIONAL AERONAUTICS AND SPACE ADMINISTRATION

Washington, D.C. 20546